VOLUME 31 JULY 1953 NUMBER 5

Canadian Journal of Physics

Editor: G. M. VOLKOFF

Published by THE NATIONAL RESEARCH COUNCIL
OTTAWA CANADA

CANADIAN JOURNAL OF PHYSICS

(*Formerly Section A, Canadian Journal of Research*)

The CANADIAN JOURNAL OF PHYSICS is published bimonthly by the National Research Council of Canada under the authority of the Chairman of the Committee of the Privy Council on Scientific and Industrial Research. Matters of general policy are the responsibility of a joint Editorial Board consisting of members of the National Research Council of Canada and the Royal Society of Canada.

The National Research Council of Canada publishes also: *Canadian Journal of Botany, Canadian Journal of Chemistry, Canadian Journal of Medical Sciences, Canadian Journal of Technology, Canadian Journal of Zoology.*

EDITORIAL BOARD

Representing

NATIONAL RESEARCH COUNCIL

DR. C. W. ARGUE (*Chairman*),
Dean of Science and Professor of Biology,
University of New Brunswick,
Fredericton, N.B.

DR. G. E. HALL,
President and Vice-Chancellor,
University of Western Ontario,
London, Ont.

DR. T. THORVALDSON,
Dean Emeritus of Graduate Studies,
University of Saskatchewan,
Saskatoon, Sask.

DR. W. H. WATSON,
Professor and Head of the Department of Physics,
University of Toronto,
Toronto, Ont.

ROYAL SOCIETY OF CANADA

Section III

DR. G. M. VOLKOFF,
Professor of Physics,
University of British Columbia,
Vancouver, B.C.

DR. T. THORVALDSON,
Dean Emeritus of Graduate Studies,
University of Saskatchewan,
Saskatoon, Sask.

Section V

DR. D. L. BAILEY,
Department of Botany,
University of Toronto,
Toronto, Ont.

DR. E. HORNE CRAIGIE,
Department of Zoology,
University of Toronto,
Toronto, Ont.

THE CANADIAN ASSOCIATION OF PHYSICISTS

DR. G. M. VOLKOFF,
Professor of Physics,
University of British Columbia,
Vancouver, B.C.

THE CHEMICAL INSTITUTE OF CANADA

DR. H. G. THODE,
Department of Chemistry,
McMaster University,
Hamilton, Ont.

Ex officio

DR. LÉO MARION (*Editor-in-Chief*),
Director, Division of Pure Chemistry,
National Research Laboratories,
Ottawa.

DR. H. H. SAUNDERSON,
Director, Division of Information Services,
National Research Council,
Ottawa.

Manuscripts should be addressed to:

DR. LÉO MARION,
Editor-in-Chief,
Canadian Journal of Physics,
National Research Council,
Ottawa, Canada.

Each manuscript should be typewritten, double-spaced, and the original and one extra copy submitted (see **Notice to Contributors** inside of back cover).

Subscriptions, renewals, and orders for back numbers should be addressed to:

Administrative Services,
National Research Council,
Ottawa, Canada.

Subscription rate: $3.00 a year; single numbers: 50 cents. Special rates can be obtained for subscriptions to more than one of the Journals published by the National Research Council

Canadian Journal of Physics

Issued by THE NATIONAL RESEARCH COUNCIL OF CANADA

VOLUME 31 JULY 1953 NUMBER 5

A RAPID-SCANNING AURORAL SPECTROMETER[1]

BY D. M. HUNTEN

ABSTRACT

A spectrometer is described which is capable of obtaining an auroral spectrum in 10 sec. with 10Å resolution. It uses a 4 by 4 in., 6000 lines/cm. grating and parabolic mirrors for focusing. The detector is a 1P21 photomultiplier cooled by dry ice, and the spectrum is recorded by a high-speed magnetic oscillograph. The amplifiers are described and a few sample spectra shown. Some relevant optical equations are collected in an appendix.

1. INTRODUCTION

For many years the spectrum of the aurora has been studied by means of fast spectrographs of low dispersion. More recent instruments have considerably higher dispersion but are little faster. Outstanding among these are the ones designed by Meinel, using a plane grating and a flat-field Schmidt camera. A spectrograph of this type was built in this laboratory by Petrie (4), and has been in use for some time. Exposures range from 15 min. to several hours depending on the brightness of the aurora.

To the eye it is evident that many types of aurora show rapid changes in both form and color, changes which cannot possibly be followed by a spectrograph. Since photoelectric devices seemed promising for such studies, a program for their investigation was initiated. It was expected that an increase in time resolution would be achieved only by a considerable sacrifice in spectral resolution, and the first trials were made with interference filters which passed some of the stronger radiations. The signals produced by a 1P21 photomultiplier were so strong that the filters were replaced with a rather crude two-prism monochromator, scanning from 3800 to 6000 Å in five minutes. This instrument gave some useful results (1), but was inconvenient and slow. The present instrument incorporates many features suggested by the experience with the older one, and is about one hundred times faster. The improvement is chiefly due to two things: replacement of the prisms by a plane grating, and refrigeration of the detector. The grating gathers more light because of its larger area (4 in. × 4 in. instead of 1½ in. × 2 in.), and allows the use of wider slits for the same spectral resolution because of its higher dispersion. Cooling the detector reduces its noise level and permits smaller signals to be detected. Collimation and focusing are done by parabolic mirrors so that the focus is independent of wave length.

[1] *Manuscript received January 2, 1953.*
Contribution from the Department of Physics, University of Saskatchewan, Saskatoon, Sask. Sponsored by the Geophysics Research Division of the Air Force Cambridge Research Center under Contract AF 19(122)-152.

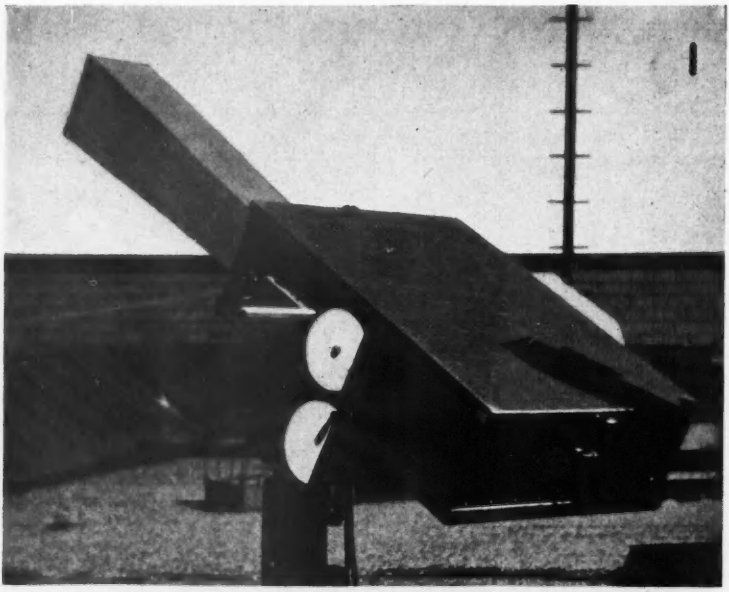

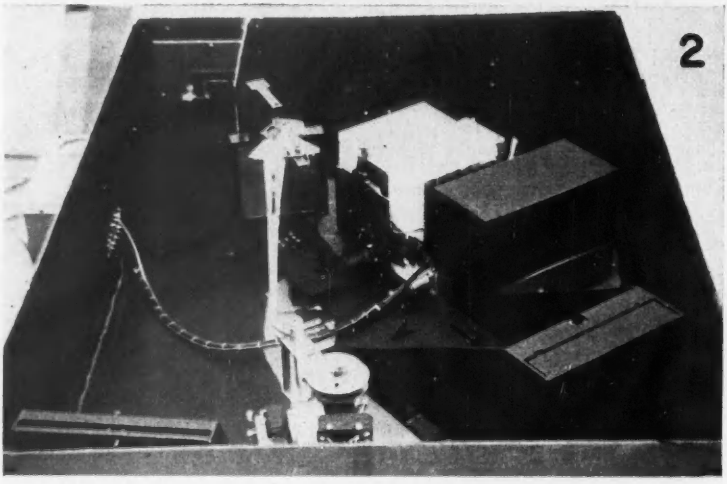

FIG. 1. Spectrometer and its mounting on the roof of the Physics Building.
FIG. 2. Interior of the spectrometer.

The spectrum is scanned, normally every 10 sec., by oscillating the grating. The spectral range covered can be chosen anywhere from 10 to 2500 Å for different problems. The slits are usually set to give 10Å resolution, since this has been found to be sufficient for most purposes. Useful spectra are obtained

from displays of medium or greater brightness for a 2500 Å range, and from all but the faintest for a 200 Å range.

The short scanning time makes it practical to take two-station photographs of the aurora being observed, so that spectra can be obtained from known heights. The spectra of short-lived forms, and rapid changes in these spectra, can be studied. Photoelectric detection is very suitable for the measurement of relative and absolute intensities, being both simpler and more accurate than photographic methods. On the other hand, it has one serious limitation: if the brightness of the aurora changes during a scan, the relative intensities recorded will be false. Most auroral forms have been found to be quiet enough to be studied with the 10-sec. scan, and sometimes it is possible to average several successive spectra and so reduce the error considerably.

2. SPECTROMETER PROPER

Mounting and Housing

These may be seen in Fig. 1. The mounting, designed by Petrie (4), permits the observation of any part of the sky; motions in altitude and azimuth are produced by worm drives.

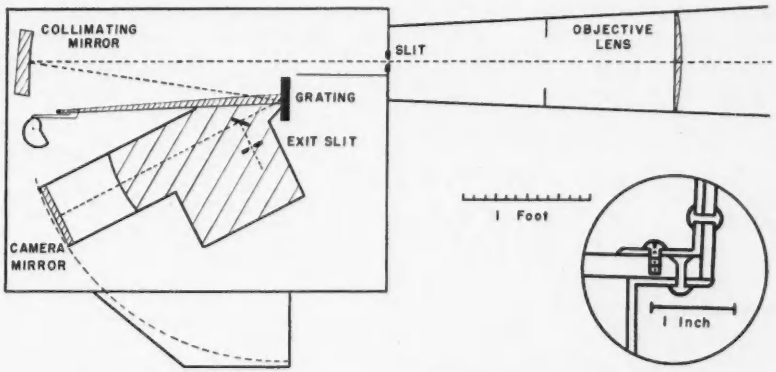

FIG. 3. Schematic drawing of the spectrometer. Inset: construction of corners of the box.

The housing, designed to be rigid but still as light as possible, is built around a base-plate of $\frac{1}{4}$-in., 24ST dural, reinforced at the edges by 1-in. dural angle, top and bottom (see inset, Fig. 3), and on the bottom by two diagonals of dural angle. Three walls are bent out of one piece of $\frac{1}{8}$-in. dural. The front wall, which carries the objective lens, is rigidly supported by the two side walls and the baffle (between grating and slit, Fig. 3). A blister in the right-hand wall allows the camera mirror to swing through a large angle. Many of these details are illustrated by Figs. 2 and 3. The lid is made of 1/16-in. dural with the edges bent down 1 in. to shed rain. A removable box structure holding the objective lens is supported by the front wall, as already mentioned. When the instrument is not in use, this box is detached and the entrance slit is covered by a dural plate; a heavy canvas cover gives further protection against weather.

Optical Parts and Scanning Mechanism

The optical line-up, illustrated by Figs. 2 and 3, is as follows: objective lens, 9-in. diameter and 27-in. focal length; entrance slit, $1\frac{1}{2}$ in. long; collimating mirror, 6-in. off-axis paraboloid of 34-in. focal length; plane grating, 4×4-in. aluminum-on-glass, 6000 lines per cm. with a blaze angle of 17.5°; focusing mirror, 6-in. on-axis paraboloid of 22-in. focal length; small 45° plane mirror; exit slit, 1 in. long, with electrically-operated shutter; and photomultiplier tube.

The objective lens produces an image of the sky in the plane of the entrance slit, which thus defines a field of view 3° high and rather narrow. For problems demanding a smaller field, the slit could of course be masked; for example, a $\frac{1}{2}$-in. length would give a 1° field. The lens need not be of high optical quality and was hence made of lucite on a lathe. One side was left plane; the other was turned to a spherical surface by the technique described in Strong (5), and then fine-ground and polished against a concave lap. Besides being easy to fabricate, lucite has the advantages of light weight and high ultraviolet transparency.

As indicated in Fig. 3, the focusing (camera) mirror, 45° mirror, exit slit, and photomultiplier are mounted on a subbase and may be removed as a unit (the "detector unit") for focusing and alignment. It is demonstrated in the Appendix that the blaze of the grating can be shifted to different wave lengths by turning both grating and detector unit through the correct angles. Suitable adjustments are provided, the grating ranging over an angle of 30°, and the detector unit over 55°. In addition, the grating is oscillated through a small angle to produce the scan. A cam rotating once every 10 sec. imparts a saw-tooth motion to a short lever (4 in. long). A long lever of adjustable length (about 20 in.) is fixed to the grating. By making the end of the long lever bear on the side of the short lever at various points, various amplitudes of oscillation can be given to the grating, and the spectral range can be adjusted, as required, by a factor of about ten to one. Changing cams allows larger factors to be obtained, so that spectral ranges from 10 to 2500 Å are available.

A second cam rotating with the first operates a microswitch which controls the clamping relay in the amplifier, and the shutter in front of the exit slit. This shutter closes during the flyback; it is made of light sheet aluminum and actuated by a telephone-type relay with the contact springs removed.

3. ELECTRONIC CIRCUITS

Detector and Housing

The detector is a 1P21 photomultiplier, cooled with dry ice to reduce the dark current and the resulting shot noise. In practice, the shot noise produced by fluctuations in the signal current is much greater than the dark noise. The box holding the dry ice is a 6-in. cube (outside dimensions) insulated with an inch thickness of Styrofoam. The resistance chain for the photomultiplier is mounted on the outside, and the leads to the tube are made of fine resistance wire, as long as possible, in order to reduce heat conduction. A double-window system is used to eliminate frosting. The outside window is kept above the dew point

by a heater. The space between is isolated and the moisture in it freezes out on a metal rim around the inside window, since it is arranged to cool first. (The above details were very kindly communicated by Dr. G. E. Kron, Lick Observatory.) The high voltage for the photomultiplier comes from a commercial regulated power supply.

Amplifiers

The circuit of the preamplifier is shown in Fig. 4, and of the main amplifiers in Fig. 5. Large amounts of negative feedback are used everywhere to stabilize the gain and give good linearity. The spectra are recorded on a Brush two-channel magnetic oscillograph. It is obvious from Fig. 6 that many strong

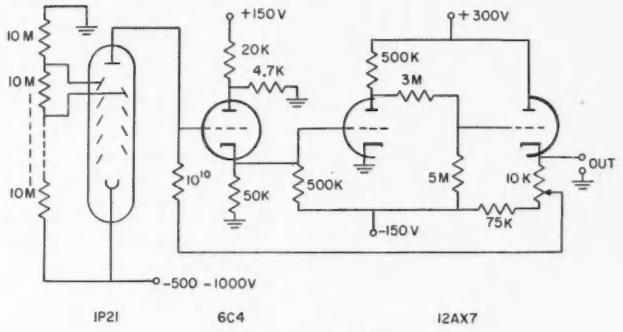

FIG. 4. Circuit of preamplifier.

radiations drive the pen off scale if the gain is large enough to show the weak ones. Hence, the other channel of the recorder (not shown in Fig. 6) is used at a lower gain so as to record the intensity of the strong features. The gain ratio can be chosen as either 3 or 10 by throwing a switch. The ratio of 3 is used for higher accuracy over a small range of intensity, and the 10 for the largest possible range.

Another unusual feature is provided: a "clamp" circuit which eliminates the zero-drift normally encountered in a direct-coupled amplifier. The signal from the preamplifier passes through a large (10 μf.) condenser to the grid of the next stage which ordinarily has no d-c. return. This permits very low frequencies (down to perhaps 0.01 cycle) to be coupled through, and the system responds essentially as though it were completely direct-coupled. However, during the flyback when the photomultiplier is in the dark, a relay grounds the grid and assures that zero light always corresponds to zero voltage. Slow drift in the photomultiplier and preamplifier is thus cut out; the gain of the main amplifiers is small enough so that they do not drift appreciably. The action is similar to that of the common system in which the light is chopped to permit a-c. amplification. The present system, though usable only when time is available for clamping, is simpler and makes more efficient use of the light.

The preamplifier (Fig. 4) is mounted on the back of the photomultiplier box. The voltage developed in the 10^{10} ohm load resistor needs no amplification;

the preamplifier is merely an impedance matching device with a gain of 1 due to negative feedback. The first tube is a 6C4 with 4 volts on the heater and 15 volts on the plate to reduce the grid current. It is mounted inside the chassis (in the dark) and the connections are soldered directly to the pins. It is used in a cathode-follower circuit. One triode of the 12AX7 is an ordinary amplifier, and the other is another cathode-follower. The heaters are connected in series and supplied with 150 ma. d-c. from a simple power supply. The other voltages are stabilized by VR-150 tubes and come from a small power supply close by.

A shielded cable leading from the roof to the top floor of the Physics Building carries the signal, the control voltage for the clamping relay, the 150 ma. heater current, and the high voltage for the photomultiplier.

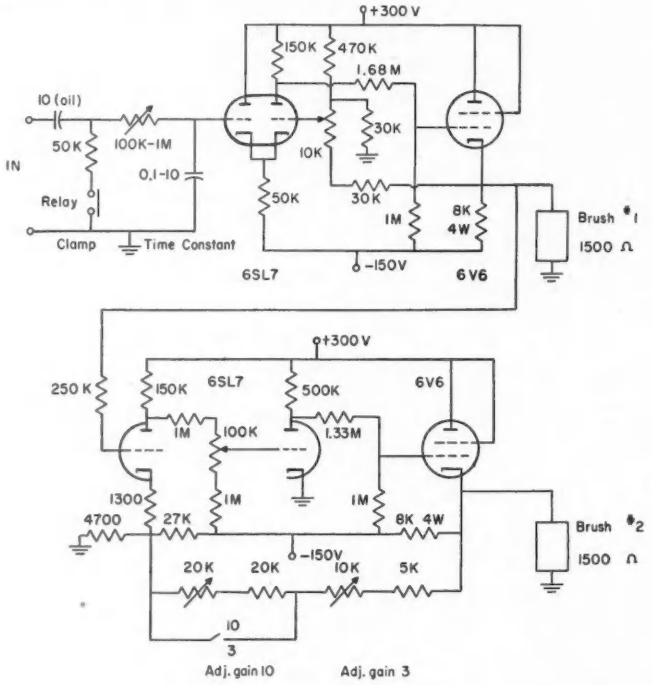

FIG. 5. Circuit of main amplifiers.

The circuit of the main amplifiers is shown in Fig. 5. The condenser in the clamp circuit was chosen for very low leakage. The 50 K resistor in series with the relay helps to average out the dark noise present during the clamping interval; without it, the clamping level might be disturbed by a noise peak occurring just before the clamp opens. A second pair of contacts on the relay opens the recorder drive circuit during the clamping interval. The operation

of the relay can be interrupted from the spectrometer, so that spectra are taken only when desired. The clamp circuit is followed by a low-pass filter whose time constant can be adjusted over the range from 0.01 to 10 sec. in order to match the width of the spectral lines. This varies greatly, depending on the scanning speed, the spectral range, and the slit widths. The time constant should be made as long as possible so as to keep down the noise.

The signal then passes to the first amplifier of gain 2. The first stage is a differential pair with the signal going to one input and the feedback to the other. This circuit is not easily driven into grid current even by large signals; such current would completely upset the action of the clamp circuit and must be avoided. The output stage is a 6V6 connected as a triode in a cathode-follower circuit; this supplies the rather large power required by the recorder (18 volts at 12 ma., each way from center). It cannot, however, give enough current to damage the recorder, no matter how large the signal.

The second amplifier takes its input from the output of the first. This is necessary because it overloads on rather small signals and the input then draws current (which is limited by the 250 K series resistor). It can therefore not be connected direct to the clamp circuit. The gain is either 3 or 10, with the change being made in the feedback network. Since a larger gain is required, the two sections of the 6SL7 are connected in cascade, and feedback is taken to the cathode of the first stage. The rather complicated feedback network allows the gain to be adjusted without much effect on the zero position. This is achieved by making the voltages at both ends of the adjustable part the same ($-$ 18 v.) for no input. The last stage is the same in both amplifiers.

4. PERFORMANCE

The instrument has been in use for several months and has been very satisfactory. Fig. 6 shows tracings of some typical spectra. Part (*a*) is from a bright normal aurora, and (*b*), from Type B red aurora, illustrates how the spectrum of this rather rare form can be caught. Part (*c*) (taken with a spectral range of 200 Å) shows one sequence of the N_2 second positive system, from aurora of only moderate brightness. Here it is the relative intensities that are of interest; they can be measured quite accurately by averaging several successive spectra. This process reduces two errors: that due to variation of the brightness of the aurora during a scan, and that due to the small number of primary photoelectrons produced by each spectral feature. The latter is the statistical error familiar in the measurement of radioactive decay; it can be quite large since only 20 or 30 electrons give full-scale deflection and the error then is around 25%. With suitable precautions, it appears that both relative and absolute intensities should be measurable more accurately than by photographic methods, and with much less work. Moreover, the greater time resolution makes the results more useful.

I am indebted to Mr. A. H. Cox for his careful machine work and useful suggestions, and to Mr. C. E. Dahlstrom and Mr. G. G. Shepherd for help with parts of the constructional and observational work.

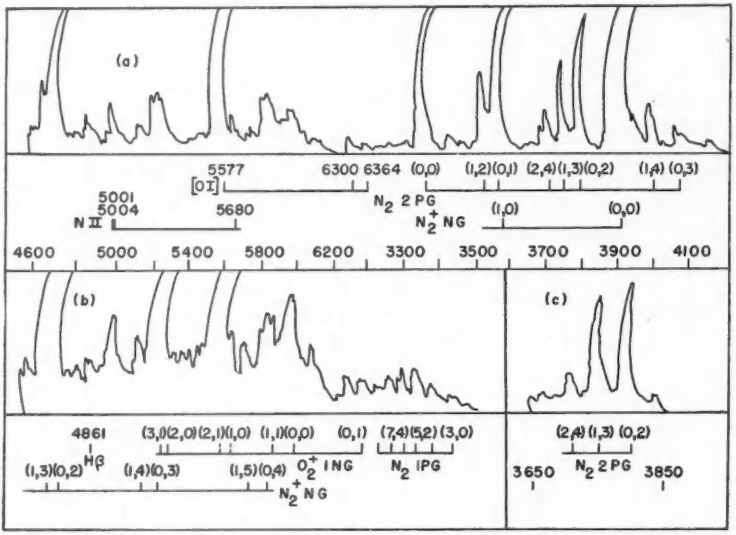

FIG. 6. Three typical spectra; scan time eight seconds, resolution 10Å. (*a*) Fairly bright aurora, showing visible region at left in first order and ultraviolet at right in second order. (*b*) Type B aurora (red lower border) with yellow filter to remove second order. Wave length scale and identifications are common to (*a*) and (*b*). (*c*) $\Delta v = 2$ sequence of N_2 second positive system, expanded to fill the whole scan.

APPENDIX I—OPTICS OF THE GRATING

Several useful formulae are derived here and gathered together for convenience. They may be used to calculate angular settings and slit widths. Fig. 7 illustrates the notation used.

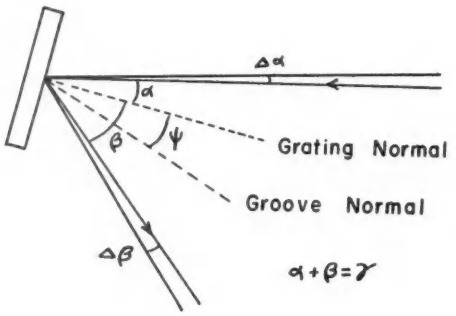

FIG. 7. Notation for Appendix I. All angles are taken positive as drawn.

Position of blaze.—The blaze can be shifted to different wave lengths by turning the grating, as was pointed out by Finkelstein (2). It is necessary to satisfy the mirror and grating equations simultaneously:

$$\begin{aligned} \alpha + \psi &= \beta - \psi, \\ m\lambda &= a(\sin\beta - \sin\alpha) \\ &= a[\sin(\alpha + 2\psi) - \sin\alpha] \\ &= 2a \sin\psi \cos(\alpha + \psi) \\ &= K \cos\gamma/2. \end{aligned}$$

The quantity $K = 2a \sin\psi$ is a constant for a given grating. For the one in this instrument it is 10,000 Å. The angle γ ranges from 35° to 90°; the corresponding range of blaze wave lengths is 9500 to 7100 Å in the first order.

Spectral range of scan.—Since the scan is produced by oscillating the grating through an angle θ, we have

$$\begin{aligned} \alpha &= \alpha_0 + \theta, \\ \beta &= \beta_0 - \theta = \alpha_0 + 2\psi - \theta \end{aligned}$$

where α_0 and β_0 are the center values. Then

$$\begin{aligned} m\lambda &= a[\sin(\alpha_0 + 2\psi - \theta) - \sin(\alpha_0 + \theta)] \\ &= 2a \sin(\psi - \theta) \cos(\alpha_0 + \psi) \\ &= 2a \cos\tfrac{1}{2}\gamma[\sin\psi \cos\theta - \cos\psi \sin\theta] \\ &\doteq 2a \cos\tfrac{1}{2}\gamma[\sin\psi - \theta\cos\psi] \text{ since } \theta \text{ is small.} \end{aligned}$$

Image width.—The image of the entrance slit gets wider as the angle of diffraction increases. This must be taken into account when the exit slit width is calculated. Starting from the grating equation:

$$\sin\beta = \frac{m\lambda}{a} + \sin\alpha \quad (\lambda \text{ constant}),$$

$$\sin(\beta + \Delta\beta) = \frac{m\lambda}{a} + \sin(\alpha + \Delta\alpha),$$

$$\sin\beta + \Delta\beta \cos\beta = \frac{m\lambda}{a} + \sin\alpha + \Delta\alpha \cos\alpha$$

since $\Delta\alpha$ and $\Delta\beta$ are small. Three terms drop out by the original equation, leaving

$$\frac{\Delta\beta}{\Delta\alpha} = \frac{\cos\alpha}{\cos\beta}.$$

It will be remembered that the dispersion varies as $1/\cos\beta$; hence the resolution varies only as $\cos\alpha$.

Image curvature.—This is important only for a resolution of 1Å or better (with the slit length used here). It has been treated by Minkowski (3) who gives the result

$$\Delta\lambda = \tfrac{1}{2}\lambda\phi^2.$$

$\Delta\lambda$ is the apparent shift in wave length at the ends of the entrance slit whose angular length is 2ϕ as seen from the collimating mirror.

REFERENCES

1. DAHLSTROM, C. E. and HUNTEN, D. M. Phys. Rev. 84: 378. 1951.
2. FINKELSTEIN, N. A. J. Optical Soc. Am. 41: 179. 1951.
3. MINKOWSKI, R. Astrophys. J. 96: 306. 1942.
4. PETRIE, W. and SMALL, R. G. Astrophys. J. 116: 433. 1952.
5. STRONG, J. Procedures in experimental physics. Prentice-Hall, Inc., New York. 1938. p. 81 and Fig. 36.

THE PHOTOELECTRIC CONSTANTS OF IODINE[1]

By D. C. West[2]

ABSTRACT

The retarding-potential method of photoelectric measurement has been applied to the determination of the work function and energy gap of a typical molecular crystal. Three allotropic forms of solid iodine, believed to be amorphous, monoclinic, and rhombic, have work functions of 6.8, 5.4, and 2.8 ev. respectively, and photoelectric thresholds of 1880, 2050, and 2360 Å. The energy gaps of the crystalline modifications are 0.6 and 2.5 ev.

I. INTRODUCTION

As far as can be ascertained from a search of the literature, no measurements have been made of the photoelectric work functions of any solid substance in the form of a molecular crystal. In particular, the recent review by Michaelson (10), listing all the known work functions of the elements, makes no mention of phosphorus, sulphur, or the halogens, all of which are molecular-crystal insulators in the solid state. This paper is a report of a preliminary measurement of the photoelectric work function of solid iodine in three allotropic crystal forms, together with a determination of the energy of the top of the filled band with reference to the Fermi energy as determined photoelectrically.

According to the generally accepted theory of the solid state, (see for example Shockley, *Electrons and holes in semiconductors* (13)) the permitted energy levels of an electron in any crystal lattice are grouped into closely-spaced, quasi-continuous bands. Two such bands are shown in Fig. 1, in which the lower band has been shaded to indicate that, in accordance with the Fermi statistical distribution, practically all the available levels in this band are occupied by electrons, while almost all the levels in the upper band are unoccupied. This corresponds to the case of an ideal intrinsic insulator. The difference in energy between the highest level of the filled band and the lowest level of the empty band is called the *energy gap*, and is herein denoted by ϵ.

At temperatures above absolute zero, a small number of electrons in the lower band are thermally excited to the upper band. As a result of this energy distribution, statistical analysis shows (13) that the Fermi level μ is very nearly halfway between the highest energy of the filled band and the lowest energy of the empty band. There are of course no available stationary states for electrons with this energy, so that an electron with this energy must either gain or lose energy by interaction with the lattice field until its energy reaches that of one of the allowed bands. Nevertheless it can be shown (13) that when two objects are brought into electrical equilibrium an exchange of charge takes place until the Fermi levels of the two objects coincide.

In actual insulators, the Fermi level is rarely in the exact center of the energy gap, because the presence of impurities even in extremely minute concentrations

[1] *Manuscript received January 12, 1953.*
Contribution of the Department of Physics, University of Toronto, Toronto, Ont.
[2] *Now with the Nova Scotia Research Foundation, Halifax, N.S.*

may alter the statistical distribution of electron energies enormously, bringing the Fermi level close to the limit of one or the other allowed band.

Fig. 1 is a schematic diagram of the energy relations at an insulator surface during photoemission. A beam of photons excites some of the electrons in the filled band AB, increasing their total energies by $h\nu$, the photon energy absorbed.

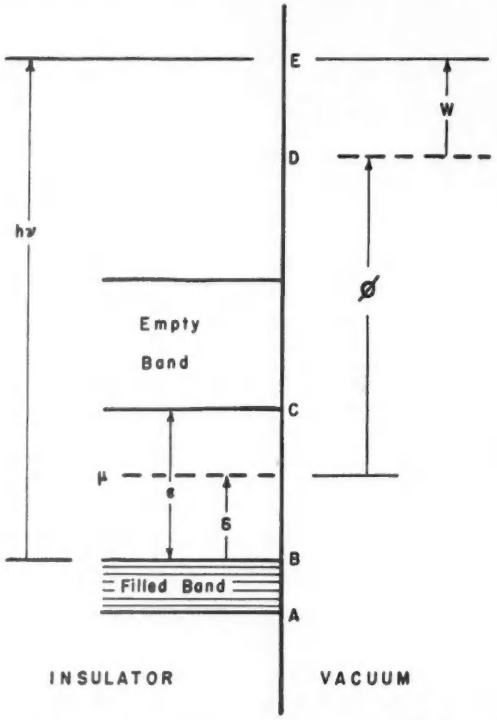

FIG. 1. Energy relations at the surface of a solid insulator during photoemission. Electron energy increases in the upward direction.

An electron from B, the top of the filled band, will attain the highest possible total energy, indicated by E. If this electron leaves the lattice it becomes a free photoelectron which can be treated classically. In particular, its kinetic energy W is equal to its total energy E minus the contact potential energy D of the surface. This kinetic energy is the quantity directly measured in the retarding-potential method used in the present work, which consists in measuring the current of photoelectrons arriving at a collector electrode whose potential with reference to the emitter can be varied.

The *work function* ϕ of a surface is defined as the difference between the energy of an internal electron at the Fermi level μ and the energy of an electron at rest at an infinite distance outside the surface. It is thus equal to the contact

potential D minus the Fermi energy, as indicated in Fig. 1. It can be measured in several ways: by finding the thermal activation energy required for thermionic emission of electrons, by comparing the contact potential with that of a material of known work function, or by photoelectric methods. Molecular crystals, because of their low melting and boiling points, are not suitable for thermionic measurements. Of the other two methods, photoelectric methods have the advantage that since practically all photoelectrons arise from the filled band it is possible by this means to measure also the maximum energy of the filled band with reference to the Fermi level (δ in Fig. 1).

In the present determinations, the photoelectric emitters were kept at ground potential, so that $\mu = 0$. They were illuminated with light of known maximum energy ($h\nu = 7.20$ ev.) which ejected photoelectrons with a maximum energy of $h\nu - \delta$, referred to the Fermi level μ. These were collected on a second electrode whose Fermi level could be increased by V ev. above that of the emitter by applying an external voltage $-V$ (the negative sign arising from the sign of the electron charge). The work function of the collector surface, ϕ_c, causes the space potential just outside the collector to become $\phi_c - V$ with respect to the emitter Fermi level.

The photocurrent becomes cut off when V is sufficiently negative to raise this surface potential to the energy of the photoelectrons from the emitter. Denoting this value of V by V_c, the *cutoff voltage*, we have

$$\phi_c - V_c = h\nu - \delta, \quad \text{or}$$

$$V_c = \delta + \phi_c - h\nu. \qquad [1]$$

Saturation of the photocurrent occurs when the interelectrode field reaches zero, at which point all the emitted electrons are collected. This condition is fulfilled when the space potentials just outside the two electrodes are the same; i.e., when $\phi_c - V$ is equal to the emitter work function ϕ_e. Denoting this value of V by V_s, the *saturation voltage*, we have

$$V_s = \phi_c - \phi_e. \qquad [2]$$

In these equations, the value of δ is effectively zero for all metals at ordinary temperatures.

Apker, Taft, and Dickey (1) have made use of this fact in determining δ for a number of semiconductors. Cutoff voltages from semiconductor emitters were compared with those from a metal reference emitter. From Equation [1] it can be seen that if ϕ_c and $h\nu$ are kept constant by using the same collector and light source, the difference between the cutoff voltages for the two emitters will be equal to the value of δ for the semiconductor. In these experiments the method has been extended to include also an interchange of collector surfaces while using the same emitter. By this means, ϕ_c can be measured from the determination of cutoff points only, which are much more accurate than saturation point measurements.

II. PHOTOCELL DESIGN

The necessary interchange of iodine and metal surfaces is most easily accomplished by providing the photocell with metal electrodes which can be cooled independently with liquid air, so that iodine layers may be deposited upon

either electrode at will. The temperature of the iodine must be kept below −50° if a vacuum of 10^{-6} mm. is to be maintained (2). After removal of an iodine layer by evaporation, the work function of the metal surface should return to a stable value—this need not be the value for a perfectly clean surface so long as it is reproducible.

Platinum electrodes were used in these experiments, since platinum is one of the few metals not attacked chemically by iodine (14, 15). Although the work function of platinum is notoriously dependent on its history (4), the work of Jacobs and Whalley (6) has shown that the work function of platinum after

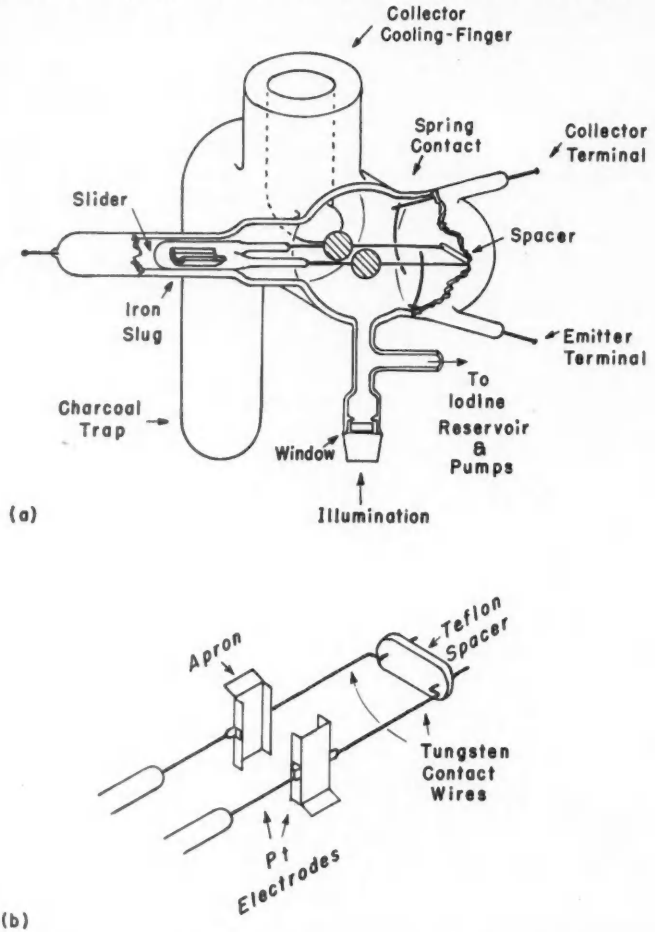

FIG. 2. Low-temperature photocell with interchangeable electrodes. (*a*) Cut-away view showing disk electrodes (shaded). (*b*) Detail of slider showing arrangement of electrical contacts and improved form of electrodes.

exposure to iodine vapor is reproducible to 20 millivolts, especially in the absence of oxygen. This constancy was confirmed in preliminary experiments in the photocells used for the present measurements.

Two types of photocell were used to obtain the measurements. The one shown in Fig. 2 made use of a movable electrode system mounted on a magnetically operated slider to enable the emitter and collector to be interchanged bodily. To allow independent cooling, a pair of cooling fingers which could be filled with liquid air (only one of which is shown in Fig. 2) were installed so as to make contact with the platinum electrodes during measurement, as shown.

To interchange electrodes, the slider was withdrawn into the side tube by the attraction of an external magnet on the iron slug. The latter was fastened inside the bulb of the slider, where it could not come into contact with the iodine vapor. When the electrodes were clear of the cooling fingers, the slider was rotated 180° by means of the external magnet and then moved forward again until the electrodes made firm contact with the cooling fingers. Electrical contact to the electrodes was made through tungsten wire springs pressing lightly against a pair of tungsten contact wires attached to the electrodes, as shown in Fig. 2*b*.

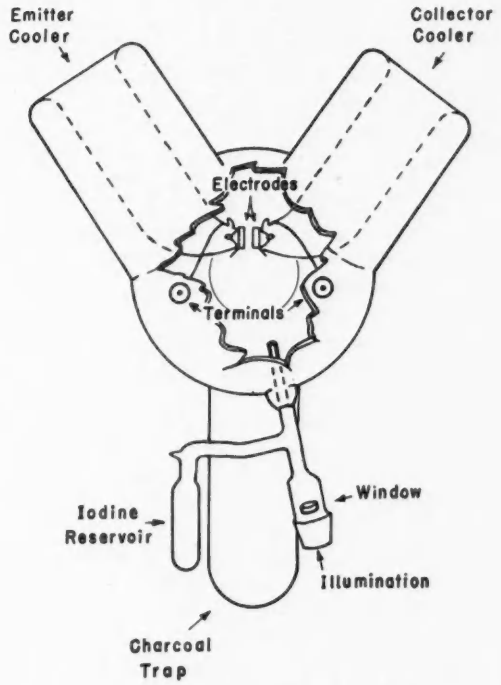

FIG. 3. Low-temperature photocell with fixed electrodes.

Electrical leakage and polarization were effectively eliminated by supporting the electrodes on long glass tubes and evacuating the interior of the slider. Polarization of the glass around the emitter terminal by the applied voltages was prevented by guard rings of silver conductive paint. The larger electrodes shown in Fig. 2*b* were found necessary to shield the glass from direct or scattered light and to isolate the interelectrode space from stray fields due to contact potential differences between the platinum electrodes themselves and their tungsten support wires. The light fell on the emitter at almost grazing incidence, the main reflected beam passing upward into the space surrounding the cooling fingers. There was thus no direct illumination of the glass surface near the electrodes to cause serious time-lags or polarization effects. Care was taken to avoid scratches on the polished platinum surfaces which might diffuse light onto the opposite electrode.

The second photocell design is shown in Fig. 3. It contained no moving parts, the electrode layers being changed solely by evaporation or deposition of iodine. To increase the effectiveness of cooling, the ends of the cooling fingers were flattened and the electrodes were pressed firmly against them by the spring action of tungsten wires passing over small projections on the glass walls of the cooling fingers. To avoid thermal conduction along the electrical connections, the leads were made of fine platinum wire (0.005 in.) several centimeters long, arranged to touch the surface of the cooling fingers for a few centimeters near the electrodes. The light beam was narrowly limited by a section of capillary tubing (1 mm. bore) trained on the center of the emitter at almost grazing incidence. The external terminals were similar to those of the first photocell. Polarization and leakage effects, with or without illumination, were undetectable.

III. AUXILIARY EQUIPMENT

An air arc was used as the source of illumination for all measurements. It was an end-on capillary discharge in air at 50–100 microns pressure, operated at constant current (usually 2.5 ma.) from a variable-voltage source of direct current at voltages up to 5000. In all experiments the same fluorite window assembly was used, being built into each cell in turn. To avoid the use of wax, which would react with iodine vapor, the window was sealed to the Pyrex support with silver chloride according to the method of Palmer (11), and annealed for 12 hr. as described by Weber and Bazzoni (17).

A spectrogram of the light source, taken in a fluorite-prism vacuum spectrograph through the courtesy of Mr. J. Galt of the McLennan Laboratory, University of Toronto, showed lines down to 1720 Å ($h\nu = 7.2$ ev.) but none at shorter wave lengths with the exception of a doubtful trace of the group of lines at 1669 Å. The relative absence of short-wave-length radiation from the light source may have been due to self-absorption in the distance between the discharge electrodes and the fluorite window, which was approximately 7 cm.

The vacuum system was designed to reduce contamination of the iodine as far as possible. Pyrex glass was used throughout, and no wax or grease was used in the high-vacuum system. The high vacuum was produced by a three-stage fractionating Octoil diffusion pump with two liquid-air traps in series. Pressures

of noncondensable gases were measured by an ionization gauge located between these two traps.

In order to reduce the pressure of permanent gases to an absolute minimum and to ensure continued freedom from contamination, each photocell was provided with a charcoal trap and sealed off after evacuation and baking. Whenever it was desired to remove an iodine layer from an electrode, the vapor was condensed in the charcoal trap, subsequent layers being formed from fresh iodine out of a reservoir attached to the cell.

The small photocurrents, which were of the order of 10^{-15} to 10^{-12} amp., were measured by means of a Lindemann-Ryerson electrometer* shunted by a high resistance. To avoid voltage errors due to the potential drop of the current across this high resistance, an accurately measured external bias current was sent through the resistor in opposition to the photocurrent. The electrometer was used to measure the small remaining unbalanced voltage across the shunt resistor.

Apart from the usual difficulties of measuring small currents and voltages, there were other disturbing effects due to the use of liquid air. One of these was the thermal potential (up to 5 mv.) developed across the high resistor by uneven temperatures, particularly after the replenishing of the liquid air. Another was electrostatic interference from bubbles rising in the liquid air cooling fingers. This effect could be avoided by shielding the liquid air electrically from the glass container, but this proved difficult to accomplish owing to the violent mechanical action of boiling liquid air on any coatings applied to the glass. The best results were obtained by inserting into the cooling finger a close-fitting grounded metal container for the liquid air, and filling the interspace between the metal and glass with mercury to provide good thermal contact.

IV. MEASUREMENTS

Great care was taken in the purification of the iodine to avoid contact with pump oil, mercury, or grease vapors, and to remove as much adsorbed air as possible. Baker's C. P. iodine (0.002% chlorine and bromine) was subjected to two vacuum fractionations, in each of which two thirds of the sample was sublimed over and half of this sublimate was then redistilled back into the original container, leaving only the middle fraction. The iodine was finally distilled into a reservoir connected to the photocell and kept cold with liquid air except when a layer was to be deposited on an electrode.

Three distinct and reproducible types of photoelectric response were obtained from iodine surfaces, depending upon their method of preparation and thermal history. It is believed that these correspond to different allotropic modifications of solid iodine.

In addition to the usual orthorhombic form, iodine has been reported by Fedorov (5) and Kurbatov (8) to occur in a monoclinic form, although Kohlschütter and Dürrenmatt (7) attribute this to an oxide or hydrate of iodine. Wahl (16) has shown that if it occurs, the monoclinic form must be metastable with respect to the rhombic form at all temperatures down to −180°C. During

Made available through the courtesy of the Nova Scotia Research Foundation.

the vacuum distillations of iodine in the present work the majority of crystals conformed to the description given by Kurbatov of "dendrites which readily fall off the walls", although a few were the usual rhombic "plates which cling tightly to the walls." In view of the purity of the materials used and the absence of oxygen and water vapor, it is concluded that the monoclinic form of iodine was actually produced in these experiments.

The two forms have the same color, and in the microcrystalline state it was impossible to distinguish between them by visual examination. However, the metastability of the monoclinic form afforded an indication of which type of photoelectric behavior was to be assigned to each modification. In several cases a black, microcrystalline surface was observed to alter its behavior from one type to the other after standing for several hours at liquid air temperature or on being warmed to room temperature—obviously as a result of a phase transformation in the iodine. The final photocurrent curves were therefore assigned to rhombic iodine and the initial curves to the monoclinic form.

A third form of solid iodine was very easily prepared by the rapid condensation of iodine vapor on glass or metal at liquid air temperatures. This was a brownish-red transparent film, apparently amorphous, which could be distinguished visually from the other two forms and gave rise to a different type of photocurrent curve. When the film was allowed to stand at liquid air temperatures or warmed, its appearance and photoelectric behavior changed irreversibly into those of monoclinic iodine. For convenience, this modification will be referred to as "amorphous", although no definite evidence as to its structure exists from X-ray diffraction.

There are thus seven independent photoelectric constants to be determined—the work function ϕ and Fermi level location δ of each form of iodine, and the work function of the reference platinum surface. Fourteen useful curves were obtained, yielding 18 determinations of cutoff or saturation voltage for various combinations of surfaces in pairs. Typical photocurrent curves are shown in Fig. 4 for various combinations of platinum and amorphous iodine surfaces. In general the saturation voltages were much less distinct than the cutoff voltages.

The measurements were combined by the method of least squares to give mean values for the seven constants, allotting only half weight to the saturation-point observations. The results are presented in Table I. The deviations of the

TABLE I

PHOTOELECTRIC CONSTANTS IN ELECTRON VOLTS

Surface	Work function	δ	Photoelectric threshold	
			Energy	Wave length
Platinum	$5.45 \pm .2$	0	$5.45 \pm .2$	2270 Å
Amorphous I_2	$6.75 \pm .2$	$-0.15 \pm .2$	$6.60 \pm .2$	1880
Monoclinic I_2	$5.41 \pm .2$	$0.65 \pm .2$	$6.06 \pm .2$	2050
Rhombic I_2	$2.78 \pm .3$	$2.47 \pm .2$	$5.25 \pm .3$	2360

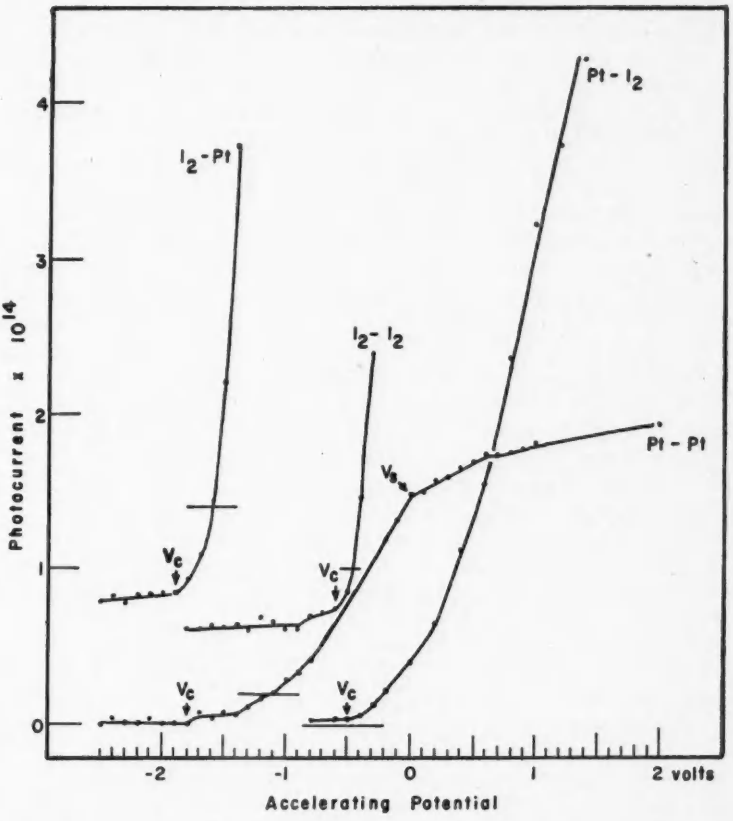

FIG. 4. Photocurrent curves for four combinations of platinum and amorphous iodine electrodes, indicated by chemical symbols. The first symbol of each pair refers to the emitter material and the last refers to the collector. V_c and V_s are cutoff and saturation points respectively. The curves are displaced vertically for clarity, the zero-current axis for each curve being indicated by a short horizontal line.

observations are all of the same order as the accuracy with which the retarding voltage was measured (0.1 volt) from which it may be concluded that the data are consistent with the theoretical relations [1] and [2] to this order of accuracy. After all possible sources of error had been considered, it was concluded that the figures in Table I are not in error by more than 0.2 ev., with the exception of the work function and total surface barrier of rhombic iodine, which may be in error by 0.3 ev.

The negative value of δ for amorphous iodine is not considered significant since it is smaller than the limits of error, and cannot be explained on any accepted theory of the solid state. It may arise from the tremendous increase

which takes place in the photoelectric efficiency of a platinum surface when amorphous iodine is deposited on it, and which is evident from Fig. 4. This increased sensitivity would tend to shift the apparent cutoff point of an amorphous surface toward more negative values of collector voltage, as occurs in the figure. It is concluded that in amorphous iodine the value of δ is zero within the limits of experimental error.

V. PREVIOUS MEASUREMENTS

Since the total energy gap ϵ must be equal to or greater than δ, the present measurements indicate a lower limit of $2.5 \pm .2$ ev. for ϵ. For comparison, at least three other types of measurement have been carried out by other workers on rhombic iodine from which values of ϵ may be derived. The first of these is the determination of conductivity as a function of temperature. The most careful work on the electrical conductivity of iodine has been done by Pochettino and Fulcheris (12) using very pure iodine over a temperature range from 4° to 41°C. It is possible from their data to calculate the width of the energy gap as 1.9 ev. This value is probably a lower limit, since the presence of impurities such as oxygen has a much greater effect on conductivity than on photoelectric cutoff, and the conductivity measurements were made in air.

The energy gap can also be found from the threshold wave length at which photoconductivity begins. Coblentz (3) carried out such an experiment on iodine using filters to study the spectral distribution. He reported a weak photoconductivity between 5300 and 5500 Å. A threshold at 5500 Å would correspond to an energy gap of 2.2 ev.

The optical absorption and dispersion of polycrystalline iodine was studied by Meier (9). His analysis of the data showed that the results could be explained by assuming two characteristic frequencies, one at 4500 Å (2.76 ev.) with a half-width equivalent to 1.0 ev., and another at 2000 Å (6.2 ev.). If the absorption at 4500 Å can be interpreted as excitation from the filled band to the center of the empty band, and if the 1.0 ev. width of this absorption corresponds roughly to the width of the upper band in energy, then the energy gap ϵ is equal to $2.76 - 0.5 = 2.3$ ev. The 2000 Å absorption may correspond to excitation to a higher band, or to absorption with photoemission.

The agreement among these values of the energy gap obtained by such diverse methods and the fact that they are all approximately equal to the value of δ found for rhombic iodine by the photoelectric method support the conclusion that in rhombic iodine at liquid air temperatures the Fermi level is very close to the bottom of the empty band. The material can therefore be considered as an *n*-type semiconductor, in which the concentration of donor impurities is greater than that of acceptors. This is understandable, since the only common acceptor impurities (other than lattice defects) in iodine would be the three elements of greater electron affinity—fluorine, chlorine, and bromine. These were stated by the manufacturer to amount to less than 20 parts per million, and must have been further reduced by the distillations. All other elements would be expected to act as donors—in particular oxygen, which is known to form relatively stable compounds with iodine.

No similar energy-gap measurements have been made for monoclinic iodine, but the same considerations of impurity concentrations imply that it is also an n-type semiconductor. The value of zero deduced for δ in amorphous iodine can be explained by assuming either that the material is a semiconductor with a total gap small compared with the error of measurement, or that the Fermi level is at the bottom of an energy gap of unknown width—that is, the material is a p-type semiconductor. Conductivity and Hall-effect measurements would be required to distinguish between these alternatives, but it appears likely that iodine may behave in a manner similar to selenium (18), which is a p-type semiconductor in the amorphous state and an n-type semiconductor in the monoclinic form.

Although iodine, in view of its physical and chemical properties, is unlikely to have any practical application as a semiconductor, the fact that its energy gap is three times that of germanium may make it very useful in fundamental studies of semiconductor behavior.

VI. ACKNOWLEDGMENTS

The work described herein was carried out at the MacLennan Laboratories of the University of Toronto, under the supervision of Dr. J. M. Anderson and Dr. R. W. MacKay. Thanks are also due to the Nova Scotia Research Foundation for assistance and to the National Research Council and Ontario Research Council for financial aid.

REFERENCES

1. Apker, L., Taft, E. A., and Dickey, J. Phys. Rev. 74: 1462. 1948.
2. Baxter, H. and Grose, M. J. Am. Chem. Soc. 37: 1016. 1915.
3. Coblentz, W. Bur. Standards Sci. Papers, 18: 585. 1922.
4. DuBridge, L. A. Phys. Rev. 31: 236; 32: 961. 1928.
5. Fedorov, E. S. Bull. Imp. Acad. Sci. St. Petersburg, 22: 287. 1905.
6. Jacobs, L. and Whalley, H. K. Proc. Roy. Soc. (London), A, 140: 489. 1933.
7. Kohlschütter, V. and Dürrenmatt, K. Helv. Chim. Acta, 22: 457. 1939.
8. Kurbatov, V. Z. anorg. Chem. 56: 230. 1908.
9. Meier, W. Ann. Physik, 31: 1017. 1910.
10. Michaelson, H. B. J. Applied Phys. 21: 536. 1950.
11. Palmer, F. Phys. Rev. 45: 556. 1934.
12. Pochettino, A. and Fulcheris, G. Atti reale accad. sci. Torino, 58: 493. 1922.
13. Shockley, W. Electrons and holes in semiconductors. Van Nostrand, Toronto. 1950.
14. Van Praagh, G. J. Chem. Soc. 798. 1933.
15. Van Praagh, G. and Rideal, E. F. Proc. Roy. Soc. (London), A, 134: 385. 1931.
16. Wahl, W. Proc. Roy. Soc. (London), A, 88: 348. 1913.
17. Weber, A. H. and Bazzoni, C. B. Rev. Sci. Instruments, 8: 170. 1937.
18. Weimer, P. K. Phys. Rev. 79: 171. 1950.

METEOROLOGICAL VARIATIONS IN THE QUANTITY OF ATMOSPHERIC OZONE OVER EDMONTON
(Lat. 53° 34′ N. Long. 113° 31′ W.)[1]

By E. H. Gowan and R. E. Leppard

ABSTRACT

Ozone observations have been made at Edmonton, Lat. 53° 34′ N. Long. 113° 31′ W. from August 2nd, 1950, to December 31st, 1952. The expected seasonal variation occurs, along with large short-term fluctuations. High values in all seasons are associated with relatively low temperatures, and low ozone values are accompanied by relatively higher temperatures. It is not yet possible to judge the degree to which the transport mechanism is responsible for ozone change, but it seems to play a large part over central Alberta.

INTRODUCTION

The Dobson (3) Ozone Spectrophotometer belonging to the Canadian Meteorological Service has been in operation at Edmonton since August 2nd, 1950. This location was chosen for several reasons.

(1) There is very well marked polar front activity, with some periods of very steady conditions.

(2) 'Chinook' conditions occur frequently and last from one to three weeks.

(3) Regular upper air data are available from two daily radio-sondes.

(4) A continental climate 800 miles from the Pacific Ocean, with the influence of the Canadian Rockies normally discernible, gives a set of conditions not yet represented in ozone studies.

THEORY AND METHODS

These need only brief reference here. Further details are readily available in the literature and in the operating manual. Craig (1) gives a good summary.

The instrument compares the intensities of two adjacent wave lengths near the short wave cutoff of the solar spectrum. The stronger of the two is reduced in intensity by a calibrated optical wedge, and they are thrown alternately on the cathode of a photomultiplier by means of a rotating shutter. The resulting alternating current is amplified, rectified, and detected by a d-c. microammeter. This meter reads zero when the two intensities at the photocell are the same, and a dial reading R identifies the corresponding position of the wedge.

When direct sunlight can be used the beam is sent vertically down into the instrument by means of a quartz prism and lens. A ground quartz disk diffuses the illumination and makes the exact direction of the beam less critical. Readings with light from the zenith can be made by removing the prism, lens, and disk. The sensitivity is such that measurement is possible even through a dense cloud.

[1] *Manuscript received February 25, 1953.*
Contribution from the University of Alberta, Edmonton, Alta.

The theory of the measurements leads to the following general equation (Dobson (2)) for the effective thickness of the ozone layer:

$$x = \frac{L_0 - L}{(\alpha - \alpha')\mu} - \frac{(\beta - \beta')m}{(\alpha - \alpha')\mu} - \frac{(\delta - \delta')\sec Z}{(\alpha - \alpha')\mu}$$

where: x = cm. of ozone at N.T.P.,
$L_0 = \log I_0/I_0'$,
$L = \log I/I'$ (The symbols I and I' represent the intensities of the two adjacent wave lengths. The subscript $_0$ indicates corresponding values at the top of the atmosphere.),
α and α' are the coefficients of ozone absorption for the two wave lengths,
μ is the slant path length through the ozone, in terms of unity for normal incidence,
m is the air mass in terms of unity for normal incidence,
β and β' are the Rayleigh scattering coefficients (9),
δ and δ' are the scattering coefficients for large particles, haze and dust, nearly independent of wave length,
Z is the zenith angle of the sun.

METHOD OF CALCULATION

(a) *Direct Sun Observations*

(1) In the first term $L_0 - L$ is evaluated by conversion of the dial reading R using the calibration constants of the wedge. A table of corrections "n", so arranged that $R - n = 100(L_0 - L)$ to a very close approximation, is supplied.

For wave lengths 3112 and 3323, $(\alpha - \alpha') = 1.15$ from the laboratory measurements of Ny and Choong (8).

For Z less than 68° the values of μ, m, and sec Z may be considered the same, and can be calculated from the value of Z at the average time of an observation. Cos Z is computed from the usual formula requiring the latitude, along with the declination of the sun and hour angle. Then the second and third terms reduce to a single one "A" which depends only on the coefficients. The bracket $(\delta - \delta')$ depends on the degree of haze or visibility, and has been taken as zero when the horizontal visibility is 12 miles or more. In other cases the visibility, available from the weather observer's reports, has been used as the criterion of haziness, since it gives a more objective measure than simply estimating haze degree. Table I summarizes the treatment of haze corrections,

TABLE I

FACTORS USED IN CALCULATIONS AS A FUNCTION OF VISIBILITY

Visibility	"A"	$\frac{\delta - \delta'}{\alpha - \alpha'}$
12 miles and over (clear)	0.095	Zero
6 to 11 miles (light haze)	0.100	0.005
3 to 5 miles (medium haze)	0.110	0.015
Under 3 miles (dense haze)	0.120	0.025

and is based on the values of "A" (the combined second and third terms) supplied by the makers and recommended for use with the instrument.

(2) Some observations during winter or late in the day at any season will be taken with Z greater than 68°. Then the fact that m refers to the whole atmosphere, while μ refers to a relatively thin layer near 22 km., becomes important and the two must be evaluated separately. A table of m as a function of Z has been computed using Bemporade's function taking into account the curvature of the earth and atmospheric refraction. This table was supplied with the instrument.

With μ refraction can be neglected because of the height (22 km.) to which it refers. Owing to the curvature of the earth the zenith angle Z' where the solar beam pierces the ozone layer is smaller than the angle Z measured at the surface. The usual equation can be used: $\sin Z' = \sin Z/(1 + h/r)$ where h is the height of the ozone layer, and r is the radius of the earth. Then $\mu = \sec Z'$.

Thus for all values of Z and for all conditions of haze a measured thickness of the ozone layer, x cm., can be obtained.

(b) Clear Zenith Sky Observations

It is not possible to calculate the amount of ozone from first principles using observations of the zenith skylight, on account of the "umkehr effect." However it has been found experimentally that there is a close relation between the ozone determined by a direct sunlight observation, and the almost simultaneous reading from a clear zenith sky. A chart based on this was prepared at Oxford and sent with the instrument, to be used with the standard wave length pair only. A calculated value of μ for the time, and the observed, corrected dial reading $(R - n)$ will give the ozone amount from the chart.

Such a chart depends on the clarity of the atmosphere, and on the relative air masses above and below the ozone. Some correction to the chart is probably needed for Edmonton whose altitude is about 2,000 ft. above sea level. A series of double observations on clear days, direct sun and zenith sky within a few minutes of each other, was therefore made. On the basis of a few months' observations it was found that if $(R - n + 7)$ were used with the Oxford chart the values of x obtained agreed closely for July and August. The numerical correction seems to be less for the other months, but insufficient observations are available to make definite conclusions possible. More data are being taken on suitable occasions.

(c) Cloudy Zenith Sky Observations

The method of the clear zenith sky can be used when there are clouds at the zenith, with an appropriate "cloud correction." This has been worked out and is still being refined, by triple observations on suitable days. Direct sun, clear zenith, and cloudy zenith observations are taken in fairly quick succession as the clouds move. Also an extra observation with a pair of longer wave lengths is made on the cloudy zenith. Charts which give a differential correction to the adjusted dial reading for a zenith observation on clouds have

been prepared on the basis of many such observations. A separate chart is provided for low, middle, and high clouds, and with these an ozone value can be found for a time when the sky is overcast.

OZONE CHANGES AND THE WEATHER MAP

From 1925 to the present time studies have been made of the daily changes in ozone and the weather map. The early work of Dobson, Harrison, and Lawrence (5) and of Meetham (7) used typical isobar patterns for low and high pressure areas. Later Dobson, Brewer, and Cwilong (4) amplified the earlier results by separating the young depressions from the older occluded ones. Tonsberg and Olsen (11) located the center of the low pressure system by the intersection of two lines representing warm and cold fronts. On any day the observing station when inside a closed isobar was marked in an appropriate position relative to the fronts of the weather map for 1800 hr. G.M.T. and the departure of the ozone daily average from the annual curve noted beside the point. A similar system was used by Fritz and Stevens (6) in the analysis of the ozone measurements made at Washington.

The Edmonton observations have also been studied by the use of two curved intersecting lines to represent the cold and warm fronts of a typical young depression. Daily averages were not used but for every ozone value measured during the day by the direct sun method the synoptic map most nearly corresponding to the observation time was examined. Many observations were timed to coincide with the regular maps. The usual technique of using tracing paper made it easy to locate the observing station in relation to the frontal system. At this point the departure of that particular ozone value (not the daily average) from the curve of 10-day means was marked. Maps have been prepared and lines of constant ozone departure have been drawn on them, representing the analysis of 333 low pressure systems.

During the investigation it was possible on three occasions to study the fluctuations of ozone as particular high pressure systems passed over Edmonton. Three common types are represented:—a large polar air mass, an anticyclone that developed over the Pacific Ocean, and a round flat high which could have been formed through separation from either of the other types by a low pressure trough.

OBSERVATIONS AND RESULTS

Observations are now available from August 2nd, 1950, to December 31, 1952, but not for every day. On many days several readings were taken to compare the three methods, or to study the influence of surface fronts.

(*A*) *Ten-day Averages and the Annual Variations*

Table II gives the daily averages obtained from direct sun observations whenever these are available. On a few days it was possible to observe only the cloudy zenith.

The 10-day averages are plotted in Fig. 1, along with a four year average (1926 to 1930) for Oxford, at a comparable latitude. The general magnitudes and the annual variation agree very well.

TABLE II

DAILY OZONE VALUES FROM AUGUST 2ND, 1950, TO DECEMBER 31ST, 1952

1950	Aug.	Sept.	Oct.	Nov.	Dec.	1951	Jan.	Feb.	Mar.	Apr.	May	June	July	Aug.	Sept.	Oct.	Nov.	Dec.	1952	Jan.	Feb.	Mar.	Apr.	May	June	July	Aug.	Sept.	Oct.	Nov.	Dec.
1	–	–	–	–	–	1	–	–	277	–	–	288	288	258	–	206	231	230	1	–	280	338	355	292	–	–	240	–	201	253	–
2	272	183	–	208	–	2	–	–	325	–	–	300	271	241	–	209	–	–	2	182	259	350	344	273	256	271	–	202	224	224	–
3	–	–	–	–	–	3	–	–	311	208	–	–	262	241	237	231	198	244	3	220	–	313	290	255	252	242	–	218	215	205	178
4	265	–	–	–	212	4	257	–	342	254	256	313	270	248	225	225	–	265	4	252	273	342	292	–	241	234	228	–	217	226	198
5	264	197	–	–	–	5	209	246	–	–	256	–	–	–	220	218	181	250	5	230	275	271	284	297	228	–	235	223	195	215	229
6	–	–	–	–	–	6	175	255	340	255	270	295	–	–	214	195	175	245	6	–	269	281	–	342	218	–	252	212	185	227	–
7	–	225	–	–	–	7	–	–	371	–	282	–	251	261	208	194	215	223	7	–	310	300	313	281	–	224	219	–	178	–	209
8	–	–	–	–	223	8	222	–	372	252	278	285	264	240	200	194	215	265	8	280	295	–	347	276	–	239	227	231	192	227	–
9	–	232	–	219	–	9	223	–	–	280	291	298	282	253	–	186	226	–	9	284	237	325	355	277	–	243	–	250	231	207	233
10	–	–	175	–	202	10	–	–	–	261	–	334	245	237	227	207	215	244	10	301	242	–	295	–	–	263	–	242	199	218	231
Av.	*267*	*209*	*175*	*214*	*213*	Av.	*217*	*250*	*333*	*252*	*272*	*302*	*267*	*248*	*219*	*207*	*207*	*245*	Av.	*250*	*268*	*316*	*320*	*286*	*239*	*245*	*234*	*226*	*204*	*222*	*213*
11	–	203	–	–	–	11	–	257	332	–	–	268	252	235	225	197	–	–	11	–	261	320	–	–	–	270	236	235	221	211	251
12	–	212	–	–	–	12	–	255	271	207	286	273	237	–	213	200	219	–	12	275	303	320	–	296	–	–	226	221	214	233	210
13	–	197	195	209	220	13	251	212	279	–	–	276	–	251	219	190	220	–	13	–	309	340	–	285	–	–	222	231	–	235	191
14	–	187	–	–	223	14	–	–	–	297	275	314	–	246	201	–	–	201	14	275	294	293	–	307	291	250	290	198	215	233	174
15	–	181	–	–	–	15	–	238	–	240	278	294	252	228	180	225	245	–	15	305	–	264	303	268	–	270	253	216	207	–	194
16	259	178	–	–	196	16	240	207	316	–	269	–	260	250	–	225	214	–	16	296	–	301	312	277	266	250	–	220	161	–	214
17	253	–	–	252	–	17	–	202	330	–	–	–	260	254	195	225	188	278	17	–	–	292	276	258	287	268	–	212	165	212	243
18	237	195	–	252	237	18	262	274	300	–	–	–	279	–	202	241	–	–	18	280	338	–	244	–	248	253	245	219	159	213	257
19	231	195	–	217	–	19	258	269	–	–	299	–	264	–	215	215	211	201	19	258	328	292	251	280	267	–	208	208	179	207	–
20	–	194	224	225	–	20	250	295	–	305	314	–	266	236	222	–	–	193	20	–	349	330	–	–	262	–	217	184	173	218	218
Av.	*245*	*193*	*209*	*231*	*219*	Av.	*252*	*245*	*305*	*262*	*287*	*285*	*259*	*243*	*208*	*215*	*216*	*218*	Av.	*282*	*312*	*304*	*277*	*282*	*270*	*260*	*237*	*214*	*188*	*220*	*217*
21	229	167	–	–	–	21	236	285	272	300	266	–	261	233	222	–	201	–	21	–	328	377	233	–	271	–	223	–	160	251	202
22	201	178	–	–	–	22	256	267	276	286	278	–	250	235	214	–	232	–	22	375	331	–	272	264	–	259	227	190	167	233	234
23	–	185	224	–	–	23	–	252	268	288	279	–	–	253	260	211	225	–	23	343	277	–	279	288	279	232	–	178	162	229	242
24	–	–	–	233	–	24	–	244	263	264	302	–	250	248	222	–	–	–	24	322	283	304	273	–	244	263	–	184	165	248	–
25	210	–	–	–	–	25	–	–	–	257	–	284	249	–	–	223	–	–	25	–	272	–	263	–	250	246	255	174	200	256	222
26	195	–	220	–	219	26	–	–	–	279	303	311	250	–	235	211	–	–	26	–	268	272	–	296	261	–	246	200	206	–	–
27	–	–	–	–	226	27	–	281	302	263	–	307	251	250	198	–	245	–	27	–	308	256	–	274	247	–	244	207	206	219	–
28	198	–	–	–	–	28	–	–	253	261	–	289	258	250	198	–	230	–	28	236	313	–	268	270	–	237	231	–	–	–	–
29	205	–	–	219	212	29	284	–	211	–	296	298	257	235	203	–	216	–	29	230	315	282	295	–	–	230	–	183	213	–	246
30	203	–	–	–	–	30	–	–	–	–	334	276	261	–	–	230	235	–	30	238	–	–	–	276	261	223	–	204	270	–	–
31	199	–	–	–	–	31	306	–	248	–	308	–	266	195	–	236	–	–	31	283	–	318	–	272	–	214	–	–	239	–	239
Av.	*205*	*177*	*222*	*226*	*219*	Av.	*271*	*268*	*262*	*274*	*296*	*294*	*255*	*238*	*218*	*223*	*225*	–	Av.	*289*	*299*	*301*	*269*	*277*	*259*	*238*	*238*	*190*	*199*	*239*	*231*

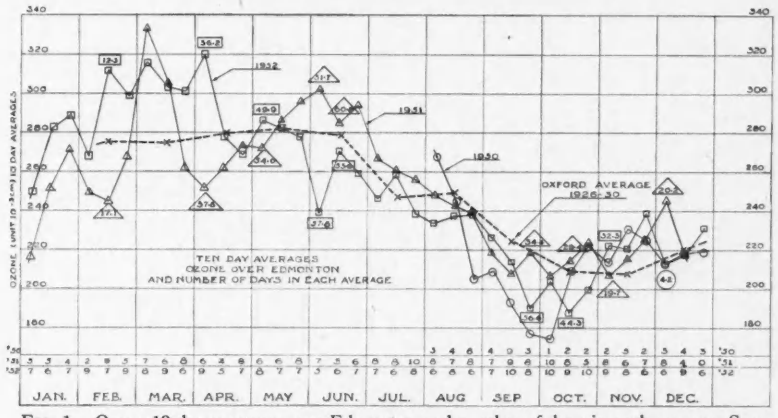

FIG. 1. Ozone 10-day averages over Edmonton and number of days in each average. Some comparative temperatures and the Oxford four year ozone average, 1926–30 are included.

(*B*) *Ozone Changes and the Weather Map*

The ozone changes associated with young depressions have been plotted on four maps representing the seasons. Lines of constant departure from the 10-day means have been drawn 0.01 cm. of ozone apart, and are shown in Figs. 2, 3, 4, and 5.

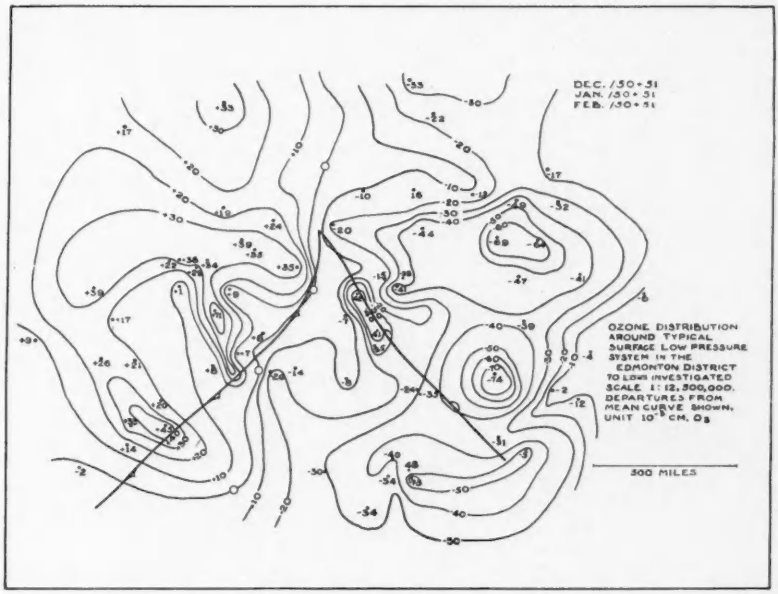

FIG. 2. Typical ozone distribution around a low pressure system. Winter—December, January, and February.

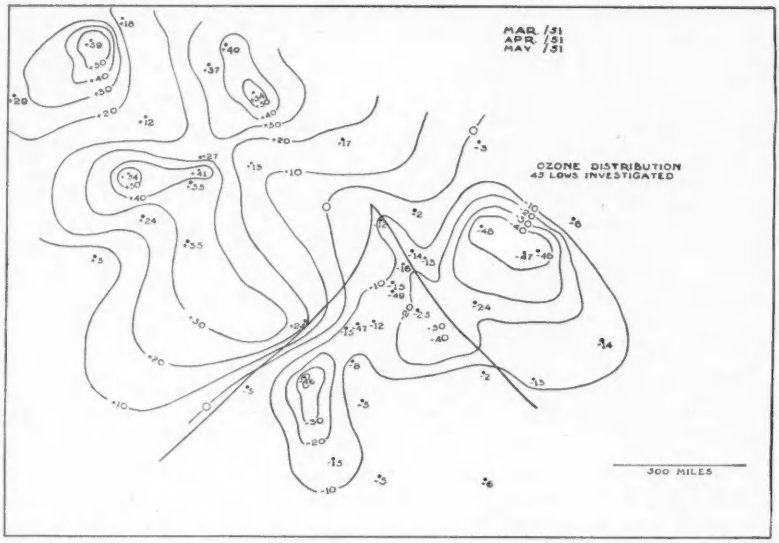

FIG. 3. Typical ozone distribution around a low pressure system. Spring—March, April, May.

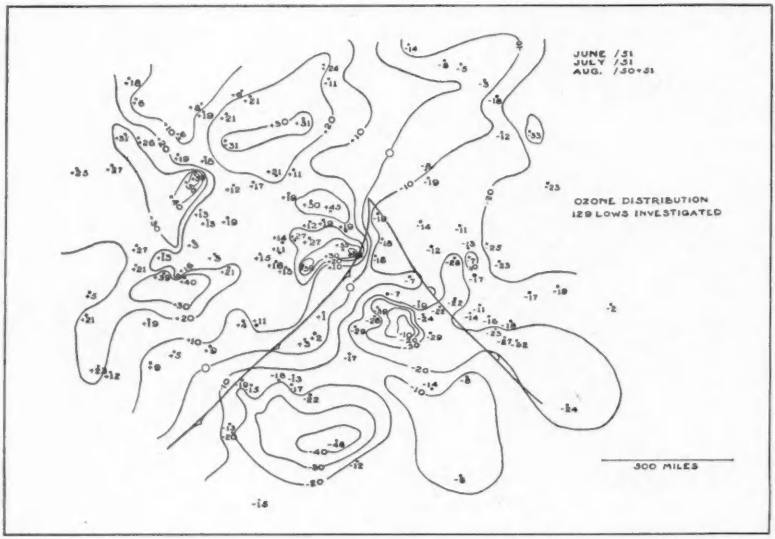

FIG. 4. Typical ozone distribution around a low pressure system. Summer—June, July, August.

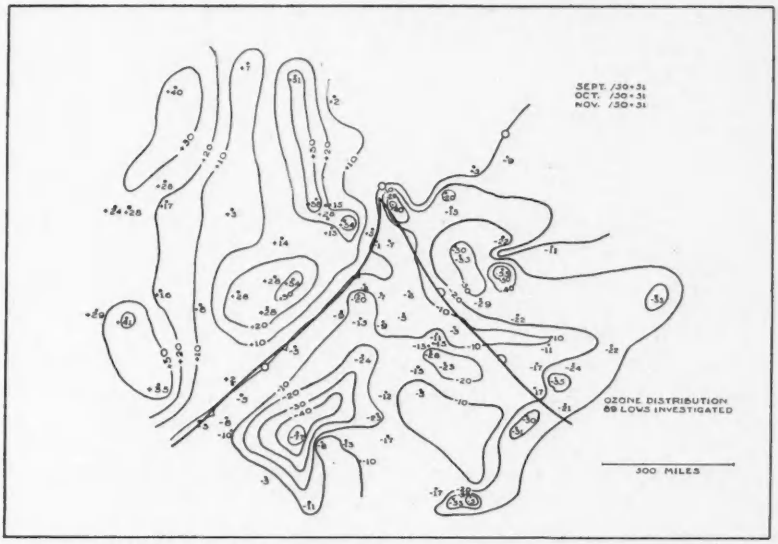

FIG. 5. Typical ozone distribution around a low pressure system. Autumn—September, October, November.

The high pressure area maps are illustrated in the next three figures. Fig. 6 shows a vigorous polar air mass which passed over the Edmonton area from

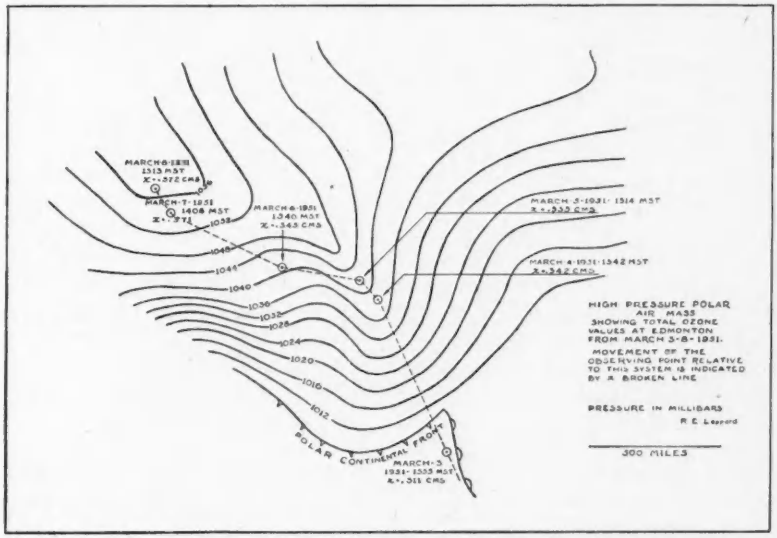

FIG. 6. Ozone changes during the passing of a vigorous high pressure polar air mass.

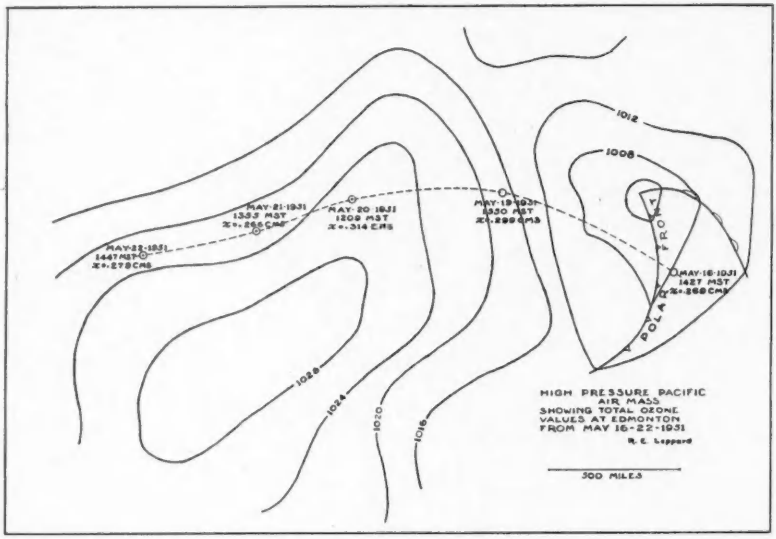

FIG. 7. Ozone changes during the passing of a large Pacific air mass.

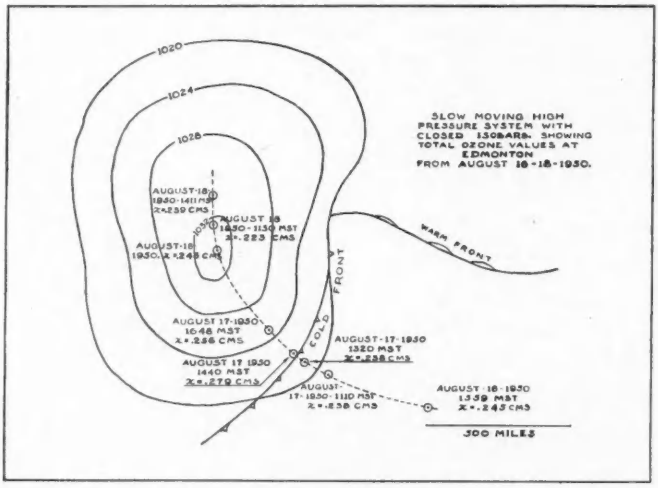
1020
1024
1028
SLOW MOVING HIGH PRESSURE SYSTEM WITH CLOSED 1508ARS. SHOWING TOTAL OZONE VALUES AT EDMONTON FROM AUGUST 16-18-1950.
AUGUST-18-1950-1411 MST X=.239 CMS
AUGUST 18 1950-1130 MST X=.223 CMS
AUGUST-18-1950 X=.248 CMS
WARM FRONT
COLD FRONT
AUGUST 17-1950 1646 MST X=.256 CMS
AUGUST 17 1950 1440 MST X=.279 CMS
AUGUST-17-1950 1320 MST X=.238 CMS
AUGUST-17-1950-1110 MST X=.238 CMS
AUGUST-16-1950 1359 MST X=.245 CMS
300 MILES

FIG. 8. Ozone changes during the passing of a small slow-moving air mass.

March 3 to 8, 1951. The anticyclone of Fig. 7 moved over the mountains from the Pacific during the period May 16 to 22, 1951. A smaller, round, shallow system passed over the observation area during August 16 to 18, 1950, and is shown in Fig. 8. The actual ozone values are given on these three diagrams.

DISCUSSION OF RESULTS

(A) In Fig. 1 (10-day averages) and in Table II (daily averages) most of the low values are associated with a strong flow of warm air from the interior of the continent (or from the middle latitudes of the Pacific Ocean) towards a depression. If the depression is vigorous enough to reach between 15 and 20 km. the lower ozone layers may be carried up by the ascending air. The total amount may then be further reduced by a rapid photochemical adjustment in the upper layers.

The high values are generally associated with polar air, perhaps accompanied by subsidence, which Reed (10) has suggested as an important mechanism for increasing the total amount of ozone. No quantitative estimate of the relative importance of ascension or subsidence effects is yet possible in the Edmonton area.

Certain cases will be observed when the same 10-day period in succeeding years has an exactly opposite ozone departure. For example, the middle 10 days of February show a low ozone in 1951, and a high one in 1952. The corresponding temperature averages are shown in frames like the points on the curve to which they refer. The comparisons agree with the transport mechanism except for the early part of December, 1950 and 1951. The low ozone here for 1950 depends on only three days' measurements, 4th, 8th, and 10th. Mean temperatures from 1st to 4th are all below zero (about $-15°$ F.), the 5th is about zero, and the next five days are about 15° F. above zero. The low ozone value is therefore really associated with this higher, shorter period average. After December 13th the average temperature dropped to near zero again, and remained there till the 19th. This was accompanied by a small rise in the ozone average. In 1951, the whole 10-day period was fairly consistent in temperature.

A few specific examples of the observed ozone, with temperature changes before and after, are given in Table III. Periods of low and high ozone are shown separately. The average temperature for each period, comprising 10 or 20 days, is also given. The high ozone part of the table shows also the lowest minimum, and the lowest 24 hr. average temperature for the central period. For five days before and after this central period, the highest maximum, highest 24 hr. average, and the five day average temperatures are given. The converse temperatures are given in the low ozone part of the table.

It will be noticed that in all seasons a high ozone and a low temperature occur together, and that the period of high ozone is preceded and followed by relatively higher temperature, which does not always show up in a five day average. The explanation is simple:—cold and warm spells are not equal in length, and do not exactly fit the averaging periods. The converse temperature relationship is true also for periods of low ozone. Particularly noteworthy are the extreme temperature changes observed in February and March. There is thus strong evidence that the transport mechanism of ozone change is of great importance in this continental location, though with a single station it is impossible to determine how the ozone in a given air mass is changing.

TABLE III

SURFACE TEMPERATURES DURING A 10 OR 20 DAY PERIOD OF OZONE MEASUREMENTS COMPARED WITH SURFACE TEMPERATURES FOR FIVE DAYS BEFORE AND FOR FIVE DAYS AFTER. ALL TEMPERATURES FROM METEOROLOGICAL RECORDS, IN DEGREES FAHRENHEIT

Five days before			Central period				Five days after		
High ozone									
Highest max.	Highest 24 hr. av.	5 Day av.	Dates	Lowest min.	Lowest 24 hr. av.	Period av. T.	Highest max.	Highest 24 hr. av.	5 Day av.
80.8	69.4	63.9	Aug. 1950 1–10	39.0	54.6	59.1	74.8	61.8	56.2
33.4	21.9	10.4	Mar. 1951 1–10	−30.3	−23.0	−12.9	37.0	24.9	10.2
73.4	57.2	53.7	May-June 1951 21–10	33.8	38.0	51.3	87.6	71.9	66.1
39.0	28.6	21.9	Dec. 1951 1–10	3.0	11.1	20.2	39.8	36.2	3.7
42.7	31.5	27.8	Feb. 1952 11–20	−11.2	− 5.1	12.3	39.0	31.2	7.2
39.0	31.2	20.2	Mar. 1952 1–10	−13.0	− 5.2	7.3	33.3	16.5	13.5
48.4	41.1	34.9	Apr. 1952 1–10	16.2	23.5	36.2	68.2	52.3	48.7
83.3	61.1	55.4	Oct. 1952 1–10	18.0	27.4	44.8	60.9	51.3	41.9
Low ozone									
Lowest min.	Lowest 24 hr. av.	5 Day av.	Dates	Highest max.	Highest 24 hr. av.	Period av. T.	Lowest min.	Lowest 24 hr. av.	5 Day av.
35.0	52.9	56.9	Sep.-Oct. 1950 21–10	88.2	68.7	44.3	29.3	37.2	40.5
−28.9	−19.5	−5.6	Feb. 1951 1–20	42.0	29.2	6.8	0.8	13.4	16.9
24.4	32.8	34.0	Apr. 1951 1–10	56.1	44.0	37.8	17.5	24.7	36.2
10.8	11.8	26.2	Nov. 1951 1–10	44.8	37.2	27.6	18.2	21.8	24.4
32.6	49.7	54.2	June 1952 1–10	81.0	67.0	57.8	43.1	50.3	52.5
38.8	47.6	51.9	Sep. 1952 21–30	86.9	64.1	56.6	18.0	27.4	39.1

(B) More detail of the way in which ozone changes with the passage of low pressure systems is apparent in the seasonal maps of Figs. 2, 3, 4, and 5. In all seasons it will be seen that low ozone is characteristic of the warm front area, and that the low values extend over 500 miles ahead of the front. This agrees with the temperature findings in a typical vertical section for the eastern part of such a weather system. There is some difference in the amount of the departure during the various three-month periods, which may be an indication of the vigor of the circulation.

The cold front seems to be very nearly the boundary separating below normal from above normal values, and the zero line passes close to the center

of the depression in all seasons. There seems to be much less transport ahead of the cold front than is the case with the warm front.

The lines of equal departure seem to show some small areas with very high or very low ozone. Most of these depend on a single observation, and cannot be given too much weight. To the extent such areas are real, however, they may be indications of change by ascension or subsidence as the case may be.

In the investigation of the three high pressure systems several important features were noticed. The polar air mass of Fig. 6 was very strong and vigorous, and produced the highest ozone value yet recorded at Edmonton. Though it moved nonuniformly, its path past the station was such that almost the steepest gradient of pressure was experienced from the center of the preceding low to the top of the high. The related extreme temperatures are found in the second row of Table III.

The high pressure system which extended in from the Pacific, Fig. 7, did not produce as great a contrast across the polar maritime front associated with it, but did show values decreasing to the rear, as observed by Dobson and others in a similar maritime air mass. The center of this shallow system passed 200 miles south of Edmonton, but the high ozone continued for a further 20 days as shown in Tables II and III.

Measurements are being continued, and it is planned to extend the analysis to include upper air data obtained by radio-sonde at Edmonton, for the period from 1950 to 1954.

ACKNOWLEDGMENTS

It is a pleasure to acknowledge support for one of the authors from a research grant of the National Research Council, through the Associate Committee on Geodesy and Geophysics. Much willing help has been given by the personnel of the Meteorological Service at Edmonton, and by several members of the Physics Department of the University of Alberta.

REFERENCES

1. Craig, R. A. Meteor. Monographs, 1. No. 2. 1950.
2. Dobson, G. M. B. Proc. Roy. Soc. (London), A, 129: 411. 1930.
3. Dobson, G. M. B. Proc. Phys. Soc. (London), 43: 324. 1931.
4. Dobson, G. M. B., Brewer, A. W., and Cwilong, B. M. Proc. Roy. Soc. (London), A, 185: 144. 1946.
5. Dobson, G. M. B., Harrison, D. N., and Lawrence, J. Proc. Roy. Soc. (London), A, 122: 456. 1929.
6. Fritz, S. and Stevens, G. C. Monthly Weather Rev. 78: 135. 1950.
7. Meetham, A. R. Quart. J. Roy. Meteor. Soc. 63: 289. 1937.
8. Ny, T. Z. and Choong, S. P. Compt. rend. 195: 309. 1932; 196: 916. 1933.
9. Rayleigh (Strutt, R. J.). Phil. Mag. 47: 375. 1899.
10. Reed, R. J. Ph.D. Thesis, Mass. Inst. Technol., Cambridge, Mass. 1949.
11. Tonsberg, E. and Olsen, K. L. Geofys. Publikasjoner Tromso. 13: No. 12. 1944.

THE DESIGN OF AN AUTOMATIC RECORDING ELECTROSCOPE AND ITS USE TO DETERMINE HALF-LIVES IN RADIOACTIVE DECAY[1]

By Rosalie M. Bartholomew, F. Brown, W. D. Howell, W. R. J. Shorey, and L. Yaffe[2]

ABSTRACT

An automatic recording electroscope has been constructed and used to determine short half-lives in radioactive decay. The operation of the instrument has been tested by comparing it with both a manually operated electroscope and a 4π type proportional β counter. The instrument produces results which are at least as accurate as any with which they may be compared. The half-lives of Co^{60m} and Al^{28} have been measured as $10.47 \pm .02$ min. and $2.27 \pm .02$ min. respectively.

INTRODUCTION

The quartz fiber electroscope (17) is a convenient instrument for the measurement of half-lives in radioactive decay. It has the advantage of simplicity and stability. A good electroscope with suitable voltage supply is capable of giving very accurate results.

The electroscope is normally a simple instrument to use. In the rate-of-drift method one observes the fiber through an eyepiece and by means of a stop watch measures the time for the fiber to move between two fixed points on the eyepiece scale. The reciprocal of this time is proportional to the disintegration rate of the sample. At the same time one measures the time elapsed since the experiment began. Readings are repeated at suitable intervals and a decay curve plotted. Certain difficulties arise when the half-life of the nuclide being measured is short (< 10 min.). It is preferable to have the disintegration rate such that the discharge time at the start of the experiment is very short. Otherwise the time taken for a single reading becomes appreciable compared to the half-life and corrections have to be made. A high initial activity is also necessary so that a measurable activity may persist over as many half-lives as possible. Not only are the discharge times short, but readings must be repeated at very short intervals in order to obtain a good decay curve. The timing of these operations by observation and stop watch is both inaccurate and tedious.

The determination of short half-lives by other counting techniques is also troublesome for essentially the same reasons. We have constructed an automatic recording electroscope which measures discharge times as short as a few seconds with an error of not greater than 1/10 sec. and takes successive readings very rapidly. The discharge times and the time elapsed since the start of the experiment are recorded for each reading. By incorporating a scaler unit and standard frequency source as part of the timing device, the discharge time may be timed to much greater accuracy. Full details are given below.

[1] *Manuscript received March 2, 1953.*
Contribution from the Chemistry and Electronics Branches, Atomic Energy of Canada Limited, Chalk River, Ontario. Issued as A.E.C.L. No. 54.
[2] *Present address: Department of Chemistry, McGill University, Montreal, Quebec.*

This instrument has been used to determine the half-lives of Al^{28} and Co^{60m}. The performance of the instrument has been checked by comparing it with a 4π type proportional β-counter (6) using Mn^{56} and also by comparison with a manually operated electroscope using Cu^{66}. These experiments show the instrument to be highly satisfactory. The results were as accurate as any value with which they could be compared. Finally the instrument is simple to operate, stable, and reliable over long periods of time.

DESCRIPTION OF APPARATUS

(1) *Introduction*

The apparatus is illustrated schematically in Fig. 1. A type TQQ Beta electroscope (9, 25) has been modified to incorporate a mask with two slits

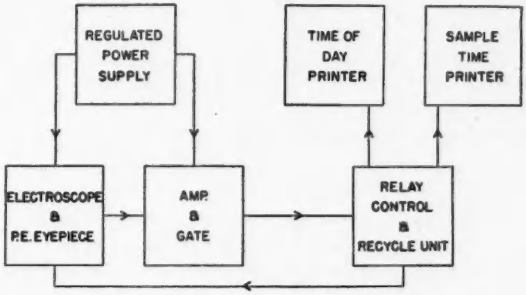

FIG. 1. Schematic illustration of apparatus.

and photomultiplier unit in place of the conventional eyepiece. The arrangement is such that light beamed via the slits onto the cathode of the photomultiplier is interrupted by the passage of the electroscope fiber as it collapses in the presence of an ionizing radiation, and produces two electrical signals corresponding to the start and stop of a timing event. These signals are fed to the relay control unit which controls the on/off period of a time printer or any other suitable time recording device. Another time printer is also employed to record the elapsed time at the beginning and end of each electroscope measurement from the start of the experiment. A recycle unit is employed to reset the system, with the exception of the elapsed time recorder, between successive measurements.

A photoelectric eyepiece system for use with an electroscope has been described elsewhere (7).

(2) *Circuit Details*

(2:1) *Electroscope and Photomultiplier Eyepiece*

The electroscope employed is the identical instrument used by Sargent, Yaffe, and Gray in these laboratories. It is fully described by these authors (25). The modifications necessary for automatic operation (see Fig. 2) consist of a solenoid charging probe which is automatically released during sample meas-

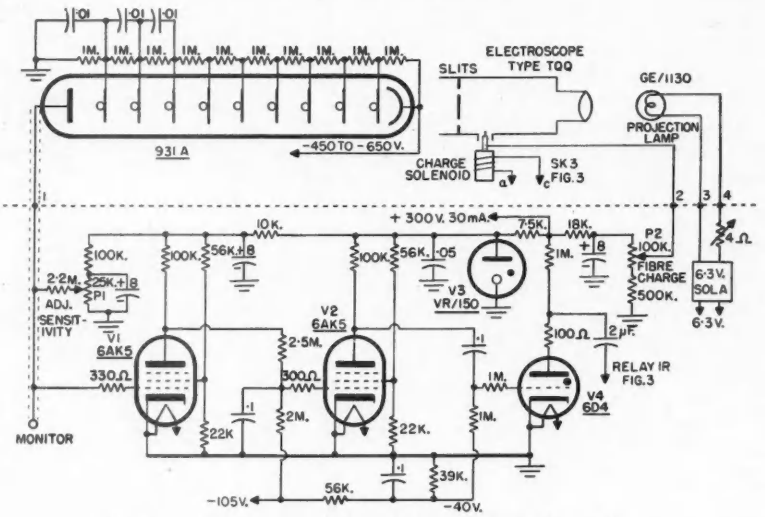

FIG. 2. Circuit diagram of photoelectric eyepiece and amplifier.

urements and a photoelectric eyepiece used in place of the conventional eyepiece. This eyepiece incorporates a mask with two slits which are 0.001 in. wide and 3/16 in. high, spaced approximately 7/16 in. apart, and a 931 A photomultiplier. The lamp used in the optical projection system is a type GE/1130, 6–8 v., operated from the 60 cycle mains through two Sola stabilizing transformers arranged in series. To ensure long life the projector lamp is run slightly under its rating, a series resistance being supplied for this purpose. A conventional stabilized power supply is used for the 931 A photomultiplier and its associated amplifier circuit.

In the absence of a signal, the grid of $V1$ is approximately 3 v. negative so that $V1$ is cut-off and $V2$ conducting. To establish the correct operating voltage at the grid of $V1$, the slider of $P1$ is set about the middle of its sweep and the lamp intensity and photomultiplier B+ adjusted until the grid voltage, using a vacuum tube voltmeter, is approximately -3 v. The final adjustment is then carried out on $P1$, which also serves the purpose of providing adjustment for slight periodic variations of the grid voltage caused by component drifts.

The correct charging voltage for the electroscope fiber, which is approximately 250 v. for this electroscope, is established by adjusting the 10-turn potentiometer $P2$, a 25-v. change being required to complete the fiber scan. Since the capacitance of the electroscope is approximately 20 $\mu\mu$F., the equivalent charge to produce the required scan is 5×10^{-10} coulombs.

(2:2) *Mode of Operation*

Fig. 3 is a circuit diagram of the relay control and recycle unit with the inset diagram illustrating the sequence of the relay switching. A function switch $S2$ enables manual or automatic operations to be performed.

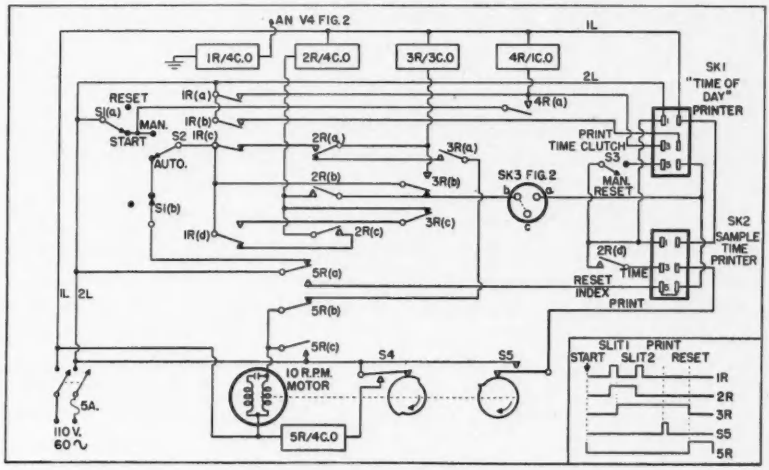

FIG. 3. Relay control and recycle unit.

In the manual setting correct functioning of the equipment can be checked by varying the electroscope fiber voltage (using potentiometer $P2$). The manual setting also permits timing measurements for individual samples to be carried out using $S1(a)$ to start and then reset the equipment at the end of the measurement.

Apart from the recycle mechanism the manual and automatic functions are similar in the mode of operation. The latter will now be described in more detail.

Having reset the equipment and set switch $S2$ to "auto", then on closing the start switch $S1(b)$, the electroscope fiber charge solenoid, Fig. 2, is energized by completion of the a-c. circuit via relay contact $3R(b)$ and the link bc of the socket $SK3$. The purpose of the link bc will be discussed later. This releases the electroscope fiber which then proceeds to collapse under the influence of the ionizing radiation. Eventually the fiber crosses the field of view of the first slit of the mask, which reduces the photomultiplier current and produces a positive signal at the grid of $V1$, which after amplification triggers the thyratron $V4$ and energizes relay $1R$. Relay $1R$ remains energized for approximately 0.2 sec., and when its contacts close the following operations are performed.

(a) Contact $1R(a)$ energizes relay $4R$ which is then maintained operated for the duration of the measurement by the hold contact $4R(a)$. This operation also starts the "time-of-day" printer connected to $SK1$.

(b) Contact $1R(c)$ energizes relay $2R$ via contact $3R(c)$ which in turn engages the time clutch of the "sample time" printer via contact $2R(d)$.

When relay $1R$ is de-energized after approximately 0.2 sec. the following take place.

(*a*) Contact $1R(d)$ via $2R(c)$ maintains $2R$ energized.

(*b*) Contact $1R(c)$ via the closed contact $2R(a)$ energizes relay $3R$.

(*c*) Contact $3R(b)$ maintains $3R$ energized and contact $2R(b)$ maintains the electroscope charge solenoid energized.

The electroscope fiber continues to collapse and when it scans the second slit of the mask relay, $1R$ is once more energized with the following sequence.

(*a*) Contact $1R(b)$ engages the print solenoid of the "time-of-day" printer and prints the elapsed time at the end of the electroscope fiber scan.

(*b*) The opening of contact $1R(c)$ releases relay $2R$ which in turn disengages the time clutch of the "sample-time" printer.

(*c*) Contact $2R(b)$ releases the electroscope charge solenoid, thereby permitting the electroscope to be recharged.

(*d*) On de-energizing relay $2R$ the circuit to recycle motor is completed via contacts $2R(a)$, $3R(a)$, and $5R(b)$. In the process of recycling the cam operated switch $S5$ is closed and prints the sample time.

Recycling continues until the cam operated switch $S4$ is closed, thereby energizing relay $5R$ which performs the following functions.

(*a*) The switching of change-over contact $5R(a)$ resets the sample time printer and advances the sample indices of the two printers.

(*b*) The opening of contact $5R(b)$ de-energizes relay $3R$.

(*c*) The closing of contact $5R(c)$ maintains the motion of the motor until switch $S4$ is opened by the action of its cam.

Recycling occupies approximately six seconds, and although this function could have been speeded up, this method, nevertheless, has certain advantages. It provides a sufficiently long and constant time for recharging and settling down of the electroscope system and also permits the scope of the system to be extended for more timing measurements. This latter feature will be discussed later in section 3.

With the exception of the d-c. relay $1R$, all relays used are of the a-c type. The printers used are the Tracerlab type SC-5A which print to the nearest 0.1 sec. Although two printers are used, it is possible to utilize only one, since the "time-of-day" printer is arranged to print the time at the beginning and end of each timing measurement. The use of two printers, however, simplifies recording for graphical purposes, provides a cross check, and also enables the scope of the system to be increased as will be discussed further in section 3.

Other additional features can be incorporated in the control unit. Should one or other of the slits in the electroscope mask fail to record the passage of the fiber, then for an unattended operation provision can be made for resetting the system. For this purpose a variable override time control, such as a Kramer Tec-timer, and a relay can be used. The time setting of the override time control, which may be periodically adjusted during the course of the experiment, is chosen to suit the timing requirements of the electroscope which is set in motion as soon as the electroscope fiber starts to collapse. If both slits register, then the override time control is automatically reset. Should one slit

fail to record, then the override control takes over and resets the system. Should both slits fail to register, then the relay is energized and an alarm sounded.

In order to reduce the number of observations during an experiment involving half-life measurements of several hours, provision is made to break the link *bc* on plug *SK*3 and insert a suitable time delay mechanism. Thus for a half-life of, say, 5 hr., a time delay of, say, 10 min. between observations can be incorporated.

(3) *Timing Accuracy and Sources of Error*

The instrument aims at an over-all accuracy of better than $\pm 1\%$ and from results of half-life measurements given in the next section this figure appears to be readily achieved.

With the present arrangement the electroscope is capable of covering a timing range of two seconds to one hour, so that it can record continuously during a decay of approximately 10 half-lives. The natural discharge time of the electroscope is approximately 250 hr. which introduces an error of only 0.4% when timing for a one hour timing measurement.

Since the electroscope is of open construction, changes of the density of the air in the collecting space caused by variations in room temperature and barometric pressure necessitate making timing corrections. Since the measurements were carried out in an air-conditioned room, temperature corrections, which are of the order of 0.15% per °F., can usually be neglected. Special attention, however, has to be paid to barometric readings where a 1% change causes a 0.7% change in the electroscope reading time. Fig. 4 shows a typical plot of electroscope time and barometer readings over a seven day interval. In these observations a standard source was employed, which discharged the electroscope in approximately 30 sec., automatic recordings being made every half hour.

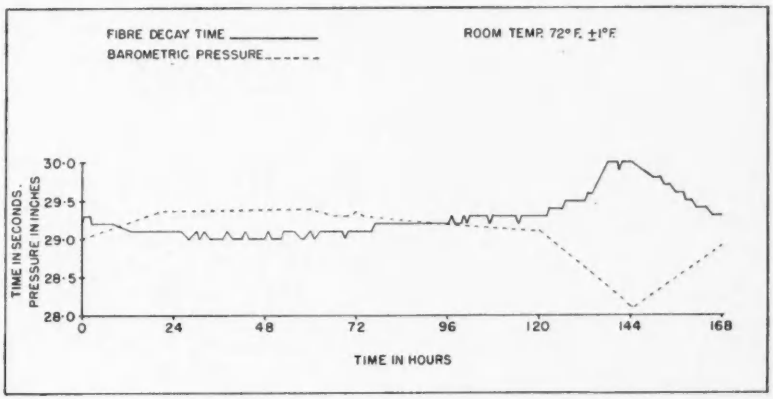

FIG. 4. Effect of barometric pressure on electroscope operation at constant temperature.

The two printers used for time recording employ 60 cycle synchronous motors and record to the nearest 0.1 sec. In practice it has been found that the frequency stability of the 60 cycle mains at Chalk River is adequate for timing purposes, the frequency variations being less than $\pm 0.3\%$. However, since the printers can only record to the nearest 0.1 sec., this corresponds to a possible 0.3% error in a 33 sec. timing operation on the electroscope, with progressively larger errors with the shorter timing intervals. To eliminate this shortcoming and improve the timing accuracy one of two alternative methods can be employed.

The first, which is suitable for half-life measurements of short-lived substances (say for half-lives of 2 to 15 min.), is to employ a scaler and a standard frequency source for timing purposes until such time as the printer can record the time directly with sufficient accuracy. Facilities for gating and resetting the scaler are provided by socket *SK*2 (Fig. 3). It is only necessary to record the scaler count, which is proportional to fiber scan time, in the interval between stopping and resetting of the scaler. The frequency of the standard is chosen to satisfy the timing accuracy required.

The other alternative is similar to the above method but provides an indirect means of automatically recording the scaler count. A method for doing this has been described elsewhere (22). Again it can be arranged with this method to record the time with the scaler until the timing accuracy is sufficient for direct time recording with the printer.

RESULTS

(1) *Copper 66*

This nuclide was identified by Heyn (16) and by Chang, Goldhaber, and Sagane (10). It emits β-rays of high energy (> 2 Mev.) (15, 29) and γ-rays of 1.72 Mev. (21). Previously recorded values for the half-life are 4.34 min. (28), which has been withdrawn, 5.05 min. (21), 5.18 min. (8), and 5.2 min. (14). A careful determination in our laboratories (25) using the identical TQQ electroscope with manual operation gave a value of 5.10 ± 0.02 min.

The copper was in the form of spectroscopically pure foil. A piece of weight 20 mgm. was irradiated in a high flux position of the NRX reactor for a few seconds and returned immediately to the laboratory by pneumatic conveyor. This foil was immediately placed in the electroscope, secured to the source holder by a very small spot of "liquisilk" adhesive. The electroscope was allowed to run long enough to record data both for the short-lived Cu^{66} and the 12.9 hr. Cu^{64} which forms a background activity. The decay curve was constructed and the 12.9 hr. component subtracted in the usual manner. The contribution due to 12.9 hr. activity at the start of the recordings was $< 1.0\%$ of the whole activity. The decay curve of Cu^{66} after subtracting the 12.9 hr. component formed a straight line over nine half-lives. The value for the half-life of Cu^{66} was 5.07 ± 0.02 min. which is in excellent agreement with the value quoted above (25).

(2) *Manganese 56*

This nuclide was identified by Livingood and Seaborg (18). It emits β and γ radiation (27). Previous values for the half-life are 2.59 hr. (18), 2.62 hr. (23), and $2.586 \pm .005$ hr. (4).

Spectroscopically pure manganese metal (6.0 mgm.) was irradiated for 30 sec. in the NRX reactor. This metal was dissolved in nitric acid. The bulk of this solution was evaporated onto the source holder of the electroscope and covered with glyptal varnish. From the remainder several thin sources were made for the 4π β-counter by evaporating aliquots onto thin gold sputtered QYNA films. The electroscope was allowed to operate automatically. The 4π counter was operated manually in the usual manner, most of the readings being taken on one source but with occasional readings on the others as a check. The value obtained from the electroscope data was 2.581 hr. (10 half-lives) and from the 4π counter data 2.576 hr. (11 half-lives). An independent measurement of this half-life made by other workers in our laboratories using a 4π counter gave a value of $2.576 \pm .002$ hr. (2).

(3) *Cobalt 60^m*

This isomer of Co^{60} was identified by Livingood and Seaborg (19) and by Heyn (16). Its β–γ radiations have been studied by Deutsch and Scharf-Goldhaber (12). The value for the half-life reported by Livingood and Seaborg (19) is 10.7 min.

Pure cobalt wire was irradiated in a high flux position of the NRX reactor for a few seconds and returned immediately to the laboratory by pneumatic conveyor. Various weights were used with suitable irradiation times. In some cases the wire was fixed to the electroscope source holder by suitable fixative, in others no fixative was used. The data are summarized in Table I.

TABLE I

Wt. Co (mgm.)	Irradiation time (sec.)	Fixative	$t_{1/2}$ (min.)	Number of half-lives measured
2.8	5	Liquisilk	10.43	4
22	5	Liquisilk	10.44	8
20	5	Graphite–collodion	10.50	6
21	5	Graphite–collodion	10.53	5
50	3	None	10.42	6
50	3	None	10.50	7
			Av. 10.47	

The average value of these six determinations gives the half-life of Co^{60m} as $10.47 \pm .02$, where the error quoted is the standard deviation. The nature of the fixative has no effect on the results.

Another sample of pure cobalt was obtained from a different source and a similar measurement made. The value of the half-life was 10.49 min. (five half-lives).

(4) *Aluminum 28*

This nuclide was identified by Amaldi *et al.* (1) and by MacMillan and Lawrence (20). Its β–γ radiation has been investigated by several workers (5, 3). Previous values for the half-life are 2.30 min. (26, 1), 2.4 min. (13), and 2.6 min. (20, 11, 24).

Aluminum metal of spectroscopic grade purity was obtained from two different sources. Samples were irradiated in a high flux position of the NRX

reactor, recovered immediately, and placed in the electroscope without any fixative on the source holder. The results are summarized in Table II.

TABLE II

Wt. Al (mgm.)		Irradiation time (sec.)	$t_{1/2}$ (graphical)	$t_{1/2}$ (least square)	Number of half-lives observed
1st material	50	10	2.280	2.284	5
	50	10	2.275	2.270	6
	50	5	2.267	2.271	5
2nd material	50	5	2.242	2.261	5
	10	60	2.260	2.257	6
		Average	2.265	2.269	

There appears to be a small but significant difference between the two materials, due no doubt to traces of impurities. Since both specimens are likely to contain similar impurities, perhaps in different amounts, it is difficult to say how close the average values above are to the true half-life of Al^{28} obtained from absolutely pure Al^{27}. A value of $2.27 \pm .02$ is perhaps reasonable.

REFERENCES

1. Amaldi, E., D'Agostino, O., Fermi, E., Pontecorvo, B., Rasetti, F., and Segre, E. Proc. Roy. Soc. (London), A, 149: 522. 1935.
2. Bartholomew, Rosalie M., Merritt, W. F., Hawkings, R. C., and Yaffe, L. Can. J. Chem. 31: 204. 1953.
3. Beris, J., Hedgran, A., and Hole, A. Arkiv. Mat. Astron. Fysik, A, 35: 412. 1948.
4. Bishop, G. R., Wilson, R., and Halban, H. Phys. Rev. 77: 416. 1950.
5. Bleuler, E. and Zunti, W. Helv. Phys. Acta, 20: 195. 1947.
6. Borkowski, C. J. Conference on absolute β counting. Preliminary report No. 8. Nuclear Sci. Ser. Natl. Research Council, Washington, D.C.
   Hawkings, R. C., Merritt, W. F., and Craven, J. Forthcoming publication.
7. Bryant, J. and Michaelis, M. R.C.C. r/7 Radiochemical Centre, Ministry of Supply, Amersham, Berks, England.
8. Cameron, A. G. W. and Katz, L. Phys. Rev. 80: 904. 1950.
9. Carmichael, H. Private communication. Chalk River, Ontario.
10. Chang, W. Y., Goldhaber, M., and Sagane, R. Nature, 139: 962. 1937.
11. Cork, J. M., Richardson, J. R., and Kurie, F. N. D. Phys. Rev. 49: 208. 1936.
12. Deutsch, M. and Scharf-Goldhaber, G. Phys. Rev. 83: 1059. 1951.
13. Ellis, C. D. and Henderson, L. J. Proc. Roy. Soc. (London), A, 156: 358. 1936.
14. Friedlander, G. and Alburger, D. E. Phys. Rev. 84: 231. 1951.
15. Gadsinski, N. N., Golotzwan, I. A., and Danilenko, A. I. J. Exptl. Theoret. Phys. U.S.S.R. 10: 1. 1940.
16. Heyn, F. A. Physica, 4: 1224. 1937.
17. Lauritsen, C. C. and Lauritsen, L. Rev. Sci. Instruments, 8: 438. 1937.
18. Livingood, J. J. and Seaborg, G. T. Phys. Rev. 54: 391. 1938.
19. Livingood, J. J. and Seaborg, G. T. Phys. Rev. 60: 913. 1941.
20. MacMillan, E. M. and Lawrence, E. O. Phys. Rev. 47: 343. 1935.
21. Meitner, L. Arkiv. Mat. Astron. Fysik, A, 33: 43. 1946.
22. Moody, N. F., Howell, W. D., Battell, W. G., and Taplin, R. H. Rev. Sci. Instruments, 22: 455. 1951.
23. Perlman, M. L. and Friedlander, S. Phys. Rev. 74: 297. 1948.
24. Ridenour, L. A. and Henderson, W. J. Phys. Rev. 52: 889. 1937.
25. Sargent, B. W., Yaffe, L., and Gray, A. P. Can. J. Phys. 31: 235. 1953.
26. Seidlitz, L., Bleuler, E., and Tendham, D. J. Phys. Rev. 76: 453, 861. 1949.
27. Siegbahn, K. Arkiv. Mat. Astron. Fysik, A, 33: 410. 1946.
28. Silver, L. M. Phys. Rev. 76: 589. 1949.
29. Sinma, K. and Yamasaki, N. Sci. Papers Inst. Phys. Chem. Research, Tokyo, 35: 16. 1938.

PHOTO-ALPHA REACTIONS IN NUCLEAR EMULSIONS[1]

By C. H. Millar and A. G. W. Cameron[2]

ABSTRACT

In experiments to search for new photonuclear reactions involving the emission of heavy particles ($Z \geqslant 2$), Ilford E1 emulsions were exposed to 240 roentgens of X radiation from the University of Saskatchewan betatron operating at energies up to 27 Mev. The plates were developed by a special "grain-gradation" technique which suppressed proton tracks and X-ray fog. The ejection of single α particles was observed from C^{13}, N^{14}, O^{16}, Ag, and Br. Multiple-pronged stars were observed due to the photodisintegration of C^{12}, N^{14}, O^{16}, and probably Ag or Br. Interpretations of these events were deduced, and cross section versus energy curves for many of them were obtained. Range–energy relationships were obtained for Be^{9}, B^{10}, and C^{12} particles in E1 emulsions.

INTRODUCTION

The first photo-alpha reaction was discovered at Zurich in 1948 by Hänni, Telegdi, and Zünti (18) who exposed nuclear research emulsions to 17.5 Mev. γ rays and observed in them three-pronged α-particle stars which they analyzed as being from the reaction $C^{12}(\gamma, \alpha)Be^{8*} \rightarrow 2\alpha$. Since that time the Zurich workers (30, 35, 36, 42, 43) have continued their research using a monochromatic γ-ray source, while a group at the British Atomic Energy Research Establishment, Harwell (8–17, 37–40, 45–47) has been doing work along similar lines using the continuous X-ray spectrum from a 24 Mev. synchrotron. The authors, making use of the 27 Mev. betatron at the University of Saskatchewan, carried out similar experiments during 1949–1950 and reported some preliminary results at that time (26–29). This paper contains a complete account of the authors' observations and their analysis of the data.

EXPERIMENTAL PROCEDURE

I. Irradiation Conditions

Ilford type E1 nuclear research emulsions, 100 microns thick, were placed in a cadmium container at the center of a 1 ft. cube of paraffin and exposed to the betatron X-ray beam so that the emulsions were "edge-on" to the beam. The paraffin–cadmium combination was designed to reduce the number of neutrons entering the emulsion and reacting with its constituents.

The X-ray beam was filtered through 20 cm. of aluminum in order to reduce preferentially the low energy portion of the bremsstrahlung spectrum. This filtering had the effect of moving the maximum photon intensity of the X-ray spectrum to about 9 Mev. which is of the order of the threshold energy for photo-alpha reactions. The spectrum used in determining cross sections was obtained from unpublished calculations by Schiff for bremsstrahlung in the forward direction corrected for absorption in the Saskatchewan betatron (21) and further corrected and renormalized to allow for the aluminum and paraffin filtering used in this experiment.

[1] *Manuscript received February 18, 1953.*
Contribution from the Physics Division, Chalk River Laboratory, Atomic Energy of Canada Limited, Chalk River, Ontario. Issued as A.E.C.L. No. 56.
[2] *Present address: Department of Physics, Iowa State College, Ames, Iowa, U.S.A.*

The total irradiation received by the plates was measured by an ionization chamber interposed in the X-ray beam. This chamber was calibrated in a separate experiment against a standard Victoreen ionization chamber placed in the plate irradiation position.

Subsequent to the main experimental work described in this paper, activation measurements of the $Cu^{63}(\gamma, n)Cu^{62}$ reaction with and without aluminum filtering indicated that up to 50% of the X-ray dosage measured in the experimental arrangement used for irradiating the photographic emulsions was due to low energy radiations produced in the filter. Factors to correct for this effect were determined experimentally and have been included in cross-section calculations.

In order to interpret the experimental observations and to estimate reaction cross sections, it was necessary to know the atomic composition of the emulsion. The atomic analysis of E1 emulsion as supplied by Ilford Limited is shown in Table I.

TABLE I

ATOMIC COMPOSITION OF ILFORD NUCLEAR RESEARCH EMULSIONS

Element	Ag	Br	I	C	H	O	N	S
Gm./cm.^{3}	1.85	1.34	0.052	0.272	0.056	0.266	0.067	0.010

In the course of this experiment five plates were studied; the data pertaining to their irradiation are given in Table II.

TABLE II

IRRADIATION AND SEARCHING DATA FOR PHOTOGRAPHIC PLATES

Plate	Irradiation (roentgens)	Maximum X-ray energy (Mev.)	Approximate area searched (cm.^{2})
A	245	24	2.1
B	242	27	12.0
C	242	17	2.7
D	242	12	2.7
E	0	—	2.7

II. Plate Development

Ilford type E1 emulsions were used in this experiment since they are comparatively insensitive to lightly-ionizing particles. X-ray fogging of the plate was minimized by the use of the following modification of Van der Grinten's (49, p. 62) "grain-gradation" developing process.

The plates were presoaked in water for five minutes and then developed for 15 min. in a freshly prepared solution consisting of:

0.5 gm. $C_6H_4(OH)_2$ (hydroquinone),
10.0 gm. Na_2SO_3,
0.5 gm. KBr,
5.0 gm. KOH,
1.0 liter H_2O (distilled).

The developer temperature was automatically maintained at 23° C. and it was found necessary to control very carefully the time of development and pH of the developer, if consistently good results were to be obtained. Development was stopped by immersion of the plates in a 2% acetic acid stop bath for five minutes after which they were processed with Kodak Acid Fixer and washed in the usual manner.

III. Plate Survey

The plates were studied on a Bausch and Lomb binocular research microscope, the finest measurements being made at a nominal magnification of 3375 diameters. Particle energies were determined from the range–energy relationships of Lattes, Fowler, and Cuer (22) for C2 emulsions,[1] altered by 3% to take into account the greater stopping power of E1 emulsions. Calculation of the results was greatly assisted by the use of an IBM calculating punch and auxiliary equipment.

The emulsion shrinkage factor was obtained from measurements made on test plates which were from the same emulsion batch and subjected to the same processing as the irradiated plates. The total shrinkage was measured by means of a precision micrometer caliper capable of measuring to 1 micron. The thickness of the developed emulsion was measured by means of the vertical fine focusing mechanism of the microscope which was calibrated by means of gauge blocks.

With the form of plate development used it proved possible to study α-particle tracks in the presence of 240 roentgens of X-ray fogging. Lightly-ionized proton tracks were occasionally visible, but were easily distinguishable from α-particle tracks. It was discovered that under certain conditions of observation the tracks of particles with charge greater than two could be distinguished from α-particle tracks (see Experimental Results, Section II). In general, however, it was not possible to determine from the appearance alone of a short, dense track whether the particle was of charge two or of greater charge. In many cases energy or momentum considerations served to identify the particle, and since in the vast majority of these cases the tracks were attributable to α particles, we assumed that all dense tracks were α-particle tracks unless it could be shown otherwise. Since lower threshold energies and Coulomb barrier heights make α-particle emission much more probable than the emission of heavier particles, we feel that this assumption is not unreasonable.

With this type of irradiation and development, energy determinations of α-particle tracks were probably slightly less accurate than normal. However, in cross-section studies it proved necessary to use class intervals of 1 Mev. in order to obtain statistically significant intensity values; consequently statistics rather than track measurements set the limit of resolution in these experiments.

[1] *Recent measurements by I. B. Berlman (Phys. Rev. 80: 96. 1950) indicate that, at energies exceeding 10 Mev., α-particle energies as determined from the curves of Lattes et al. may be low by a factor ranging from 0.4% at 12 Mev. to 3.6% at 16 Mev. Applying this correction to our data produces a negligible effect on the general results.*

EXPERIMENTAL RESULTS

I. Single α-Particle Tracks

A. Energy Spectrum

Single α-particle tracks were the most common events observed in the plates. True single α-particle tracks must be attributed to α particles ejected from silver and bromine, the principal heavy nuclei present in the emulsion, because, in the case of a heavy element emitting an α particle, conservation of momentum allows the residual nucleus very little recoil energy, and its motion in the emulsion is not observable. In the case of a light element emitting an α particle the track of the recoiling nucleus is long enough to be measured, and, as will be shown in Section II, this recoil track may frequently be identified.

Similar areas were searched in all plates, and the α-particle energy spectra—normalized to conditions of equal X-ray dosage and area searched—are plotted in Fig. 1. The spectra have been corrected for the escape of tracks from the emulsion—see Appendix I(A)—and for "background" tracks arising from α particles emitted by naturally radioactive contaminants in the emulsion. This background spectrum was obtained by surveying the unirradiated plate E which was from the same emulsion batch and subjected to the same development as the irradiated plates. Background tracks formed about 5% of the tracks measured on plate A.

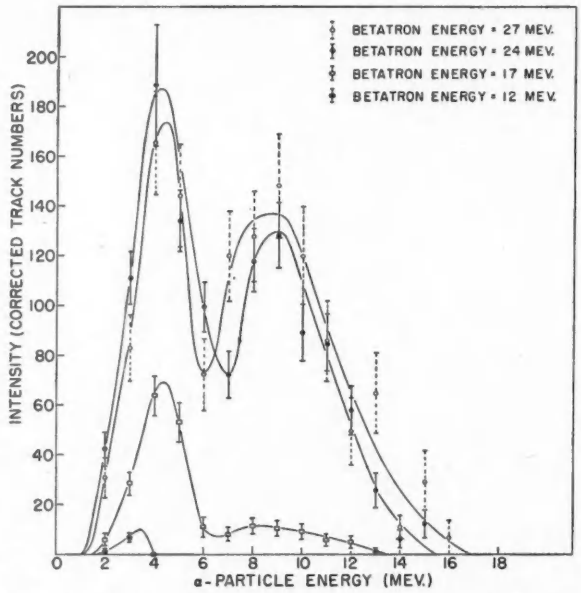

FIG. 1. Energy distributions of single α particles from the photodisintegration of silver and bromine as found in photographic emulsions irradiated with filtered bremsstrahlung with maximum energies of 12, 17, 24, and 27 Mev.

It will be noted that at the higher irradiation energies the spectra of these single α particles have two peaks, one at about 4 Mev. with a width at half maximum of 2.5 Mev., and one at about 9 Mev. with a width of 5 Mev. As the irradiation energy is lowered, the 9 Mev. peak diminishes more rapidly than does the 4 Mev. one until at an irradiation energy of 12 Mev. only a trace of the 4 Mev. peak remains.

The nuclear evaporation theory developed by Blatt and Weisskopf (3, Chap. VIII) should be applicable to middle-weight nuclei excited by X rays of the energies available in these experiments, and we have therefore calculated the α-particle spectra predicted by this theory in order to compare them with the experimental results. The details of this calculation together with the values of the various parameters used and the approximations made are described in a previous paper (25) in which the study of these single α particles has been extended by the use of 70 Mev. bremsstrahlung.

The theoretically predicted curves are shown in Fig. 2 for the plates irradiated with energies of 27, 24, and 17 Mev., and the high energy peaks observed

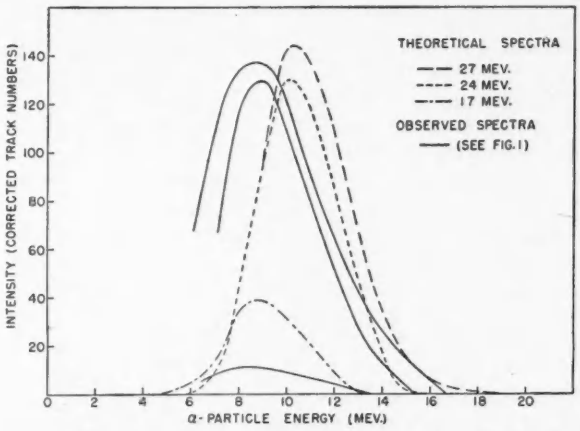

FIG. 2. Theoretical energy distributions of single α particles from the photodisintegration of silver and bromine irradiated with bremsstrahlung. Broken lines show calculated curves for various bremsstrahlung energies; solid curves are corresponding experimental values (see Fig. 1).

at these energies have been included for purposes of comparison. The calculated curves are based on the assumption that simple (γ, α) reactions account for the majority of the α-particle tracks observed. These curves have been normalized so that the peak of the 24 Mev. calculated curve is equal in intensity to that of the experimental curve.

It will be seen that the theory predicts few α particles with energies less than about 6 Mev. and consequently offers no explanation for the sharp peaks observed in the 4 to 5 Mev. region. There is, on the other hand, rough agreement of the observed high-energy peaks with the calculated spectra as

to limits of particle energy, relative intensity, and peak position. It will be noted, though, that the calculated peaks tend to occur at an energy about 1 Mev. greater than the observed peaks, and that the calculated relative intensity of the 17 Mev. curve is several times greater than observed. In view of the qualitative nature of the assumptions made in the theoretical estimate of the spectra (25), it is believed that the disagreement between the theoretical and observed spectra is within the limits of error of the computation. Thus the nuclear evaporation theory provides a description of the shape of the spectrum of α particles from bromine and silver irradiated with bremsstrahlung which is compatible with the observed results for α particles of energies greater than about 6 Mev.

This theory, on the other hand, predicts that few α particles of energies less than 6 Mev. will be ejected from bromine and silver; however a narrow peak in the 4 to 5 Mev. energy region is consistently observed and these observations have been repeated by Haslam and co-workers at Saskatchewan (19). These authors have explained the observed low energy peaks in terms of "threshold-favored" multiple reactions in bromine and silver. In such reactions the excited nucleus first emits a neutron, proton, or γ ray which leaves the residual nucleus with an excitation in excess of the binding energy of an α particle but not of a proton or neutron. Thus the emission of an α particle is the only mode of *particle* emission by which this residual nucleus may lose its energy of excitation, and the α particles emitted in reactions of this type are believed to give rise to the low energy peaks in the observed spectra. Most of the detailed arguments in favor of this interpretation are given in Haslam's (19) paper, but some further points should be noted.

Such "threshold-favored" α-particle emission has to compete only with γ-ray emission as the mode of nuclear de-excitation, and calculations based on the Gamow theory of α-particle emission (2, p. 163) and the Weisskopf theory of γ-ray lifetimes (3, Chap. XII) indicate that the probabilities for either type of decay are of similar magnitude, so that the proposed reaction mechanism is not improbable. It should be noted, however, that if a 4 or 5 Mev. α-particle track originates from an oxygen or nitrogen nucleus, the recoiling residual nucleus—by the observation of which such a reaction is distinguished from an event in silver or bromine—would have a range of less than 2 microns and might easily be misinterpreted by the observer. Very few photo-alpha events in oxygen or nitrogen have been identified in which the range of the recoiling residual nucleus is of this order—see Section II following—and therefore the possibility exists that some of the low energy α particles included in the observed spectra may arise from photo-alpha events in light elements.

B. Angular Distribution

In studying angular distribution of α-particle tracks with respect to γ-ray direction in a plate irradiated in the "edge-on" position it is more accurate to reject tracks dipping steeply into the emulsion and to allow for them by means of a geometrical factor than to attempt to distinguish and measure tracks at all angles. In this work we have chosen to reject tracks with dip angles greater than 45° before shrinkage.

In addition a rather complex escape correction factor must be applied to the data to account for tracks leaving the emulsion. This is given in Appendix I(B).

Figs. 3 and 4 show the angular distributions of the tracks in plate A in the 4 and 9 Mev. peaks, and in neither case is there a statistically significant deviation from the normalized isotropic distribution curve which is included for comparison.

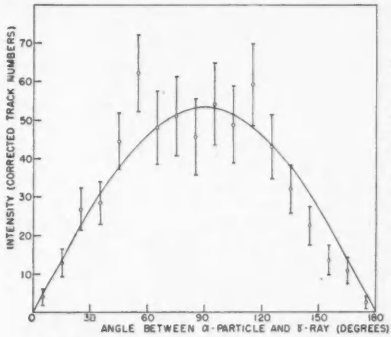

Fig. 3. Angular distribution with respect to γ-ray direction of single α particles in the 3 to 6 Mev. energy region. These are possibly ejected by photons from silver and bromine (see text).

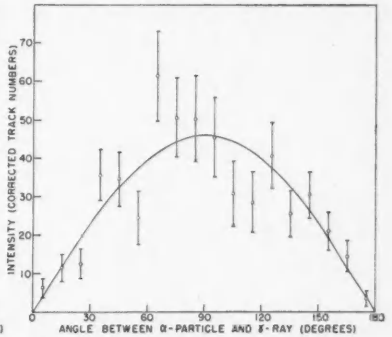

FIG. 4. Angular distribution with respect to γ-ray direction of single α particles in the 7 to 11 Mev. energy region ejected by photons from silver and bromine.

II. Recoil Tracks

A. Identification

In searching plate A several examples were found of tracks such as those shown in Fig. 5. The interpretation of these events as the reactions $N^{14}(\gamma, \alpha)B^{10}$

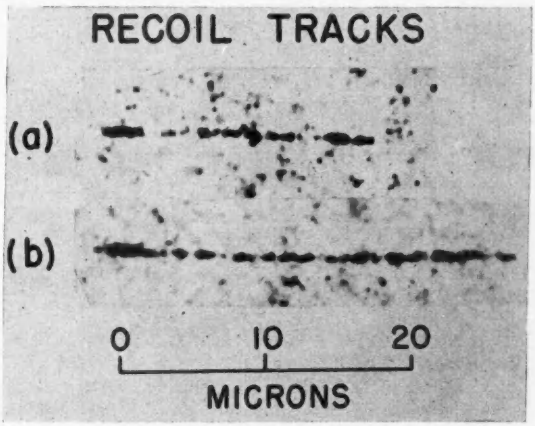

FIG. 5. Recoil tracks (*a*) $N^{14}(\gamma, \alpha)B^{10}$, (*b*) $O^{16}(\gamma, \alpha)C^{12}$.
The short, heavily-ionized stub of the recoiling nucleus is visible on the left end of each event.

and $O^{16}(\gamma, \alpha)C^{12}$, with the recoiling residual nucleus giving rise to the short, densely-ionized stub at the origin of the α-particle track, has been reported previously by the authors (26).

In outline, the method of analysis of a particular event was to calculate the energy of the recoil nucleus ($E_r(\alpha)$) from the energy of its associated α particle using the principle of conservation of momentum. Two values of $E_r(\alpha)$ were thus obtained depending on which of the two above reactions was assumed to describe the event. Another estimate of the energy of the recoil nucleus ($E_r(R)$) could be made directly from its range in the emulsion, two values again being found depending on which reaction was assumed. For each event the difference ($E_r(\alpha) - E_r(R)$) as calculated assuming the $O^{16}(\gamma, \alpha)C^{12}$ reaction was plotted against the same expression calculated for the $N^{14}(\gamma, \alpha)B^{10}$ reaction. The results are shown in Fig. 6 from which it may be seen that in

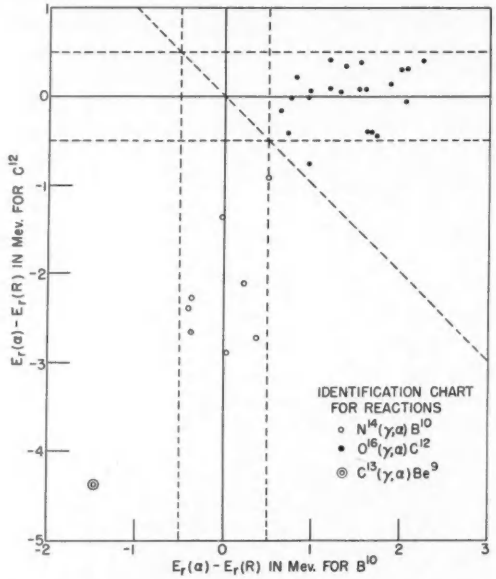

FIG. 6. Diagram for the analytical separation of the two types of recoil events found in plate A. This chart enables the separation of $O^{16}(\gamma, \alpha)C^{12}$ and $N^{14}(\gamma, \alpha)B^{10}$ to be made.

general this difference as calculated for what is presumed to be the correct assumption is less than 0.5 Mev. while it is considerably greater for the alternative assumption. One point which appears to disagree with both assumptions is shown double-circled in the figure.

In calculating $E_r(R)$ it was necessary to know the range–energy relationship for the recoiling nucleus. This may be obtained from the α-particle range–energy curve if the effective charge of the recoiling ion is known. Though the effective charge diminishes as the particle slows down, we found that over the

limited range of energies involved in this experiment it was sufficiently accurate for purposes of distinguishing between two reactions to use an "average effective charge" for each type of recoil nucleus and from this to compute a range–energy relationship which is valid over a limited range (See Section II(D)).

In searching plate B the stringent criteria set for an acceptable recoil track in plate A were relaxed somewhat in order to amass data for cross-section and angular distribution measurements. That is, where in plate A only those events in which the length of the recoil track could be unambiguously measured were included in the survey, in plate B *all* "recoil" events were counted including some where a separated grain caused uncertainty as to the exact point of the recoil track termination. Fig. 7 shows the identification chart for

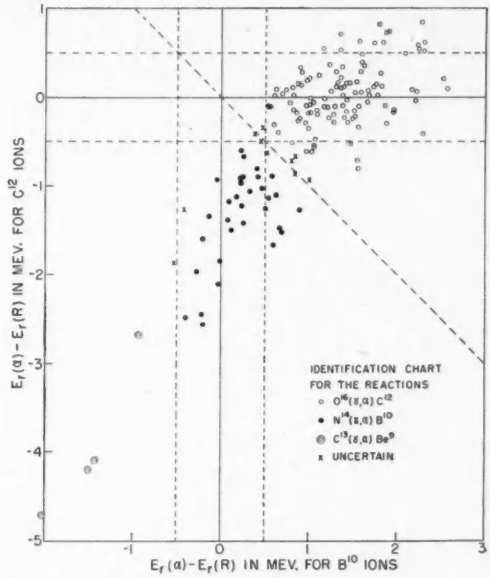

FIG. 7. Diagram for the separation of $O^{16}(\gamma, \alpha)C^{12}$ and $N^{14}(\gamma, \alpha)B^{10}$ events found in plate B.

the 159 recoil events found in the second plate, and though the division between the two reactions is not as sharp as formerly it is still quite clear.

In Figs. 6 and 7 there are double-circled points in the lower left-hand corner which seem to indicate the presence of a (γ, α) reaction in some nucleus lighter than N^{14}. A possible reaction is $C^{12}(\gamma, \alpha)Be^{8}$, but it is known (41) that Be^{8} is unstable by 0.09 Mev.[1] against disintegration into two α particles and in Section IV of this paper it is shown that the lifetime of Be^{8} is less than 5×10^{-14}

[1] *Recent measurements by D. J. Donahue, K. W. Jones, M. T. McEllistrem, and H. T. Richards (Bull. Am. Phys. Soc. 27 (No. 5): 7. 1952) give a value of 0.096 ± 0.003 Mev. for the disintegration energy of* Be^{8}.

sec. Since it may be shown that in the above reaction the Be^8 would take about 10^{-12} sec. to come to rest in the emulsion, this interpretation of the observed events is very improbable.

It is possible to explain these events by assuming that the above reaction occurs and that the two α particles from the immediate Be^8 decay are closely collinear and thus produce a track resembling that of a heavier recoil nucleus. If, however, we accept this explanation and make the reasonable assumption that the Be^8 break-up vector is randomly oriented with respect to the Be^8 line of flight, it may be shown that in this experiment only 4% of the distintegration α particles will appear collinear. Since the comparatively large number of three-pronged stars which the noncollinear disintegrations would produce were not observed (See Section III), we conclude that only a fraction of the observed events can be accounted for in this manner.

The authors favor the interpretation that these events are $C^{13}(\gamma, \alpha)Be^9$ reactions occurring in the 1.1% of C^{13} present in the normal isotopic mixture of carbon, since they occur with a frequency about 1% of that of the (γ, α) reaction in C^{12} (See Section III). On the basis of this assumption an analysis to separate these events from the $N^{14}(\gamma, \alpha)B^{10}$ events has been made and the identification chart is shown in Fig. 8.

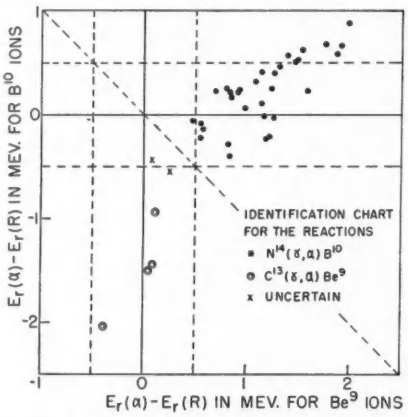

FIG. 8. Diagram for the separation of $N^{14}(\gamma, \alpha)B^{10}$ events from those events in which an anomalously long recoil track is observed, on the assumption that these latter events are $C^{13}(\gamma, \alpha)Be^9$ reactions.

To summarize, the authors feel that the "recoil" events observed in the emulsions may be interpreted as the tracks from $O^{16}(\gamma, \alpha)C^{12}$, $N^{14}(\gamma, \alpha)B^{10}$, and $C^{13}(\gamma, \alpha)Be^9$ reactions occurring in the emulsion constituents.

B. Angular Distribution of the Reaction $O^{16}(\gamma, \alpha)C^{12}$

The numbers of the different types of "recoil" events observed were roughly proportional to the numbers of parent nuclei present in the emulsion, with the result that only in the case of the $O^{16}(\gamma, \alpha)C^{12}$ reaction were sufficient data

obtained to make any statistically significant estimation of the angular distribution or cross-section variation for the reaction. Fig. 9 shows the angular distribution of the ejected α particles with respect to the incoming γ-ray direction. It will be noted that the standard deviations are large owing to the fact that only 112 measurements could be used for this graph.

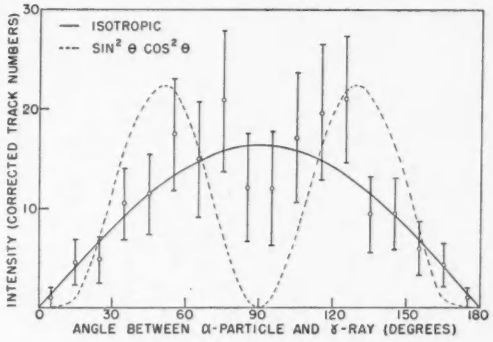

FIG. 9. The angular distribution of α particles from the reaction $O^{16}(\gamma, \alpha)C^{12}$. The points are fitted with isotropic and $\sin^2\theta \cos^2\theta$ curves normalized for equal areas.

Welton (44) and Preston (32) have assumed a pure electric quadrupole interaction of the γ ray with the O^{16} nucleus which leads to an angular distribution for this reaction of the form $\sin^2\theta \cos^2\theta$. In Fig. 9 a normalized curve of this form is shown dotted and it will be seen that the experimental points do not agree with it, though it is possible that some $\sin^2\theta \cos^2\theta$ component may be included. The experimental points provide a fairly good fit to the isotropic curve (shown solid), and, since a true isotropic distribution is not theoretically possible if the reaction proceeds via the ground state of C^{12}, it would seem necessary to assume that some events must involve excited levels of C^{12} in order to explain the observed angular distribution.

C. Cross Section for the Reaction $O^{16}(\gamma, \alpha)C^{12}$

The energy of the γ ray which initiated a particular (γ, α) event in O^{16} may be obtained by summing (*a*) the kinetic energies of the reaction products, (*b*) the excitation energies of the reaction products, and (*c*) the binding energy of the α particle (7.15 Mev.). Of these, only (*b*) is uncertain since by observing the tracks one cannot tell whether or not the particles that made them were in the ground state. Fortunately there are no known excited states of the α particle which can be formed with the energies available in this experiment. There are, however, several excited levels of C^{12} (20) which might enter into this reaction so that the energy of the γ ray initiating a particular event cannot be determined with certainty.

However, on the assumption that only the ground state of C^{12} is produced in the (γ, α) reaction in O^{16}, we have computed the relative cross-section curve

shown in Fig. 10 from our experimental data, and it will be seen that this curve peaks at a γ-ray energy of 17 or 18 Mev. and has a width at half maximum of about 5 Mev.[1] From our observations the absolute value of the peak

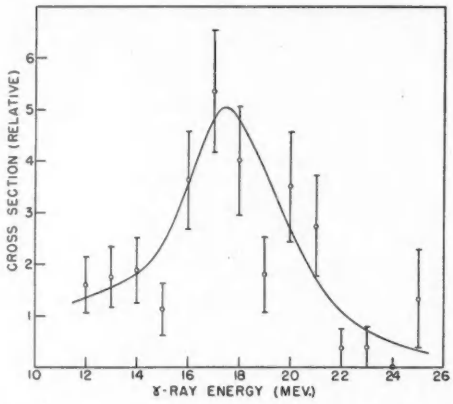

FIG. 10. The variation of cross section for the reaction $O^{16}(\gamma, \alpha)C^{12}$ with γ-ray energy.

cross section is 2.6×10^{-29} cm.^{2} but this may be low by a considerable factor because of recoil tracks incorrectly identified as single α-particle tracks (see Section I(A) above).

A calculation by Preston (33) based on a four α-particle model of the O^{16} nucleus gives 4.4×10^{-29} cm.^{2} for the peak cross section but both this and our value are much lower than Wäffler's (43, 30) experimental value of $1.8 \pm 0.5 \times 10^{-28}$ cm.^{2} for this cross section at a γ-ray energy of 17.5 Mev.

D. Recoil Ion Range–Energy Relationship

The identification of the (γ, α) reactions makes it possible to obtain range–energy relationships for the various recoil nuclei in E1 emulsion.

In each of the $O^{16}(\gamma, \alpha)C^{12}$ events observed in plate B the energy of the recoiling C^{12} ion has been computed from the energy of its associated α particle. These energies, plotted against the range of the corresponding C^{12} ion, are shown in Fig. 11. The solid line is the curve derived from the standard α-particle range–energy relationship for E1 emulsion (22) by use of the functional relation

$$[1] \qquad \frac{E}{M} = f\left(\frac{Z_{eff}^{\,2} R}{M}\right)$$

in which E, M, and R represent the energy, mass, and range of the ion and Z_{eff} is its average effective charge. The value $Z_{eff}(C^{12}) = 3.75$ used to obtain

[1] *Reference (30) shows that at a γ-ray energy of 17.5 Mev. most of the $O^{16}(\gamma, \alpha)C^{12}$ reactions involve the ground state of C^{12}.*

this fit is slightly higher than the value 3.62 previously published (26) which was based on only 23 examples of the $O^{16}(\gamma, \alpha)C^{12}$ reaction found in plate A.

The curves W_1 and W_2 are derived from range–energy relationships for C^{12} ions measured by Wrenshall (48) for two different gas mixtures noted in the figure. Wrenshall's curves were expressed in terms of standard air, and have been recalculated by the present authors for E1 emulsion by the use of

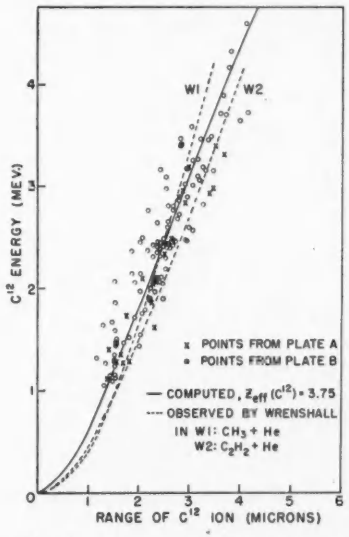

Fig. 11. The range–energy relation for C^{12} ions in E1 emulsion. The experimental points are fitted with a curve computed for $Z_{eff}(C^{12}) = 3.75$ and are also compared to the reduced experimental range–energy curves of Wrenshall for C^{12} ions in air.

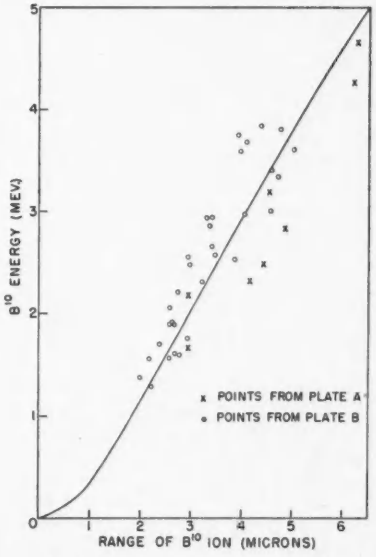

FIG. 12. The range–energy relation for B^{10} ions in E1 emulsion. The experimental points are fitted with a curve computed for $Z_{eff}(B^{10}) = 3.12$.

de Carvalho's (5) stopping power formula which is independent of the ionic charge. The good agreement with our data adds further corroboration to our identification of the $O^{16}(\gamma, \alpha)C^{12}$ reaction.

Fig. 12 shows the range–energy relationship for B^{10} ions in E1 emulsion. The solid curve is derived as before using $Z_{eff}(B^{10}) = 3.12$, a value again slightly higher than that previously quoted (26)—2.96—which was based on only eight points.

Since it is felt that the reaction $C^{13}(\gamma, \alpha)Be^{9}$ offers the most probable explanation for the seven recoil tracks that are incompatible with the two principal (γ, α) reactions (see Fig. 8) it is also possible to obtain a range–energy relationship for Be^{9} ions. This is shown in Fig. 13, the solid curve having been computed for $Z_{eff}(Be^{9}) = 2.72$.

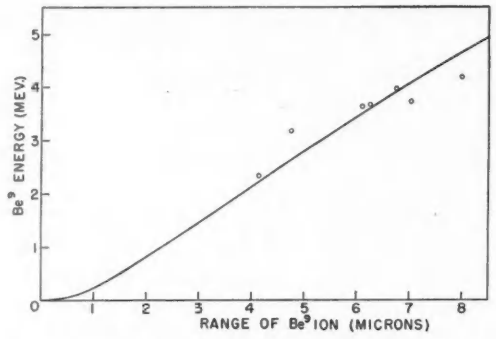

FIG. 13. The range–energy relation for Be^9 ions in E1 emulsion. The experimental points are fitted with a curve computed for $Z_{eff}(Be^9) = 2.72$.

III. Carbon Stars

A. Reaction Mechanism

Fig. 14 is a picture of a typical "carbon star" produced by the photodisintegration of C^{12} into three α particles. Hänni *et al.* (18) originally reported this reaction as proceeding via the 3 Mev. excited level of Be^8, i.e. $C^{12}(\gamma, \alpha)Be^{8*} \rightarrow 2He^4$.

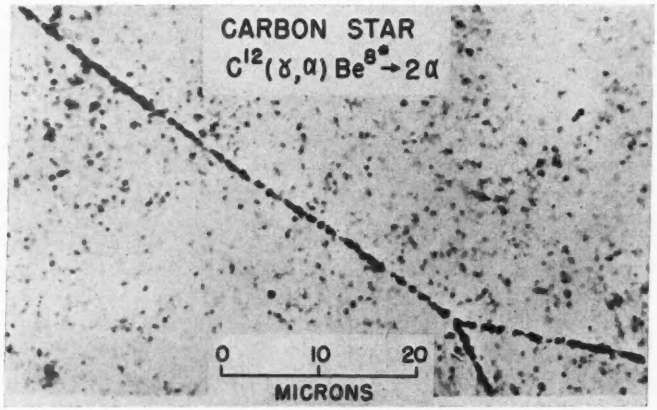

FIG. 14. Photomicrograph of a carbon star, due to the reaction $C^{12}(\gamma, \alpha)Be^{8*} \rightarrow 2\alpha$. The longest α-particle track is from the most probable "initial" α particle in this instance.

To confirm this interpretation we have measured (in plate A) 213 three-pronged α-particle stars each identified as a carbon star by visual estimation that the tracks proceed outward from the center and that linear momentum is conserved. By means of two separate methods of analysis described below we have been able to show that the above equation describes the reaction in the majority of cases, but that a small number of disintegrations proceed via the ground state of Be^8.

In the first method of analysis we assume that the C^{12} nucleus undergoes a primary (γ, α) reaction leaving a Be^8 nucleus which subsequently breaks up into two α particles, "i" and "j". It can be shown from conservation of energy and momentum that the energy of the Be^8 level may be calculated from the equation

$$[2] \quad E^* = \tfrac{1}{2}(E_i + E_j) - (E_iE_j)^{\frac{1}{2}}\{\cos(\beta_i - \beta_j)\cos\alpha_i\cos\alpha_j + \sin\alpha_i\sin\alpha_j\}$$

where E^* is the excitation energy of the Be^8 nucleus measured from the state of two separate α particles, and E, α, and β are, respectively, the energy, azimuthal angle, and dip angle of the particles denoted by subscripts. Since the initial α particle cannot usually be identified by inspection, the value of E^* must be computed for three possible cases in each star. Only one of these values can be correct, so that, if the mechanism proposed by Hänni *et al.* describes the reaction, a frequency distribution of all E^* values thus obtained should be found to have one-third of the values forming a peak at about 3 Mev., the other two-thirds forming a general background. Fig. 15 shows that this is approximately the distribution obtained, which indicates that, in the majority of cases at least, the proposed reaction is valid.

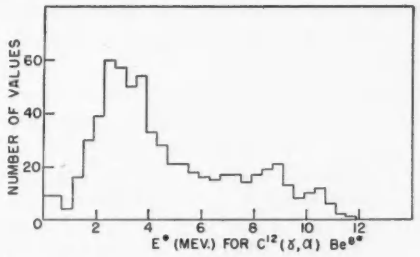

FIG. 15. Search for Be^{8*} in carbon stars. The presence of Be^{8*} as an intermediate nucleus would give a peak at 3 Mev. formed by one-third the points.

A second method of analyzing this reaction is to plot a frequency distribution curve of the "relative energies" of the individual α particles in each star. We define relative energy (ϵ) as the ratio of the actual energy (E) of an individual α particle to the maximum energy which an α particle could obtain in a star with the same available kinetic energy of disintegration. It then follows from conservation of energy and momentum that

$$[3] \quad \epsilon = 1.5\,E/E_T$$

where E_T is the sum of the α-particle energies in the star, and the γ-ray momentum has been neglected. The observed distribution of relative energies is shown in Fig. 16.

The three most probable reactions by which a C^{12} nucleus might disintegrate into three α particles are

(*a*) $C^{12}(\gamma, 3\alpha)$,

(*b*) $C^{12}(\gamma, \alpha)Be^8$; $Be^8 \rightarrow 2He^4$,

(*c*) $C^{12}(\gamma, \alpha)Be^{8*}$; $Be^{8*} \rightarrow 2He^4$.

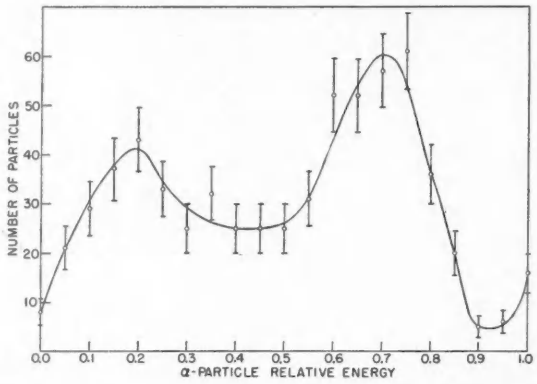

FIG. 16. The observed distribution of relative energies among the prongs of the carbon stars.

Considering first reaction (*a*), it may be shown (31) that to conserve energy and linear momentum in an isotropic break-up of a body into three parts the distribution function of the relative energies of the emitted particles will be of the form $f(\epsilon) = N\epsilon^{\frac{1}{2}}(1 - \epsilon)^{\frac{1}{2}}$ where N is a normalizing factor. The real values of this function form a semiellipse between $\epsilon = 0$ and $\epsilon = 1$. The perturbation that Coulomb and angular momentum barriers will introduce into this function will tend to lower the extreme ends of the curve and raise the middle slightly.

In the case of reaction (*b*), if we make use of the cross-section variation with γ-ray energy as determined in Section B below, and assume that the Be^8 break-up vector is randomly oriented with respect to the Be^8 line of flight, it may be shown that to conserve energy and linear momentum all first-emitted α particles will have relative energies of about 0.99. The spectrum of the Be^8 disintegration α particles will be in the form of a broad peak about a relative energy of 0.31.

Reaction (*c*) via a 3 Mev. level of Be^8 (assumed to be narrow to simplify calculations) leads to a relative energy distribution with a broad peak at 0.70 from the first-emitted α particles, with the remainder giving a fairly constant distribution at relative energies up to this peak value.

Fig. 17 shows theoretical relative energy curves for these three possible reactions, normalized to include equal numbers of stars. Comparison of the experimental results of Fig. 16 with these curves indicates that the majority of the events are of type (*c*) but that a few events of type (*b*) must also be included if the rise in the observed curve at a relative energy of 1.0 is to be accounted for. However, the possibility that a few events of type (*a*) occur cannot be ruled out, and indeed, the small peak in the relative energy distribution which occurs at 0.2 is not easily explained in terms of any of these three proposed reactions.[1]

[1] *Telegdi (Phys. Rev. 84: 600. 1951) shows that a magnetic dipole γ-ray interaction will lead to a small peak in the $\epsilon = 0.2$ region.*

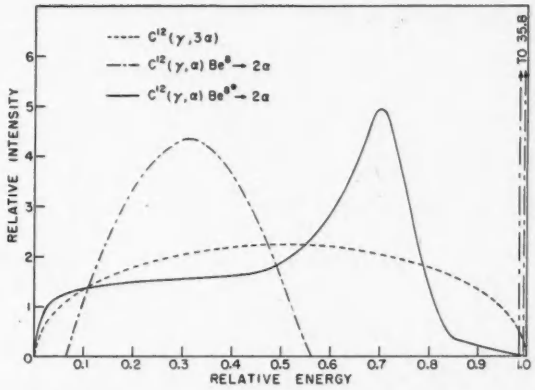

FIG. 17. Predicted relative energy distributions of the prongs of carbon stars for three assumed modes of disintegration.

Detailed consideration of the 21 stars in which there is an α particle of relative energy 0.93 or greater shows that, because of the γ-ray energy involved, 13 could only have been caused by the C^{12} disintegration via the ground state of Be^{8}, while the eight others could have been caused either by this reaction or by a disintegration via the excited state of Be^{8}. We thus conclude that, for the γ-ray energies considered in this experiment, the reaction $C^{12}(\gamma, \alpha)Be^{8} \rightarrow 2\alpha$ accounts for from 6–10% of the carbon disintegrations. This is in agreement with the work of Goward, Telegdi, and Wilkins (8).

B. Cross Section for the Reaction $C^{12}(\gamma, \alpha)Be^{8*} \rightarrow 2He^{4}$

The energy of the γ ray initiating a particular star is given by

$$E_\gamma = E_T + Q \qquad [4]$$

where E_γ is the γ-ray energy (Mev.), E_T is the total kinetic energy of the α particles, and Q (7.34 Mev.) is the threshold energy of the reaction.

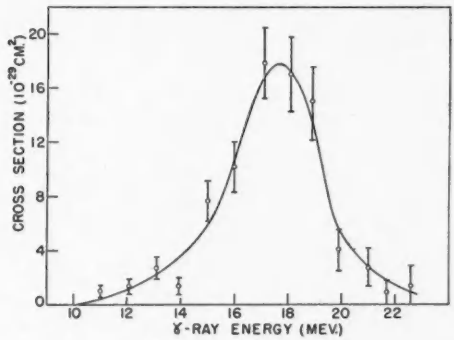

FIG. 18. The variation with γ-ray energy of the cross section for the reaction $C^{12}(\gamma, \alpha)Be^{8*}\rightarrow 2\alpha$.

By computing E_γ for each star, and multiplying the number of events in each energy interval by (*a*) a correction factor ($C_f = 1.21$) to allow for stars in which accurate measurements of all three prongs were not possible because of fogging, and (*b*) an energy-dependent correction factor (C_e) to allow for escape of star prongs from the emulsion (see Appendix I(C)), it was possible to obtain an absolute determination of the cross section for the reaction $C^{12}(\gamma, \alpha)Be^{8*} \rightarrow 2He^4$ over a considerable range of γ-ray energy. This is plotted in Fig. 18. It will be noted that a resonance-type curve is obtained, with a peak cross section of 1.8×10^{-28} cm.^{2} at a γ-ray energy between 17 and 18 Mev., and having a width at half maximum of about 4 Mev. This curve is in good agreement with the work of Wilkins and Goward (46) and with the theoretical conclusions of Telegdi and Verde (35).

C. Angular Distributions in the Reaction $C^{12}(\gamma, \alpha)Be^{8*} \rightarrow 2He^4$

(1) *Angular distribution of initial* α *particles with respect to the incident* γ*-ray direction.*—Since the Be^{8*} level is very broad (4) it is impossible to identify with absolute certainty which is the initial α particle in a given star. We have, however, in each $C^{12}(\gamma, \alpha)Be^{8*}$ reaction identified as the most probable initial α particle that one for which the complementary pair of α particles leads to the

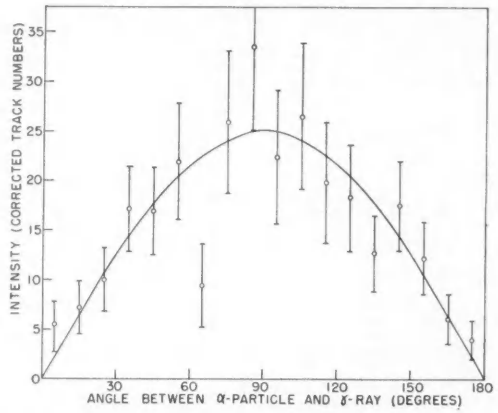

FIG. 19. The angular distribution of the initial α particle in carbon stars with respect to γ-ray direction. The solid line is the isotropic curve fitted to the points on the basis of equal areas.

most probable value of E^* as determined from the level shape curve of Bonner *et al.* (4). With this identification the angular distribution of the most probable initial α particles with respect to the incident γ-ray direction has been calculated as described in Experimental Results, Section I(B), the resulting data being plotted in Fig. 19. There appears to be no significant deviation from the solid curve which represents a normalized isotropic distribution.

(2) *Angular distribution of Be^{8*} break-up vector with respect to Be^{8*} line of flight.*—It may be shown that η, the angle between the Be^{8*} break-up vector and the Be^{8*} line of flight, is given by

[5] $$\eta = \cos^{-1}\left[\frac{E_i - E_j}{\{2E^*[E_i + E_j + 2(E_j E_j)^{\frac{1}{2}}\{\cos(\beta_i - \beta_j)\cos\alpha_i\cos\alpha_j - \sin\alpha_i\sin\alpha_j\}]\}^{\frac{1}{2}}}\right]$$

where the parameters are as previously defined. Fig. 20 shows a plot of frequency versus angle η and it may be seen that it does not deviate significantly from the normalized isotropic distribution curve drawn in for comparison.

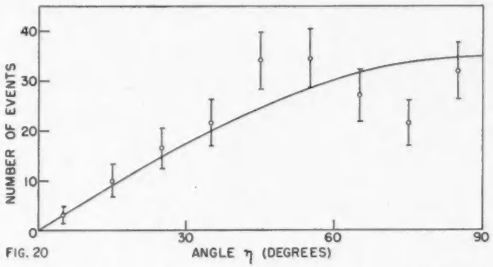

FIG. 20

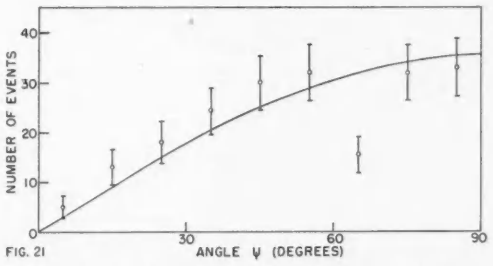

FIG. 21

FIG. 20. The angular distribution of the Be^{8*} break-up vector with respect to the Be^{8*} line of flight. The solid line is the istropic curve fitted to the points on the basis of equal areas.

FIG. 21. The angular distribution of the Be^{8*} break-up vector with respect to the γ-ray direction in carbon stars. The solid line is the isotropic curve fitted to the points on the basis of equal areas.

(3) *Angular distribution of Be^{8*} break-up vector with respect to γ-ray direction.*—From the width of the Be^{8*} level it is deduced that the lifetime of this state is of the order of 10^{-21} sec. (4) which means that the secondary disintegration can occur while the Be^{8*} is still within the range of nuclear force of the primary α particle. This could conceivably lead to an anisotropic distribution of the Be^{8*} break-up vector with respect to the incident γ-ray direction. It may be shown that ψ, the angle between these two vectors, is given by

[6] $$\psi = \cos^{-1}\left[\frac{E_i^{\frac{1}{2}}\cos\beta_i\cos\alpha_i - E_j^{\frac{1}{2}}\cos\beta_j\cos\alpha_j}{(2E^*)^{\frac{1}{2}}}\right].$$

The frequency distribution of ψ is shown in Fig. 21 on which a normalized isotropic curve is sketched in for comparison. Again no significant deviation is observed.

In all cases, these angular distribution measurements are in agreement with the results of Telegdi and Zünti (36).

IV. Oxygen Stars

A. Reaction Mechanism

Fig. 22 shows a photomicrograph of two types of four-pronged α-particle stars attributed to the photodisintegration of O^{16} into four α particles. The two examples in Fig. 22 (*a*), which are typical of the majority of stars, show no obvious relation among the prongs other than conservation of linear momentum

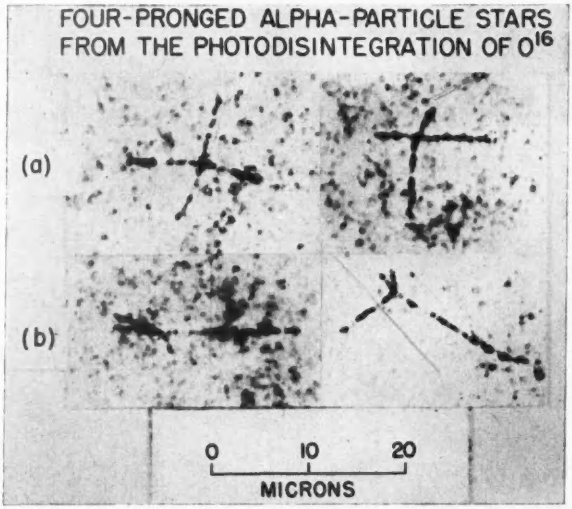

FIG. 22. Photomicrographs of oxygen stars. (*a*) Examples of the reaction $O^{16}(\gamma, 4\alpha)$. (*b*) Examples of the reaction $O^{16}(\gamma, Be^8)2\alpha$. The typical "V"-configuration of the α particles from the disintegration of the ground state Be^8 is visible in the latter stars.

which serves to identify an oxygen star. However, the two examples in Fig. 22 (*b*) each have two short, nearly equal tracks with a small angle between them. This configuration was observed in about one-third of all oxygen stars.

It was considered possible that this second type of star represented a photodisintegration of O^{16} in which Be^8 in the ground state was formed as an intermediate disintegration product. Since Be^8 is unstable by 0.09 Mev. (41) against spontaneous decay into two α particles, the break-up momentum of this decay when added to the recoil momentum of the Be^8 ion would give rise to this characteristic "V" configuration.

In order to test this postulate, the value of E^* was calculated from equation [2] for those pairs of tracks classified by visual examination as arising from

the break-up of Be^8. Though these E^* values are subject to considerable uncertainty since the α particles from the secondary disintegration of Be^8 are only a few microns in length, it may be seen from the histogram in Fig. 23 that they are of the order of 0.1 Mev. in accord with the 0.09 Mev. decay energy of Be^8.

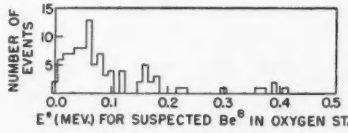

FIG. 23. The observed energies of disintegration of the Be^8 nuclei in the reaction $O^{16}(\gamma, Be^8)2\alpha$.

Goward and Wilkins (13) in studying this reaction have also concluded that in a high percentage of O^{16} photodisintegrations Be^8 is an intermediate product. Of the 303 oxygen stars found in plate B, 119 probably show Be^8 while the remaining 184 do not.

Having thus separated these disintegrations into two classes depending upon whether or not Be^8 is present, it remains to identify the exact mechanism of these two types of reaction. Nine possible processes are listed below.

(*a*) $O^{16} + h\nu \rightarrow 2Be^8$; $2Be^8 \rightarrow 4He^4$

(*b*) $O^{16} + h\nu \rightarrow Be^8 + Be^{8*}$; $Be^8 \rightarrow 2He^4$; $Be^{8*} \rightarrow 2He^4$

(*c*) $O^{16} + h\nu \rightarrow He^4 + C^{12*}$; $C^{12*} \rightarrow He^4 + Be^8$; $Be^8 \rightarrow 2He^4$

(*d*) $O^{16} + h\nu \rightarrow 2He^4 + Be^8$; $Be^8 \rightarrow 2He^4$

(*e*) $O^{16} + h\nu \rightarrow He^4 + C^{12*}$; $C^{12*} \rightarrow He^4 + Be^{8*}$; $Be^{8*} \rightarrow 2He^4$

(*f*) $O^{16} + h\nu \rightarrow 2He^4 + Be^{8*}$; $Be^{8*} \rightarrow 2He^4$

(*g*) $O^{16} + h\nu \rightarrow 2Be^{8*}$; $2Be^{8*} \rightarrow 4He^4$

(*h*) $O^{16} + h\nu \rightarrow He^4 + C^{12*}$; $C^{12*} \rightarrow 3He^4$

(*i*) $O^{16} + h\nu \rightarrow 4He^4$

Considering first those stars containing Be^8, we note that equations (*a*) to (*d*) above are possible descriptions of the events. Of these, (*a*) would give rise to a very characteristic double-"V" track which would be easily recognized. We observed only two stars that could be attributed to this reaction and Goward (16) has found a few others. Thus reaction (*a*) describes very few, if any, of the events.

To check whether reaction (*b*) applies, values for E^* were calculated (equation [2]) for the two prongs of each star that do not form the characteristic "V". If reaction (*b*) obtains, the frequency distribution of *all* these values should form a broad peak about an energy of 3 Mev. Fig. 24 shows that this is not the case so that this mechanism cannot account for many of the observed events.

If (*c*) describes the reaction it may be shown that, neglecting the small momentum contribution of the incident γ ray, the value of E', the total

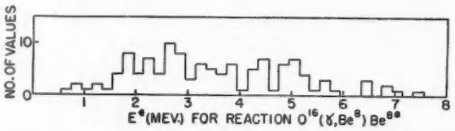

FIG. 24. Search for the 3 Mev. excited state of Be^8 as an intermediate product in the reaction $O^{16}(\gamma, Be^8)2\alpha$. If this state is present, all points should take the form of the Be^{8*} level at 3 Mev.

kinetic energy released in the disintegration of the excited C^{12} nucleus, is given by

$$E' = E_T - 4/3\, E_1 \qquad [7]$$

where E_T is the total energy of the four α particles and E_1 is the energy of the α particle first emitted. If, for each star, each of the prongs not associated with the Be^8 decay is in turn considered to be the first emitted α particle and the value of E' calculated, one half of the points in a frequency distribution of E' values should give the value of the C^{12} excited level above the state of three separate α particles.

It is known that an energy level exists in C^{12} at 9.7 Mev. (20) (i.e. 2.3 Mev. above the ground state energy of three separate α particles) and it has recently been shown (1) that in the positron decay of N^{12} a small fraction of the disintegrations lead to this particular level which subsequently breaks up with the emission of an α particle leaving Be^8 in the ground state.

Goward and Wilkins (13) in studying oxygen stars containing Be^8 conclude that the disintegration does indeed take place via this 9.7 Mev. C^{12} level and estimate a true level width of about 1.3 Mev. from their observed width of 1.8 Mev. Fig. 25 shows the frequency distribution of E' values calculated from our data and though there is a broad maximum in the region of 1.5 to 4.0 Mev., to ascribe these points to a single level with $E' = 2.3$ Mev. would necessitate a level width of the order of 2 Mev. Gibson (7), studying the neutrons from the $B^{11}(d, n)C^{12*}$ reaction, obtained an experimental width of about 0.5 Mev. for the 9.7 Mev. C^{12} level, and Malm and Buechner (24) studying magnetically analyzed α particles from the $N^{14}(d, \alpha)C^{12*}$ reaction observed a width of the order of 0.15 Mev. for this same level.

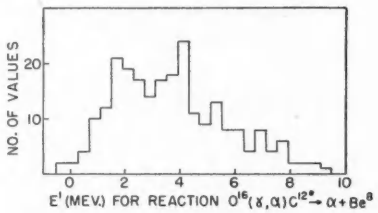

FIG. 25. Search for an excited state of C^{12} as an intermediate product in the reaction $O^{16}(\gamma, Be^8)2\alpha$. If such a state is present, one half the points should form a superposed peak with the C^{12*} level shape.

It would thus appear that reaction (*c*) via the 9.7 Mev. level of C^{12} may account for some of the oxygen stars containing Be^8, but to postulate that all disintegrations take place in this manner leads to an apparent level width much greater than is observed in other more precise experiments. No other C^{12} levels are known (20) that decay via α emission to the ground state of Be^8 with the exception of one at 16.1 Mev. (8.7 Mev. above three α particles) and, as may be seen from Fig. 25, there is little evidence for disintegration via this level.

Reaction (*d*) appears, then, as the only other reasonable decay scheme, and the authors feel that this offers the most probable description of the majority of the disintegrations containing Be^8.

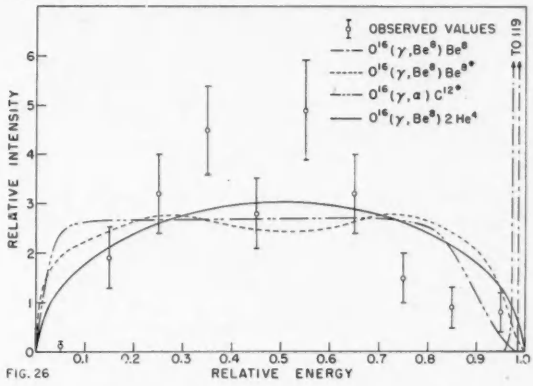

FIG. 26

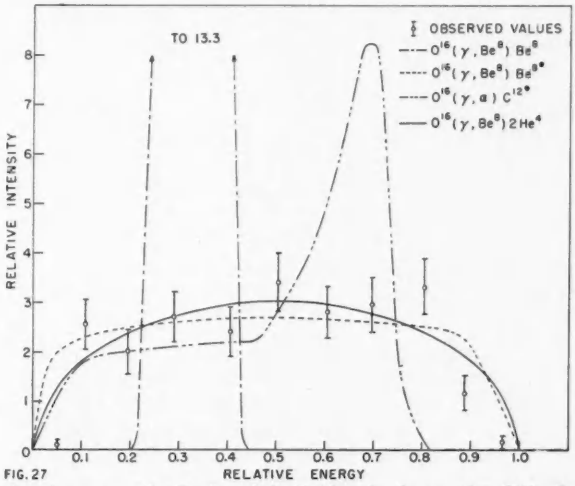

FIG. 27

FIG. 26. Relative energy distribution of the Be^8 ions in the reaction $O^{16}(\gamma, Be^8)2\alpha$. Predicted distributions for various assumed reactions are included for comparison purposes.

FIG. 27. Relative energy distribution of the α particles in the reaction $O^{16}(\gamma, Be^8)2\alpha$. Predicted distributions for various assumed reactions are included for comparison purposes.

Confirmation of this conclusion is obtained by a study of the relative energy distributions of the disintegration products. Assuming that Be^8 in the ground state is formed as an intermediate product of the reaction and that the two α particles from its disintegration may be identified by inspection it follows that the relative energy of the Be^8 particle (neglecting γ-ray momentum) may be obtained from the expression

$$[8] \qquad \epsilon_{Be^8} = \frac{E_j + E_k - 0.09}{\frac{1}{2}(E_T - 0.09)}$$

where E_j and E_k are the energies of the α particles resulting from the Be^8 decay, and E_T is the total energy in the star, all energies being expressed in Mev. The term 0.09 Mev. is the disintegration energy of Be^8.

By incorporating the relative cross-section variation found in Section B below it is possible to calculate the distribution functions for the Be^8 particles for the assumed reactions (*a*) to (*d*), and these are shown in Fig. 26. It will be noted that this method of analysis definitely eliminates reaction (*a*) as a possible explanation of the events, but leaves reactions (*b*), (*c*), and (*d*) as possibilities.

In a similar manner the relative energy distributions of the two α particles not associated with the Be^8 disintegrations have been computed for the four possible reactions and these, together with the observed distribution, are shown in Fig. 27. Here we note that only equations (*b*) and (*d*) provide interpretations compatible with the observed results.

Thus the study of relative energy distributions indicates that equations (*b*) and (*d*) are the two most likely equations describing the reaction. However, the energy level analysis allows only equations (*c*) and (*d*). We thus conclude that equation (*d*) describes the majority of O^{16} disintegrations in which Be^8 in the ground state is formed as an intermediate product.

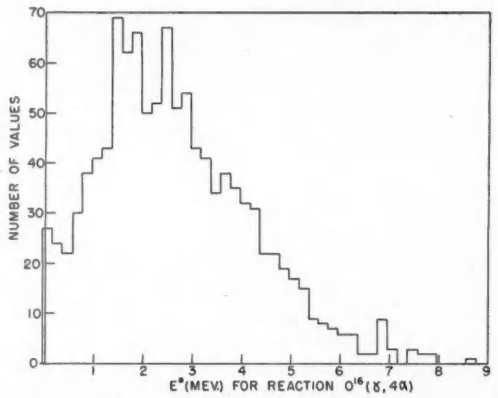

FIG. 28. Search for the 3 Mev. excited state of Be^8 as an intermediate product in the reaction $O^{16}(\gamma, 4\alpha)$. For the reaction $O^{16}(\gamma, \alpha)C^{12*} \rightarrow He^4 + Be^{8*}$, one-sixth the values should form a superposed peak at 3 Mev.; for the reaction $O^{16}(\gamma, Be^{8*})Be^{8*}$, one-third the values should form a similar peak.

Considering now those oxygen stars in which Be^8 in the ground state does not occur, we see that reactions (*e*) to (*i*) provide possible interpretations. Of these (*e*), (*f*), and (*g*) contain Be^{8*} as an intermediate product so that if values for E^* are calculated for each of the six possible combinations in each star, the frequency distribution of the values should have one-sixth of the total number forming a peak at 3 Mev. if reaction (*e*) or (*f*) obtains, or one-third of the total number in this peak if reaction (*g*) obtains. As may be seen in Fig. 28 the frequency distribution curve decreases smoothly through the 3 Mev. region thus ruling out these three reactions as possible interpretations for the majority of cases.

To test whether equation (*h*) applies, four possible values of E' were computed for each star according to equation [7] and their frequency distribution is shown in Fig. 29. If the disintegration proceeds via a single C^{12} excited level, one-quarter of the points should form a peak at the energy by which the level exceeds the energy of three separate α particles. As may be seen in Fig. 29 there is no evidence for a peak at 2.3 Mev. (corresponding to the known 9.7 Mev. level in C^{12}) nor for a sharp peak at any other energy.

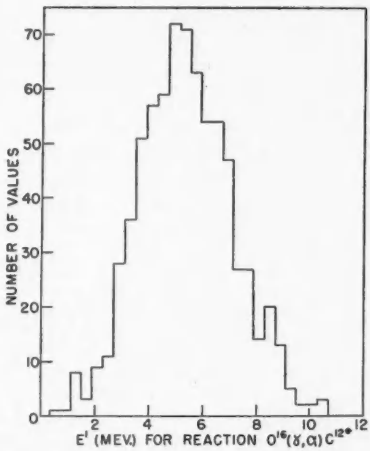

FIG. 29. Search for an excited state of C^{12} as an intermediate product in the reaction $O^{16}(\gamma, 4\alpha)$. If such a state occurs one-fourth the values should form a superposed peak with the C^{12*} level shape.

This leaves reaction (*i*), the single-stage break-up into four α particles, as the only remaining possibility, and this the authors believe to be the correct description of the event in the majority of cases. In order to confirm this hypothesis the frequency distribution of the relative energies of the α particles in these stars was computed according to the equation

$$\epsilon_i = 1.33\, E_i/E_T, \tag{9}$$

and this is shown in Fig. 30.

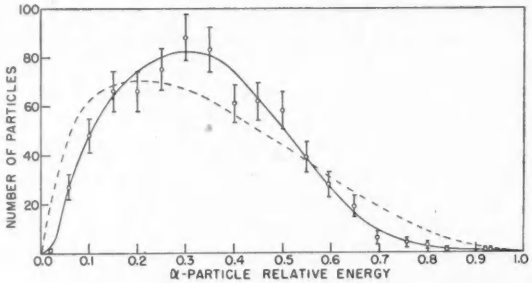

FIG. 30. Relative energy distribution of the α-particle energies from the reaction $O^{16}(\gamma, 4\alpha)$. The predicted curve for this type of reaction—uncorrected for spin or Coulomb barrier—is shown dotted.

Conservation of energy and linear momentum in a four-body disintegration lead to a distribution function for the energies of the resultant particles which has the form $f(\epsilon) = N\epsilon^{\frac{1}{2}}(1 - \epsilon)^2$ (31) and, as in the case of the three-body split-up, angular momentum and Coulomb barriers will tend to decrease the numbers of very low and very high energy particles emitted. The magnitude of this perturbation is difficult to estimate, but an uncorrected curve of the above function is shown dotted in Fig. 30 and there would appear to be qualitative agreement between this curve and the observed distribution function.

We conclude that the simplest interpretation of the photodisintegration of O^{16} into four α particles is that it is a single stage reaction in about two-thirds of the cases, and in the other one-third of the disintegrations two of the α particles are initially bound together to form Be^8 in the ground state.

B. Cross Section for the Photodisintegration of Oxygen

The energy of the γ ray initiating a particular oxygen star is given by equation [4], where Q is 14.5 Mev., the binding energy of the four α particles in O^{16}. From the observed numbers of stars, the known emulsion composition, and the betatron spectrum, it is possible to compute the absolute cross section for the photoproduction of oxygen stars over a considerable range of γ-ray energies. Fig. 31 shows the curves for both the three-body and four-body disintegration of oxygen. It may be noted that both curves have a peak at a γ-ray energy of about 22 Mev., but at higher energies the cross section for the three-body disintegration falls off more rapidly than does that for the four-body one.[1]

C. Lifetime of Be^8

Of the oxygen stars that contained Be^8 as an intermediate product about 20% showed two apparent centers of disintegration and these were originally interpreted (29) as indicating that the Be^8 nucleus had traveled some distance through the emulsion prior to decaying into two α particles. With this interpre-

[1] *Recent extensive observations by Goward and Wilkins (A.E.R.E. Memo G/M 127) indicate a fine structure within our apparent resonances in the cross sections for both carbon and oxygen stars. Insufficient data have been obtained in our experiment to confirm their observation.*

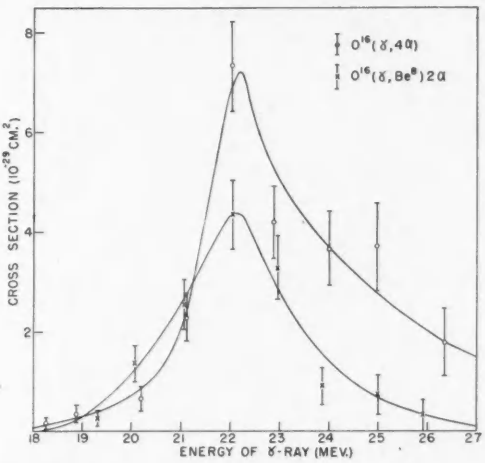

FIG. 31. The variation of the cross section with γ-ray energy for the reactions $O^{16}(\gamma, 4\alpha)$ and $O^{16}(\gamma, Be^{8})2\alpha$.

tation an estimate of 5×10^{-14} sec. was made for the half-life of Be^{8}. However, Wilkins and Goward (47) failed to find any "double disintegration" stars in a similar experiment so the experiment was repeated using a C2 emulsion irradiated with 50 roentgens of 70 Mev. peak energy bremsstrahlung from the Queen's University synchrotron.[1] Of 38 oxygen stars containing Be^{8} found in this plate, six showed two apparent disintegration centers, confirming the earlier observations.

In order to ascertain whether such stars could arise as the result of one of two closely collinear α particles in an O^{16} star being scattered in mid-flight and thus producing an apparent double disintegration star, a statistical study of the scattering of low energy α-particle tracks was carried out. This study indicated that, in fact, about one-fifth of all oxygen stars containing Be^{8} would be expected to show two apparent centers of disintegration because of scattering. Thus from this experiment we may conclude only that the half-life of Be^{8} is less than 5×10^{-14} sec.

V. Nitrogen Three-pronged Stars

A. Reaction Mechanism

In searching plate B, 34 examples were found of three-pronged stars which differed from stars arising from the disintegration of C^{12} in that an apparent momentum unbalance existed among the three prongs. An example of such an event is shown in Fig. 32. Further it was observed that the momentum unbalance could be corrected by increasing the magnitude of one of the particle momentum vectors without change of direction. This suggested that these

[1] *We are indebted to Dr. J. A. Gray of Queen's University for carrying out this irradiation for us.*

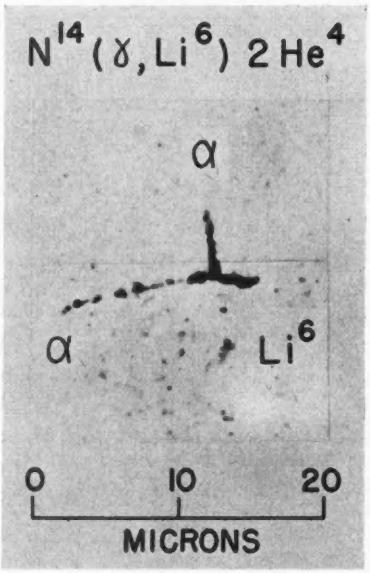

FIG. 32. Photomicrograph of a star due to the reaction $N^{14}(\gamma, Li^6)2\alpha$.

stars arose from the disintegration of some light nucleus into two α particles and a slightly heavier ion, and these events have subsequently been identified with the disintegration of N^{14} into two α particles and a Li^6 nucleus which was first discovered by Wilkins and Goward (45) in a similar experiment. In order to confirm this identification a range–energy relationship for Li^6 ions in E1 emulsion has been deduced from Farragi's (6) values for Li^7 ions in C2 emulsion in the manner described in II(D) above. This leads to a value for Z_{eff} of 2.5 for lithium ions over the small range of energies involved here, which is in reasonable qualitative agreement with the effective charges of other light ions. A momentum analysis confirmed the postulate as to disintegration products but to determine the exact reaction mechanism requires further analysis.

The following reactions are possibilities:

(*a*) $N^{14} + h\nu \rightarrow Li^6 + Be^8$; $Be^8 \rightarrow 2He^4$,

(*b*) $N^{14} + h\nu \rightarrow Li^6 + Be^{8*}$; $Be^{8*} \rightarrow 2He^4$,

(*c*) $N^{14} + h\nu \rightarrow He^4 + B^{10*}$; $B^{10*} \rightarrow He^4 + Li^6$,

(*d*) $N^{14} + h\nu \rightarrow 2He^4 + Li^6$.

Reaction (*a*) may be eliminated since the characteristic small "V" configuration of the tracks of the two α particles from the decay of Be^8 was not observed.

If reaction (*b*) describes the disintegration all values of E^* (computed according to equation [2] for the two α particles in each star) should form a broad peak at 3 Mev. Fig. 33 shows that this is not the case.

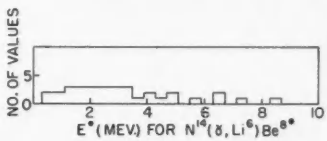

FIG. 33. Search for a 3 Mev. excited state of Be^8 as an intermediate product in the reaction $N^{14}(\gamma, Li^6)2\alpha$. If such a state occurs all values should form the 3 Mev. level shape of Be^{8*}.

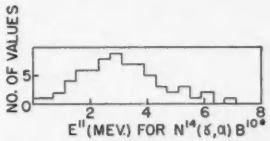

FIG. 34. Search for an excited state of B^{10} as an intermediate product in the reaction $N^{14}(\gamma, Li^6)2\alpha$. If such a state occurs one half the points should form its level shape.

If, as in reaction (*c*), the disintegration takes place via an excited level of B^{10} it may be shown that

$$E'' = E_T - 1.4\,E_i \qquad [10]$$

where E'' is the energy by which the excitation energy of the B^{10} level exceeds the binding energy of He^4 and Li^6 to form a B^{10} nucleus. E_i is the energy of the initial α particle and E_T is the total kinetic energy of the star. Two values of E'' were computed for each star, assuming that each α particle in turn was the initial one. If equation (*c*) obtains, one half of these values should form a peak at an energy corresponding to the B^{10*} level. In Fig. 34 it may be seen that this is not the case.

We conclude therefore that the reaction involved is probably the single-stage three-body break-up described by equation (*d*). Unfortunately the number of stars found was insufficient to compute confirmatory relative energy distributions.

B. Cross Section

The small number of nitrogen three-pronged stars observed makes an accurate determination of the cross-section variation impossible. However, making use of the escape correction factor derived for carbon stars one obtains cross-section values as shown in Fig. 35 (assuming that the Li^6 nuclei are not

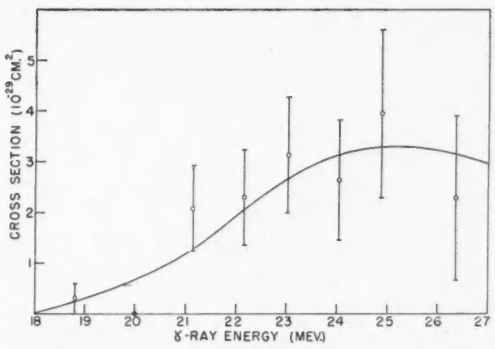

FIG. 35. The variation of cross section with γ-ray energy of the reaction $N^{14}(\gamma, Li^6)2\alpha$, assuming that the Li^6 ions are not left in excited states.

left in excited states). The main conclusion one may draw from this curve is that the cross-section peak is much broader than in the photo-alpha reactions involving oxygen.

VI. Nitrogen Four-pronged Stars

In searching plate B two stars were found in which there were three short α-particle tracks and a fourth long track which was very lightly ionized, as shown in Fig. 36. It is believed that these arise from the photodisintegration of nitrogen into three α particles and either a deuteron, or a proton and neutron separately. Momentum analysis and energy considerations show that

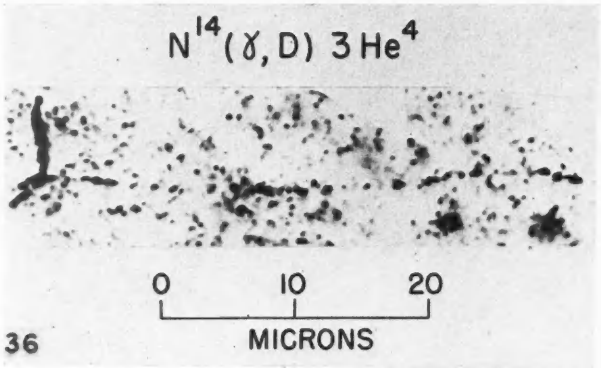

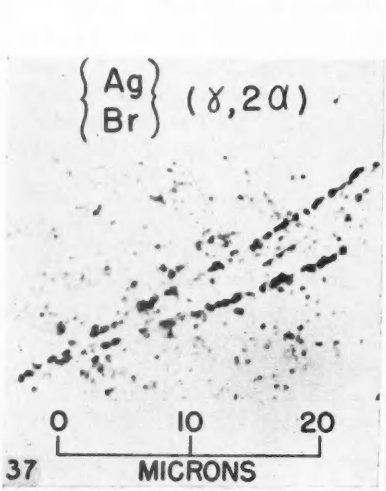

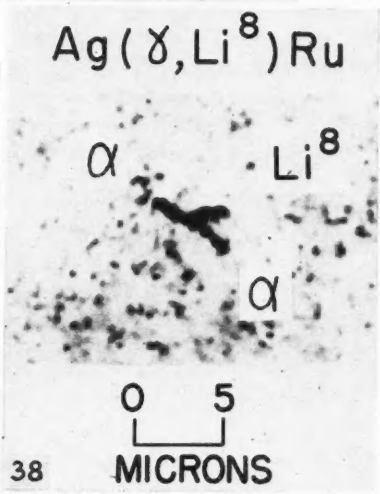

FIG. 36. Photomicrograph of a nitrogen four-pronged star, due to the reaction $N^{14}(\gamma, d)3\alpha$.
FIG. 37. Photomicrograph of a "V" track, probably due to a $(\gamma, 2\alpha)$ reaction in a heavy nucleus.
FIG. 38. Photomicrograph of a "hammer" track, possibly due to the photoejection of Li^8 from a silver nucleus.

in one star the singly charged particle emitted is indeed a deuteron; however, in the other star the momentum analysis—which is somewhat uncertain owing to the shortness of the α-particle tracks—indicates that the neutron and proton may have been separated.

The fact (34) that E1 emulsions are perceptibly more sensitive to deuterons than to protons coupled with the fact that, under our conditions of irradiation and development, proton tracks are not normally measurable, leads us to believe that the most probable description of the reactions is $N^{14} + h\nu \rightarrow 3He^4 + H^2$. Similar events have been observed by Goward (17).

VII. Double α-Particle Emission

Fig. 37 shows a photonuclear event in which two α particles originate from the same point. Seven such events were noted in plate B, and it is possible that others with a greater angle between them were incorrectly classified as scattered single α-particle tracks.

Since no recoil track is visible, it is presumed that these tracks arise from the photoejection of two α particles from a silver or bromine nucleus. The threshold energies for such a reaction are about 5 to 6 Mev. for silver and 10 to 12 Mev. for bromine, so that adequate energy is available for the reaction to take place in either atom. Further, the possibility that other singly charged or neutral particles are emitted in the same reaction cannot be ruled out since such particles would not leave observable tracks.

Insufficient data are available to check whether this event represents the photoejection of an excited Be^{8*} nucleus from a heavy atom which would also explain these "V"-tracks. Such ejection would be greatly inhibited by the potential barrier.

VIII. Hammer Tracks

In studying plate B five examples were found of three-pronged stars which had the appearance of "hammer" tracks similar to those found in cosmic ray stars (Fig. 38). These tracks were presumed to arise from the photoejection from silver of a Li^8 particle, which, after coming to rest, decayed by β-particle emission, the Be^{8*} so formed immediately breaking up into two α particles of equal but oppositely directed momenta. This observation, together with an estimate of 1 microbarn for the reaction cross section, has been reported previously (27).

The Li^8 ion energies of from 1.0 to 5.7 Mev. which were observed are far less than the potential barrier energy, and indicate an abnormally large penetrability for Li^8 particles. Though evidence for a similar great penetrability is found in the case of low energy α particles (see Section I), the theoretical improbability of this reaction requires that such an interpretation be carefully scrutinized.

Subsequent to the original study of these tracks, plates developed to show singly charged particles have indicated that the $N^{14}(\gamma, d)3He^4$ reaction is much more common than was observed in plate B, and the possibility exists that some such stars in which only the three α-particle tracks were observed might have been interpreted as "hammer" tracks. It is felt, therefore, that

more conclusive evidence for the photoejection of Li^8 is required before this interpretation of these stars can be generally accepted.

SUMMARY

A study of nuclear research emulsions irradiated with a spectrum of X rays of energies up to 27 Mev. has revealed reactions involving the emission of heavy particles ($Z \geqslant 2$) in all major constituents of the emulsion. In reactions for which sufficient data were available, cross-section "resonances" were found such as appear typical of many photonuclear reactions. These reactions and their properties are summarized in Table III. Included in the table are the values of the integrated cross sections for the various reactions which have been obtained by graphical integration of the experimental curves. Levinger and Bethe (23) show that the integrated cross sections for all modes of photodisintegration of a nucleus are expected to be of the order of 1 Mev-barn so that it may be seen from the table that (γ, α) reactions occur in but a small fraction of all photonuclear disintegrations.

TABLE III

SUMMARY OF EXPERIMENTAL RESULTS

Observed reaction	Resonance peak energy (Mev.)	Peak cross sections (microbarns)	Resonance width (Mev.)	Integrated cross sections (Mev-barns)	Angular distribution
$Br(\gamma, \alpha)As$ $Ag(\gamma, \alpha)Rh$	9 Mev. (α-particle energy)		5 (α-particle energy)		Isotropic
$Br(\gamma, n\alpha)As$ $Ag(\gamma, n\alpha)Rh$ (identity uncertain)	4 Mev. (α-particle energy)		2.5 (α-particle energy)		Isotropic
$O^{16}(\gamma, \alpha)C^{12}$	17.5	50 (approximately)	5	24×10^{-4}	Isotropic (approximately)
$N^{14}(\gamma, \alpha)B^{10}$					
$C^{13}(\gamma, \alpha)Be^9$					
$C^{12}(\gamma, \alpha)Be^{8*}$	17.5	180	4	8.4×10^{-4}	Isotropic
$C^{12}(\gamma, \alpha)Be^8$		15 (approximately)			
$O^{16}(\gamma, 4\alpha)$	22.2	70	3	3.0×10^{-4}	
$O^{16}(\gamma, Be^8)2\alpha$	22.2	40	3	1.4×10^{-4}	
$N^{14}(\gamma, Li^6)2\alpha$		40 (approximately)	Broad	$> 1 \times 10^{-4}$	
$N^{14}(\gamma, d)3\alpha$ $N^{14}(\gamma, pn)3\alpha$					
$Ag(\gamma, Li^8)Ru$ (identity uncertain)		1 (average)			
$Ag(\gamma, 2\alpha)Tc$ $Br(\gamma, 2\alpha)Ga$					

As by-products of the main research, the range–energy relationships for C^{12}, B^{10}, and Be^{9} ions in E1 emulsion have been determined over a limited energy range.

ACKNOWLEDGMENTS

During the course of this experiment we have been greatly assisted by several persons, to whom we should like to express our gratitude.

To Dr. R. N. H. Haslam and his colleagues at the University of Saskatchewan for their co-operation in making the betatron irradiations for us.

To Drs. B. W. Sargent, T. D. Newton, J. D. Jackson, and M. A. Preston for their interest and advice on the experiment.

To R. G. Hayman, J. A. Cooke, Miss A. R. Rutledge, and C. Scully for their assistance in searching the plates and making the calculations.

To the members of the IBM section of the Chalk River Project for the use of their calculating machinery and their assistance in its operation.

APPENDIX I

Escape Correction Factors

A. Single α-Particle Tracks Observed at All Angles

If tracks of length L microns are randomly oriented in an emulsion of thickness t microns, and conditions of observation are such that tracks which end within 2 microns of either surface cannot be distinguished from those which escape, it may be shown that the escape correction factor C_e by which the observed number of tracks wholly within the emulsion must be multiplied to obtain the total number of tracks which originate in the emulsion is given by

$$C_e = \frac{1}{1 - \dfrac{L}{2(t-4)}}.$$

This factor is valid for values of $L < t$, a condition which obtains in this experiment for all but the most energetic α particles observed.

B. Single α-Particle Tracks Observed in Defined Angular Intervals

The escape correction factor, C_e, for tracks observed in an angular interval about the mean angle θ is given by

$$C_e = \frac{1}{1 - \dfrac{L \sin\theta}{(t-4)} \dfrac{(1 - \cos\phi_{\max})}{\phi_{\max}}}$$

where L and t are as defined previously, θ is the angle between the γ-ray direction and the track direction, and

$$\sin\phi = \sin\beta / \sin\theta$$

where β is the angle of dip of the track measured from the plane of the emulsion surface.

$$\phi_{\max} = \pi/2 \text{ when } \theta \leqslant \pi/4, \text{ and}$$

$$\sin\phi_{\max} = \frac{\sin\pi/4}{\sin\theta} \text{ when } \theta > \pi/4\,.$$

This relationship is independent of the angular distribution of the particles.

C. Carbon Stars

The escape correction factor used for carbon stars is based on the assumption that the average effective depth of a star in the emulsion is the sum of three terms as follows:

(1) the average vertical projection of the range of a randomly oriented α particle having two-thirds the "initial" kinetic energy of the star,

(2) the average vertical projection of the range of a randomly oriented α particle having one-sixth the "initial" kinetic energy of the star,

(3) the average vertical projection of a randomly oriented α particle having one-half the Be^{8*} disintegration energy.

On the basis of these assumptions, which take into account the mechanism of the reaction, the correction factor for carbon stars becomes

$$C_e = \frac{1}{1 - \dfrac{(L_1 + L_2 + L_3)}{2(t-4)}}$$

where L_1 is range in microns of an α particle having an energy of

$$\tfrac{2}{3}(E_T - 3)\text{Mev.},$$

L_2 is range in microns of an α particle having an energy of

$$\tfrac{1}{6}(E_T - 3)\text{ Mev.},$$

L_3 is range in microns of an α particle having an energy of

1.5 Mev. (i.e. 4.8 microns).

Since C_e varies only from 1.04 to 1.45 as the γ-ray energy increases from 11 to 24 Mev., further refinements in the calculation will lead to only second order changes in C_e.

D. Oxygen Stars

The escape correction factor for oxygen stars is based on the assumption that the average effective depth of a star in the emulsion is the diameter of a sphere having a radius of $\frac{3}{4}R$ where R is the range in microns of an α particle having an energy of $\frac{1}{4}E_T$ Mev. The correction then becomes

$$C_e = \frac{1}{1 - \dfrac{3R}{2(t-4)}}.$$

Since in this experiment the range of C_e is from 1.05 to 1.19, it will be seen that any further refinement in the calculation will lead only to second order changes in the magnitude of C_e.

REFERENCES

1. ALVAREZ, L. W. Phys. Rev. 80: 519. 1950.
2. BETHE, H. A. Revs. Modern Phys. 9: 69. 1937.
3. BLATT, J. M. and WEISSKOPF, V. F. Theoretical nuclear physics. John Wiley and Sons, Inc., New York. 1952.
4. BONNER, T. W., EVANS, J. E., MALICH, C. W., and RISSER, J. R. Phys. Rev. 73: 885. 1948.
5. DE CARVALHO, H. G. Phys. Rev. 76: 1729. 1949.
6. FARRAGI, H. Compt. rend. 229: 1223. 1949.

7. GIBSON, W. M. Proc. Phys. Soc. London, A, 62: 586. 1949.
8. GOWARD, F. K., TELEGDI, V. L., and WILKINS, J. J. Proc. Phys. Soc. London, A, 63: 402. 1950.
9. GOWARD, F. K., TITTERTON, E. W., and WILKINS, J. J. Nature, 164: 661. 1949.
10. GOWARD, F. K., TITTERTON, E. W., and WILKINS, J. J. Proc. Phys. Soc. London, A, 62: 460. 1949.
11. GOWARD, F. K., TITTERTON, E. W., and WILKINS, J. J. Proc. Phys. Soc. London, A, 63: 172. 1950.
12. GOWARD, F. K. and WILKINS, J. J. Proc. Phys. Soc. London, A, 63: 662. 1950.
13. GOWARD, F. K. and WILKINS, J. J. Proc. Phys. Soc. London, A, 63: 1171. 1950.
14. GOWARD, F. K. and WILKINS, J. J. Proc. Phys. Soc. London, A, 63: 1173. 1950.
15. GOWARD, F. K. and WILKINS, J. J. Proc. Phys. Soc. London, A, 64: 93. 1951.
16. GOWARD, F. K. and WILKINS, J. J. Proc. Phys. Soc. London, A, 64: 94. 1951.
17. GOWARD, F. K. and WILKINS, J. J. Proc. Phys. Soc. London, A, 64: 312. 1951.
18. HÄNNI, H., TELEGDI, V. L., and ZÜNTI, W. Helv. Phys. Acta, 21: 203. 1948.
19. HASLAM, R. N. H., CAMERON, A. G. W., COOKE, J. A., and CROSBY, E. H. Can. J. Phys. 30: 349. 1952.
20. HORNYAK, W. F., LAURITSEN, T., MORRISON, P., and FOWLER, W. A. Revs. Modern Phys. 22: 291. 1950.
21. JOHNS, H. E., KATZ, L., DOUGLAS, R. A., and HASLAM, R. N. H. Phys. Rev. 80: 1062. 1950.
22. LATTES, C. M. G., FOWLER, P. H., and CUER, P. Proc. Phys. Soc. London, A, 59: 885. 1947.
23. LEVINGER, J. S. and BETHE, H. A. Phys. Rev. 78: 115. 1950.
24. MALM, R. and BUECHNER, W. W. Phys. Rev. 81: 519. 1951.
25. MILLAR, C. H. Can. J. Phys. 31: 262. 1953.
26. MILLAR, C. H. and CAMERON, A. G. W. Phys. Rev. 78: 78. 1950.
27. MILLAR, C. H. and CAMERON, A. G. W. Phys. Rev. 79: 182. 1950.
28. MILLAR, C. H. and CAMERON, A. G. W. Proc. Roy. Soc. Can. 44: 201. 1950.
29. MILLAR, C. H. and CAMERON, A. G. W. Phys. Rev. 81: 316. 1951.
30. NABHOLZ, H., STOLL, P., and WÄFFLER, H. Phys. Rev. 86: 1043. 1952.
31. NEWTON, T. D. Proc. Roy. Soc. Can. 44: 215. 1950.
32. PRESTON, M. A. Phys. Rev. 80: 307. 1950.
33. PRESTON, M. A. Private communication.
34. ROTBLAT, R. *In* Progress in nuclear physics I. *Edited by* O. R. Frisch. Academic Press, Inc., New York. 1950.
35. TELEGDI, V. L. and VERDE, M. Helv. Phys. Acta, 22: 380. 1949.
36. TELEGDI, V. L. and ZÜNTI, W. Helv. Phys. Acta, 23: 745. 1950.
37. TITTERTON, E. W. Nature, 165: 721. 1950.
38. TITTERTON, E. W. Proc. Phys. Soc. London, A, 63: 915. 1950.
39. TITTERTON, E. W. Proc. Phys. Soc. London, A, 63: 1297. 1950.
40. TITTERTON, E. W. and GOWARD, F. K. Phys. Rev. 76: 142. 1949.
41. TOLLESTRUP, A. V., FOWLER, W. A., and LAURITSEN, C. C. Phys. Rev. 76: 428. 1949.
42. WÄFFLER, H. and YOUNIS, S. Helv. Phys. Acta, 22: 414. 1949.
43. WÄFFLER, H. and YOUNIS, S. Helv. Phys. Acta, 22: 614. 1949.
44. WELTON, T. A. Phys. Rev. 79: 399. 1950.
45. WILKINS, J. J. and GOWARD, F. K. Proc. Phys. Soc. London, A, 63: 663. 1950.
46. WILKINS, J. J. and GOWARD, F. K. Proc. Phys. Soc. London, A, 64: 201. 1951.
47. WILKINS, J. J. and GOWARD, F. K. Proc. Phys. Soc. London, A, 64: 849. 1951.
48. WRENSHALL, G. A. Phys. Rev. 57: 1095. 1940.
49. YAGODA, H. Radioactive measurements with nuclear emulsions. John Wiley and Sons, Inc., New York. 1949.

EFFECT OF RADAR SENSITIVITY ON METEOR ECHO DURATIONS[1]

By D. W. R. McKinley

ABSTRACT

Meteor echo durations were observed simultaneously with two radar systems having a power sensitivity ratio of 33 db. An experimental relation between echo duration and system sensitivity is obtained which shows that the duration of meteor echoes varies slowly, but significantly, with system parameters. Curves are furnished to correct observed durations to zenithal durations, applicable to any system using a horizontal half-wave dipole antenna.

INTRODUCTION

Recent contributions to the theory of meteoric ionization (1, 3) have indicated that Lovell's formula (5) does not apply to meteors producing long enduring echoes. Greenhow (1) has stated that the duration, T, of an enduring echo depends on the electron line density, α, according to the relation

[1] $$T = \alpha/4\pi DN_c$$

where D is the diffusion coefficient and N_c the critical density for the wave length employed. Greenhow and Hawkins (2) further claim that this means the electron densities may be obtained directly from the echo durations independently of the parameters of the apparatus. It will be shown here that the length of the long enduring echoes is independent of the radar parameters to a first order of approximation only, and that, for certain applications, the echo durations should be corrected for variations in transmitter power, receiver sensitivity, and antenna pattern. For example, both Greenhow and Hawkins (2) and Lindblad (4) have made use of Millman's observed relation between echo duration and visual magnitude (8), after correcting the average visual magnitudes to zenithal magnitudes, but without correcting the radar durations to zenithal values.

In a previous paper (6) the dependence of meteor echo rates on transmitter power was investigated experimentally. The great majority of the echoes in these experiments were of short duration and the effect of the more enduring echoes was statistically insignificant, hence the conclusion remains valid that Lovell's formula applies to the fainter meteors. These records of the Ottawa high–low power tests have recently been analyzed further to determine the connection between power and echo duration.

HIGH–LOW POWER OBSERVATIONS OF ECHO DURATIONS

The equipment used in these experiments was described in some detail in the earlier report (6). To sum up, the high-power transmitter radiated 200 kw. peak pulses on 9.22 m. and the low-power transmitter 100 watt peak pulses on 9.55 m., each using a half-wave horizontal dipole one-quarter wave above

[1] *Manuscript received April 2, 1953.*
Contribution from the Radio and Electrical Engineering Division, National Research Laboratories, Ottawa, Canada. Issued as N.R.C. No. 3017.

ground. In this particular experiment the power of each transmitter was determined with an error not exceeding 5%, therefore the power ratio was 33.0 ± 0.5 db. In all other respects, e.g., receiver and display characteristics, transmitter pulse width, and repetition frequency, the two systems were maintained as closely alike as possible, and the receivers and displays were interchanged at intervals, to eliminate further any possible discrepancies.

From approximately twelve hours of film records obtained on Jan. 3, 1951, the durations of 210 echo pairs were measured, reading the time to the nearest 0.05 sec. for echoes less than 1 sec., and to 0.1 sec. for longer echoes. The durations of the echoes were read independently from each record, and are the time intervals during which the echoes were above noise (neglecting momentary fades), without reference to a theoretical starting time. In a few cases the echo appeared on the low-power film slightly later than on the high-power record, the delay being a fraction of the total difference in durations, but in most instances the echoes started simultaneously, or within 0.1 sec. The low-power durations were grouped in arbitrary time intervals, since the existence of a low-power echo was the criterion of selection. No echo appeared on the low-power record that did not also show on the high-power display and in all cases, without exception, the low-power duration was the shorter. Among those echoes missed entirely by the low-power set were many of the longest durations on the high-power system, indicating that there is no simple connection between echo amplitude and duration.

It was evident from a preliminary consideration of the data that the general trend of the durations was exponential, hence it appeared advisable to average the common logarithms of the individual durations in the selected intervals. See Table I. For example, the average log duration, log T_l, of the 62 meteor echoes occurring in the low-power duration interval 0.1 to 0.25 sec. was -0.850, and the average log duration, log T_h, of the corresponding high-power echoes was -0.144. The last row of Table I shows the difference in the logs, i.e., the log of the ratio of the durations on high and low power.

TABLE I

Low power duration interval, sec.	0.1–0.25	0.3–0.45	0.5–0.95	1.0–1.9	2.0–3.9	4.0–9.9	10.0–19.9	20.0–39.5	40.0→
No. of pairs	62	43	24	19	20	24	10	5	3
log T_l	−0.850	−0.464	−0.196	0.166	0.411	0.826	1.145	1.45	1.80
log T_h	−0.144	0.124	0.296	0.625	0.813	1.133	1.520	1.71	1.95
log(T_h/T_l)	0.706	0.588	0.492	0.459	0.402	0.307	0.375	0.26	0.15

In Fig. 1, log (T_h/T_l) is plotted against log T_l. A straight line may be drawn through the experimental points, provided one interprets it judiciously. The deviations from the mean of the individual measurements in the short-duration classes were greater than in the long-duration intervals. This was counterbalanced by the greater numbers in the short-duration classes, so

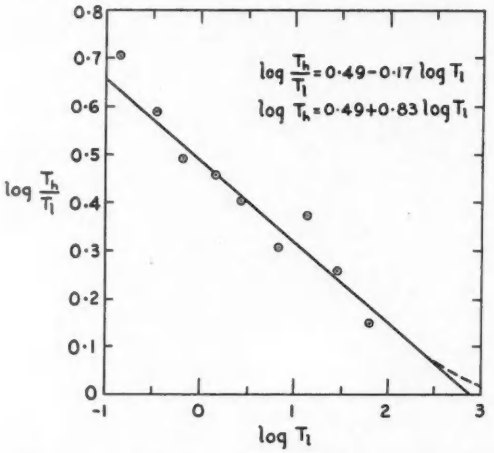

FIG. 1. Experimental relation between the logarithm of the ratio of high and low power durations and the logarithm of the low power durations.

there is no experimental reason to weight any one mean value more than another. However, since many of the echoes of less than one-second duration may be expected to obey Lovell's formula, which implies an exponential fall-off of echo power with time, there may be doubt concerning the validity of the straight line to the left of log $T_l = 0$. If echoes of duration shorter than 0.1 sec. could have been measured accurately, it is possible that the observed points would curve upward to the left of log $T_l = -0.5$.

Extrapolating the line to meet the axis log $(T_h/T_l) = 0$, it would appear that echoes of the order of 1000 sec. duration should last the same time on both radars. Such echoes are extremely rare and one might have to wait years for observational confirmation. In thousands of hours of operating the high-power radar we have detected only six echoes over nine minutes in duration (7) and they all occurred in a short interval on the night of Aug. 4, 1948. The graph should not cross the axis log $(T_h/T_l) = 0$, but it may approach the axis asymptotically, as suggested by the dashed line.

The power level of the high-power transmitter is 33 db. above that of the low-power one, hence the corresponding values of log T_l and log T_h taken from Table I, or read from the line of Fig. 1, yield two points 33 db. apart on the decay curve of the meteor echo power. The saturation level of the receivers was about 24 db. above the minimum detectable signal, and a few echoes reached saturation on the low-power system, hence they were at least 57 db. above noise level on the high-power system. However, most of the echoes were below saturation on the low-power receiver and were thus in the range 33 db. to 57 db. above the limiting sensitivity of the high-power equipment.

If one were to assume an exponential decay of echo power with time, of the form log P = log $P_0 - kT$, the data of Table I and Fig. 1 may be used to

determine k and log P_0 for selected values of T. In Table II, 10 log P_0 is the echo power ratio, in decibels above the limiting sensitivity of the high-power system, which should have been received from the meteor at or near the beginning of the echo.

TABLE II

COMPUTED INITIAL ECHO POWER, ASSUMING EXPONENTIAL DECAY

T_h (sec.)	0.46	0.84	3.1	8.0	21	54	141	367
10 log P_0 (db.)	42	45	49	54	63	79	113	237

From Table II it will be seen that for durations up to about eight seconds the computed initial echo powers are within the observed range 33–57 db. This does not prove that the short-duration echoes necessarily have an exponential decay but at least it admits the possibility. On the other hand, the initial echo powers for the longer durations are considerably in excess of the observed powers so that the exponential decay curve definitely cannot apply to them. The observations, therefore, lend support to the theories put forward by Greenhow (1), and Kaiser and Closs (3) which predict a steep drop in echo power near the end of the echo.

RELATION BETWEEN ECHO DURATION AND SYSTEM PARAMETERS

The observational data of Fig. 1 apply over the range of durations from 0.2 to 200 sec. for the transmitter power ratio of 33 db. It should be safe to interpolate between the two experimental power levels and also to extrapolate with some caution. The equation of the empirical straight line of Fig. 1 may be written as

$$\log T_h = b + m \log T_t . \qquad [2]$$

Divide the logarithmic power range between 0 and 33 db. into a large number, N, of equal intervals. The straight lines corresponding to each of these intervals will have the same form, and for the first interval the equation is

$$\log T_1 = b_1 + m_1 \log T_t , \qquad [3]$$

where $b_1 \to 0$ and $m_1 \to 1$ as the number of intervals is increased indefinitely. The n^{th} interval will have the equation

$$\log T_n = b_1(1 + m_1 + m_1^2 \ldots + m_1^{n-1}) + m_1^n \log T_t , \qquad [4]$$

which must be the same as Equation 2 when the last interval is reached. Solving for b_1 and m_1 in terms of b and m, Equation 4 becomes

$$\log T_n = \frac{b(1 - m^{n/N})}{1 - m} + m^{n/N} \log T_t . \qquad [5]$$

Putting in the numerical values of b and m from Fig. 1 and rewriting, we obtain the general relation

$$\log (T_s/T_x) = 2.88\,(1 - 0.83^{x/33}) - (1 - 0.83^{x/33}) \log T_x . \qquad [6]$$

If we observe an echo duration T_x with an equipment whose sensitivity is x db. above (or below) that of another equipment, having an arbitrary power level of 0 db., the equivalent duration, T_s, of the echo on the second, or "standard" equipment, may be found from Equation 6. It may be noted that there is an infinite set of values of m and N that will satisfy Equation 5; the values $m = 0.83$ and $N = 33$ are only one set which happened to arise from these experimental conditions. Had the experiment been done with another power ratio, W, it is implied that another slope, M, would have been obtained, such that $0.83^{1/33} = M^{1/W}$.

Fig. 2 shows graphs computed from Equation 6 at 10 db. intervals, from -20 db. to $+50$ db. As the observed echo powers were occasionally in excess

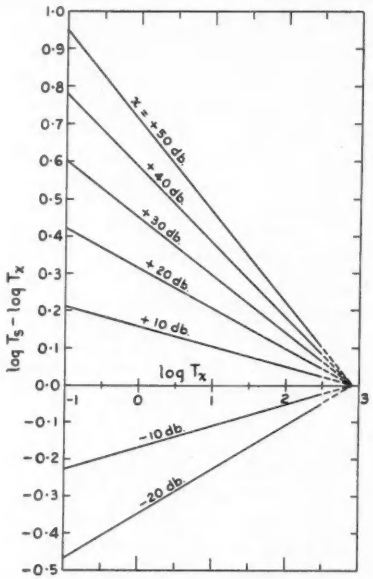

FIG. 2. Graphs computed for 10 db. intervals showing correction to be added to the observed duration T_x, obtained with one system of sensitivity x db. relative to a second system, to give the duration T_s that would be obtained with the second system.

of $+57$ db. the graphs should be useful up to $+50$ db. at least, and similarly they should be reasonably valid to -20 db. Until further experimental evidence is available the use of the graphs should be limited to $-0.8 < \log T_x < 2.5$.

The observations were based on a difference in transmitter power, but there is no reason to believe that a similar change in receiver sensitivity or in antenna gain would not yield the same results. As will be seen in the next section some important practical applications of this relation between duration and over-all system sensitivity are the correction for echo durations observed off the axis

of an antenna beam, the correction for durations observed at different ranges, and the correction for both factors combined.

It should be noted that no attempt has been made to allow for the slight difference in frequency of the high and low power systems. If one assumes the durations to vary as the squares of the wave lengths (9) the ordinates of the line in Fig. 1 would be shifted downward by an amount 2 log (9.22/9.55) $= -0.03$, which is small, but not inappreciable. However, a preliminary examination of the echo durations obtained at Ottawa on 9.22 m., 5.35 m., and 2.83 m. indicates that the square law does not hold for the longer echoes. This material will be analyzed elsewhere. It is of interest to note that Greenhow (1) also finds for long-duration echoes that the exponent falls below unity. If a wave length correction were to be applied to Fig. 1, it is probable that the short-duration points would be affected most and the long-duration points least. Hence one might expect, instead of a downward displacement of the line, a change of slope from -0.17 to -0.165 or -0.16. As we have not yet obtained quantitative information on this problem we shall not make any wave length correction for the present.

ZENITHAL CORRECTION FOR ECHO DURATIONS

From the discussion above it will be apparent that the durations of echoes detected at long ranges will require a correction to bring them to equivalent durations at a standard range, say $R = 100$ km., because the echo power will fall off at least as R^{-3}. The power loss may be proportional to R^{-4} for very long enduring echoes where the meteoric column may be expected to have lost its cylindrical form and to behave more like a spherical reflector. The variation in power with antenna gain in the direction of the meteor is even more important.

The antenna pattern of the full-scale dipole used in the Ottawa meteor work has not been measured directly, but measurements on small-scale models at higher frequencies have generally confirmed the theoretical patterns for this dipole configuration. It is unlikely that the pattern of the antenna as actually used will depart appreciably from the predicted patterns except at low elevations, where buildings and trees may be expected to distort the field. The power gain of a horizontal half-wave dipole mounted one-quarter wave above a ground plane is given by

$$G_{\perp} = G_0 \sin^2 (\tfrac{1}{2}\pi \cos z) , \qquad [7]$$

in the vertical plane normal to the dipole axis, and by

$$G_{||} = G_0 \sin^2 (\tfrac{1}{2}\pi \cos z) \cdot \frac{\cos^2 (\tfrac{1}{2}\pi \sin z)}{\cos^2 z} , \qquad [8]$$

in the vertical plane containing the dipole axis; where the angle z is measured from the zenith in the specified plane, and G_0 is the gain in the zenith.

Fig. 3, Curve $G_{\perp}$ shows one-half of the computed vertical pattern of the Ottawa dipole in the East–West plane, the dipole axis being North–South. A decibel scale of power ratio is used to bring out the detail better at low

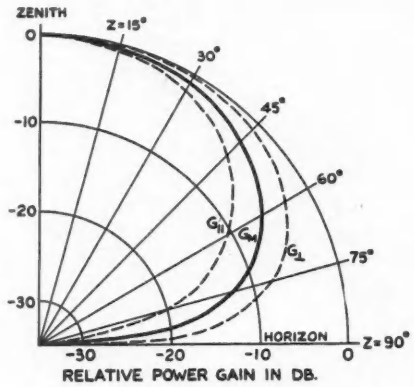

FIG. 3. Antenna patterns of a half-wave horizontal dipole, one-quarter wave above ground.
Curve $G_\perp$ —normal to axis of dipole.
Curve $G_{||}$ —parallel to axis of dipole.
Curve G_M —adopted mean pattern.

elevations above the horizon. Curve $G_{||}$ shows the pattern in the North–South plane. For intermediate azimuth angles similar patterns may be calculated which will lie between $G_\perp$ and $G_{||}$, but these would be of value only in precise work where the meteor position was known accurately. For the present purposes a mean gain curve was computed, which is shown in Fig. 3, Curve G_M.

The attenuation with range was assumed to be R^{-3}, hence the power P received from an echo at a range R and the corresponding angle z, relative to the power P_0 that would be received from the same meteor overhead at range $R = H$, is given by

[9] $$P = P_0 G_M^2 (H/R)^3 .$$

Three values of H were selected as typical regions where meteors occur: $H = 90$, 100, and 110 km. The ranges and antenna gains to these regions were computed on a curved earth basis and inserted in Equation 9. Fig. 4 shows the

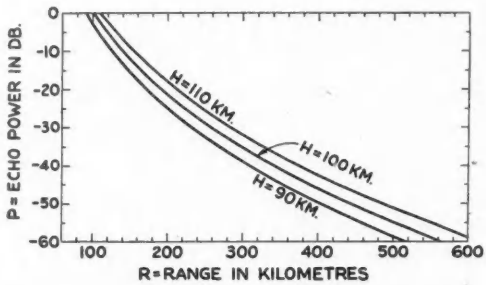

FIG. 4. Echo power from a meteor at range R and height H expressed in decibels below the echo power of the same meteor overhead at range $R = H$.

relative meteor echo power in decibels to be expected from a meteor at range R and height H. These curves apply only to the half-wave dipole, but they are independent of the wave length, the transmitter power, or the receiver sensitivity.

A similar series of graphs to those shown in Fig. 2 was drawn, one for each of the values of P corresponding to the range R read from Fig. 4, using the $H = 100$ km. curve only. For example, at $R = 180$ km. the echo power is 18 db. below the zenithal power, or in other words the system sensitivity is 18 db. above the standard, so the slope of this line may be computed by putting $x = 18$ in Equation 6. From these graphs values of $\log T_0 - \log T_{x(R)}$ may be read for selected values of $\log T_{x(R)}$ and a series of curves may be drawn as shown in Fig. 5. Here, $\log T_0$ is the log of the echo duration the

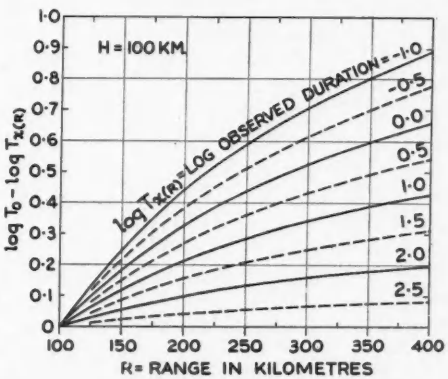

FIG. 5. Chart for the correction of observed durations to zenithal durations. Applicable to systems with the antenna pattern of Fig. 3. The chart is computed for a height $H = 100$ km. but may be used for other heights by readjusting the observed ranges by means of Fig. 4.

meteor would have had if it had occurred in the zenith, or $\log T_0 - \log T_{x(R)}$ is the amount to be added to the log of the observed duration to correct it to zenithal duration. For example, an echo enduring for 100 sec. at a range of 250 km. would have a zenithal duration of 136 sec.; a 10 sec. echo at 250 km. would be 19 sec. long overhead; a 1 sec. echo at the same range should be corrected to 2.7 sec. The orientation, with respect to the line of sight, of the "corrected" zenithal meteor is tacitly assumed to be the same as that of the observed distant meteor.

While Fig. 5 is computed for $H = 100$ km. it may be used for any other height by readjusting the observed range to the range at $H = 100$ on the same power level in Fig. 4. For example, an echo at $H = 90$ km. and $R = 310$ km. converts to $H = 100$ km. and $R = 340$ km. by moving horizontally along the -40 db. line. One then enters Fig. 5 with $R = 340$ km.

If the attenuation of the long-duration echoes were assumed to vary as R^{-4}, one should lower the curves of Fig. 4 by $\log (H/R)$, which would proportionally raise the curves of Fig. 5. A long-duration echo presents much the same

appearance when viewed simultaneously from widely different aspects, which suggests a target of spherical rather than cylindrical nature, with an attenuation at least greater than the inverse third power. The corrections in Fig. 5 should be regarded as minimum corrections, particularly for the longer durations.

Fig. 5 will be used in revising the duration–magnitude graphs now under preparation in the combined Ottawa meteor program. A preliminary glance at the graph published by Millman (Fig. 2 of Ref. 8) indicates that the correction for meteors of log $T = 0$, occurring at an average range of about 150 km., may raise the short-duration end of this line by 0.2 units, while for the meteors with log $T = 2$ the correction should be somewhat less, despite the greater average range of these meteors. The slope of the line may be decreased slightly as a consequence. This correction has an effect of the same order of magnitude as that of the correction of visual magnitude to zenithal magnitude, e.g., in Fig. 1 of Ref. 1, it puts the lower end of the dashed line, drawn by Greenhow and Hawkins and marked "zenithal magnitude", nearly up to the original line, taken from Millman and marked "apparent magnitude". Consequently, the duration correction and the magnitude correction may be regarded as equally important, especially if workers wish to extrapolate the relation to values as small as log $T = -0.7$ as Lindblad (4) has done. However, it is not suggested that attempts should be made to apply either correction to the early data furnished by Millman, as we intend to publish shortly an account of the echo duration versus visual magnitude observations embracing much more data, for several strong showers and for nonshower meteors, with these corrections taken into consideration.

The Ottawa radar set, working at a peak power of 200 kw. detected several meteors per hour between the ranges 550 and 650 km., under shower conditions. (These were not usually photographed because the recorded range was limited to 260 km. as a rule, except when it was extended for auroral observations.) From Fig. 4, the echo power from these meteors was 60 db. below their zenithal echo power. In other words, had these meteors occurred in the zenith a transmitter with a peak power of one-fifth of a watt would have produced echoes of the same strengths and durations! However, the high-power transmitter pattern intersects a much larger volume of the meteoric region between 550 and 650 km. than the very low power system does overhead for the same spread of echo power, hence the low-power set will not see very many echoes. In fact, the over-all rate ratio should be 1000: 1 (6).

This tremendous variation in meteor echo strengths emphasizes a point that may have escaped the notice of some workers, namely, that a nominally high gain antenna invariably has side lobes and, while these lobes may be 15 to 20 db. down from the main lobes, one can still detect significant numbers of meteors in the side lobes which cannot be resolved from the wanted meteors occurring in the main lobe, especially as the side lobes frequently intersect a considerably larger part of the meteoric region.

Even if a narrow beam antenna could be built with no side lobes at all the difficulty would still remain. One cannot tell whether an echo of a given

duration is a low-amplitude echo occurring on the axis of the beam or a high-amplitude echo occurring off the axis where the pattern is many decibels down from the maximum; owing to the narrowness of the beam the echoes cannot well be distinguished in range, particularly if the beam is inclined from the vertical. The first echo requires no duration correction but the second one may need a substantial correction. There thus appears to be some advantage in using a very broad beam, at least for measuring rates and durations.

In a recent paper (7) the statement was made that an attenuation of the order of 50 db. would be needed to account for the observed reduction in echo strength from the aurora overhead, compared to the echo strength at 300–600 km. Auroral echoes saturating the receiver have been observed at ranges up to 1000 km. with the Ottawa radar used in the meteor program. From Table III of that paper the average height of the auroral sources from which these echoes were obtained was probably 200 km. or lower. Assuming that the auroral rays reflect radio waves in a similar manner to meteor trails, the curves of Fig. 4 are applicable. The auroral echo power, corrected to zenithal value, would then be a minimum of 36 db. (antenna pattern) + 20 db. (range) + 24 db. (receiver saturation) or a total of 80 db. Similarly, the saturating auroral echoes at a height of 100 km. and a range of 500 km. have an echo power of 55 db. (from Fig. 4) + 24 db. (receiver saturation) or a total of 79 db. However, when the auroral display is actually in the zenith, only an occasional weak echo can be detected at all, which suggests that our earlier estimate of the attenuation factor for overhead auroral echoes should be increased to 80 db. or more.

REFERENCES

1. GREENHOW, J. S. Proc. Phys. Soc. London, B, 65: 169. 1952.
2. GREENHOW, J. S. and HAWKINS, G. S. Nature, 170: 355. 1952.
3. KAISER, T. R. and CLOSS, R. L. Phil. Mag. 43: 1. 1952.
4. LINDBLAD, BERTIL-ANDERS. Trans. Chalmers Univ. Technol. Gothenburg, No. 129. 1952.
5. LOVELL, A. C. B. and CLEGG, J. A. Proc. Phys. Soc. London, 60: 491. 1948.
6. McKINLEY, D. W. R. Can. J. Phys. 29: 403. 1951.
7. McKINLEY, D. W. R. and MILLMAN, PETER M. Can. J. Phys. 31: 171. 1953.
8. MILLMAN, PETER M. J. Roy. Astron. Soc. Can. 44: 209. 1950.
9. PINEO, V. C. and GAUTIER, T. N. Science, 114: 460. 1951.

GRID IONIZATION CHAMBER MEASUREMENTS OF ELECTRON DRIFT VELOCITIES IN GAS MIXTURES[1]

By W. N. English[2] and G. C. Hanna

ABSTRACT

Electron drift velocities have been measured in the low X/p region from 0.05 to 0.5 volts per cm. per mm. mercury which is an important one for the calculation of collection times in electron pulse chambers. The grid ionization chamber method is rapid and convenient and gives an accuracy of about 10%. Mixtures of the noble gases neon, argon, krypton, and xenon with carbon dioxide and/or methane have been studied, as well as a number of unpurified "tank" gases. In the mixtures used there are anomalies, or humps, in the drift velocity curves which seem to be correlated with the "Ramsauer" electron free paths in the four noble gases. There is a striking difference in the effect of carbon dioxide and of methane when added in small amounts to the noble gases, which is attributed mainly to the difference in electron mean free path in these two gases, but may also be an indication of a difference in electron energy distributions.

INTRODUCTION

The time required to collect electrons in a pulse ionization chamber is a parameter of great importance. This "collection time" determines the counting rate that can be handled, and the pulse "build-up" probability.* It also imposes a limit on the low frequency cutoff of the associated amplifier that may well determine the signal to noise ratio. In coincidence work it is obviously of direct importance.

For any gas the drift velocity v is a function of X/p where X is the applied field strength (in volts per cm.) and p is the pressure (in mm. mercury). For most common gases there is some information on v, but attempts to calculate collection times for various gas fillings in a large pulse ionization chamber revealed that only meager data existed on electron drift velocities in the region of X/p concerned, and none for some of the most useful gas mixtures.

The existing data had been obtained mainly by the diffusion methods developed by Townsend and co-workers (7), and by Nielsen and Bradbury using Loeb's electron shutter (11). Klema and Allen (10) have reported a study of argon, nitrogen, and argon + nitrogen mixtures by a pulse rise method using α particles which bears some similarity to that used in the present work. Their values for "pure" argon did not agree with Nielsen. Hudson (8), using an X-ray ionization method, obtained still a different curve.

Since this present work was undertaken two further measurements have been reported. Kirshner and Toffolo (9) have reported a study done by Hudson's method which agrees well with Nielsen's curve. Colli and Facchini (5) have repeated Klema and Allen's experiment using carefully purified argon

[1] *Manuscript received February 11, 1953.*
Contribution from Atomic Energy of Canada Ltd., Chalk River, Ontario. Issued as A.E.C.L. No. 57.

[2] *Now at Pacific Naval Laboratory, Esquimalt, B.C.*

* *The probability of a multiple superposition of small unwanted pulses simulating a large wanted pulse; for example, a very high α particle rate will interfere with the counting of fission fragments.*

and obtained good agreement with Nielsen's results. They found, as also did Kirshner and Toffolo, that addition of the appropriate fraction of a per cent of nitrogen, a likely impurity, would produce curves similar to those of Klema and Allen or of Hudson for "pure" argon.

In the present work no purification, other than freezing out in liquid nitrogen, was used. The runs of "tank" samples of the noble gases were done to obtain a base curve. Once a fraction of a per cent of carbon dioxide or methane had been added it was assumed that the effect of original polyatomic impurities in the noble gas would not be significant.

METHOD

Since electron drift velocities for the calculation of collection times were unknown, it seemed logical to reverse the process and try to deduce the drift velocity from the observed rise of the electron pulse. For this purpose a grid chamber of the type developed by Bunemann, Cranshaw, and Harvey (4) was set up as shown in Fig. 1. A collimated source of alpha particles—either Pu^{239} (5.16 Mev.), Am^{241} (5.48 Mev.), or Cm^{242} (6.08 Mev.)—was mounted on the cathode, and the gas pressure adjusted so that the alpha tracks reached almost to the grid. The grid voltage, obtained from a potential divider, was adjusted so that the grid was just negative enough not to capture electrons.

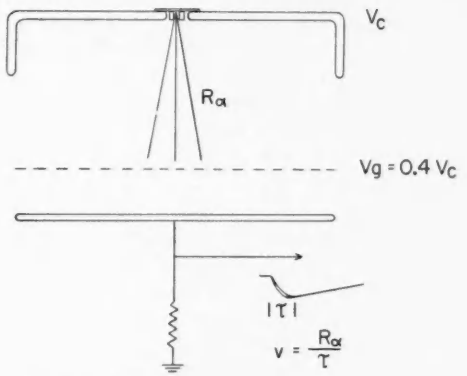

FIG. 1. Grid ionization chamber and α source.

A negative pulse then appears at the collector as the column of electrons produced by each alpha particle passes through the grid. The electron drift velocity is given to a first approximation by the range of the alpha particle in the chamber, divided by the rise time of the electron pulse.

The alpha particle pulse was amplified using an AEP model 1409 (triode-input) low-noise preamplifier followed by an AEP model 1444 fast linear amplifier (12), and displayed on a triggered oscilloscope.

The full band width of the amplifier system, some 10 Mc./sec., was restricted, by the usual differentiating and integrating time constants, to reduce

amplifier noise. Since the pulse rise-times varied over a very wide range (from about 0.5 to 150 μsec.) the amplifier time-constants were adjusted to suit the particular rise-time being measured. The integrating time-constant was kept considerably shorter and the differentiating time-constant some 10 or 20 times longer than the pulse rise-time.

Time calibration of the oscilloscope was checked in two ways. In the first, the oscilloscope calibrator, a ringing circuit, was excited by a suitable subharmonic (5th to 10th) of its natural frequency obtained from a beat frequency oscillator. The oscillator frequency was then counted using two "scales of 64" in series as a frequency divider. In the second a length of RG11U cable was used as a pulse-forming line in conjunction with a Western Electric hydrogen-filled mercury relay. The generally accepted propagation velocity of 200 meters/μsec. gave agreement with the first calibration. There was a 0.2 μsec. delay in the start of the oscillograph sweep. This was corrected by extrapolating the initial rise visually to the base line.

The alpha particles from the source were collimated to remove the most oblique tracks, and thus to improve the ratio of wanted to unwanted counts. Of the remaining tracks only those closely parallel to the field were accepted since measurements were confined to the slow-rise edge of the narrow envelope appearing on the oscilloscope screen. This selection presented no difficulty since all pulses had the same amplitude, and the edge was sharply defined.

The uniformity of the electric field in various designs of plane parallel grid chamber was examined by means of a rubber membrane model. It was found that a rim on the cathode (which is circular in the present apparatus) is almost as good as a single guard ring, and eliminates one feed-through insulator. A plot of equipotentials in a chamber similar to the present one is shown in Fig. 2. The field is seen to be quite uniform in the central region where the measurements are made.

To change X/p the applied voltage was varied, pressure being kept constant. Except where otherwise indicated, the pressure was atmospheric. The upper limit of X/p is set by the maximum voltage (about 5 kv.) that can be introduced through a conveniently compact insulator without noise pulses, and by the need for adequate stopping power in the gas, while the lower limit corresponds to the lowest voltage at which usable pulses could be obtained with the particular gas in use, which was often as little as 10 v.

Pressures in the vicinity of one atmosphere were measured on an "Ashcroft" bourdon gauge; pressures from 0–20 mm. mercury and 0–40 mm. mercury on two barometrically compensated capsule gauges made by Edwards & Co. Care was taken to ensure mixing in the gas mixtures. For small percentage additions, the minor component was added to a small manifold of calibrated volume and then swept into the chamber by the main component. In proceeding to the next filling the gas was in general pumped out and discarded, but in the case of xenon it was frozen out in a liquid nitrogen trap connected to the chamber. With neon and krypton, neither of which could be frozen out satisfactorily, a convection system was used to ensure adequate mixing.

The gas purity attained was that employed in careful ionization chamber work. The chamber used for all the gases but hydrogen was of mild steel,

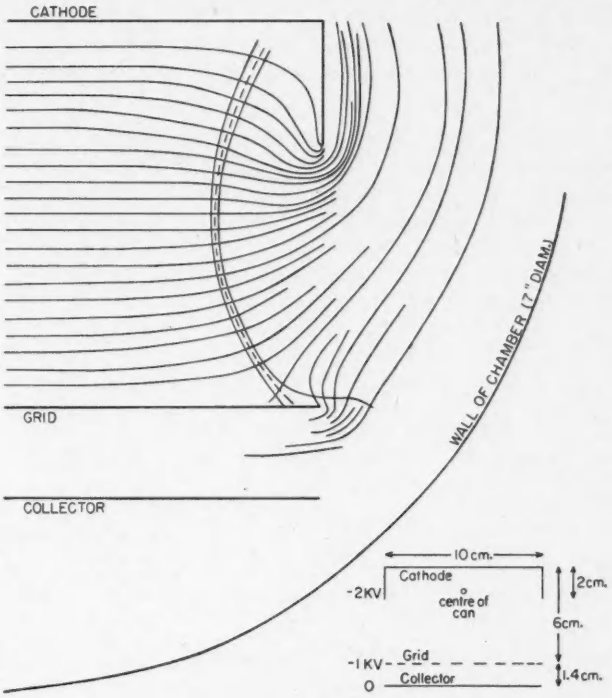

FIG. 2. Plot of equipotentials in a grid ionization chamber similar to the present one.

volume 2750 cc., and had brass fittings and copper plumbing. It was sealed with a lead gasket. Valves were diaphragm type with teflon seats. The chamber was evacuated with an oil diffusion pump and baked at 190° C. for 21 hr. at the beginning of the work. It was subsequently thoroughly flushed and evacuated when changing gas fillings.

The main feature of the present method is the ease and rapidity with which useful results can be obtained. In common with the method of Klema and Allen it uses electrons from alpha-particle ionization, but the tracks are parallel rather than perpendicular to the field and thus confined to the most uniform field region. The effect of the grid is to make all pulses of equal amplitude,* regardless of track orientation, which makes selection of the appropriate pulses for measurement very easy. This is further aided by collimation of the source to reduce the number of oblique tracks.

EXPERIMENTAL RESULTS

Drift velocities shown are calculated from alpha range divided by pulse rise time. There are two effects in the chamber which tend to make the velocity derived from this simple expression too small. The first is diffusion, the second

* *Neglecting the effect of recombination, i.e., lack of saturation, at very low* X/p.

is the time taken for the electrons to cross the grid-collector space, which we shall call the transit time correction. These corrections are discussed in Appendix I. The results given in Fig. 3 to Fig. 21 have not been corrected.

Hydrogen

A preliminary run was made in hydrogen to see whether the method gave results concordant with the careful measurements of Bradbury and Nielsen (2). Hydrogen must be purified to achieve electron collection at the pressure necessary for adequate stopping power. Hence the work was done in a large chamber fitted with a uranium purifier (6). Unfortunately, grid microphonics due to a noisy location reduced the signal to noise ratio considerably. However, the agreement, as shown in Fig. 3, is considered significant.

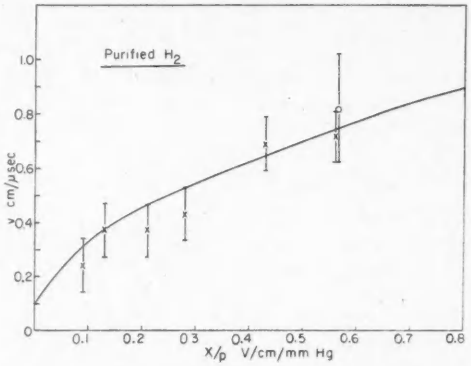

FIG. 3. Drift velocity of electrons in hydrogen. The curve of Bradbury and Neilsen is shown for comparison.

Tank Argon

In order to have a base for comparison with argon mixtures some measurements were done in tank argon, although it was realized that purity is all important in the monatomic gases, and that the results would apply only to the particular conditions of the experiment. It was found that the X/p region below 0.2, which contained an interesting "hump", was particularly sensitive to the history (i.e. purity) of the gas filling. Fig. 4 shows the drift velocities measured in the same filling of "Matheson" lecture bottle argon ("99.6%") at different intervals up to five days. Fig. 5 shows a similar series for "Canadian General Electric" cylinder argon ("99.6%"). A comparison of the "21 hr. Matheson" and the "3 day C.G.E." curves, with the results of Klema and Allen, and of Nielsen is shown in Fig. 6 and discussed in a later section. Also shown is a run at $\frac{1}{2}$ atmosphere pressure. The signal to noise ratio was poorer at the lower pressure since the alpha particle was not stopped in the cathode grid space, so that the displacement of this curve is not significant. There seems to be a second maximum in the drift velocity at about $X/p = 0.5$. As it was outside the effective range of the present apparatus it was not studied further.

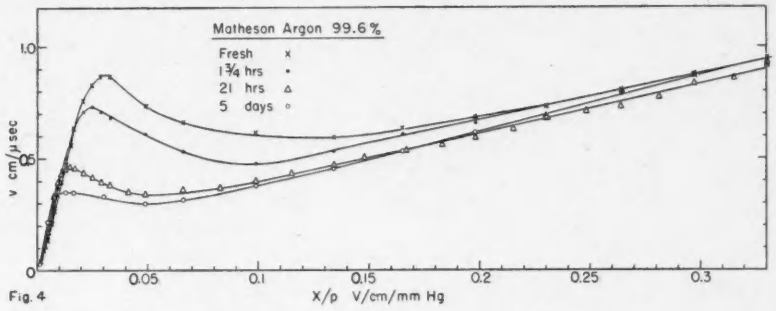

Fig. 4

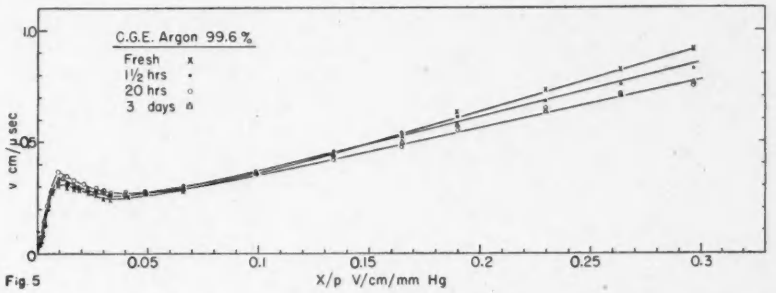

Fig. 5

FIGS. 4 and 5. Effect of "aging" (i.e. purity) on drift velocity of electrons in tank argon.

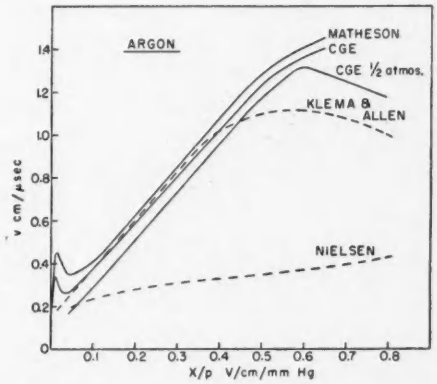

FIG. 6. Drift velocity of electrons in argon; comparison of results. "Matheson" and "C.G.E." refer to manufacturers of gas samples used in present work.

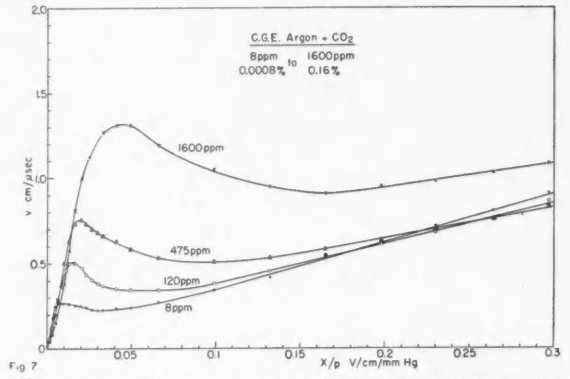

Fig. 7

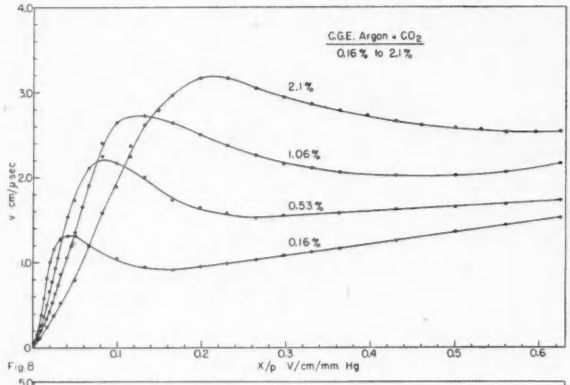

Fig. 8

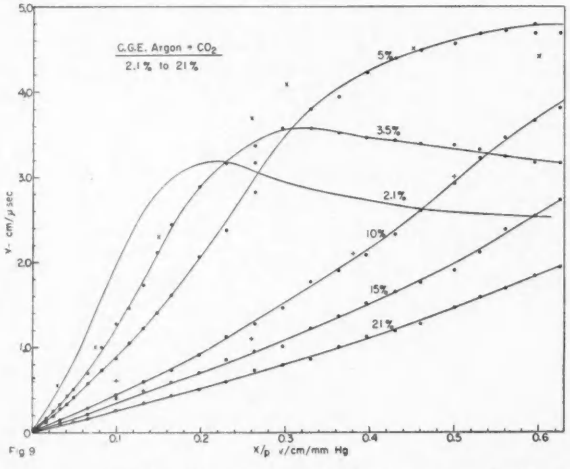

Fig. 9

FIGS. 7, 8, and 9. Drift velocity of electrons in argon + carbon dioxide mixtures.

Carbon Dioxide

In the range of X/p studied (0 to 1.0 v./cm./mm. mercury) it was found impossible to achieve saturation* in carbon dioxide, using the "bone-dry" grade (99.956%), even after freezing and pumping. Because of the resulting poor signal to noise ratio the measurements of drift velocity were not very reproducible ($\pm 10\%$). Within this accuracy it was found that

$$v = 0.6\ (X/p)\ \text{cm./}\mu\text{sec.}$$

This relation is in agreement with the results of Skinker (15), over the limited range of (X/p) studied.

Argon Plus Carbon Dioxide

This is a much used mixture of good stopping power. Published data consisted of two meager curves for 5% and 10% carbon dioxide by Rossi and Staub (14). A series of 12 curves with carbon dioxide content varying from 8 parts per million to 21% is shown in Figs. 7, 8, and 9. Gases used were C.G.E. tank argon and Matheson lecture bottle carbon dioxide (99.5%). No purification was used although this would be desirable for carbon dioxide ratios greater than 5%. A purer grade of carbon dioxide ("bone-dry"—99.956%) was obtained in cylinders and used for some later runs.

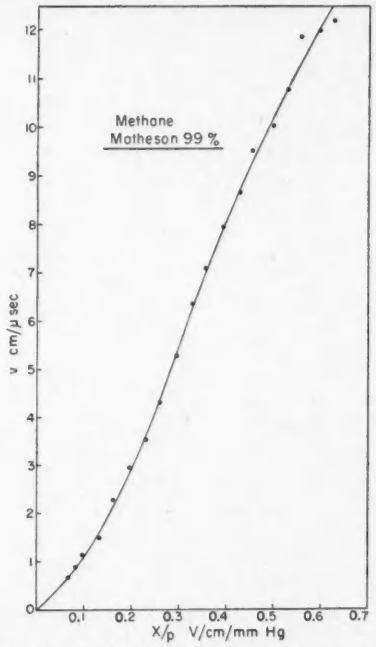

FIG. 10. Drift velocity of electrons in methane.

* *By "saturation" we mean the collection of all the electrons produced in the gas filling by the ionization process. Attainment of saturation is indicated by a constant pulse amplitude as X/p is increased.*

Methane

This gas has the useful properties of good stopping power and large hydrogen content. Matheson methane (99.0%) straight from a lecture bottle gave electron pulses. Results were greatly improved by freezing out the methane with liquid nitrogen and pumping for a few minutes. The resulting drift velocity curve is shown in Fig. 10. Methane is apparently very "fast" indeed.

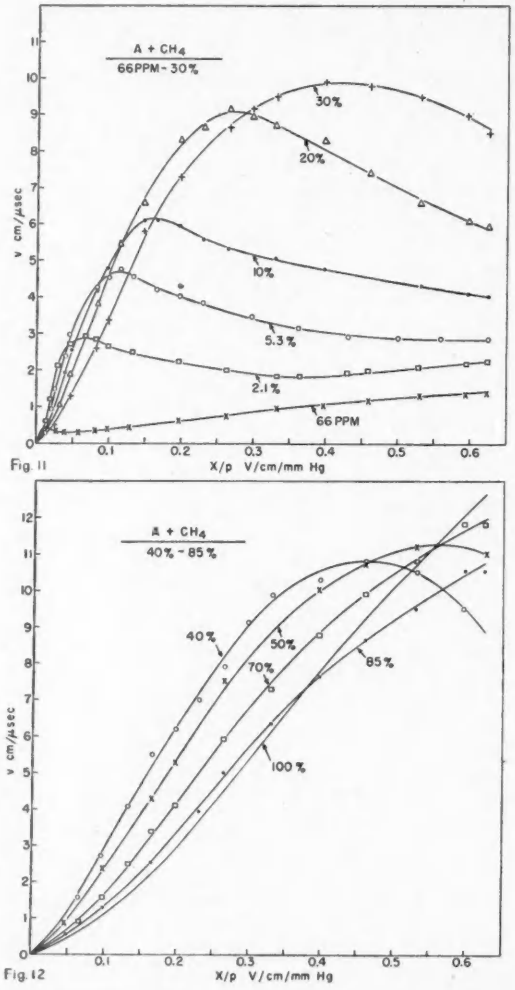

FIGS. 11 and 12. Drift velocity of electrons in argon + methane mixtures.

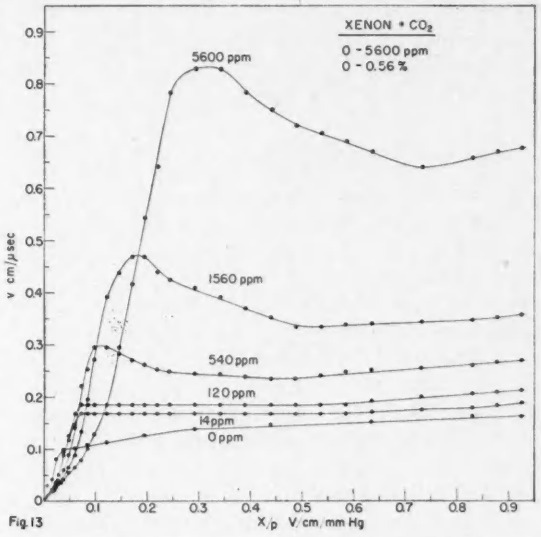

Fig. 13

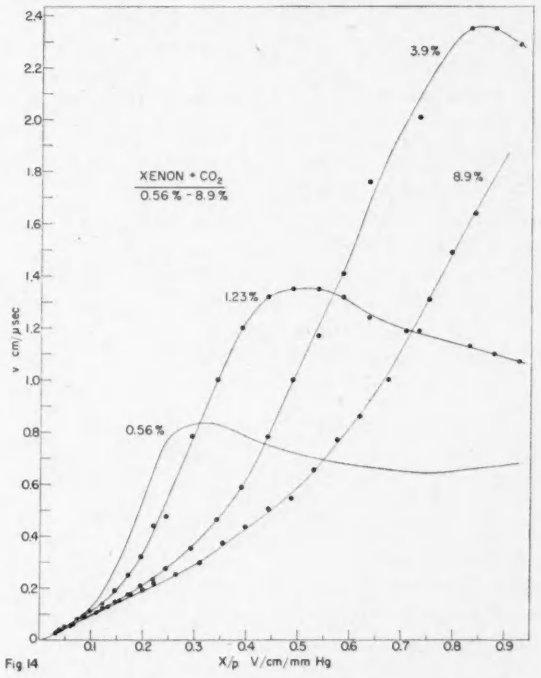

Fig. 14

FIGS. 13 and 14. Drift velocity of electrons in xenon + carbon dioxide mixtures.

Argon Plus Methane

The low electron loss and extremely high drift velocity found in methane suggested its use for "moderating" the electrons in argon. A series of 10 curves ranging from 66 parts per million to 85% methane in argon is shown in Figs. 11 and 12.

Xenon and Xenon Plus Carbon Dioxide

Xenon is of practical importance because of its high particle stopping power and high absorption coefficient for X-rays. It is also of interest because it shows a variation of mean free path with electron energy rather similar to argon (see for example Reference 3). The "spectroscopically pure" gas used was obtained from Linde in pyrex flasks. Chamber pressure was 550 mm. mercury. It was found that the xenon curves varied with time, the maximum drift velocity (at $X/p = 0.15$) increasing from 0.16 to 0.42 cm./μsec. in 24 hr. It returned to closely the same curve when the gas was frozen out by liquid nitrogen and pumped. This was checked several times. Once a fraction of a per cent of carbon dioxide had been added the variation with time disappeared.

Since only one filling of xenon was available, the procedure for adding carbon dioxide was to freeze out first the previous filling, then the added carbon dioxide, into a cold trap in liquid nitrogen. Subsequent evaporation appeared to provide adequate mixing, for no variation of the gas properties with time could be found. Drift velocity curves for xenon plus carbon dioxide up to 8.9% carbon dioxide are given in Figs. 13 and 14. The mixtures are slow compared to argon mixtures, and are harder to saturate, but in some applications this may be more than compensated by the lower pressure required for a given stopping power.

Neon and Neon Plus Carbon Dioxide

Neon has found considerable application as a counting gas since it gives electron multiplication at low X/p. It is generally inferior to argon for ionization chamber work, because of its lower electron drift velocity, and particularly because of its low breakdown potential. In fact all the drift velocity curves obtained here were terminated by breakdown. Neon appears to have a peak in the mean free path/electron energy curve when the kinetic theory value for zero field is taken into account, but this peak is less pronounced than in argon.

Since only a limited amount of neon was available, the one filling was retained, and the gas was mixed after addition of carbon dioxide by convection circulation through a heated side tube. Drift velocity curves for neon, and for neon + carbon dioxide mixtures are given in Figs. 15 and 16.

Argon Plus Nitrogen

The nitrogen used was Matheson "pre purified" grade—nominally 99.9%. Argon nitrogen mixtures have been rather thoroughly investigated (5, 9, 10). It was thought advisable to see whether the present method gave results in agreement with previous work. Drift velocity curves are shown in Figs. 17 and 18, and results are compared in Fig. 19. When the transit time correction

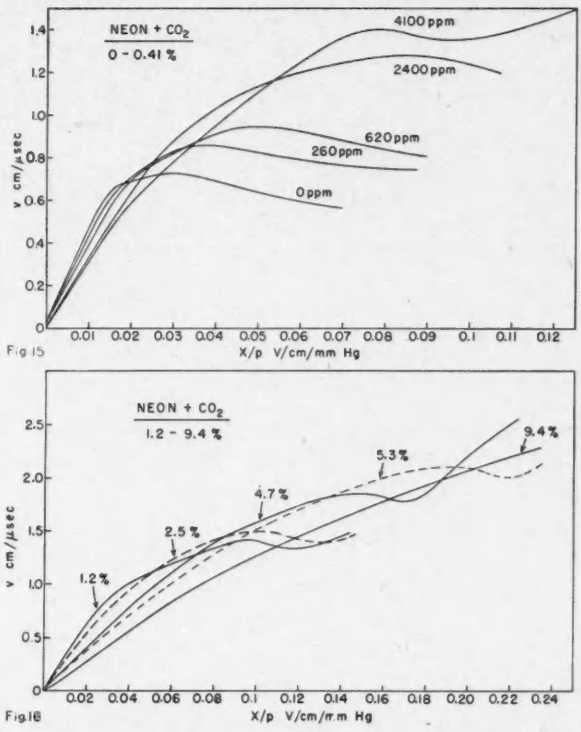

FIGS. 15 and 16. Drift velocity of electrons in neon + carbon dioxide mixtures.

has been applied (Appendix I) agreement with Klema and Allen (10) is within the accuracy of the present measurements, for nitrogen concentrations of 1% or greater. For such concentrations Klema and Allen's results are in satisfactory agreement with the later studies of Colli and Facchini (5) and Kirshner and Toffolo (9).

Krypton, Krypton Plus Carbon Dioxide, and Krypton Plus Methane

Krypton has been used extensively in proportional counters for X-ray work. The procedure used in the present work was the same as that described for neon. The "spectroscopically pure"* krypton gas was obtained from Linde in a cylinder; carbon dioxide (bone-dry grade, 99.956%) and methane (C.P. grade, 99.0%) were from Matheson cylinders. A complete series on carbon dioxide mixtures was done first, then a series on methane mixtures with a new krypton filling. The two curves on straight krypton differed slightly, so that curves from the two series should not be compared quantitatively where less

* *Analysis of Kr "spec. pure" $O_2 < 5$ p.p.m.; $H_2 < 5$ p.p.m.; $N_2 < 500$ p.p.m.; $Xe < 1\%$; $H_2O < 3$ p.p.m.: slight trace of other gases.*

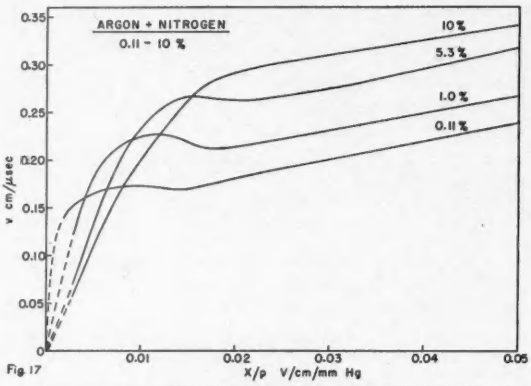

Fig. 17

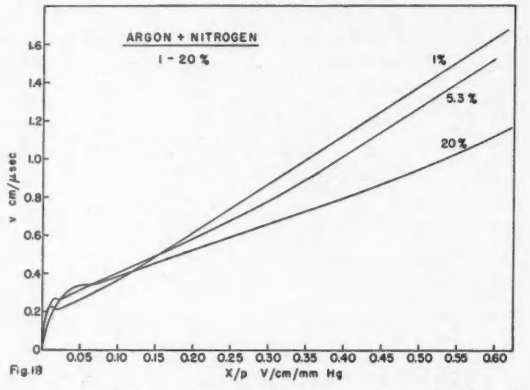

Fig. 18

FIGS. 17 and 18. Drift velocity of electrons in argon + nitrogen mixtures.

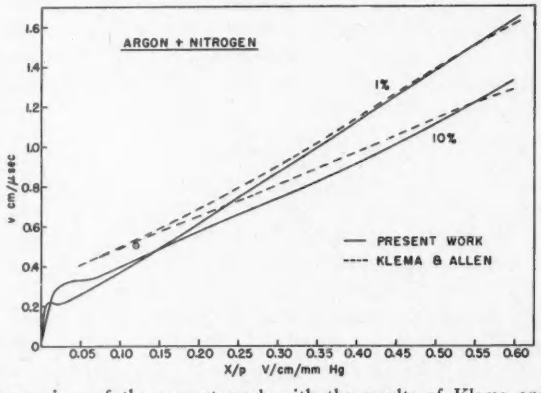

FIG. 19. Comparison of the present work with the results of Klema and Allen. The point ⊙ indicates the position of the present curves after the transit time correction has been applied.

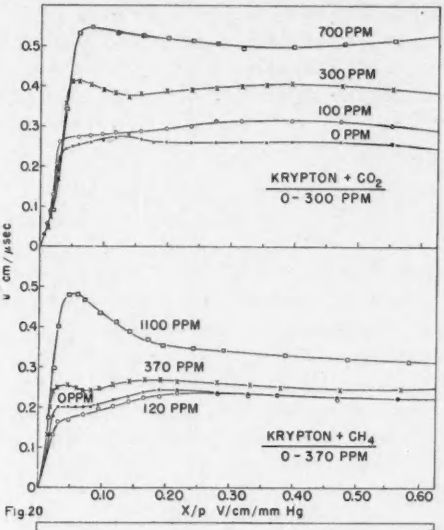

Fig. 20

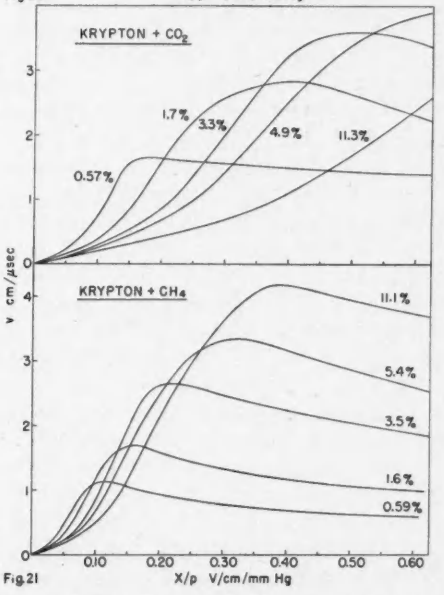

Fig. 21

FIGS. 20 and 21. Electron drift velocities in krypton + carbon dioxide mixtures and krypton + methane mixtures.

than about 400 parts per million of carbon dioxide or methane was added. These curves are shown in Fig. 20. The somewhat poor reproducibility of the two tank krypton runs is typical of the behavior of the noble gases mentioned

earlier. By repeated baking, soaking, and pumping, much better reproducibility could be achieved, as was done with argon. This would not mean that the gas was pure—merely that the amount of polyatomic impurity did not change with time. Curves for higher percentages of carbon dioxide and methane are shown in Figs. 20 and 21, and these may be strictly intercompared.

Saturation Characteristics

The variation of pulse amplitude with X/p is as important as the drift velocity curve from a practical viewpoint. However the saturation characteristic is in general much more sensitive to gas purity. Loss of pulse amplitude is due to columnar recombination and to the attachment of electrons to form negative ions, which, being relatively very slow, are lost to the pulse in a "fast" electron collecting system such as the present one.

The attachment probability changes with electron energy, thus the preferential removal of electrons of a certain energy might be expected to produce a change in the energy distribution. This effect however will be negligibly small, even with extreme electron loss, since the redistribution of energy between the remaining electrons is a very rapid process compared with the lifetime of even the most readily attached electrons.*

Thus the drift velocity measurements have not been invalidated by the presence of electron capturing impurities. Of course these impurities will affect the energy distribution, and alter the drift velocity, in a noble gas, but only because they provide inelastic collisions, not because of their attachment properties. Where an additional moderator is present in appreciable quantity their effect is negligible.

The saturation curves obtained in the present work were doubtless significantly influenced by small quantities of impurities, such as oxygen and water vapor, and are not characteristic of the gases investigated in a truly pure state. However they are of interest as showing what can be readily achieved in a metal system using commercial tank gases without any purification other than, in some cases, freezing in liquid nitrogen and pumping.

To save space the saturation characteristics have been condensed in Fig. 22 which shows the field required to achieve saturation. With low concentrations of moderating gas the shape of the saturation curve is irregular, indicated by dotted lines in the figure, as increasing X/p first increases and then decreases the pulse amplitude. This, we believe, is due to electron attachment to impurities which have either a definite energy threshold (e.g. water vapor), or pronounced resonance (e.g. oxygen) at a fairly high energy. As the concentration of moderator is increased, the agitational velocity decreases, and such effects rapidly disappear, particularly as, at the same time, the drift velocity increases. An independent investigation of argon + carbon dioxide mixtures by one of

* *This can be seen as follows: the redistribution time, t_r say, will be of the order of or less than $(\lambda/u)\ (1/f)$ since in $(1/f)$ collisions an electron can suffer energy changes of the order of its mean energy. λ is the m.f.p. for collision, f the fractional energy loss per collision, and u the agitational velocity. The lifetime against attachment, t' say, will be $(1/h)\ (\lambda'/u)$ where h is the attachment probability, and λ' the m.f.p. for collision with the impurity causing attachment. Thus $(t_r/t') \leqslant (\lambda/f)/(\lambda'/h)$. Now $(f/\lambda) = (f'/\lambda') + (f_a/\lambda_a) + (f_c/\lambda_c)$. Where the subscripts a and c refer respectively to the main constituent (e.g. argon) and the moderating gas (if any), f' is the energy loss per collision in the impurity. Thus $(f/\lambda) > (f'/\lambda')$ and therefore $(t_r/t') < (h/f')$ which is always very small, e.g. $\leqslant 10^{-2}$ even at the resonance in oxygen.*

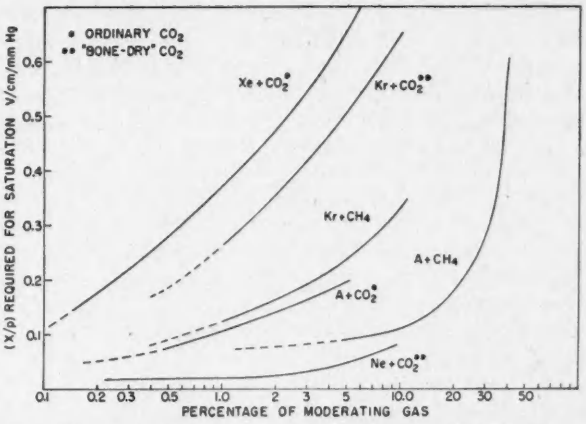

FIG. 22. Saturation properties of gas mixtures. The dotted portions indicate irregular values, believed due to attachment.

us (G. C. Hanna) at an earlier date showed that the high field of the grid-collector space (where X/p is 2.2 times that shown on the scale of Fig. 22) was responsible for the irregularity.

DISCUSSION

A. *Accuracy of Method*

Inaccuracies in the measurements arise mainly from two causes, errors in the estimation of rise times, and uncertainties in correcting for diffusion and grid-collector transit time.

The first is most serious at high drift velocities where short rise times (as short as 0.5 μsec.) are encountered. The reproducibility of observations was excellent but absolute errors of up to 10% at very high values of v may well be present. At lower values of v the accuracy is obviously better except in a few cases (notably carbon dioxide) where, at low X/p, the signal to noise ratio was poor owing to lack of saturation. This region is fortunately not of great practical interest.

It is difficult to know just what correction for diffusion should be applied, but it is certainly very small except for the undiluted noble gases, where the measurements are in any case vitiated by the presence of impurities.

The correction for grid-collector transit time is more serious. It has been computed in Appendix I on the assumption that the measured rise time includes the small portions of increasing and decreasing slope at the beginning and end of the pulse rise. Because it is necessary to set the oscilloscope triggering threshold above the amplifier noise level some at least of the initial part of the pulse will be missed. The correction will accordingly be an overestimate. It is considered that errors here will lie between 5 and 10%.

Summarizing—the over-all precision of the measurements is expected to be about 10%. At high drift velocities, particularly in the region of a resonance

in v where a rather large transit time correction is involved, the accuracy will be less. Where earlier data are available for comparison the agreement obtained is reassuring.

The great advantage of the method lies in the ease and rapidity with which the measurements can be made. This has made it feasible to study a wider range of gas mixtures than has been done before.

B. *The Effect of Molecular Additives on the Behavior of Noble Gases*

The gas mixtures that have been chosen for study are those useful in ionization chambers and counters, where, because of its good saturation characteristics and/or high atomic number, a noble gas forms the main constituent. Various molecular gases have been used as additives. The added gas, with its low lying molecular energy levels, serves to decrease the velocity of agitation of the electrons.

On a simple model the drift velocity will be proportional to the electric field acting on the electron, and to the time between collisions during which it acts, i.e.

$$v = \text{const } (\lambda/u)\ (X/p)$$

where λ/p = electron mean free path at the pressure p,

u = electron velocity of agitation,

X = electric field strength,

v = electron drift velocity.

The molecular gas serves to decrease u. This will in itself increase v, and in addition, the noble gases, argon, krypton, and xenon, and to a lesser extent neon, show electron free paths which *increase* as the electron velocity is decreased, which greatly enhances the effect. Thus the extreme sensitivity of electron drift velocity, in the pure noble gases, to contamination by molecular gas impurities is easily understood.

Klema and Allen (10) had explained the marked difference between their drift velocity results and the earlier results of Nielsen (13) and others as due to the superior purification achieved by passing their gas continuously over hot calcium. In the present work no purification of the "tank" noble gases was attempted, other than, in some cases, freezing out in liquid nitrogen. This was partly because adequate purification is very difficult, but mainly because the object of the work was to study gas mixtures under the conditions obtaining in careful ionization chamber work. Thus the values found for electron drift velocities in the samples of noble gases alone are dependent on the particular conditions of the experiment, as is clearly shown in Figs. 4 and 5. Once a fraction of a per cent of a molecular gas has been added, however, the effect of the original impurities is negligible.

It is interesting to note that the present results on unpurified tank argon (Fig. 6) are close to those of Klema and Allen, which would suggest that these workers did not in fact have pure gas. This suggestion has been confirmed recently by Kirshner and Toffolo (9) and Colli and Facchini (5) who obtained results in pure argon in good agreement with those of Nielsen.

An interesting feature of the present curves for noble gas mixtures is the sharp peak in the drift velocity which occurs at low X/p for "tank" gas, and for small percentage of additives, and which moves up in X/p as the amount of molecular moderating gas is increased. Two possible explanations of this peak have been considered.

At an early stage it was thought that it might be due to the excitation of a low-lying energy level, or close group of levels, in the moderating gas. Two difficulties arise: first, that higher energy levels would be expected to give similar peaks at higher values of (X/p), whereas only one peak has been observed. Second, the transition from tank argon to the curves with small amounts of carbon dioxide and methane is so smooth that this same molecular level (or a very similar one) would have to be involved. This is also true for neon, krypton, and xenon.

It is more tempting to associate this peak with the "Ramsauer effect", the maximum in free path observed in these gases for electrons of low energies. Unfortunately our identification of the drift velocity peak with the Ramsauer maximum cannot be made complete, because we have no data on the mean agitational velocity of electrons in any of the noble gases below about $X/p = 0.1$. The values for higher X/p have been derived by the Townsend diffusion method which is discussed below. Furthermore the electron free path determined by Ramsauer and others is for monoenergetic electrons suffering a rather small change in direction. We are concerned with the mean free path for large momentum changes for a distribution of electron energies which is known to be non-Maxwellian (11, p. 201).

The bulk of the data which we have on the behavior of electrons moving in collision equilibrium in a gas has been obtained by the diffusion methods introduced by Townsend some 30 years ago, and developed by Townsend, Bailey, and their co-workers. This work has been summarized by Healey and Reed (7). The basic assumptions of the diffusion treatment are that the distribution of electron agitational velocities is Maxwellian* and that the electrons are in collision equilibrium with the gas molecules so that the mean electron energy is some constant times the energy of agitation of the gas molecules. The value of this constant depends on X/p and on the gas being studied. The treatment considers only the average velocity of agitation, and assumes an average energy loss per collision and mean free path that are essentially constant over the range of electron energies involved at a given X/p.

This treatment is evidently an approximate one. Because of the mathematical complexity of more exact models it has been used extensively, and can yield useful results. An example is given in Appendix II where the properties of argon + carbon dioxide mixtures are calculated from data on argon and on carbon dioxide.

The results of Appendix II suggest strongly that the observed peak in the drift velocity is a direct consequence of the Ramsauer maximum, but, although the rest of the discussion is based on this hypothesis, it must be admitted

* *The effect of other distributions on the numerical values of the parameters deduced from the experimental data is discussed, to some extent, by Healey and Reed (7, p. 70).*

that conclusive proof is lacking. In deciding between this and the alternative hypothesis of resonant energy loss in the moderating gas, the crucial experiment would be to examine the drift velocity in very pure argon (and neon, krypton, and xenon) in the very low (X/p) range (< 0.05 v./cm./mm. mercury) for the presence of a peak or at least a "step". This was not possible in the present apparatus since adequate purification could not be achieved. There is a slight indication of such a feature in the curves of Nielsen and of Colli and Facchini for purified argon, but unfortunately they do not give any detail below $(X/p) = 0.1$.

C. *Difference between Carbon Dioxide and Methane*

It is instructive to compare the effects of the two different moderating gases methane and carbon dioxide on the noble gases neon, argon, krypton, and xenon.*

We will examine three characteristics of the drift velocity peak, which we have attributed to the Ramsauer maximum.

(i) The magnitude of the drift velocity at the peak. Since v is (at least roughly) proportional to (λ/u) (X/p) we may use the value of $v/(X/p)$ at the peak as a measure of the effective value of (λ/u), the time between collisions at unit pressure (averaged over the spread of electron energies involved).

(ii) The width of the drift velocity peak. For relatively low concentrations of moderating gas this width will be determined by the width of the Ramsauer maximum, or by the width of the electron energy distribution, whichever is the greater.

(iii) The value of (X/p) at which the peak occurs. An increase in the concentration of the molecular gas slows the electrons down and requires an increase in (X/p) to speed them up again to optimum energy. The increase in (X/p) required is a measure of the moderating efficiency of the gas.

(i) Fig. 23 shows the variation of $(v/X/p)_{\text{peak}}$, the "peak mobility", as the amount of moderating gas is increased.

The most striking feature is that the peak mobility decreases with increasing carbon dioxide concentration, but remains constant for methane. This is not unexpected. The electron free path in methane is some five times as great as in carbon dioxide near the energy of the Ramsauer maximum of argon (Ramsauer and Kollath, Brüche (3)). Thus the value of λ in the mixture will be larger in argon + methane than in argon + carbon dioxide and less dependent on the concentration of moderating gas. Since the values of u involved will be somewhat similar in the two cases, the peak mobility, which is a measure of the effective value of (λ/u), will also be larger and more constant for argon + methane. This behavior is also characteristic of krypton + methane and krypton + carbon dioxide mixtures. That the relative decrease in peak mobility in krypton + carbon dioxide is less pronounced than in argon + carbon dioxide is no doubt due to the maximum electron free path in krypton

* *This was not in mind when the measurements were made and the series is therefore not entirely complete.*

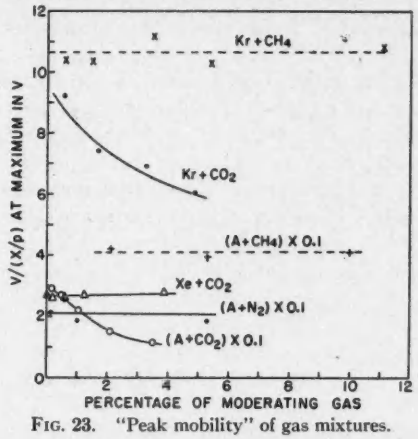

FIG. 23. "Peak mobility" of gas mixtures.

being considerably smaller than in argon, and at higher energy, where the electron free path in carbon dioxide is larger.

In xenon + carbon dioxide mixtures the peak mobility remains essentially constant, the electron free path in xenon being still smaller and that in carbon dioxide still greater.

The behavior of argon + nitrogen mixtures is anomalous: nitrogen has an electron free path similar to carbon dioxide and would therefore be expected to produce similar effects. In fact the peak mobility in argon + nitrogen appears to be independent of nitrogen concentration; however the few points available are rather scattered.

At very low concentrations the effective mean free path of the gas mixture will be that of the pure noble gas, for the particular electron energy distribution conferred by the moderating gas. The peak mobility would therefore be expected to be independent of the moderator (at low concentrations) if *either* the different moderators produced the same electron energy distribution *or* the spread in electron energies were, for either moderator, less than the width of the Ramsauer maximum. We would hardly expect the former condition to be fulfilled since the variation of electron free path with energy is very different in carbon dioxide and methane, and thus the width of the Ramsauer maximum relative to the spread in electron energies must be the determining factor.

The Ramsauer maximum in argon is considerably narrower than in krypton. It would therefore not be surprising if there were a difference between the peak mobility in argon + methane and argon + carbon dioxide but not in krypton + methane and krypton + carbon dioxide at low concentrations. Fig. 23 appears to give a higher value for argon + methane which suggests that methane produces a narrower electron energy distribution than carbon dioxide. However, an examination of the data on argon + carbon dioxide and argon + methane at concentrations of 50 p.p.m. or less does not show this difference and it may not be real.

(ii) A rough comparison of the percentage widths of the drift velocity peaks in argon + carbon dioxide and argon + methane has been made at 10% down from the peaks. The methane peaks are always narrower than the carbon dioxide peaks, which is consistent with the narrower electron energy distribution suggested above. They increase in width very little with increased methane concentration, whereas the carbon dioxide peaks broaden rapidly. This may be due to a progressive broadening of the electron energy distribution with increasing carbon dioxide concentration, but would also be explained by the greater "flattening" by the shorter electron free path of carbon dioxide. For krypton mixtures the data with carbon dioxide are inadequate. The behavior of krypton + methane is curious in that the peak width increases with increasing methane concentration more rapidly than argon + methane. We would expect that the smaller free path and broader resonance in krypton would make the peak width less sensitive to the properties of the moderating gas.

(iii) In Fig. 24 the value of X/p at the peak is plotted against the percentage of moderating gas. It is apparent that there are two sequences of increasing (X/p) for a given percentage; neon, argon, krypton, xenon and (nitrogen), methane, carbon dioxide, and that the curves increase in steepness in the same order.

Assuming that the drift velocity peak occurs at a value of u close to that of the Ramsauer maximum, and that the mean free path of the mixture is determined at least mainly by the noble gas, the increase of $(X/p)_{peak}$ in the first sequence (neon–xenon) receives a natural explanation. The Ramsauer

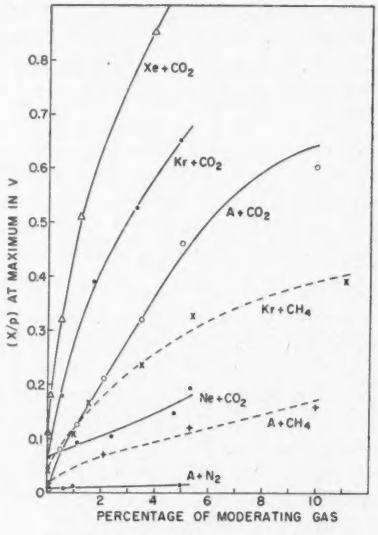

FIG. 24. "Moderating efficiency."

maxima occur at higher values of u and involve smaller values of λ in moving up the series neon, argon, krypton, xenon. Thus more speeding up of the electrons is required (increase in u), which is inherently more difficult (decrease in λ). The value of $(X/p)_{peak}$ must therefore increase.

As the collisions with the moderating gas become more frequent and more inelastic a larger value of (X/p) will be required to speed the electrons up to the optimum velocity u. Thus $(X/p)_{peak}$ is expected to increase as (f/λ) for the moderator increases, where f is the fractional energy loss per collision. This ratio is certainly higher for carbon dioxide than for nitrogen, and, while no data are available for energy loss in methane, the much larger value of mean free path suggests that in this case (f/λ) may well have an intermediate value. A semiquantitative treatment of the behavior of $(X/p)_{peak}$ in argon + carbon dioxide is given in Appendix II.

D. *Comparison with Molecular Energy Levels*

At an early stage in the experiments it was hoped to relate the difference in moderating action between methane and carbon dioxide to some significant feature of the molecular energy levels of these gases. These levels are shown in Fig. 25 with λ/u plotted on the same energy scale. It is apparent that the

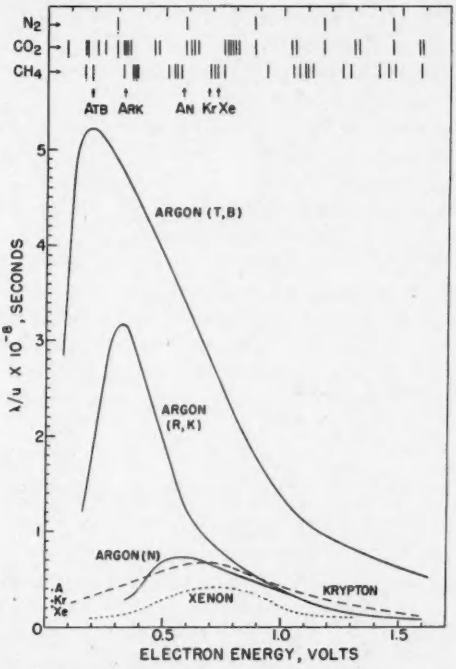

FIG. 25. Molecular energy levels and λ/u. T.B. = Townsend and Bailey, R.K. = Ramsauer and Kollath, N = Normand. The kinetic theory values for zero applied field are indicated in the lower left-hand corner.

uncertainty in the location of λ/u maximum is such that no detailed comparison with any specific energy levels can be made. Neither does any obvious relation emerge from an over-all examination of the level schemes.* On the other hand, the present measurements were confined to a few gases of interest in ionization chamber work. It is certain that a much more searching experiment could be devised which might well yield new information on the behavior of the electron energy distributions, or on the molecular levels, or both. One point of considerable interest would be to examine critically the areas of agreement and disagreement of the Townsend diffusion treatment with the results obtained.

E. *Behavior of Methane*

The behavior of methane as an ionization chamber gas deserves a few final words. It is very fast indeed and with suitable purification not difficult to saturate.

The drift velocity obtained in this work is in radical disagreement with the semiempirical formula published by Snyder (16)

$$v = (0.75(X/p) + 1.5)\text{cm.}/\mu\text{sec.}$$

Beghian and Halban (1) have used this formula to calculate the collection time in a cylindrical high pressure methane chamber. They obtain a value of 0.7 μsec. using Snyder's formula, and a measured collection time of 1.0 μsec. Using the present experimental v values, the calculated collection time is 0.84 μsec. The disagreement with Snyder's formula would be much worse but for the fact that the X/p range in their chamber is nearly centered about the point where the two v curves cross (at an angle of about 45°).

As a moderating gas methane has an advantage over the more usual carbon dioxide of giving remarkably high drift velocities at low values of X/p. Mixtures with less than 35% methane are readily saturated, and doubtless this percentage could be increased by greater care with gas purity. The fast drift velocity observed for methane and its mixtures appears to be associated with the long mean free path in this gas at the critical electron energy. As pointed out by Brode (3) this is a result of the symmetrical structure of the methane molecule which gives it an electronic configuration similar to that of a noble gas.

ACKNOWLEDGMENTS

The writers are indebted to Dr. L. G. Elliott and to Professor L. B. Loeb of the University of California for helpful criticism. They are grateful to Mr. O. W. Schwer whose indefatigable assistance in the construction and operation of the apparatus, and in the processing of the results, made the work possible.

* *It should be pointed out that the maximum drift velocity corresponds to the maximum in* (λ/u) (X/p), *which, since u increases with* (X/p), *is at higher energy than the maximum in* (λ/u). *Thus more levels are involved than the comparison with* (λ/u) *would suggest.*

APPENDIX I—CORRECTIONS TO THE SIMPLE FORMULA FOR DRIFT VELOCITY

A. *Diffusion Correction*

There is a well-known relation between diffusion and mobility, which is independent of any kinetic theory assumptions (11, p. 179). For electrons it is

$$k/D = Ne/\eta P$$

where $k = (v/X)$ = mobility in cm.^{2}/volt-sec.,

D = coefficient of diffusion,

P = pressure in dynes/cm.^{2} at N.T.P.,

N = number of molecules/cm.^{3} at N.T.P.,

e = electronic charge,

η = ratio of energy of agitation of free electrons to energy of agitation of gas molecules.

Numerically

$$D = 0.0235\eta(v/X).$$

Einstein's classical analysis of Brownian movement (11, p. 174) gives a gaussian distribution for the distance diffused by a particle in a given time, with the average distance equal to $\sqrt{4Dt/\pi}$.

Substituting for D and putting $t = L/v$,

$$\bar{x} = \sqrt{\frac{4 \times 0.0235}{\pi}} \sqrt{\frac{L\eta}{X}}$$

is the average distance diffused in crossing a gap L in a field X. $\bar{x}$ is independent of the drift velocity v, but depends on $\sqrt{\eta}$, the ratio of electron agitational velocity to molecular agitational velocity. The diffusion seriously affects only the end of the electron pulse in the experimental arrangement adopted since the other end of the electron track has to cross only a small gap. The actual value of L was 6.4 cm.

The parameter η has been measured for many gases by the diffusion methods introduced by Townsend, and the results have been summarized by Healey and Reed (7). From these data $\bar{x}$ can be calculated (for the appropriate L) as a function of X/p and compared with R, the range of the α-particle (4.75 cm.). $(\bar{x}/R)$ will be a measure of the fractional change in pulse rise time due to diffusion.

Argon

X/p	η	$\bar{x}$ (cm.)	$(\bar{x}/R)$, %
0.1	85	0.46	9.7
0.2	120	0.35	8.4
0.71	240	0.30	6.2

As X/p increases in this range $\bar{x}$ decreases steadily. Since the correction is less than 10%, it has been omitted to simplify reduction of data. Below $X/p = 0.1$

there is no information, except that $\eta = 1$ at $X/p = 0$. The electron mean free path shows a rather sharp maximum in this range, so that interpolation for η is unjustifiable. We can only say that the diffusion error is unknown, and may be large.

Neon

X/p	η	$\bar{x}$ (cm.)	$(\bar{x}/R)$, %
0.06	23.5	0.31	6.5
0.1	34.5	0.295	6.2
0.6	158	0.082	1.7

Thus the diffusion error is not over 6.5%.

Xenon

We have no data on η. Since the variation of electron mean free path with energy is similar to that in argon, and since the first excitation potential is considerably lower (8.3 compared to 11.6 volts) we might hope that η, and the effect of diffusion, would be less than in argon.

Krypton

For similar reasons the effect is again expected to be less than in argon.

Hydrogen, Nitrogen, Carbon Dioxide, Methane, etc.

Because of the low-lying molecular energy levels, η is much less and the diffusion correction is negligible.

Mixtures of Monatomic and Diatomic or Polyatomic Gases

The low-lying molecular levels will again be effective. Presumably any effect on the observed drift velocity will be due to reduced agitational velocity, so that the diffusion correction can be neglected in mixtures where an appreciable change in v is observed.

B. *Grid-collector Transit Time Correction*

The voltage of the collector will start to rise, rather slowly at first, as the first electrons pass through the grid into the grid-collector region. The rate of rise of voltage continues to increase until the most densely ionized section of the α-particle track reaches a point about halfway between grid and collector. It then falls with decreasing ionization density until the last electron passes through the grid, at which instant it falls rapidly to zero as the last electron reaches the collector.

The whole process takes a time t equal to the difference in times between the first electron reaching the grid and the last electron reaching the collector. Clearly $t = R/v + d/v_1$, where v and v_1 are the drift velocities in the cathode-grid and grid-collector fields respectively, R is the α-particle range (unless $R > D$, the cathode-grid spacing, in which case R must be replaced by D), and d is the grid-collector spacing.

We have given curves of $v' = R/t = R/(R/v + d/v_1)$. Therefore $v = v'[1 - (dv')/(Rv_1)]^{-1}$.

In actual practice the difference between v and v' will depend somewhat on the criterion used for full pulse amplitude, on the bias level for triggering the oscilloscope, and on the finite differentiating time constant. In general the correction will be somewhat less than given by this equation.

To calculate the correction we need to know v_1, the drift velocity in the grid-collector field, which in our case is 2.2 times the cathode-grid field. It is generally sufficiently accurate to use for v_1 the value of v' at the (2.2 times) greater X/p, which is obtainable directly from the curves. The value of $d/R = 1.45/4.75 = 0.30$.

To give an idea of the error involved we consider two simple cases

(i) $v = \text{const.} \times (X/p)$,

therefore $v_1 = 2.2\, v$,

whence $v = 1.12\, v'$, a correction of 12%;

(ii) $v = \text{constant, i.e. } v_1 = v$,

whence $v = 1.23\, v'$, a correction of 23%.

In cases where the drift velocity decreases with X/p, the correction will be still larger.

It has not been feasible to apply the transit time correction to the considerable number of curves in this paper. In view of the large variation in behavior from one gas mixture to another, the usefulness of the curves for selecting an appropriate filling for an ionization chamber, and for calculating the collection time, is not seriously impaired. If more accurate values of the drift velocity are needed, the correction for grid-collector transit time can be applied by a straightforward step-by-step process.

APPENDIX II—THE BEHAVIOR OF MIXTURES OF ARGON AND CARBON DIOXIDE

It was suggested in the "Discussion" that the present experimental results could be interpreted on the hypothesis that the peak in the drift velocity v at low (X/p) is associated with the maximum in the electron free path characteristic of the noble gases at low electron energy, the Ramsauer effect.

This hypothesis can only be justified if we can show that the value of (X/p) giving the drift velocity peak does in fact produce electron energies that lie in the region of the Ramsauer maximum. Direct experimental data are not available, but the average electron energy can be calculated as a function of (X/p)—though only approximately—if the behavior of the constituents separately is known. Argon and carbon dioxide have been studied in the appropriate energy range by the diffusion methods of Townsend.

It has been pointed out above that the available data are not really adequate for our purpose. Only an *average* value for the electron agitational velocity is available, without information on the distribution of velocities. This average value of u, and the numerical values of λ (the mean free path) and f (the fractional energy loss per collision) are derived from the experimental diffusion data on the assumption that neither λ nor f vary appreciably over the range of electron velocities involved at any given (X/p). This assumption is clearly

not justified in the region of the Ramsauer maximum in argon. The spread of electron velocities, it may be mentioned, is probably responsible for the fact that Townsend and Bailey's diffusion experiments on λ in argon give a considerably broader maximum than Ramsauer and Kollath's data using monoenergetic electrons. (See Fig. 25.) Clearly Townsend and Bailey's data will be more appropriate for our present purpose, though they will still not be really applicable unless the electron energy distribution is the same in our system (argon + carbon dioxide) as it was in theirs. Now Townsend and Bailey's data are derived from the study of a mixture of argon + hydrogen, using the known properties of hydrogen. They were, in fact, forced to assume that the electron energy distribution is the same in argon + hydrogen as in hydrogen. In using their data we extend this assumption to include argon + carbon dioxide and carbon dioxide.

This is not a very satisfatory foundation, though various arguments have been put forward (7, p. 75) in favor of the conclusion that the distribution does not vary markedly from one gas to another. However, lacking any more promising line of attack, it seems worth while to pursue this one in the hope that, although considerable quantitative errors may arise, it will provide a definite indication of whether or not the Ramsauer maximum is involved. It turns out that the predicted behavior of argon + carbon dioxide is in surprisingly good agreement with experiment.

The behavior of the mixture is calculated in the following way. If λ is the mean free path measured at a pressure of 1 mm. mercury and f is the average fractional energy loss per collision, and the subscripts a, c, and m denote respectively argon, carbon dioxide, and the mixture; then for a system containing a fraction F of carbon dioxide we may write

$$1/\lambda_m = (1 - F)/\lambda_a + F/\lambda_c, \tag{1}$$

$$f_m/\lambda_m = (1 - F)f_a/\lambda_a + Ff_c/\lambda_c. \tag{2}$$

At a particular value of (X/p) in the mixture the electrons will have an agitational velocity u and a drift velocity v where

$$v = 0.815\ (e/m)\ (X/p)\ (\lambda_m/u), \tag{3}$$

$$v^2 = 0.407\ f_m\ u^2. \tag{4}$$

Equations [3] and [4] are the standard equations of Townsend diffusion theory; their derivation, including the values of numerical constants which depend on the energy distribution, is given by Townsend (17, p. 50). Equation [3] merely expresses quantitatively the fact that the drift velocity is proportional to (field strength) $\times$ (time between collisions). Equation [4] may be justified as follows: in going a distance d in the direction of the field, which takes a time d/v, during which the electron makes $(up/\lambda)\ (d/v)$ collisions, the field does work (Xed). This must equal the energy communicated to the gas molecules, which is $f\ m\ u^2/2$ per collision. Whence

$$(Xed) = (up/\lambda)\ (d/v)\ f\ m\ u^2/2,$$

which, using equation [3] to eliminate (X/p), gives equation [4].

Rewriting equations [3] and [4] and substituting numerical values we have

[3a] $$(X/p) = 6.97 \times 10^{-16}\, uv/\lambda_m$$

[4a] and $$v = 0.637\, u(f_m)^{1/2}.$$

Substitution from [4a] gives

[5] $$(X/p) = 4.44 \times 10^{-16}\, u^2(f_m)^{1/2}(\lambda_m)^{-1}.$$

$\lambda_a, \lambda_c, f_a$, and f_c are known as functions of u, and thus, for a given u, λ_m and f_m are available, from equations [1] and [2], for substitution into equations [5] and [4a] to give (X/p) and v corresponding to this value of u. Choosing successively increasing values of u, the over-all result is the calculation of u and v as functions of (X/p).

It may be noted that for all but the very smallest values of $F(\leqslant 10^{-5})$, $f_a/\lambda_a \ll F f_c/\lambda_c$ and equation [2] reduces to

[2a] $$f_m = F f_c \lambda_m/\lambda_c\,.$$

A detailed computation of the particular case $F = 1.6 \times 10^{-3}$ has been made and is summarized in Table I. Fig. 26 shows a plot of v against X/p, and

TABLE I

$u \times 10^{-7}$ (cm./sec.)	E (e.v.)	λ_a* (cm.)	λ_c** (cm.)	λ_m (cm.)	f_c/λ_c** (cm.$^{-1}$)	$f_m \times 10^4$	$v \times 10^{-6}$ (cm./sec.)	X/p (v./cm./mm. Hg)
2	0.11	0.9	0.01	0.79	4.0	50.5	0.90	0.017
3	0.25	1.45	0.021	1.30	2.9	60.3	1.48	0.0238
4	0.45	1.6	0.031	1.48	2.1	49.5	1.79	0.0336
5	0.70	1.2	0.040	1.14	1.5	27.5	1.67	0.0507
6	1.01	0.75	0.047	0.73	1.2	14.0	1.44	0.0813
7	1.37	0.40	0.054	0.40	1.0	6.4	1.13	0.137
8	1.79	0.30	0.058	0.30	0.9	4.3	1.05	0.195
9	2.25	0.22	0.059	0.22	0.9	3.2	1.02	0.290
10	2.80	0.18	0.057	0.18	0 9	2.6	1.02	0.390
7.9	1.74	0.30	0.059***	0.30	0.78***	3.74	0.97	0.177
9.9	2.74	0.18	0.0476	0.18	0.99	2.92	1.08	0.413
13.6	5.20	0.11	0.036_7	0.11	1.38	2.43	1.35	1.15

* *Data from Townsend and Bailey.*
** *From graph of Rudd's results.*
*** *Data of Skinker.*
} *Quoted in Healey and Reed* (7).

for comparison, the experimental curve, which has been corrected* for grid-collector transit time (see Appendix I). The agreement with experiment is surprisingly good, and suggests strongly that the peak in the drift velocity corresponds directly to the maximum in λ_a.

Mixtures with F less than 3.5×10^{-2} show a drift velocity peak. For these only the position and size of this peak have been calculated, assuming that for these fairly small concentrations it occurs at $u = 4 \times 10^7$ cm./sec. $= u_0$, say (as it does with $F = 1.6 \times 10^{-3}$),

where $$\lambda_a = 1.6 \text{ and } \lambda_c = 0.031.$$

Therefore $\lambda_m = \lambda_a/(1+F\lambda_a/\lambda_c) = 1.6/(1 + 52F)$ at $u = u_0$.

* *This correction may be an overestimate.*

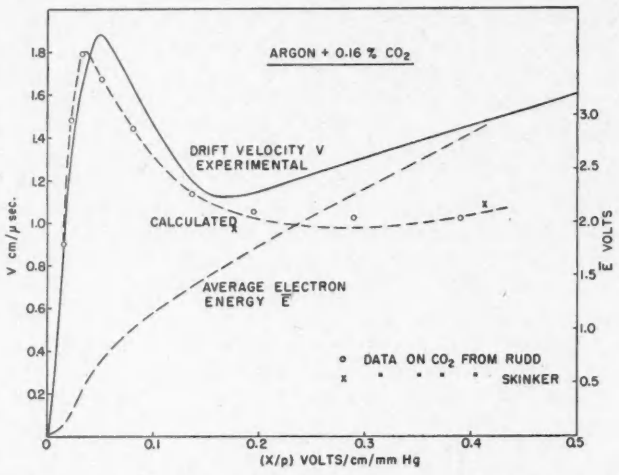

FIG. 26. Comparison of calculated drift velocity in argon + 0.16% carbon dioxide with experimental values corrected for grid-collector transit time.

Writing $\delta^2 = (1 + 52F)$ it is easily seen that our assumption of the peak being given by $u = u_0$ will be accurate only for δ nearly equal to unity, i.e. where the behavior of the mixture is controlled by the maximum in λ_a with negligible "flattening" by λ_c.

For $u = u_0$, $f_c = 0.065$ and equation [2a] becomes

$$f_m = F f_c \lambda_m / \lambda_c = 3.35\ F\delta^{-2}.$$

Substituting in equations [4a] and [5],

$$v \text{ peak} = (46.7/\delta)\ \sqrt{F} \text{ cm./}\mu\text{sec.}$$

$$(X/p) \text{ peak} = 0.812\ \delta\sqrt{F} \text{ volts/cm./mm. mercury.}$$

A comparison with corrected experimental data is given in Table II. Again

TABLE II

F	δ	v peak		(X/p) peak	
		Calc'd	Exptl.	Calc'd	Exptl.
8.0×10^{-6}	1.000	(0.13)	0.34	(0.0023)	~0.01
1.2×10^{-4}	1.003	0.51	0.72	0.0089	~0.015
4.75×10^{-4}	1.012	1.00	1.0_2	0.018	0.02
1.6×10^{-3}	1.041	1.80	1.8_3	0.034	0.045
5.3×10^{-3}	1.175	2.90	3.1	0.070	0.085
1.06×10^{-2}	1.246	3.8_5	3.8	0.103	0.12
2.1×10^{-2}	1.445	4.6_9	4.4	0.156	0.21
3.5×10^{-2}	1.679	5.3_2	4.9	0.260	0.32

agreement is good except for very small F where the simplification of equation [2] into equation [2a] is inadmissable. As F increases to give values of δ signifi-

cantly greater than unity the position of the drift velocity peak shifts, as expected, to higher X/p. With further increase in F the effect of λ_c becomes still more important and the peak is finally flattened out.

REFERENCES

1. BEGHIAN, L. E. and HALBAN, H. H. Proc. Phys. Soc. London, A, 62: 395. 1949.
2. BRADBURY, N. E. and NIELSEN, R. A. Phys. Rev. 49: 388. 1936.
3. BRODE, R. B. Revs. Modern Phys. 5: 527. 1933.
4. BUNEMANN, O., CRANSHAW, T. E., and HARVEY, J. A. Can. J. Research, A, 27: 191. 1949.
5. COLLI, L. and FACCHINI, U. Rev. Sci. Instruments, 23: 39. 1952.
6. ENGLISH, W. N. Rev. Sci. Instruments, 22: 598. 1951.
7. HEALEY, R. H. and REED, J. W. The behaviour of slow electrons in gases. The Wireless Press, Sydney, Australia. 1941.
8. HUDSON, DONALD E. MDDC. 524. 1946.
9. KIRSHNER, J. M. and TOFFOLO, D. S. J. Applied Phys. 23: 594. 1952.
10. KLEMA, E. D. and ALLEN, J. S. Phys. Rev. 77: 661. 1950.
11. LOEB, L. B. Fundamental processes of electrical discharge in gases. John Wiley & Sons, Inc., New York. 1939.
12. MOODY, N. F. and HOWELL, W. D. Chalk River Report IM-8. 1950.
13. NIELSEN, R. A. Phys. Rev. 50: 950. 1936.
14. ROSSI, B. B. and STAUB, H. H. Ionization chambers and counters. McGraw-Hill Book Company, Inc., New York. 1949.
15. SKINKER, M. F. Phil. Mag. 44: 994. 1922.
16. SNYDER, T. M. MDDC. 243. 1945.
17. TOWNSEND, J. S. Electrons in gases. Hutchinson & Co. Ltd., London. 1947.

THE $O^{16}(\gamma, n)O^{15}$ and $O^{18}(\gamma, p)N^{17}$ REACTIONS[1]

By R. Montalbetti[2] and L. Katz

ABSTRACT

The cross section for the $O^{16}(\gamma, n)O^{15}$ reaction has been determined by detecting the emitted neutrons, and the cross section for the $O^{18}(\gamma, p)N^{17}$ reaction has been determined by detecting the delayed neutrons following the decay of the N^{17} nucleus. Both cross sections exhibit a slowly rising portion for some 3 Mev. above threshold, followed by the usual large resonance shaped curve. This anomalous behavior is discussed in the light of present photonuclear theories.

INTRODUCTION

An investigation of the (γ, n) cross sections in N^{14} and O^{16} as measured by residual activity revealed that their shapes were different from the cross-section curves for the elements of higher atomic weight (5). The cross sections are characterized by an initial slowly rising portion followed by the usual resonance shaped curve, whereas those for such elements as copper and iron, for example, are characterized only by the resonance shaped curve. Previous work at Pennsylvania (9) had indicated that the (γ, p) reaction in O^{18} also exhibited an initial slowly rising portion. In order to establish definitely the above-mentioned anomaly in both the (γ, n) and (γ, p) reactions a re-examination of both cross sections was carried out in greater detail.

EXPERIMENTAL PROCEDURE

The $O^{16}(\gamma, n)O^{15}$ reaction has been previously studied in this laboratory by detecting the induced O^{15} activity (5). In the present experiment we detected the emitted neutrons which result from this reaction. This was accomplished by thermalizing these neutrons in a paraffin cylinder surrounding the sample and an enriched boron trifluoride counter. In order to effectively reduce the background due to electron pile-up at the instant of the γ-ray burst, the pulses from the BF_3 counter were gated. Only those pulses which occurred at least 20 μsec. after the γ-ray burst and not later than 1000 μsec. after this burst were registered. A complete description of this apparatus will be given in a separate publication.

The most convenient method for studying the (γ, p) reaction in O^{18} is to detect the delayed neutrons from the N^{17} nucleus. This was the method used by the Pennsylvania workers (9). The half-life of these delayed neutrons has been measured by Alvarez (1) and found to be to 4.14 sec. He also determined their mean energy as 1 Mev. In order to detect these neutrons, it was necessary to transfer an irradiated sample quickly to a neutron detector and since a boron trifluoride counter was also used in this experiment, it was necessary to thermalize them.

Ordinary water was used as the sample material. It was made to flow through a conical shaped cavity placed in the betatron beam where it was

[1] *Manuscript received February 27, 1953.*
Contribution from the Betatron Group, University of Saskatchewan, Saskatoon, Sask.
[2] *Present address: Radio Physics Lab., Defence Research Board, Ottawa.*

irradiated. The experimental arrangement is shown in Fig. 1. The irradiated water was conducted in $\frac{3}{8}$ in. copper tubing to the control room and made to spiral around the BF_3 counter. The delayed neutrons were thermalized in the paraffin surrounding this system.

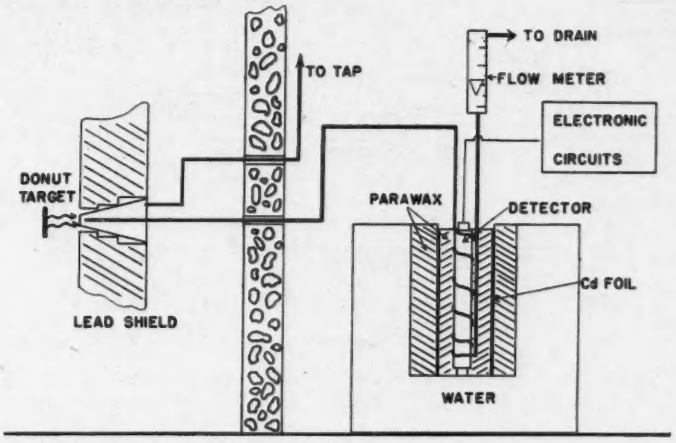

FIG. 1. Experimental arrangement used for detecting the delayed neutrons resulting from the $O^{18}(\gamma, p)N^{17} \xrightarrow[\beta^-]{} O^{17*} \rightarrow n + O^{16}$ reaction.

Many neutrons are ejected by the γ-ray bursts from the lead shield in front of the betatron and are scattered to form a large undesirable background. Fortunately this background is short lived and is almost completely gone 1000 μsec. after the γ-ray pulse. Neutron shielding and a gating circuit were used to minimize this background. (*a*) The BF_3 counting system was surrounded by a large tank of water, paraffin, and cadmium foil as indicated in Fig. 1. (*b*) Since the betatron operates at 180 c.p.s. giving 5500 μsec. between γ-ray bursts there is an essentially background-free period in the interval 2000–5000 μsec. following each γ-ray pulse; using a gating procedure, advantage was taken of this background-free period for counting. This gating procedure is illustrated at the bottom of Fig. 2. The circuits used in this experiment are shown in block diagram in this same figure. With these precautions the background counting rate was kept at about 1% of the delayed neutron counting rate.

The water flow was so adjusted that it remained some five seconds in the conical cavity during which time it was irradiated. It reached the BF_3 counter 3.8 sec. after leaving the cone and then spiralled around the counter for 4.2 sec. Before discharging, the water was caused to flow through a flow meter. Since we are only interested in the relative shape of the activation curve it was sufficient to hold the flow steady. Variations in the flow rate tend to cancel themselves when the counting rate is reduced to counts per unit mass of irradiated water per 100 r. of irradiation. This can be seen from an equation given in the Pennsylvania paper (9). It was also checked experimentally by us.

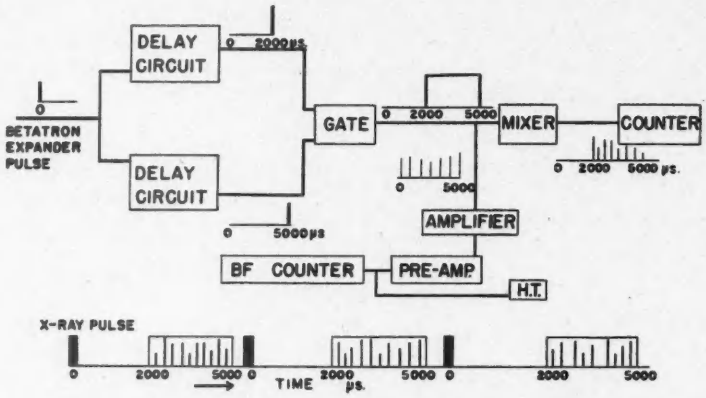

FIG. 2. Electronic circuitry used in the $O^{18}(\gamma, p)N^{17}$ experiment.

RESULTS

The activation curve for the $O^{16}(\gamma, n)O^{15}$ reaction is shown in Fig. 3 by the circles. This corresponds to the number of neutrons emitted per 100 r. of irradiation per mole of sample as the maximum energy of the bremsstrahlung beam from the betatron is varied. The activation curve obtained by the residual activity method is shown by the crosses on the same diagram. A

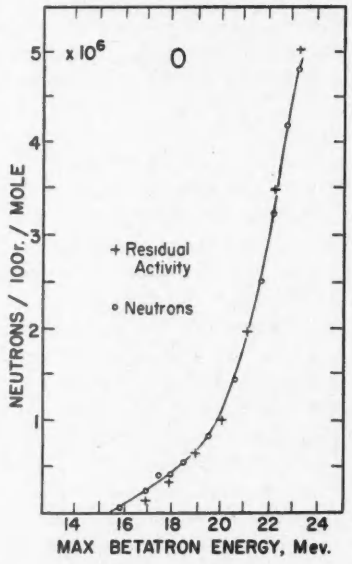

FIG. 3. Neutron yield curve for the $O^{16}(\gamma, n)O^{15}$ reaction: O neutrons detected directly, + measurements of the induced O^{15} activity.

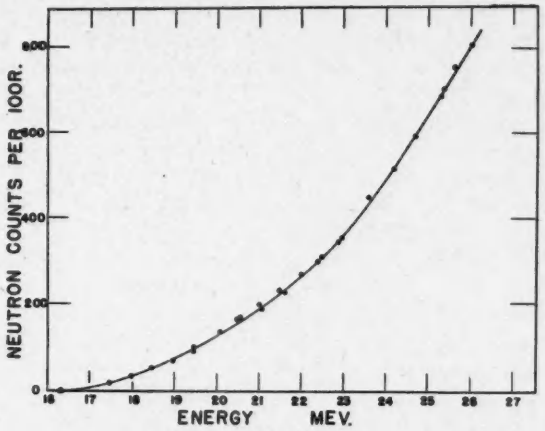

FIG. 4. Delayed neutron yield curve from the reaction $O^{18}(\gamma, p)N^{17}$.

description of the procedure used to normalize the neutron detector apparatus will be given in the forthcoming paper.

The activation curve for the delayed neutrons resulting from the $O^{18}(\gamma, p)N^{17}$ reaction is shown in Fig. 4. In this case the apparatus was not calibrated and the activation curve indicates only the relative yield per unit mass of O^{18} per roentgen. Considerable effort would have been required to obtain an absolute calibration of our apparatus. We felt this was not justified since our main interest was in the shape of the cross-section curve which did not require an absolute calibration.

Both activation curves were analyzed by the Photon Difference method (6) and the resulting cross-section curves are shown in Figs. 5 and 6.

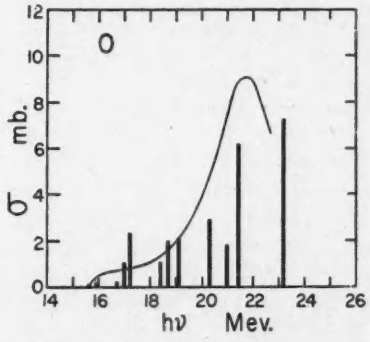

FIG. 5. Cross section for the $O^{16}(\gamma, n)O^{15}$ reaction. The vertical lines are placed at energies where a detailed study of the activation curve shown in Fig. 3 shows abrupt changes in slope. The magnitude of the change in slope or level strength is represented by the heights of the vertical lines.

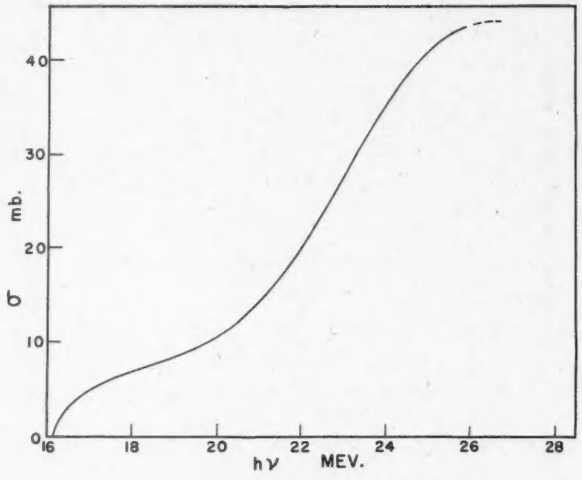

FIG. 6. Cross section for the $O^{18}(\gamma, p)N^{17}$ reaction.

DISCUSSION

The anomaly previously observed in the initial portion of the oxygen photoneutron cross-section curve is substantiated by the results of this experiment. Both curves show a portion rising slowly from approximately 3 Mev. above threshold. The curves then exhibit the usual peaked characteristics (named Giant Resonance by Peaslee) of other photonuclear reactions.

According to the statistical theory of nuclear reactions the process considered above may be represented by the following equation:

$$\sigma(\gamma, x) = \sigma_c(\gamma)G_c(x)$$

where

$\sigma(\gamma, x)$ = cross section for the (γ, x) reaction,
$\sigma_c(\gamma)$ = cross section for the formation of a compound nucleus by photon absorption,
$G_c(x)$ = probability for the emission of x as compared to the total probability for the de-excitation of the nucleus.

The observed shape of $\sigma(\gamma, x)$ as a function of photon energy cannot be explained by considering the variation of $G_c(x)$ with energy, since as the energy is increased the onset of any new competing processes would cause $G_c(x)$ to decrease rather than increase. The increase in $\sigma(\gamma, x)$ beyond the initial slowly rising portion must therefore be attributed to a change in photon absorption cross section $\sigma_c(\gamma)$. We will present three tentative mechanisms which may account for this increase.

1. The original explanation for the anomalous behavior of these curves presented by Johns *et al.* (5) was based on a mechanism suggested by Blatt and Weisskopf (2). According to the latter authors the electric dipole photon absorption is suppressed below 15 Mev. In this region $\sigma_c(\gamma)$ is made up of

electric quadrupole, magnetic dipole, and contributions from the incipient electric dipole. At higher energies the onset of strong electric dipole photon absorption results in the rapidly rising cross-section curve. If this explanation is to be valid, it must be assumed that the change-over from suppressed to allowed electric dipole transitions occurs at ∽ 19 Mev. in the oxygen nucleus. The fact that quadrupole photon absorption does take place at energies below 20 Mev. is indicated by the results of Millar and Cameron (quoted by Preston (8)) who observed ground state transitions in the reaction $O^{16}(\gamma, \alpha)C^{12}$ at these energies. Gell-Mann and Telegdi (3) have recently pointed out that according to isotopic spin considerations this reaction can proceed to the ground state only by quadrupole photon absorption.

2. Recent work in this laboratory has indicated that photon absorption by O^{16} occurs, at least in part, into discrete nuclear levels. The position of the levels and their relative activation strength have been previously reported (4).

These levels and their relative strength are indicated on the $O^{16}(\gamma, n)O^{15}$ cross-section curve of Fig. 5 by vertical lines. It is remarkable that the level strength follows the cross-section curve so well. It is tempting to suggest that this curve is a smooth envelope of the unresolved discrete energy levels. Complete details will be given in a forthcoming paper.

3. In a recent article Peaslee (7) has suggested a somewhat different process to account for the shoulder on the cross-section curve. Assuming a one-particle weak γ-interaction, and that the nuclear ground state can be described as a single product of independent particle wave functions, he was able to show that the giant resonance results from (*a*) electric dipole transitions in which the wave functions of the initial and final state almost completely overlap; and (*b*) the compound state having a particular structure which corresponds to coherent excitation of the neutrons and protons into countercurrent oscillation. He attributes the flat portion of the cross-section curve to either incoherent electric dipole excitation or coherent electric quadrupole and/or magnetic dipole excitation.

The three points of view given above for the behavior of the oxygen photonuclear cross section are not necessarily in disagreement with each other. Each, from its own point of view, may be equally valid.

The authors would like to thank Dr. A. G. W. Cameron for his assistance during the course of these experiments.

REFERENCES

1. ALVAREZ, L. Phys. Rev. 75: 1128. 1949.
2. BLATT, J. M. and WEISSKOPF, V. F. Theoretical nuclear physics. John Wiley and Sons, Inc., New York. 1952. p. 654.
3. GELL-MANN, M. and TELEGDI, V. L. Private communication.
4. HASLAM, R. N. H., KATZ, L., HORSLEY, R. J., CAMERON, A. G. W., and MONTALBETTI, R. Phys. Rev. 87: 196A. 1952. (Complete paper to be published.)
5. JOHNS, H. E., HORSLEY, R. J., HASLAM, R. N. H., and QUINTON, A. Phys. Rev. 84: 856. 1951.
6. KATZ, L. and CAMERON, A. G. W. Can. J. Phys. 29: 518. 1951.
7. PEASLEE, D. C. Phys. Rev. 88: 812. 1952.
8. PRESTON, M. A. Phys. Rev. 80: 307. 1950.
9. STEPHENS, W. E., HALPERN, J., and SHER, R. Phys. Rev. 82: 511. 1951.

THE DECAY OF THE POPULATIONS OF NEON ATOMS IN THE $2p^5 3s$ LEVELS[1]

By Donald J. Eckl

ABSTRACT

Improved apparatus has been designed to determine the rate of decay after excitation of the populations of the four states in the $1s^2 2s^2 2p^5 3s$ configuration of neon. An absorption method is employed. Measurements show that the population of the $^3P_2$ state decays exponentially. The decay curves for the $^3P_1$ and $^3P_0$ states may be expressed as the sum of two exponential rates of decay. Atoms in the $^1P_1$ state disappear very rapidly making measurements difficult; the decay is assumed to be exponential. Curves of mean life as obtained from these exponentials are plotted against pressure for all four states. The initial populations of the four states, determined from initial absorption, are of the order of 10^9 atoms per cc. and are plotted as a function of pressure. Within the limits of error the populations so calculated are the same for different absorption lines.

I. INTRODUCTION

In a gaseous discharge the mean life of the average excited atom, which loses its energy by the emission of electric dipole radiation, is of the order of 0.01 μsec., but certain excited atoms in metastable states may have a mean life as long as a few thousand microseconds. It is in connection with the study of these metastable states that interest in the present problem was first aroused. Since ordinary transitions by the emission of electric dipole radiation are forbidden to metastable atoms by the selection rules, the loss of energy by atoms in these states must be attributed in varying degrees to the mechanisms listed below.

(*a*) Diffusion to the walls and electrodes, resulting in a loss of energy by the ejection of electrons. The rate of decrease of population due to this process should be inversely proportional to the pressure of the gas.

(*b*) Collisions of the first and second kinds with normal atoms, producing rates of decay proportional to pressure.

(*c*) Collisions with other metastable atoms, an effect proportional to the square of the number of such atoms.

(*d*) Collisions with "foreign" atoms resulting in the ionization of these impurities (Penning effect), an effect dependent both on the pressure of the gas and the partial pressure of the impurity.

(*e*) Upward transitions to nonmetastable states by absorption of radiant energy and subsequent downward transitions to other states by emission of radiation.

(*f*) Emission of quadrupole radiation with a mean life of the order of seconds.

Under the conditions of the present experiment only the first two processes are of importance.

[1] *Manuscript received October 14, 1952.*
Contribution from the McLennan Laboratory, University of Toronto, Toronto, Ont.

Most successful experimental work on the determination of the mean lives of atoms in metastable states has involved the measurement of the absorption of incident radiation of the proper frequency by these excited atoms after the source of excitation has been removed, and the employment of this method has led to the use of neon in all but a few cases. Neon is especially useful from an experimental standpoint because its absorption lines, in this case those terminating in one of the first four excited levels, are in the visible part of the spectrum as shown by the wave lengths given in the term scheme in Fig. 1.

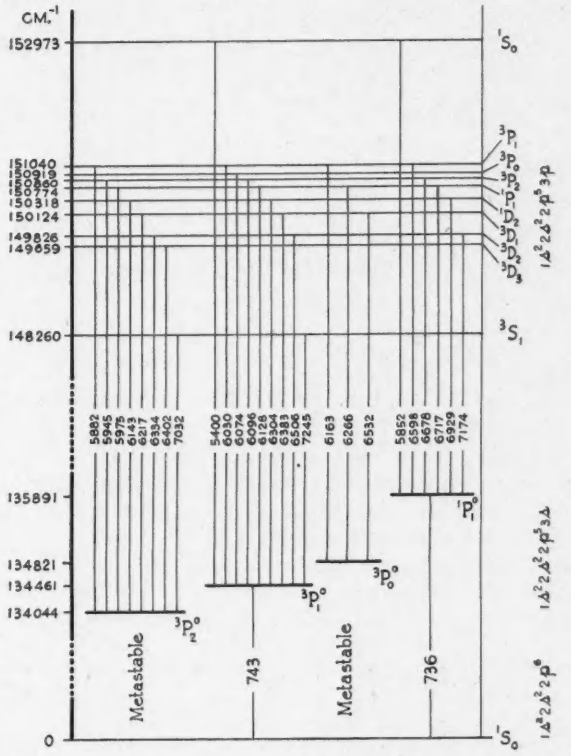

FIG. 1. Term scheme for neon (first two excited configurations only).

The early work done by Meissner and Graffunder (9), Dorgelo and Washington (4), Anderson (1), and Lippert (8) on the comparatively long-lived $^3P_2$ state of neon showed that the mean lives of atoms in metastable states could be as long as a few milliseconds. Grant (5) with the benefit of more modern experimental techniques was able to obtain a lifetime–pressure curve for the $^3P_2$ state of neon as well as some interesting facts about the decay of the other three states of the first excited configuration. His results show the

need for lifetime–pressure curves for all four states, if a more complete picture of the mechanisms involved in the decay of the populations of these states is to be obtained. The present research was undertaken to obtain such curves and to check certain peculiar features of the decay curves for the populations of the $^3P_0$ and $^3P_1$ states indicated by the work of Grant (5). To this end more extensive and accurate electronic apparatus was designed and employed.

II. THE THEORY OF ABSORPTION

Suppose a beam of light of intensity I_0 and frequency ν is incident on an absorbing layer of gas. The transmitted intensity I at frequency ν is given by

[1] $$I = I_0 e^{-k_\nu L}$$

where L = the thickness of the absorbing layer,

k_ν = a frequency dependent parameter called the absorption coefficient of the gas.

For the conditions encountered in the typical absorption experiment Mitchell and Zemansky (10) give as an approximation

[2] $$k_\nu = k_0 e^{-\omega^2}$$

[3] where $$\omega = \frac{2(\nu - \nu_0)}{\Delta\nu_D}\sqrt{\ln 2},$$

and ν_0 is the frequency at the center of the absorption line, and $\Delta\nu_D$ is the Doppler half width. The quantity k_0 is given by

[4] $$k_0 = \frac{1}{4\pi\Delta\nu_D}\sqrt{\frac{\ln 2}{\pi}}\,\lambda_0^2\,\frac{g_A}{g_B}\,A(A,B)\,N(B)$$

where λ_0 = the wave length corresponding to ν_0,

g_A and g_B = the respective statistical weights of states A and B,

$A(A,B)$ = the Einstein coefficient for spontaneous transitions from state A to state B,

$N(B)$ = the number of atoms per cubic centimeter in state B.

The absorption A is defined by

[5] $$A = 1 - I/I_0.$$

Now assuming that the emission line frequency dependence can be represented by

[6] $$I_\nu = I_{\nu_0} e^{-(\omega/\alpha)^2}$$

where I_{ν_0} is the center intensity

[7] and $$\alpha = \frac{\text{emission line breadth}}{\text{absorption line breadth}}$$

and that $I_0 = \int I_\nu d\nu$, Mitchell and Zemansky (10) give the following series for A:

[8] $$A = \frac{k_0 L}{\sqrt{(1+\alpha^2)}} - \frac{(k_0L)^2}{2!\sqrt{(1+2\alpha^2)}} + \ldots - (-1)^n\frac{(k_0L)^n}{n!\sqrt{(1+n\alpha^2)}}.$$

If α is small so that $\alpha^2 \ll 1$, this may be written

[9] $$1 - A = I/I_0 = e^{-k_0 L}.$$

[10] or $$\ln(I_0/I) = k_0 L = ML\lambda_0 f_{AB} N(B)$$

where M is a constant and f_{AB} is a quantity called the strength of a line given by

[11] $$f_{AB} = \frac{mc}{8\pi^2 e^2} \lambda_0^2 \left(\frac{g_A}{g_B}\right) A(A, B).$$

III. THE THEORETICAL DECAY CURVES

A theory dealing with the decay of the population of metastable states in a discharge tube after the removal of excitation was developed by Zemansky (11) through the solution of a differential equation containing diffusion and collision terms. Under ordinary experimental conditions, except for very small values of t, his solution reduces to

[12] $$N = N_0 e^{-t/\tau}$$

where N = the average number of metastable atoms per cubic centimeter,
N_0 = a constant representing the initial density of metastable atoms,
τ = the mean life of the excited state given by the expression

[13] $$\frac{1}{\tau} = \frac{B}{p} - Cp.$$

This theory depicts the decay of the population of atoms in a single isolated metastable state as a result of the loss of energy by diffusion and collisions with the assumption that no further metastable atoms are produced once electrical excitation has been removed. Such a theory may serve as a guide in predicting experimental results, but it has since become apparent that any complete and accurate theory must take into account the effects of the close proximity of adjacent levels and the resonance radiation emitted by atoms in neighboring nonmetastable levels. The use of Zemansky's solution for $N(B)$ in Equation 10 gives

[14] $$\ln (I_0/I) = R_\lambda N(B) = R_\lambda N_0 e^{-t/\tau}$$

where R_λ is constant for any particular absorption line.

[15] Or $$\ln \ln (I_0/I) = -t/\tau + \text{constant}.$$

The validity of this expression depends on the accuracy of certain approximations. If α is not small, the simple expression of Equation 9 is no longer justifiable. The use of the complete series given in Equation 8 results in a curve with a reduced negative slope at $t = 0$, which gradually in the first 2τ sec. approximates the slope $1/\tau$ predicted by Equation 15. As α is increased the initial departure from $1/\tau$ becomes greater. Moreover, the series in Equation 8 involves $\lambda_0 f_{AB}$ so the slope of the decay curve for large α will depend to some extent on the particular absorption line used, a result observed by several of the earlier investigators. If the number N_0 of absorbing atoms is small, the slope will be $1/\tau$ regardless of the size of α.

IV. THE EXPERIMENTAL METHOD

The experimental method involves the measurement of values of I_0/I corresponding to values of t so that a decay curve of the type given by Equation 15 can be plotted and the mean life obtained from its slope. A simplified diagram of the apparatus is given in Fig. 2. All voltage signals and timing

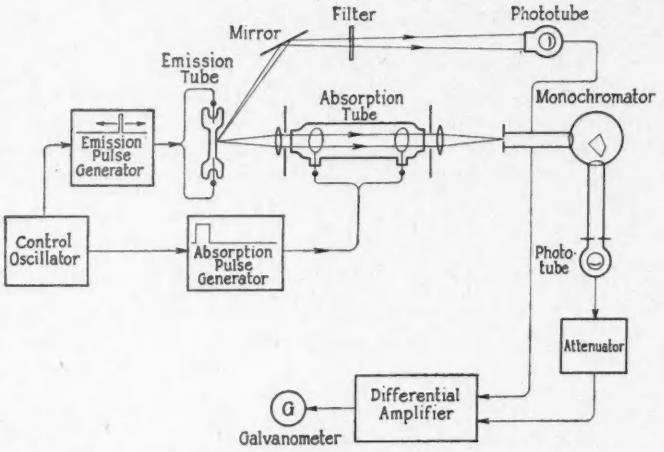

FIG. 2. Simplified block diagram.

intervals originate with the control oscillator which is a sinusoidal audio-oscillator operating at 2000 cycles per second. The absorption pulse generator applies a rectangular voltage pulse of 500 μsec. duration to the absorption tube at the beginning of the sequence, exciting the neon and producing metastable atoms. At any interval after the end of the absorption pulse from zero to 500 n μsec., where n is an integer, the emission pulse generator acts to produce an 18 μsec. flash at the emission tube. Two light signals are taken from this tube, one passing through a red filter to a phototube where it serves as a reference signal, and the other passing through the absorption tube where it may be partially absorbed if excited atoms still remain. This latter signal is applied to a monochromator where a single line terminating in the state under study is selected and passed on to a phototube, the output of which is fed to an attenuator. Both the reference and absorbed signals are then applied to a differential amplifier which produces an output, observable as a galvanometer deflection, proportional to the difference between the input signals. The differential amplifier is first adjusted for zero galvanometer setting with the absorption tube turned off and with a large attenuator setting. Then when the absorption tube is turned on, the attenuator setting is reduced until approximately zero galvanometer deflection is again obtained, at which time the value of $\log(I_0/I)$ can be found from the calibrated attenuator scale and galvanometer reading. Measurements are made first at the longest delay

interval, and then for shorter delay times, each 500 μsec. less, until zero delay is reached. Then a repeat run is made in the opposite direction ending with very small absorption.

Electronic Circuits

The complete block diagram of the system is given in Fig. 3 along with representative wave forms. The trigger pulses which are spaced at 500 μsec. intervals and control all timing are produced in the emission tube channel (200 series on Fig. 3) and appear as negative pulses at the output of V203 and

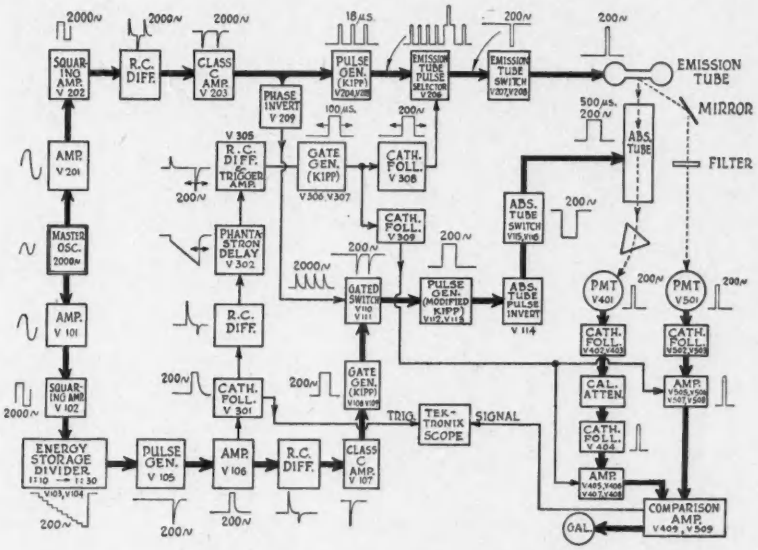

FIG. 3. Complete block diagram.

positive pulses at the output of V209. The absorption channel (100 series) employs an energy storage type counter (2) as a frequency divider together with a thyratron pulse generator V105, the combination serving to reduce the pulse repetition rate by a factor of 10 or higher. The amplifier V106 removes the unstable peak from the pulse produced by the thyratron. The gate generator, a cathode-coupled one-shot multivibrator, produces one positive gate 1500 μsec. long for every 10 of the original trigger pulses. This gate and the first two trigger pulses add to bring the switch V110, V111 out of cut-off, providing two negative trigger pulses 500 μsec. apart which occur at the beginning of each sequence. These pulses serve to turn on and off the absorption pulse generator which is a modified cathode-coupled one-shot multivibrator. The output of this circuit turns on the absorption tube for 500 μsec. by effectively grounding the grid of the switch tube V116 as shown in Fig. 4.

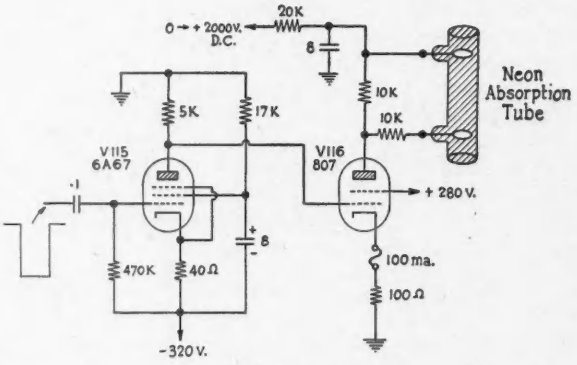

FIG. 4. Absorption tube switch.

The delay channel (series 300) operates by means of a phantastron-type delay circuit (2, 3) using a 6SA7 tube which triggers a gate generator at a variable time interval after the thyratron pulse to produce a 100 μsec. emission gate voltage.

The emission pulse generator V204, V205 is a cathode-coupled one-shot multivibrator which produces an 18 μsec. positive pulse for each negative trigger pulse from V203. One emission pulse is selected by the gate signal and this turns on the emission tube by an arrangement similar to that shown in Fig. 4. The principal wave forms for the complete sequence of operation are given in Fig. 3 and actual photographs of voltage and light pulses are shown in Fig. 5.

In previous work Grant (5) had passed successive pulses of light through the absorption tube at regular intervals following the extinction of the absorption tube and photographed the resulting pattern produced on an oscilloscope by the photomultiplier output. A pattern of this type for the λ5945 line is shown in Fig. 6. Since it was desirable to measure much smaller absorptions than could be measured on such patterns, a comparison method using only one pulse from the emission tube in each cycle was adopted. Many pulses were averaged by the equipment to eliminate the effects of the large noise present. Part of this noise is the result of changes in intensity at the emission tube and this is reduced by the use of the reference signal, but the major portion results from the statistical fluctuations in the small number of electrons produced at the cathode of the phototube by one emission pulse. Calculations show that the signal to noise ratio of about 5: 1 for the emission flash is accounted for by this process. It was impractical to increase the light reaching the cathode by a worth-while factor. As some 3000 pulses were averaged with the present method, the signal to noise ratio was improved by a factor of about 55.

Type 931A photomultiplier tubes with approximately 100 volts per stage are used as pickup devices in both reference and absorption channels. The output of each phototube is fed directly to a cascode-type cathode follower

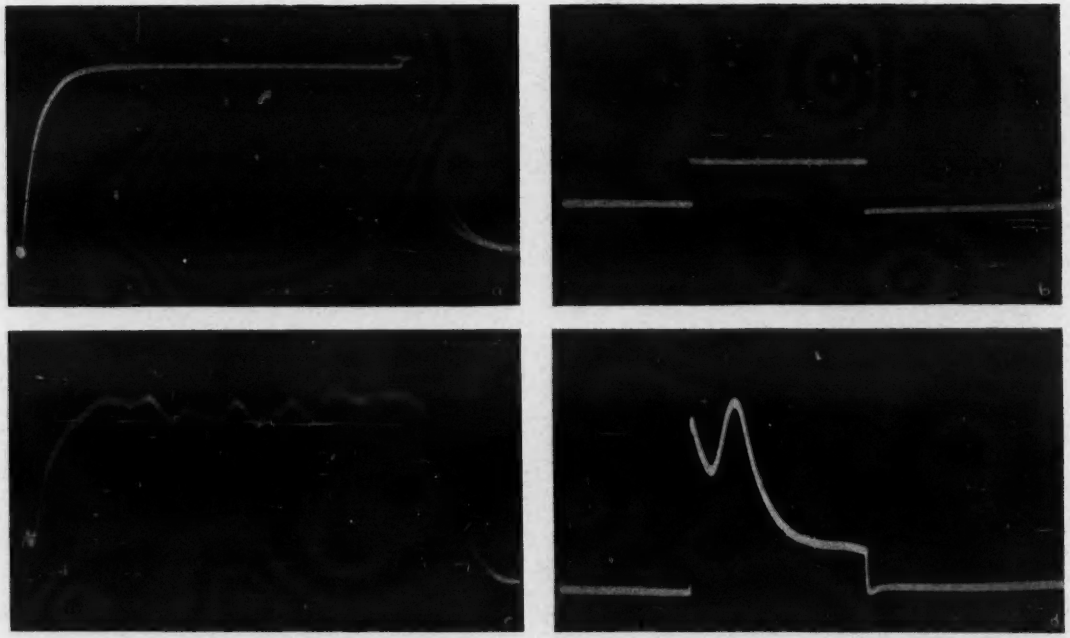

FIG. 5. Applied voltage and light output at emission and absorption tubes.
(*a*) Voltage applied to emission tube. Pulse duration is 18 μsec.
(*b*) Voltage applied to absorption tube. Pulse duration is 500 μsec.
(*c*) Light output from emission tube at a pressure of approximately 2 mm.
(*d*) Light output from absorption tube at a pressure of 6.2 mm.

FIG. 6. Absorption pattern for λ5945 at 1.3 mm. Hg.

with an effective generator impedance of 60 ohms which prevents attenuator changes on the absorption side from affecting the voltage output. The attenuator was carefully calibrated by means of a specially designed a-c. bridge

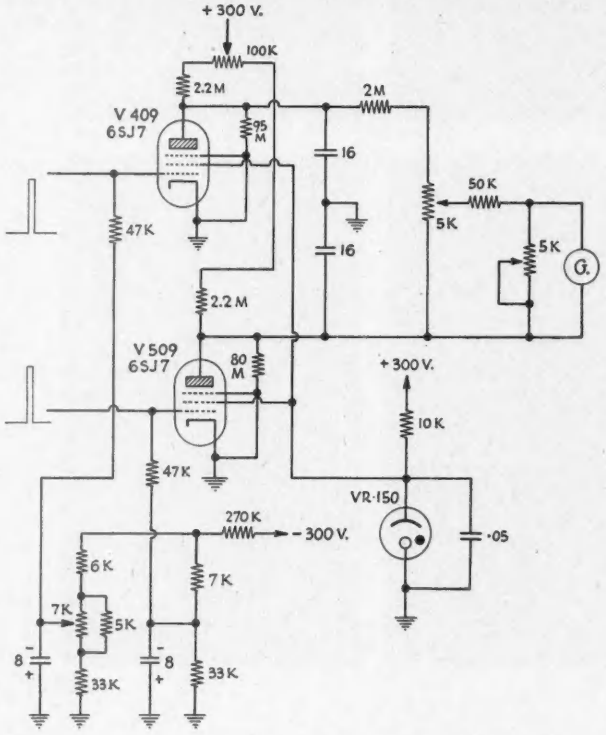

FIG. 7. Comparison amplifier.

circuit at frequencies up to 30 kc. and is accurate enough to allow logarithms to be read to three decimal places. A cathode follower with a high input impedance keeps the circuits following from loading the attenuator.

The 100 μsec. pedestal which selects the emission tube signal is used to gate the two amplifiers as well, allowing V407 and V507 to conduct only during the time that light from the emission tube is being received and therefore eliminating the dark noise from the phototubes and the light output from the absorption tube. The frequency response of the amplifier is arranged to cut out all noise frequencies above the necessary signal range. The comparison stage is shown in Fig. 7, the 16-mf. condensers giving the integrating effect over many pulses.

V. THE APPARATUS

Absorption tube.—The absorption tube is cylindrical with an inside diameter of 4.7 cm. and a length of 35 cm. between its two plane windows which have a diameter of 3.5 cm. The electrodes are circular loops of 40-mil tungsten wire, 30 cm. apart, with a diameter of 4 cm. Baffles placed at either end of the absorption tube each have a circular opening of 2.8 cm. diameter, and serve to limit the light beam from the emission tube to the central part of the absorption tube, thus reducing the effect of higher order terms in Zemansky's solution.

The emission tube.—The emission tube consists of a 1 mm. bore capillary, 3 cm. long, and has 40-mil "spike" electrodes in a cylindrical bulb at each end. The narrow bore reduces self-absorption and consequently α. Baffles are employed to limit the active length of the capillary.

The monochromator.—The monochromator is a specially constructed instrument employing a constant deviation prism with a dispersion of 139.7 Å per mm. at 6000 Å and a curved exit slit to separate the spectral lines.

The pressure gauges.—The neon pressures are measured with an oil manometer using octoil-S which has been distilled under vacuum. This gauge is separated from the remainder of the system by a liquid air trap. A VG-1A ionization gauge is used to measure the pressure when the system is evacuated.

The optical filter.—A Wratten type E-23 filter, passing only wave lengths above 5700 Å, is employed in the reference channel to limit the response to the orange-red portion of the spectrum.

The vacuum system.—The vacuum is obtained by means of a mercury diffusion pump followed by a liquid air trap. The entire system is constructed of pyrex and sections are separated by stopcocks. Despite the large number of stopcocks the pressure can be brought down to 1×10^{-6} mm. on the ionization gauge. The attainment of such low pressures involves extensive working of the stopcocks to remove dissolved gases from the grease. Dow-Corning silicone high vacuum grease is used because of its stability even at high temperatures. The effect of the presence of the stopcocks on the experimental results was checked by making two runs on the sample of gas, the first immediately after the gas had been placed in the absorption tube, the second 48 hr. later. There was no measurable difference in the decay times obtained from the two runs.

The electrodes in the absorption tube were outgassed by heating to incandescense by means of an r-f. induction heater for eight hours. The walls of the entire eystem were flamed until heating no longer increased ionization gauge readings.

The power supplies.—With the exception of the two high voltage supplies for the discharge tubes all power supplies are electronically regulated. In addition a Sorenson regulator is used to keep the line voltage constant.

The neon gas.—The gas used was spectroscopically pure neon supplied by Linde Air Products Company. A potassium pool discharge tube is available for further purification but in practice no improvement was obtained by using this bulb.

VI. THE EXPERIMENTAL RESULTS

A representative set of decay curves for the quantity log log (I_0/I), one for each of the four excited levels at a pressure of 2.0 mm., is given in Fig. 8. The two sets of points in each case represent one continuous run starting with the circles at low values of absorption, going to maximum absorption, and then returning with the x's.

The accuracy of the equipment is such that values of log (I_0/I) can be measured to 0.001 under steady conditions. This means that an absorption as

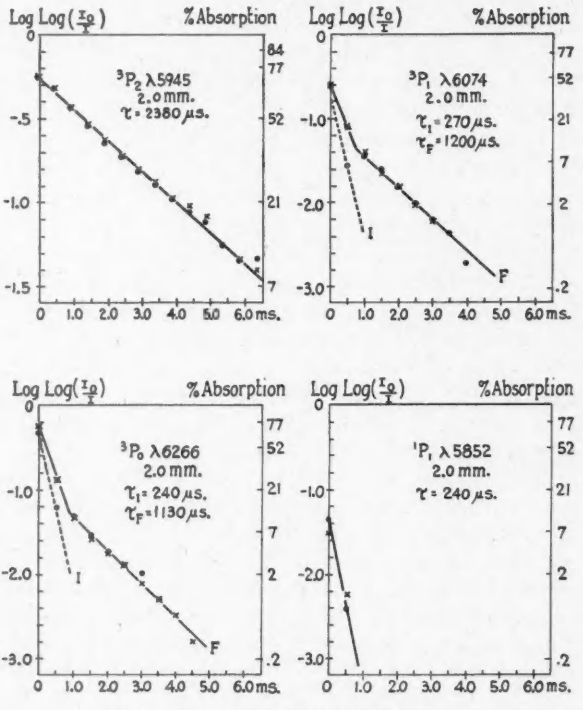

FIG. 8. A representative set of decay curves.

small as 0.2% can be measured. Since the points are plotted on a log log scale small errors become more serious as the value of the ordinate increases.

In the case of the $^1P_1$ state initial absorptions are very small (2% or less) and no absorption is measurable after 500 μsec. Therefore the second point is difficult to separate from noise fluctuations so errors may be of the same order as the measured value.

All curves obtained for the $^3P_2$ state are very nearly straight lines, indicating an exponential decay. The curves for the $^3P_1$ and $^3P_0$ states both show two distinct slopes which may be interpreted as two exponentials. By extrapolating the final slope toward zero and subtracting the extrapolated values from the actual curve it is possible to obtain the smaller exponential time constant.

Zemansky's theory indicates that at small values of t, because of higher order terms, there should be a departure from exponential decay. The initial slopes in the $^3P_0$ and $^3P_1$ curves cannot be attributed to this effect. First, the times involved are not sufficiently short. Also an approximate evaluation of the coefficients shows that the second order term should be negative and therefore decrease, rather than increase, the rate of decay. It can be shown, moreover, that the maximum life of the second order term should occur at a pressure approximately twice that for the first order, which is not the case here.

The departure from the simple theory cannot be attributed to the absorption of light and resulting upward transitions from the metastable states. Baffles around the absorption tube shut out ordinary stray light. Also since the absorption tube population is sampled only once per cycle at the time of measurement by the emission tube light pulse, this pulse can have no possible effect on the shape of the decay curve.

Data on the $^1P_1$ state are limited because of the fast decay but a straight logarithmic curve is assumed.

Lifetime–Pressure Curves

Plots of mean life against pressure on logarithmic scales for the $^3P_2$ and $^1P_1$ states are given in Fig. 9. The $^3P_1$ state is shown in Fig. 10 with separate curves plotted for the short and long rates of decay. Similar curves are plotted in Fig. 11 for the $^3P_0$ state. The curves are deliberately drawn to give more weight to the higher points since impurities would tend to make mean lives low.

According to theory the lifetime–pressure curve for metastable states should have the form of Equation 13, which would mean that the slopes at extremities of the curve should be 45°, corresponding to the first power exponent of pressure. The actual slope for the $^3P_2$ state is 33° at the high pressure end, corresponding to an exponent of 0.6, a value which has been confirmed by Grant (6).

An empirical equation giving a fairly good fit to the experimental points is

$$1/\tau = 230p^{-0.6} + 180p^{0.6}. \tag{16}$$

It is possible to obtain expressions for the lifetime–pressure curve without the somewhat artificial fractional exponents by the introduction of a constant term. The empirical expression

$$\frac{1}{\tau} = \frac{165}{p} + 50p + 150 \tag{17}$$

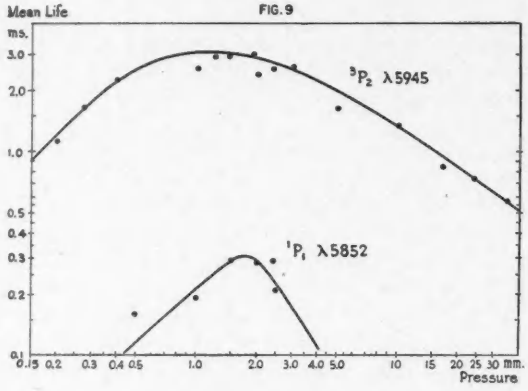

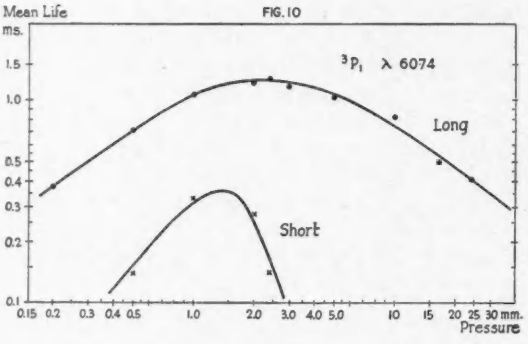

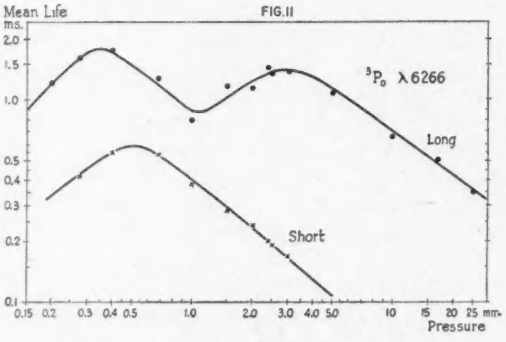

FIG. 9. Mean life against pressure: $^3P_2$, $^1P_1$.
FIG. 10. Mean life against pressure: $^3P_1$.
FIG. 11. Mean life against pressure: $^3P_0$.

fits the data reasonably well as shown in Fig. 12. A similar fit for the experimental points is the expression

$$[18] \qquad \frac{1}{\tau} = \frac{17}{p^2} + 40p + 300$$

also shown in Fig. 12. In both of the latter expressions there is a decay represented by the constant term with a mean life of a few milliseconds independent of pressure to be accounted for.

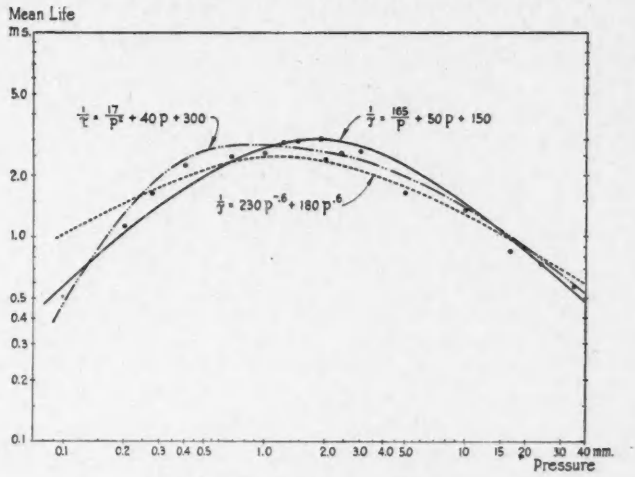

FIG. 12. Empirical curves: $^3P_2$ state.

The composite curves given in Fig. 13 show regions where two excited states have nearly the same mean life. This is particularly true in the case of the $^3P_0$ and $^3P_1$ states where there is some overlap over the entire pressure range. The separation between the $^3P_1$ and $^3P_0$ states is only 360 cm.$^{-1}$ and collisions of atoms in either state with normal atoms can easily involve energy changes of this magnitude. The rate of decay of the two states seems to be governed by that of the $^3P_1$ nonmetastable state. The relatively long persistence of atoms in the $^3P_1$ and $^1P_1$ states may possibly be attributed to the imprisonment of resonance radiation.

Initial Number of Metastable Atoms as a Function of Pressure

From Equation 10

$$[19] \qquad N(B) = \left\{\frac{mc}{\pi e^2 L}\sqrt{\frac{2\pi RT}{M}}\right\}\frac{1}{\lambda_0 f_{AB}}\log\,(I_0/I).$$

Values of f_{AB} are given by Ladenburg (7). Therefore it is possible to plot the variation with pressure in the number of atoms in a given state at the end of the excitation pulse in the absorption tube. Since measurements were made

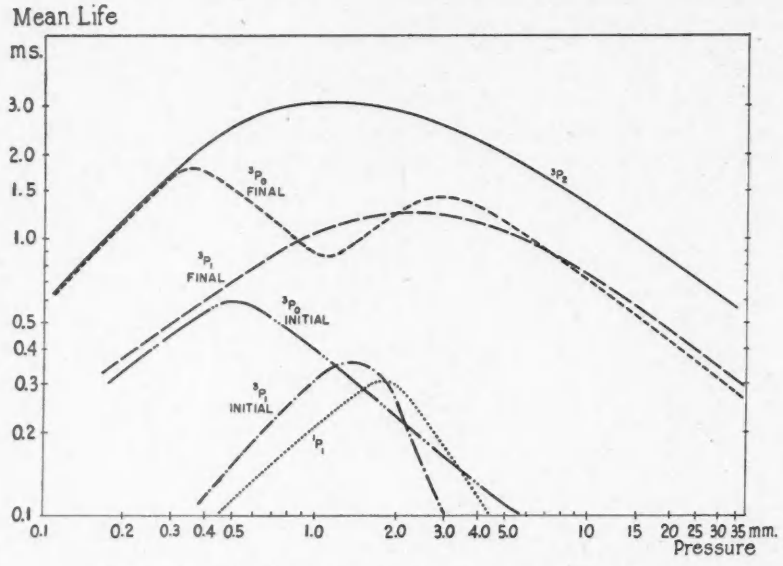

FIG. 13. Composite picture of mean lives of all states against pressure.

for the $^3P_2$ state at 0.68 mm. using several different absorption lines, an indication of the accuracy of this method may be obtained from data below:

$\log\left(\frac{I_0}{I}\right)$ at $t = 0$	λ(Å)	f_{AB}	$\frac{1}{\lambda f_{AB}} \log\left(\frac{I_0}{I}\right) \propto N(B)$
.912	6143	.19	7.8×10^4
.650	6334	.13	7.9×10^4
.631	5945	.09	10×10^4
.370	5882	.07	9×10^4
.147	5976	.03	8×10^4

The numbers in the right-hand column should be proportional to the number of atoms in the $^3P_2$ state at the end of the absorption pulse at 0.68 mm. and should therefore be constant. The variation is not inconsistent with the uncertainties in the values of the f-numbers. The curves of $N(B)$ against pressure for the four states are shown in Fig. 14. At 1 mm. there is roughly one atom in the $^3P_2$ state out of every 23 million, the actual numbers given being only approximate since absolute f-values are not certain. The relative magnitudes, however, are experimental results, and the ratio of populations at the maximum is 15:5:2 as opposed to the statistical weights of 5:3:1, indicating that current densities were probably not high enough to produce saturation of the populations.

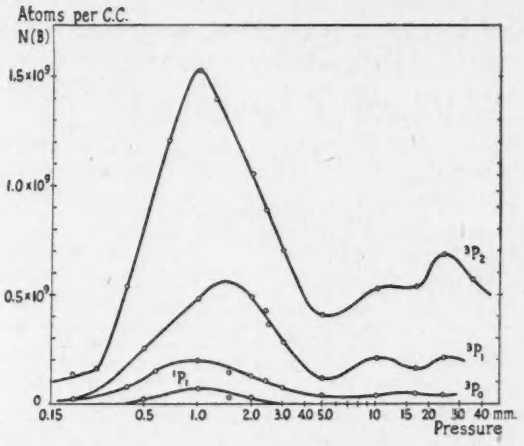

FIG. 14. Initial number of excited atoms as a function of pressure.

VII. CONCLUSION

The more accurate measurements described above have made it evident that the system of four levels in neon cannot be adequately described by the simple theory (11). Further work with other gases, e.g., xenon, and other temperatures will be necessary before a complete theory can be developed.

The author particularly wishes to express his thanks to Profs. J. M. Anderson and R. W. McKay of the Department of Physics of the University of Toronto for their assistance and encouragement during the course of the work.

REFERENCES

1. ANDERSON, J. M. Can. J. Research, 7: 434. 1932.
2. CHANCE, B., *et al.* Waveforms. Vol. 19. M.I.T. Radiation Laboratory Series. McGraw-Hill Book Company, Inc., New York. 1949.
3. CLOSE, R. N. and LEBENBAUM, M. T. Electronics, 21: 100. April, 1948.
4. DORGELO, H. B. and WASHINGTON, T. P. Koninkl. Akad. Wetenschap. Amsterdam, 30: 33. 1927.
5. GRANT, F. A. Can. J. Research, A, 28: 339. 1950.
6. GRANT, F. A. Univ. of Maryland. Private communication.
7. LADENBURG, R. Revs. Modern Phys. 5: 243. 1933.
8. LIPPERT, W. Ann. phys. 30: 136. 1937.
9. MEISSNER, K. W. and GRAFFUNDER, W. Ann. phys. 84: 1009. 1927.
10. MITCHELL, A. C. G. and ZEMANSKY, M. W. Resonance radiation and excited atoms. Cambridge at the University Press. 1934.
11. ZEMANSKY, M. W. Phys. Rev. 34: 213. 1929.

SECOND ORDER NUCLEAR QUADRUPOLE EFFECTS IN SINGLE CRYSTALS

PART I. THEORETICAL[1]

By G. M. Volkoff

ABSTRACT

The dependence of electric quadrupole splitting of nuclear magnetic resonance absorption lines in single crystals on crystal orientation in an external magnetic field is investigated theoretically following earlier work of Pound, of Volkoff, Petch, and Smellie, and of Bersohn. Explicit formulae are given, applicable to non axially symmetric crystalline electric field gradients ($\eta \neq 0$), and valid up to terms of the second order in the quadrupole coupling constant $C_z \equiv eQ\phi_{zz}/h$, for the dependence of the absorption frequencies on the angle of rotation of the crystal about any arbitrary axis perpendicular to the magnetic field. Some formulae including third order effects in C_z are also given. It is shown that an experimental study of the dependence of this splitting on the angles of rotation about any two arbitrary mutually perpendicular axes is sufficient, when second order effects are measurable, to yield the values of $|C_z|$, η, and the orientation of the principal axes of the electric field gradient tensor at the nuclear sites. In the case that the direction of one of the principal axes is known from crystal symmetry, a single rotation about this axis gives the complete information.

A new method of determining nuclear spin I is proposed which depends on comparing first and second order shifts of the resonance frequencies of the strong inner line components. The method will be of interest in those cases where the total number $2I$ of line components can not be unambiguously ascertained owing to the outer line components being excessively broadened and weakened by crystal imperfections.

1. INTRODUCTION

Since the original work of Pound (16) and Dehmelt and Krüger (7) the electric quadrupole interaction of nuclei (of spin I necessarily greater than 1/2) with their surroundings in crystals has received a considerable amount of attention. Both the observations, and their theoretical interpretation, now extend over a wide range of experimental conditions.

At one extreme lies the work on so-called pure quadrupole spectra in which transitions between the energy levels of a non spherically symmetric nucleus in an inhomogeneous crystalline electric field are observed by a resonance method in the absence of an external static magnetic field. In this case the sample need not be a single crystal, but may be polycrystalline. The quantities which may be experimentally determined, both in the cases of nuclei of half integral and of integral spin greater than 1/2, are the absolute value of the quadrupole coupling constant $|C_z| \equiv |eQ\phi_{zz}/h|$, and the asymmetry parameter of the electric field gradient tensor ϕ_{ij} at the nuclear site defined by $\eta \equiv (\phi_{xx} - \phi_{yy})/\phi_{zz}$ where the three second derivatives of the electrostatic potential ϕ are taken along the three principal axes of ϕ_{ij}. In the one special but frequently occurring case of $I = 3/2$ only a single relation between $|C_z|$ and η is obtained experimentally from pure quadrupole spectra. However, in some cases it may be known from crystal symmetry that $\eta = 0$, so that $|C_z|$ may still be determined.

[1] *Manuscript received April 28, 1953.*
Contribution from the Department of Physics, University of British Columbia, Vancouver, B.C. Work supported by grants from the National Research Council of Canada.

No information on the orientation of the principal axes of ϕ_{ij} with respect to the crystallographic axes is given when a polycrystalline sample is used.

Theoretical and experimental results on pure quadrupole spectra in crystals with axially symmetric field gradient tensors $\phi_{ij}(\eta = 0)$ were first given by Dehmelt and Krüger (7). The theory was extended to crystals with non axially symmetric $\phi_{ij}(\eta \neq 0)$ by Krüger (9), and observations for a non axially symmetric crystal were reported by Dehmelt and Krüger (8). Bersohn (3) also gives the theory for the non axially symmetric case. A number of papers by Allen (1), Dean and Pound (6), Livingston (12), Meal (13), Watkins and Pound (19), and others, give applications of such pure quadrupole spectra observations to chemical problems. Townes and Dailey (17) discuss some implications of such work for the theory of chemical binding.

At the other extreme lies the work on single crystals placed in a uniform external magnetic field H_0 of sufficient strength to make the Zeeman energy μH_0 for a nucleus considerably larger than the quadrupole coupling energy $eQ\phi_{zz}$. In this case the quadrupole coupling produces only a small splitting of the magnetic resonance absorption line. Carr and Kikuchi (4) gave the first order theory of the angular dependence of this splitting for axially symmetric crystals ($\eta = 0$). Pound (16) gave both experimental and theoretical results for $\eta = 0$, stating his theoretical results to terms of the third order in the ratio $eQ\phi_{zz}/\mu H_0$. Becker (2) reported further experiments on the rotation of crystals with $\eta = 0$. Volkoff, Petch, and Smellie (18) generalized Pound's theory (16) to non axially symmetric crystals ($\eta \neq 0$), restricting their discussion to terms of the first order in the above ratio of quadrupole to Zeeman energy. They also showed on an experimental example that, when only first order effects are observable, three rotations of the crystal about three arbitrary mutually perpendicular axes are needed to give complete information on the orientation of the principal axes of ϕ_{ij} at the nuclear sites, the value of η, and the absolute value of the quadrupole coupling constant $|C_z|$. Bersohn (3) gives a general theoretical expression for the energy levels in a non axially symmetric crystal ($\eta \neq 0$) to terms of the third order in the above ratio, but he does not give explicit formulae for the dependence of the observed frequencies on crystal rotation in a form directly applicable to analysis of experiments.

The present paper extends to second and third order terms our previous generalization (18) of Pound's theory (16) to non axially symmetric crystals. It verifies Bersohn's expression for the energy levels and, using it as a starting point, presents explicit calculations of the dependence on crystal orientation of the frequencies of the components of the magnetic resonance line split by the quadrupole interaction. Results for $\eta \neq 0$ are given up to terms of the third order in the ratio of quadrupole to Zeeman energy. A companion paper, Part II Experimental (14), immediately following the present Part I, presents experimental results on the Al^{27} line in spodumene, and analyzes them with the aid of the present theory. It is found that terms up to the second order in the above ratio are definitely needed to obtain agreement with experimental results. Preliminary results of these experiments and their analysis have been reported by Petch, Volkoff, and Cranna (15).

To complete this brief survey of the whole field we may mention in passing the results available to date for values of H_0 which are intermediate between the above two extreme cases, and which can not be successfully treated by the perturbation theory approach of Pound (16) or of the present paper, based on the smallness of $eQ\phi_{zz}/\mu H_0$.

When $0 < \mu H_0/eQ\phi_{zz} \ll 1$ we have the case of Zeeman splitting of pure quadrupole lines. This case has been treated by Krüger (9), Krüger and Meyer-Berkhout (10), Dean (5), and Bersohn (3). In this approach μH_0 is treated as a small perturbation on $eQ\phi_{zz}$. This method applied to single crystals also yields in addition to η and $|C_z|$, the orientation of the principal axes of ϕ_{ij}.

When $\mu H_0 \approx eQ\phi_{zz}$ it is not possible to treat either of these two interaction energies as a perturbation on the other, and secular determinants have to be solved explicitly. Krüger (9) discusses the case of nuclei of spin $I = 3/2$ in an axially symmetric crystal ($\eta = 0$). The calculations of Weiss (20) and Whitmer *et al.* (21) on the Stark splitting of paramagnetic resonance absorption lines may be taken over for special orientations of crystals with $\eta = 0$, containing nuclei of spin $I = 3/2$. Lamarche and Volkoff (11) have obtained theoretical results for nuclei of spin $I = 5/2$ in a non axially symmetric crystal ($\eta = 0.95$) for the complete range $0 \leqslant \mu H_0/eQ\phi_{zz} < \infty$. An attempt is in progress to observe one particular spectrum in a non axially symmetric crystal over a range of this ratio wide enough to link the pure quadrupole spectrum with the region in which the quadrupole interaction produces only a small splitting of the Zeeman line.

Section 2 of this paper obtains the basic formulae to terms of order C_z^3 for the frequency splitting $\nu' - \nu''$ between a pair of satellites and for the frequency shift $\bar{\nu} - \nu_0$ of the center of gravity of the satellite pair from the unperturbed Larmor frequency ν_0 both expressed in terms of the irreducible components $(\nabla E)_q'$ of the crystalline field gradient tensor in the laboratory coordinate system.

In section 3 effects of crystal rotation are explicitly introduced by expressing $(\nabla E)_q'$ in terms of the components of (∇E) in a coordinate system fixed with respect to the crystal, and the angle θ which measures the rotation of the crystal about an axis perpendicular to the magnetic field. Explicit formulae are given for $\nu' - \nu''$ and $\bar{\nu} - \nu_0$ as functions of θ to terms of order C_z^2.

In section 4 the kind of information available from such crystal rotations is discussed. A new method of nuclear spin determination is proposed which does not depend on counting the total number $2I$ of line components, but involves a comparison of the first and second order frequency shifts for the strongest innermost pair of line components. This will be of particular interest when the spin is large, and the outer line components are broadened and weakened by crystal imperfections, so that it is difficult to be certain that none have been missed.

In section 5 the method of analyzing the experimental information given by a crystal rotation about an arbitrary direction in the crystal is presented. It is shown how $|C_z|$, η, and the orientation of the principal axes may be determined from the experimental curves of $\nu' - \nu''$ or $\bar{\nu} - \nu_0$ as functions of θ. It is shown that when the quadrupole coupling is large enough to make second order

effects observable two crystal rotations about two arbitrary mutually perpendicular axes are in general sufficient to give a complete analysis of the field gradient tensor at the nuclear sites.

Section 6 gives the simplified analysis of a crystal rotation in the case that the axis of rotation is known to coincide with one of the principal axes of the field gradient tensor.

In section 7 a collection of formulae is given for the cases that the axis of rotation is known to be either parallel or perpendicular to a principal axis of ϕ_{ij}. These formulae are useful in computing $\nu' - \nu''$ and $\bar{\nu} - \nu_0$ from given values of C_z, η, and principal axes orientation.

The companion paper (14) immediately following this one presents an experimental application of the above theory.

2. DERIVATION OF THE BASIC FORMULAE

We consider a nucleus in a single crystal placed in a uniform external magnetic field H_0 and restrict our attention to the case that the electric quadrupole interaction of the nucleus with its surroundings in the crystal is small compared to its Zeeman energy, but large compared to the dipole–dipole interactions with other nuclei. In this case the quadrupole interaction splits the nuclear magnetic resonance line into several components producing line structure, while dipole–dipole interactions will contribute only to the line width of the individual components. As long as we are concerned only with the gross structure of the line in terms of the number and frequency separation of its components, but not with the width of the individual components, we may neglect the dipole–dipole interactions, and consider each nucleus individually as being acted upon by the given H_0 and a given crystalline electric field gradient ∇E.

The electrostatic interaction

[1] $$F = \mathbf{Q} \cdot \nabla \mathbf{E}$$

given by the scalar product of the nuclear electric quadrupole moment tensor with the electric field gradient tensor may in this case be regarded as a perturbation on the Zeeman energy

[2] $$\mathfrak{H}_Z = -g\beta H_0 I_z$$

where H_0 is chosen as the z direction. The expression for the quadrupole moment tensor operator in terms of the angular momentum operators I_x, I_y, I_z may be found in References (7), (9), and (16). The five components of ∇E in its irreducible form are given by:[2]

[3]
$$(\nabla E)_0 = \tfrac{1}{2}\phi_{zz},$$

$$(\nabla E)_{\pm 1} = \mp \frac{1}{\sqrt{6}} [\phi_{xz} \pm i\phi_{yz}],$$

$$(\nabla E)_{\pm 2} = \frac{1}{2\sqrt{6}} [\phi_{xx} - \phi_{yy} \pm 2i\phi_{xy}]$$

[2] *Dr. Bersohn has kindly confirmed that in equation (12) of Ref. (3), which is the same as our equation [3], the double sign in front of the expression for $(\nabla E)_{\pm 1}$ has been omitted through a typographical error, and must be introduced before equation (14) of Ref. (3) is used.*

with

$$[4] \qquad \phi_{xy} \equiv \frac{\partial^2 \phi}{\partial x \partial y} = -\frac{\partial E_x}{\partial y}, \text{ etc.}$$

The energy of that perturbed Zeeman level which in the limit of zero perturbation is characterized by the magnetic quantum number m is given by standard perturbation theory up to terms of the third order in F by:

$$[5] \qquad E_m = E_m{}^0 + E_m{}^{(1)} + E_m{}^{(2)} + E_m{}^{(3)} + \ldots$$

with

$$[6] \quad E_m{}^0 = -mg\beta H_0,$$

$$[7] \quad E_m{}^{(1)} = F_{mm},$$

$$[8] \quad E_m{}^{(2)} = \sum_i{}' |F_{mi}|^2/(E_m{}^0 - E_i{}^0),$$

$$[9] \quad E_m{}^{(3)} = \sum_i{}' \sum_j{}' F_{mi}F_{ij}F_{jm}/(E_m{}^0 - E_i{}^0)(E_m{}^0 - E_j{}^0) - \sum_i{}' |F_{mi}|^2 F_{mm}/(E_m{}^0 - E_i{}^0)^2.$$

The matrix elements F_{ij} in the representation which diagonalizes the Zeeman energy operator [2] are tabulated in Refs. (3) and (16). Inspection of the form of these matrix elements shows in conjunction with equations [7]–[9] that $E_m{}^{(i)}$ is an even function of m for odd i and vice versa. By substituting the known values of F_{ij} into equations [7]–[9] one may obtain after a straightforward but somewhat tedious calculation explicit expressions for $E_m{}^{(i)}$. Bersohn (3) gives such explicit expressions in his equation (14).

Finally, the frequency $\nu_m = |E_m - E_{m-1}|/h$ of the $m \leftrightarrow m-1$ transition is given by:

$$[10] \quad \frac{\nu - \nu_0}{\nu_0} = \pm \lambda(2m-1)\frac{(\nabla E)'_0}{eq} + \frac{\lambda^2}{3} P_2(m) \pm \frac{\lambda^3}{3}(2m-1)\, P_3(m) + 0(\lambda^4)$$

with

$$[11] \quad P_2(m) \equiv c_2(m)\left|\frac{(\nabla E)'_{\pm 2}}{eq}\right|^2 - c_1(m)\left|\frac{(\nabla E)'_{\pm 1}}{eq}\right|^2,$$

$$[12] \quad P_3(m) \equiv k_1(m)\left|\frac{(\nabla E)'_{\pm 1}}{eq}\right|^2 \frac{(\nabla E)'_0}{eq} - k_2(m)\left|\frac{(\nabla E)'_{\pm 2}}{eq}\right|^2 \frac{(\nabla E)'_0}{eq} - \frac{k_3(m)}{\sqrt{6}} \frac{(\nabla E)'^2_{+1}(\nabla E)'_{-2} + (\nabla E)'^2_{-1}(\nabla E)'_{+2}}{(eq)^3}.$$

In equations [10]–[12] the primes on the components of ∇E indicate that these[3] are expressed in terms of the laboratory coordinate system x', y', z' in which z'

[3] *Here, as in Ref. (18), it is assumed that all the nuclei of a given species in a unit cell of the crystal are in positions equivalent insofar as ∇E is concerned. If this is not the case the observed absorption lines will correspond to a superposition of lines due to each nonequivalent position taken separately. The results below are stated explicitly only for the case of equivalent positions.*

coincides with H_0. If $eq \equiv \phi_{zz}$ represents one of the eigenvalues of the tensor ϕ_{ij}, then the other two eigenvalues may be written as $\phi_{xx} = -eq(1-\eta)/2$ and $\phi_{yy} = -eq(1+\eta)/2$. If the value of the asymmetry parameter η is restricted to the interval $0 \leqslant \eta \leqslant 1$, then ϕ_{xx}, ϕ_{yy}, ϕ_{zz} are arranged in order of increasing absolute values. However, the value of η need not be so restricted, and in that case eq is not necessarily the largest eigenvalue, but merely the eigenvalue which corresponds to that principal axis which has been arbitrarily designated as the z axis. Three quadrupole coupling constants can be defined:

[13] $$C_z \equiv eQ\phi_{zz}/h$$

with corresponding expressions for C_x and C_y. The unperturbed Larmor frequency for the nucleus is given by

[14] $$\nu_0 = |\mu| H_0/hI = |\gamma| H_0/2\pi .$$

Experimentally this frequency may be defined as the resonance frequency for the nucleus in question at a site where the time average of the electric field gradient vanishes, as is normally the case in a liquid. The dimensionless parameter λ, which is a measure of the importance of the quadrupole coupling compared to the separation of the Zeeman levels, is defined by:

[15] $$\lambda \equiv \frac{3C_z}{2I(2I-1)\nu_0} .$$

The coefficients $c_i(m)$ and $k_i(m)$ in equations [11], [12] are given by:

[16]
$$\begin{aligned} c_1(m) &= 4[(I+\tfrac{3}{2})(I-\tfrac{1}{2}) - 6(m-\tfrac{1}{2})^2], \\ c_2(m) &= 2[(I+\tfrac{3}{2})(I-\tfrac{1}{2}) - 3(m-\tfrac{1}{2})^2], \\ k_1(m) &= 12I(I+1) - 40m(m-1) - 27, \\ k_2(m) &= 2[3I(I+1) - 5m(m-1) - 6], \\ k_3(m) &= 3[8I(I+1) - 20m(m-1) - 15]. \end{aligned}$$

The signs of the first and third order terms of equation [10] are both to be chosen (in the case of H_0 coinciding with the $+z'$ axis) opposite to the sign of the nuclear gyromagnetic ratio γ. As may be seen from equations [16] if m is replaced by $-(m-1)$, so that the $-(m-1) \leftrightarrow -m$ transition is considered in place of the $m \leftrightarrow m-1$ transition, the $c_i(m)$ and $k_i(m)$ remain unchanged. The sign of the second order term in equation [10] is therefore the same for both these transitions, while the signs of the first and the third order terms are reversed when m is replaced by $-(m-1)$. However, since experimentally there seems to be no way of distinguishing which one of these two transitions one is dealing with (except, in principle at least, by the use of extremely low temperatures), the sign of λ, and therefore of the quadrupole coupling constant C_z, will remain undetermined.

A particular case of formula [10] has been given by Pound (16) corresponding to $I = 5/2$, and to a special set of orientations of a uniaxial single crystal obtained by rotating the crystal about an axis perpendicular to the plane containing H_0 and the axis of symmetry of the crystal. Setting $I = 5/2$, $\lambda = 2\Delta\nu/\nu_0$, and using equation (18) of Ref. (16) for the special form of ∇E corresponding to a uniaxial

crystal in the above special set of orientations, it may be verified that our equation [10] reduces[4] to Pound's equations (22)–(24). Another particular case for $I = 3/2$, $\eta = 0$ has been given by Becker (2).

In the case of half integral I the resonance line has a central component $\frac{1}{2} \leftrightarrow -\frac{1}{2}$, and $I - \frac{1}{2}$ pairs of satellites $m \leftrightarrow m - 1$ and $-(m - 1) \leftrightarrow -m$ with $I \geqslant m > \frac{1}{2}$. We shall refer to such a pair by stating the largest of the four m values involved. In the case of integral I there is no central component, but there are I pairs of satellites with $I \geqslant m > 0$. The frequency difference between the two members of each pair of satellites is given by:

$$[17] \qquad (\nu' - \nu'')_m = 2\nu_0\lambda(2m - 1)\left[\frac{(\nabla E)'_0}{eq} + \frac{\lambda^2}{3} P_3(m) + 0(\lambda^4)\right].$$

The displacement with respect to the unperturbed Larmor frequency ν_0 of the center of gravity $\bar{\nu}_m \equiv (\nu' + \nu'')_m/2$ of each such pair of satellites, or of the central component, is given by:

$$[18] \qquad \bar{\nu}_m - \nu_0 = \tfrac{1}{3}\lambda^2\nu_0 P_2(m) + 0(\lambda^4).$$

In our earlier paper (18) we considered only such weak quadrupole interactions for which it is permissible to neglect all powers of λ higher than the first. This means that to the first order the central component, and the center of gravity of each pair of satellites, shows no displacement as a result of quadrupole interaction, while the frequency difference of each pair of satellites is given by:

$$[19] \qquad (\nu' - \nu'')_m = \frac{3(2m - 1)}{I(2I - 1)} \cdot \frac{e^2qQ}{h} \cdot \frac{(\nabla E)'_0}{eq}.$$

This formula was the starting point of the calculations of our earlier paper (18).

In the present paper we extend our calculations to the second order in λ to explain the observed dependence on crystal orientation of the shift $\bar{\nu}_m - \nu_0$ of the central component and of the center of gravity of each pair of satellites in the case of somewhat stronger quadrupole coupling. Equations [17] and [18] are the basic formulae.

3. ROTATION OF THE CRYSTAL ABOUT AN AXIS PERPENDICULAR TO THE MAGNETIC FIELD

As in Ref. (18) we introduce an arbitrary rectangular set of axes X, Y, Z fixed with respect to the crystal, and study the relation between the components of ∇E in this system of axes, and in the laboratory system of axes x', y', z', as the crystal is rotated about, say, its X axis which is kept in coincidence with the y' axis perpendicular to H_0. The initial position of the crystal, in which the angle of rotation is zero, is chosen so that Y, Z coincide with z', x'. This transformation may, of course, be obtained from the general theory of the representations of the rotation group as indicated by Bersohn (3). However, the results may also

[4] *Prof. Pound has kindly informed us that on checking the third order terms of his equations he finds that $197z^2 - 17$ in his equation (23) and $279z^2 + 6$ in his equation (22) should be replaced respectively by $225z^2 - 33$ and $285z^2 + 3$. Our expression reduces to this corrected form of Pound's equations.*

be readily obtained in an elementary way by direct substitution in terms of Cartesian coordinates following the procedure of equations (7), (8) of Ref. (18). The transformation is then given by:

$$(\nabla E)'_0 = \tfrac{1}{4}(\phi_{YY} + \phi_{ZZ}) + \tfrac{1}{4}(\phi_{YY} - \phi_{ZZ})\cos 2\theta_X - \tfrac{1}{2}\phi_{YZ}\sin 2\theta_X,$$

$$[20]\quad (\nabla E)'_{\pm 1} = \frac{1}{\sqrt{6}}[\mp\{\phi_{YZ}\cos 2\theta_X + \tfrac{1}{2}(\phi_{YY} - \phi_{ZZ})\sin 2\theta_X\} - i\{\phi_{XY}\cos\theta_X - \phi_{ZX}\sin\theta_X\}],$$

$$(\nabla E)'_{\pm 2} = \frac{1}{2\sqrt{6}}\left[\frac{3}{2}(\phi_{YY} + \phi_{ZZ}) - \frac{1}{2}(\phi_{YY} - \phi_{ZZ})\cos 2\theta_X + \phi_{YZ}\sin 2\theta_X \pm 2i(\phi_{ZX}\cos\theta_X + \phi_{XY}\sin\theta_X)\right].$$

Combination of the first of equations [20] with the first order term of equation [17] leads to the following expression[5] which has been discussed in detail in Ref. (18):

$$[21]\quad (\nu' - \nu'')_X = \tfrac{1}{2}(2m-1)(a_X + b_X\cos 2\theta_X + c_X\sin 2\theta_X) = \tfrac{1}{2}(2m-1)[a_X + R_X\cos 2(\theta_X - \delta_X)] = \tfrac{1}{2}(2m-1)[L_0 + L_1 S_X]$$

with

$$[22]\quad \begin{aligned} a_X &\equiv L_0 + \tfrac{1}{2}L_1 = \nu_0\lambda(\phi_{YY} + \phi_{ZZ})/eq, \\ b_X &\equiv R_X\cos 2\delta_X = \nu_0\lambda(\phi_{YY} - \phi_{ZZ})/eq, \\ c_X &\equiv R_X\sin 2\delta_X = -2\nu_0\lambda\phi_{YZ}/eq, \\ R_X &\equiv \tfrac{1}{2}L_1, \\ S_X &\equiv \cos^2(\theta_X - \delta_X). \end{aligned}$$

We may always choose δ_X in the range $-\frac{1}{2}\pi < \delta_X \leqslant \frac{1}{2}\pi$, so as to make $R_X \geqslant 0$. A simultaneous reversal of sign of a_X, b_X, c_X and a change of δ_X by $\pi/2$ leaves $R_X \geqslant 0$. Similar expressions for the Y and Z rotations may be obtained by cyclic permutation of subscripts.

Substitution of the last two equations [20] into equations [18] and [11] gives the extension of the above theory to the second order in λ. The second order contributes nothing new to the splitting of each pair of satellites, but gives a shift of the center of gravity $\bar{\nu}_m$ of each pair and of the central component. Thus, for the X rotation:

$$[23]\quad (\bar{\nu}_m - \nu_0)_X = n_X + p_X\cos 2\theta_X + r_X\sin 2\theta_X + u_X\cos 4\theta_X + v_X\sin 4\theta_X = n_X + P_X\cos 2(\theta_X - \gamma_X) + U_X\cos 4(\theta_X - \delta_X)$$

[5] *The a, b, c of equations [21], [22] differ from the A, B, C of Ref. (18) only by the factor (2m − 1)/2 to make them independent of m. They satisfy the same identities as A, B, C.*

with

$$n_X = \frac{1}{576\nu_0}[18c_2 a_X{}^2 + (c_2 - 4c_1)(b_X{}^2 + c_X{}^2) + 4(c_2 - c_1)(c_Y{}^2 + c_Z{}^2)],$$

$$p_X \equiv P_X \cos 2\gamma_X = \frac{1}{576\nu_0}[-12c_2 a_X b_X + 4(c_2 + c_1)(c_Y{}^2 - c_Z{}^2)],$$

[24] $$r_X \equiv P_X \sin 2\gamma_X = \frac{1}{576\nu_0}[-12c_2 a_X c_X + 8(c_2 + c_1)c_Y c_Z],$$

$$u_X \equiv U_X \cos 4\delta_X = \frac{1}{576\nu_0}(c_2 + 4c_1)(b_X^2 - c_X^2),$$

$$v_X \equiv U_X \sin 4\delta_X = \frac{1}{576\nu_0}(c_2 + 4c_1)\, 2b_X c_X,$$

where c_1 and c_2 are functions of I and m defined by equation [16], and a_X, b_X, c_X, c_Y, c_Z are defined in terms of ϕ_{ij} by equation [22]. Comparison of b_X and c_X in equation [22] with the last two equations [24] shows that we are indeed justified in using the same δ_X in both cases, and gives

[25] $$R_X = 24[\nu_0 U_X/(c_2 + 4c_1)]^{\frac{1}{2}},$$

[26] $$U_X = \pm (u_X^2 + v_X^2)^{\frac{1}{2}}$$

where the sign of U_X is chosen in agreement with that of $(c_2 + 4c_1)$. Two possible values of δ_X differing by $\pi/2$, both lying in the range $-\frac{1}{2}\pi < \delta_X \leqslant \frac{1}{2}\pi$, may be found to satisfy equation [24], corresponding to a simultaneous reversal of sign of b_X, c_X in equation [22]. If $c_Y = c_Z = 0$ then $r_X/p_X = c_X/b_X$ and we may choose $\gamma_X = \delta_X$, which does not necessarily vanish. If $c_Z = c_X = 0$ then $r_X = v_X = 0$, and $\gamma_X = \delta_X = 0$. Similar expressions for rotations about the Y and Z axes may be obtained by cyclic permutation of subscripts. In the case that one of the X, Y, Z axes coincides with a principal axis that pair of c_X, c_Y, c_Z which refers to the other two axes will vanish, so that we may choose $\gamma = \delta$ for all three axes, and equation [23] may be written in the form:

[27] $$\bar{\nu} - \nu_0 = K_0 + K_1 s + K_2 s^2$$

where $s \equiv \cos^2(\theta - \delta)$, and the coefficients n, P, U of equation [24] are related to the K_i of equation [27] by:

[28] $$\begin{aligned} n &\equiv K_0 + \tfrac{1}{2}K_1 + \tfrac{3}{8}K_2, \\ P &\equiv \tfrac{1}{2}(K_1 + K_2), \\ U &\equiv \tfrac{1}{8}K_2. \end{aligned}$$

Equations [21] and [23] give the explicit dependence of the first order splitting and of the second order shift of the resonance frequencies of satellite pairs on the angular position of the crystal in the constant external magnetic field. In the former case only constant terms, and terms in 2θ are involved. In the latter case terms in 4θ occur as well. These two equations lie at the basis of analyzing experimental results on crystal rotations.

4. SUMMARY OF INFORMATION AVAILABLE FROM CRYSTAL ROTATIONS

The following points should be noted in connection with equations [21] and [23].

1. It is seen from equations [21], [22], and [15] that the magnitude of the first order splitting between the two members of a pair of satellites is independent of ν_0 and therefore of H_0. Also, the first order splitting of various pairs of satellites differs only by the constant factor $(2m - 1)/2$, but has the same dependence on crystal orientation. There is no second order contribution to the splitting at all, a deviation from first order splitting occurring only if third order effects are observable. If third order effects are not observable the splittings of all pairs of satellites vanish for the *same* crystal position.

2. It is seen from equations [23], [24], [22] that the central component and the centers of gravity of various satellite pairs do not show a first order shift at all. The second order shift is inversely proportional to ν_0, and therefore to H_0. The Fourier coefficients n, p, r, u, v depend on m through c_1 and c_2 defined by equations [16]. Therefore the dependence on crystal orientation of the shift of the center of gravity of each satellite pair will vary from pair to pair. There is no third order contribution to the shift at all, the next term being of the fourth order.

3. If second order effects are negligible, and the centers of gravity of all satellite pairs lie at ν_0, crystal positions may be found for which all the line components merge into a single line at ν_0. This was observed in Ref. (18) in the case of the Li^7 line in spodumene. When second order effects become pronounced it will no longer be necessarily possible to find a crystal position in which all the line components merge into a single line. The crystal position, which will cause the splitting of each satellite pair to vanish, will in general correspond to a different shift from ν_0 for each coalesced satellite pair.

4. The Fourier coefficients a, b, c, n, p, r, u, v, in equations [21], [23], or the equivalent set a, R, n, P, U and the phase angles γ, δ may be experimentally determined by a Fourier analysis of the observed dependence of $\nu' - \nu''$, and of $\bar{\nu} - \nu_0$ on crystal orientation for a rotation about *any* arbitrary axis perpendicular to H_0. With this in view it is recommended that readings be taken for, say, 12 or 24 *equally* spaced positions of the crystal so that standard methods of Fourier analysis of experimental curves, as given for instance by Whittaker and Robinson (22), are directly applicable. Although only second and fourth harmonics are expected in equations [21] and [23] the analysis of the 12 point curve is made into all harmonics up to the sixth cosine, and the fifth sine term. This guarantees a least squares fit for the second and fourth harmonics. In equation [21] for any arbitrary choice of X axis it is always possible to choose the Y axis so as to make $c_X = 0$, i.e., to make $\delta_X = 0$ or $\pi/2$, so that the curve [21] is symmetrical about $\theta_X = 0$. This direction is not necessarily of any direct crystallographic significance. If, however, the curve [23] is symmetrical about the same point, so that $\gamma_X = \delta_X = 0$ or $\pi/2$, then it means that in addition to $C_X = 0$ we have $C_Z = 0$ or $C_Y = 0$, or both $C_Z = C_Y = 0$. Corresponding to each of these three possibilities in turn, either the Y axis, or the Z axis, or both, are principal axes of the

ϕ_{ij} tensor at the nuclear sites. Similar results for rotations about the other two axes may be obtained by cyclic permutation of X, Y, Z.

5. A new method of determining the nuclear spin I is available, which is alternative to counting the $2I$ components into which the magnetic resonance line is split by the quadrupole interaction. This is of interest in those cases where I is large, and where, owing to crystal imperfections, the satellites for high m values are so broad and weak that it is difficult to be certain that none have been missed. For a rotation about an arbitrary axis empirical values of R (or b and c) may be obtained from a Fourier analysis of $\nu' - \nu''$ of equation [21] for the innermost (strongest) pair of satellites ($m = 3/2$ for half integral I, or $m = 1$ for integral I). Likewise, empirical values of U (or u and v) may be obtained from a Fourier analysis of $\bar{\nu} - \nu_0$ of equation [23] either for the same innermost satellite pair, or for the central component ($m = \frac{1}{2}$) for half integral I. These empirical Fourier coefficients determine $c_2 + 4c_1$ in equations [25] or [24]. c_2 and c_1 are in turn related to the spin I by equation [16]. The nuclear spin I may then be found from any one of the alternative expressions:

$$[29] \quad \frac{c_2 + 4c_1}{18} \equiv (I + \tfrac{3}{2})(I - \tfrac{1}{2}) - \tfrac{17}{3}(m - \tfrac{1}{2})^2 = \frac{32\nu_0 U}{R^2} = \frac{32\nu_0 u}{b^2 - c^2} = \frac{16\nu_0 v}{bc}.$$

The values of R (or b and c) as defined in equation [21] are independent both of ν_0 and m. The second order coefficients U (or u and v) of equation [23] are inversely proportional to ν_0 and depend on m. Thus the value of m to be inserted into equation [29] depends on whether the empirical values of U (or u and v) are obtained from the central component or from one of the satellite pairs.

6. To obtain a complete determination of the tensor $\nu_0 \lambda \phi_{ij}/eq$, i.e. an evaluation of the quadrupole coupling constant $|C_z| \equiv |eQ\phi_{zz}/h|$, of the asymmetry parameter $\eta = (\phi_{xx} - \phi_{yy})/\phi_{zz}$, and of the orientation of the principal axes of the tensor ϕ_{ij}, one must obtain experimentally five quantities: c_X, c_Y, c_Z and any pair a_i, b_i ($i = X, Y, Z$). The procedure of Ref. (18) may then be followed[6] to obtain the desired information.

7. If only the first order effects of equation [21] are observable, then, as shown in Ref. (18), *three* rotations of the crystal about three mutually perpendicular, but otherwise arbitrary, axes are required to give c_X, c_Y, c_Z, a_i, b_i. If the orientation of one of the principal axes is known in advance from crystal symmetry, and this axis is used as the X axis of crystal rotation (this fixes $c_Y = c_Z = 0$), then a *single* rotation about this axis is sufficient to determine the three remaining quantities a_X, b_X, c_X.

8. If the second order shifts of equation [23] are observable, then at first glance it might appear that a single rotation about an arbitrary axis should be sufficient to provide complete information. If satellites are visible, then a_X, b_X, c_X are available from the analysis of the first order effect of equation [21], and one might then hope to obtain c_Y and c_Z from the second and third of equations [24]. Even if no satellites are visible, but only the central component $m = \frac{1}{2}$ of the line for half integral I appears, one might still expect that the five experimental

[6] *A typographical error in equation (20) of Ref. (18) should be corrected by replacing the index 1/2 by 1/3.*

Fourier coefficients of equation [23] should uniquely determine the five quantities a_X, b_X, c_X, c_Y, c_Z through equations [24]. However, it is clear that since only terms quadratic in c_Y, c_Z appear in equations [24], we can determine only the relative sign between c_Y and c_Z, but not their sign relative to a_X, b_X, c_X. This will leave an ambiguity in the orientation of the principal axes. Moreover, if only the central component is visible, there will be an ambiguity in the value of a_X. It turns out that both these ambiguities can in general be removed by a *second* rotation of the crystal about an axis perpendicular to the first one, so that *two* rotations are sufficient in the general case. As in the case of the first order effects, a *single* rotation about a *known* principal axis turns out to be sufficient to give a complete analysis, even if only the central component alone is visible.

5. DETAILED ANALYSIS OF THE ROTATION ABOUT AN ARBITRARY AXIS

We now proceed to a more detailed analysis of the rotation in the case of an arbitrary choice of the axis of rotation. We shall consider two cases: (i) when at least the first pair of satellites ($m = 3/2$ for half integral I, $m = 1$ for integral I) is visible, and (ii) when only the central component ($m = \frac{1}{2}$) is visible for a half integral I.

In case (i) the spin I can be determined from equation [29], so that in subsequent discussion the coefficients c_1 and c_2 are assumed to be known. In case (ii) the spin I has to be known in advance to obtain the absolute value of the quadrupole coupling constant, but the asymmetry parameter η and the orientation of the principal axes may be determined without a knowledge of I.

Case i.—The set of constants a_X, b_X, c_X, or a_X, R_X, δ_X is obtained from a Fourier analysis of the experimental curve of the form of equation [21] for the splitting $\nu' - \nu''$ between the "innermost" pair of satellites ($m = \frac{1}{2}$ or $m = 1$ for half-integral or integral spin respectively). Independent values of b_X, c_X (or R_X, δ_X) may be obtained from the experimental values of u_X, v_X in equation [23], with the aid of U_X, δ_X obtained from equations [26] and [24]. R_X is given by equation [25]. b_X and c_X are then given in terms of R_X and δ_X by equations [22]. The first three of equations [24] now determine the three real quantities a_X, c_Y, c_Z by the conditions:

$$(c_Y + ic_Z)^2 = S_X e^{2i\gamma_X} + a_X T_X e^{2i\delta_X},$$

$$c_Y^2 + c_Z^2 = M_X - N a_X^2, \qquad [30]$$

with S_X, T_X, M_X, N given in terms of the experimental Fourier coefficients, and the known constants c_1, c_2 by:

$$S_X = \frac{576\nu_0 P_X}{4(c_1 + c_2)},$$

$$T_X = \frac{3c_2}{c_1 + c_2} R_X, \qquad [31]$$

$$M_X = \frac{576\nu_0}{4(c_2 - c_1)}\left[n_X + \frac{4c_1 - c_2}{4c_1 + c_2} U_X\right],$$

$$N = \frac{9c_2}{2(c_2 - c_1)}.$$

Here the sign of P_X in

$$P_X = \pm (p_X^2 + r_X^2)^{\frac{1}{2}} \tag{32}$$

depends on which one of the two possible values of γ_X differing by $\frac{1}{2}\pi$ and restricted to the range $-\frac{1}{2}\pi < \gamma_X \leqslant \frac{1}{2}\pi$ is selected in conformity with equation [24]. The relative signs of a_X, b_X, c_X are determined by equations [22], [30], [31] irrespectively of which of the two possible values of δ_X differing by $\pi/2$ is selected, since all three quantities simultaneously reverse sign if δ_X is changed by $\pi/2$. Two values of a_X are given in general by the two real roots a_X' and a_X'' of:

$$M_X - Na_X^2 = [S_X^2 + 2a_X S_X T_X \cos 2(\gamma_X - \delta_X) + a_X^2 T_X^2]^{\frac{1}{2}}. \tag{33}$$

Only that root need be taken into account which agrees with the value of a_X determined from the Fourier analysis of equation [21], and this serves as an independent experimental check on that value. The values of c_Y and c_Z may then be determined from equation [30] which will yield their sign relative to each other, but not relative to a_X, b_X, c_X. This corresponds to a possible reflection of the principal axes system in the YZ plane. To determine which is the actual orientation of the principal axes system, a second rotation about the Y axis may be performed, which will fix the relative sign between c_Z and c_X, and between c_Y, b_Y, and a_Y. Use of the identities

$$\begin{aligned} a_X &= \tfrac{1}{2}(b_Y - a_Y) = -\tfrac{1}{2}(b_Z + a_Z), \\ b_X &= -\tfrac{1}{2}(3a_Y + b_Y) = \tfrac{1}{2}(3a_Z - b_Z) \end{aligned} \tag{34}$$

will then fix the relative sign between c_Y and a_X, b_X. Thus two rotations about two mutually perpendicular axes will determine the five quantities a_X, b_X, c_X, c_Y, c_Z up to a common sign (corresponding to our inability of determining the sign of the quadrupole coupling constant). If the X and Y axes should both happen to be picked perpendicular to a principal axis, then $c_X = c_Y = 0$ and the sign of c_Z relative to a_X, b_X still remains undetermined. However, in this case the complete information is available from a single rotation about the Z axis, as will be shown below.

Case ii.—If only the central component $m = \frac{1}{2}$ of a line for half integral I is observable, then the direct information on a_X, b_X, c_X from equation [21] is not available, but two rotations are still sufficient. We note from equations [16] that for $m = \frac{1}{2}$

$$c_1 = 2c_2 = 4(I + \tfrac{3}{2})(I - \tfrac{1}{2}) \tag{35}$$

so that in equations [25], [31] R_X, $S_X^{\frac{1}{2}}$, T_X, and $M_X^{\frac{1}{2}}$ are all proportional to $[(I + \frac{3}{2})(I - \frac{1}{2})]^{-\frac{1}{2}}$. This shows that a_X, b_X, c_X, c_Y, c_Z, and therefore the eigenvalues of $\lambda\nu_0\phi_{ij}/eq$, will all be proportional to this same factor, while the asymmetry parameter and the principal axes orientation will be independent of this factor. In this case we have no guide from $\nu' - \nu''$ as to which of the two roots of equation [33] is the correct one, but we can find the correct one by performing a second rotation about the Y axis, determining two possible values of a_Y, and seeing which values satisfy the identities [34].

6. SIMPLIFIED ANALYSIS OF ROTATION ABOUT A KNOWN PRINCIPAL AXIS

The situation is considerably simplified if the orientation of one of the principal axes is known in advance from crystal symmetry, and this axis is chosen as the X axis of rotation. We then have $c_Y = c_Z = 0$, so that we may take $\delta_X = \gamma_X$ in equations [23], [24], and consequently equations [27], [28] hold. Two values of δ_X differing by $\frac{1}{2}\pi$ and lying in the interval $-\frac{1}{2}\pi < \delta_X \leqslant \frac{1}{2}\pi$ can be obtained from the experimental curves of either $\pm(\nu' - \nu'')$ of equation [21], or $\bar{\nu} - \nu_0$ of equation [23] plotted against θ_X by observing the two values of θ_X differing by $\frac{1}{2}\pi$, and both lying in the range $-\frac{1}{2}\pi < \theta_X \leqslant \frac{1}{2}\pi$, about which the curve is symmetrical.

In case that at least one pair of satellites is visible the values of a_X, R_X can be obtained directly from the experimental curve [21]. As shown in Ref. (18) the three eigenvalues $\nu_0\lambda$, $-\nu_0\lambda(1 \pm \eta)/2$ of the tensor $\nu_0\lambda\phi_{ij}/eq$ are then given by:

$$[36] \qquad -a_X,\ \tfrac{1}{2}(a_X \pm R_X)\,.$$

The eigenvalue $-a_X$ corresponds to the principal axis coincident with the X axis of rotation. The eigenvalue $\frac{1}{2}(a_X + R_X)$ corresponds to that principal axis which coincides with the magnetic field when $\theta_X = \delta_X$.

If no satellites are visible, but only the central component $m = \frac{1}{2}$ for a line with half integral I, we can still obtain the complete analysis by making use of experimental values of n_X, P_X, U_X in equation [23] with $\gamma_X = \delta_X$. R_X is given by equation [25], while from equation [30] with $c_Y = c_Z = 0$ we obtain:

$$[37] \qquad \begin{aligned} a_X &= -S_X/T_X = -48\nu_0 P_X/c_2 R_X, \\ a_X^{\,2} &= M_X/N = \frac{32\nu_0}{c_2}\left[n_X + \frac{4c_1 - c_2}{4c_1 + c_2}\,U_X\right]. \end{aligned}$$

The first of equations [37] gives both the magnitude of a_X, and its sign, while the second of equations [37] gives a check on the magnitude of a_X. The eigenvalues are then given by equation [36] as before, and the value of η and the assignment of the principal axes is obtained as before. If the value of I is not known in advance the eigenvalues will contain, through c_1 and c_2 given by equation [35], a common unknown factor $[(I + \frac{3}{2})(I - \frac{1}{2})]^{-\frac{1}{2}}$ which will not interfere with the evaluation of η or of δ_X.

The above completes the determination of the eigenvalues and the orientation of the principal axes of the tensor $\lambda\nu_0\phi_{ij}/eq$ both in the general case of arbitrary orientation of the axes, and in the special case when the orientation of one of the principal axes is known in advance. The corresponding quadrupole coupling constants can then be determined by multiplying the eigenvalues by $2I(2I-1)/3$ in accordance with equation [15]. If one wishes to restrict the asymmetry parameter $\eta = (\phi_{xx} - \phi_{yy})/\phi_{zz}$ to the range $0 \leqslant \eta \leqslant 1$ then the labels x, y, z must be attached to the principal axes in such a way as to make the x axis correspond to the eigenvalue with the smallest absolute value, and the z axis to the one with largest absolute value. Alternatively, if η is left unrestricted in value, then the principal axes may be named quite arbitrarily.

7. SOME EXPLICIT FORMULAE FOR THE CASE OF KNOWN ORIENTATION OF ONE OF THE PRINCIPAL AXES

In the special case when the orientation of one of the principal axes is known in advance, and this axis is chosen as the X axis of rotation, it is useful to have explicit expressions for the coefficients in equations [21], [23] for the X, Y, Z rotations in terms of I, m, ν_0, C_z, η, and the angle δ between the Y axis and a second principal axis. If the value of the asymmetry parameter η is not restricted in advance to the range $0 \leqslant \eta \leqslant 1$, we may call the principal axis coincident with the X rotation axis the x axis of ϕ_{ij} (corresponding to the eigenvalue $-eq(1-\eta)/2$), and we may denote the angle between the y principal axis (corresponding to the eigenvalue $-eq(1+\eta)/2$) and the Y axis by δ. A positive δ implies that a positive rotation about the X axis will bring the y axis into the position along H_0, initially occupied by the Y axis. We have then:

$$
\begin{aligned}
&\phi_{XX} = \phi_{xx} = -\tfrac{1}{2}\, eq(1-\eta),\\
&\phi_{YY} = \cos^2\delta\ \phi_{yy} + \sin^2\delta\ \phi_{zz} = \tfrac{1}{4}\, eq[(1-\eta) - (3+\eta)\cos 2\delta],\\
&\phi_{ZZ} = \sin^2\delta\ \phi_{yy} + \cos^2\delta\ \phi_{zz} = \tfrac{1}{4}\, eq[(1-\eta) + (3+\eta)\cos 2\delta],\\
&\phi_{XY} = \phi_{ZX} = 0,\\
&\phi_{YZ} = -\cos\delta \sin\delta\ (\phi_{yy} - \phi_{zz}) = \tfrac{1}{4}\, eq(3+\eta)\sin 2\delta.
\end{aligned}
\tag{38}
$$

This leads in accordance with equations [22] to the following expressions for the coefficients in equations [21]:

$$
\begin{aligned}
&a_X = \tfrac{1}{2}\,\nu_0\lambda(1-\eta),\\
&b_X = -\tfrac{1}{2}\,\nu_0\lambda(3+\eta)\cos 2\delta,\\
&c_X = -\tfrac{1}{2}\,\nu_0\lambda(3+\eta)\sin 2\delta,\\
&a_Y = -\tfrac{1}{4}\,\nu_0\lambda[(1-\eta) - (3+\eta)\cos 2\delta],\\
&b_Y = \tfrac{1}{4}\,\nu_0\lambda[3(1-\eta) + (3+\eta)\cos 2\delta],\\
&c_Y = 0,\\
&a_Z = -\tfrac{1}{4}\,\nu_0\lambda[(1-\eta) + (3+\eta)\cos 2\delta],\\
&b_Z = -\tfrac{1}{4}\,\nu_0\lambda[3(1-\eta) - (3+\eta)\cos 2\delta],\\
&c_Z = 0,
\end{aligned}
\tag{39}
$$

with

$$
\nu_0\lambda = \frac{3C_z}{2I(2I-1)}. \tag{40}
$$

It may be seen that in the last of equations [21] and its analogues for Y and Z rotations we have for the X, Y, Z rotations respectively:

$$
\begin{aligned}
&X\colon\ L_0 = 2\nu_0\lambda, \quad L_1 = -(3+\eta)\nu_0\lambda,\\
&Y\colon\ L_0 = -(1-\eta)\nu_0\lambda, \quad L_1 = [(3+\eta)\cos^2\delta - 2\eta]\nu_0\lambda,\\
&Z\colon\ L_0 = [2-(3+\eta)\cos^2\delta]\nu_0\lambda, \quad L_1 = [-(3-\eta) + (3+\eta)\cos^2\delta]\nu_0\lambda.
\end{aligned}
\tag{41}
$$

Similarly in equations [27] we have for the X rotation:

$$
\begin{aligned}
K_0 &= \tfrac{1}{4}c_2\eta^2\,\frac{\nu_0\lambda^2}{18},\\
K_1 &= -[\tfrac{1}{4}c_1(3+\eta)^2 + \tfrac{1}{4}c_2\eta(3+\eta)]\,\frac{\nu_0\lambda^2}{18},\\
K_2 &= \tfrac{1}{16}(c_2+4c_1)(3+\eta)^2\,\frac{\nu_0\lambda^2}{18};
\end{aligned}
\tag{42}
$$

for the Y rotation:

$$K_0 = \tfrac{1}{16}\, c_2(3+\eta)^2 \frac{\nu_0\lambda^2}{18},$$

$$[43]\quad K_1 = -\{\tfrac{1}{4}c_1[4\eta^2 + 3(1-\eta)(3+\eta)\cos^2\delta] + \tfrac{1}{8}c_2(3+\eta)[2\eta + 3(1-\eta)\cos^2\delta]\}\frac{\nu_0\lambda^2}{18},$$

$$K_2 = \tfrac{1}{16}\,(c_2 + 4c_1)[2\eta - (3+\eta)\cos^2\delta]^2 \frac{\nu_0\lambda^2}{18};$$

and for the Z rotation:

$$K_0 = \{-\tfrac{1}{4}c_1(3+\eta)^2\cos^2\delta\sin^2\delta + \tfrac{1}{16}\,c_2[2\eta - (3+\eta)\cos^2\delta]^2\}\frac{\nu_0\lambda^2}{18},$$

$$[44]\quad K_1 = \{\tfrac{1}{4}c_1[-(3-\eta)^2 + (3+\eta)(9-\eta)\cos^2\delta - 2(3+\eta)^2\cos^4\delta] + \tfrac{1}{8}c_2[2\eta(3-\eta) + (3+\eta)^2\cos^2\delta\sin^2\delta]\}\frac{\nu_0\lambda^2}{18},$$

$$K_2 = \tfrac{1}{16}\,(c_2 + 4c_1)[(3-\eta) - (3+\eta)\cos^2\delta]^2 \frac{\nu_0\lambda^2}{18}.$$

Special cases of equations [27], [42], [43] for $I = 5/2$, $m = 1/2$ (central component of the line for a nucleus with spin 5/2) were given in our preliminary communication (15). It may be noted that equations [43] and [44] remain unchanged if δ is replaced by $-\delta$, but that the sign of δ is uniquely determined by the X rotation through S_X of equation [22].

The correctness of the algebraic substitutions of equations [39] into equations [24], [28] which lead to equations [41]–[44] may be checked by noting that the results for the Z rotation are obtained from those for the Y rotation by replacing S_Y by $1 - S_Z$, $\cos^2\delta$ by $1 - \cos^2\delta$. Similarly, the results for the X rotation are obtained from those for the Y rotation by setting $\delta = 0$ in the Y results, and replacing η by $-\eta$ and S_Y by $1 - S_X$. Finally, the X results may be obtained from the Z results by setting $\delta = \pi/2$, changing η into $-\eta$, and S_Z into S_X. These transformations follow from considering the consequences of relabelling the axes.

8. SUMMARY OF RESULTS

Electric quadrupole interaction, if not excessively strong, splits a nuclear magnetic resonance line in a single crystal into $2I$ components, whose frequency differs from the unperturbed Larmor frequency ν_0 by an amount which depends on the angle θ through which the crystal has been rotated about an axis perpendicular to the magnetic field.

The frequency splitting $\nu' - \nu''$ between a pair of satellites depends only on odd powers of the quadrupole coupling constant C_z, and to the first order in C_z contains only terms independent of θ, and involving 2θ as given by equation [21].

The frequency shift $\bar{\nu} - \nu_0$ of the center of gravity of a pair of satellites depends only on even powers of C_z, and to the second order in C_z contains terms independent of θ, and involving 2θ and 4θ as given by equation [23].

Fourier analysis of experimental curves of $\nu' - \nu''$ and $\bar{\nu} - \nu_0$ as functions of θ yields a set of Fourier coefficients from which $|C_z|$, η, and the orientation of the principal axes of ∇E may be found by methods of section 5 in the general case, and by the simpler methods of section 6 when the axis of rotation is known to coincide with a principal axis of ∇E.

Conversely, given $|C_z|$, η, and the orientation of the principal axes, the expected dependence of $\nu' - \nu''$ and $\bar{\nu} - \nu_0$ on θ may be quickly computed from formulae of section 7 applicable to those cases when the axis of rotation is either parallel or perpendicular to a principal axis of ∇E. In the more general case results of section 3 may be used.

A new method of measuring nuclear spin is described in section 4.

All the above points are illustrated on the experimental example of the Al^{27} line in spodumene in the companion paper (14) immediately following this one.

9. ACKNOWLEDGMENTS

The continuing financial aid of the National Research Council of Canada in the form of grants-in-aid of the experimental program which gave rise to this work is gratefully acknowledged. I am indebted to my experimental co-workers and students Dr. H. E. Petch and Mr. N. G. Cranna for many stimulating discussions of the above theory, and for checking parts of it.

REFERENCES

1. ALLEN, H. C. J. Am. Chem. Soc. 74: 6074. 1952.
2. BECKER, G. Z. Physik, 130: 415. 1951.
3. BERSOHN, R. J. Chem. Phys. 20: 1505. 1952.
4. CARR, E. F. and KIKUCHI, C. Phys. Rev. 78: 1470. 1950.
5. DEAN, C. Phys. Rev. 86: 607. 1952.
6. DEAN, C. and POUND, R. V. J. Chem. Phys. 20: 195. 1952.
7. DEHMELT, H. G. and KRÜGER, H. Naturwissenschaften, 37: 111. 1950; Z. Physik, 129: 401. 1950.
8. DEHMELT, H. G. and KRÜGER, H. Z. Physik, 130: 385. 1951.
9. KRÜGER, H. Z. Physik, 130: 371. 1951.
10. KRÜGER, H. and MEYER-BERKHOUT, U. Z. Physik, 132: 221. 1952.
11. LAMARCHE, G. and VOLKOFF, G. M. Can. J. Phys. In press.
12. LIVINGSTON, R. J. Chem. Phys. 19: 1434. 1951; 20: 1170. 1952. J. Phys. Chem. 1953. In press.
13. MEAL, H. C. J. Am. Chem. Soc. 74: 6121. 1952.
14. PETCH, H. E., CRANNA, N. G., and VOLKOFF, G. M. Can. J. Phys. 31: 837. 1953.
15. PETCH, H. E., VOLKOFF, G. M., and CRANNA, N. G. Phys. Rev. 88: 1201. 1952.
16. POUND, R. V. Phys. Rev. 73: 1247. 1948; 79: 685. 1950.
17. TOWNES, C. H. and DAILEY, B. P. J. Chem. Phys. 20: 35. 1952.
18. VOLKOFF, G. M., PETCH, H. E., and SMELLIE, D. W. L. Can. J. Phys. 30: 270. 1952.
19. WATKINS, G. D. and POUND, R. V. Phys. Rev. 85: 1062. 1952.
20. WEISS, P. R. Phys. Rev. 73: 470. 1948.
21. WHITMER, C. A., WEIDNER, R. T., HSIANG, J. S., and WEISS, P. R. Phys. Rev. 74: 1478. 1948.
22. WHITTAKER, E. T. and ROBINSON, G. The calculus of observations. Blackie and Son Ltd., London. 1924.

SECOND ORDER NUCLEAR QUADRUPOLE EFFECTS IN SINGLE CRYSTALS

PART II. EXPERIMENTAL RESULTS FOR SPODUMENE[1]

By H. E. Petch,[2] N. G. Cranna,[3] and G. M. Volkoff

ABSTRACT

Experiments on the splitting of the Al^{27} resonance absorption line in a single crystal of $LiAl(SiO_3)_2$ (spodumene) are described, and are used to illustrate the second order theory of Part I. $|eQ\phi_{zz}/h|$ for Al^{27} nuclei in spodumene is found to be 2950 ± 20 kc./sec. $\eta \equiv (\phi_{xx} - \phi_{yy})/\phi_{zz}$ at Al sites is found to be 0.94 ± 0.01. The x principal axis (corresponding to the smallest eigenvalue ϕ_{xx}) of ϕ_{ij} at the Al sites is found to coincide with the b axis of the monoclinic spodumene crystal. The other two principal axes lie in the ac plane with the y axis (corresponding to the intermediate eigenvalue ϕ_{yy}) making an angle of $56° \pm \frac{1}{2}°$ with the crystal c axis towards the a axis. The y principal axis at the Al sites and the z principal axis at the Li sites appear to point at the projection of the nearest oxygen ion in each case. The new method of spin determination proposed in Part I is checked by confirming the known value $I = 5/2$ for Al^{27}.

1. INTRODUCTION

In the immediately preceding companion paper (7), Part I Theoretical, a survey and bibliography were given of the various experimental and theoretical studies that have been made to date of the electric quadrupole interaction of non spherically symmetric nuclei with the electric field gradients existing at the sites of such nuclei in single crystals. The theory of the case when the nuclear electric quadrupole interaction is somewhat smaller than the Zeeman energy of the nuclei in an external uniform magnetic field H_0 was then considered in detail. Explicit formulae were derived by second and third order perturbation theory for the dependence of the nuclear resonance frequencies on the angle of rotation of the crystal about an axis perpendicular to H_0. The results were stated for arbitrary (a) nuclear spin I, (b) magnetic quantum number m of the states involved in the transition, (c) ratio of quadrupole to Zeeman energy $eQ\phi_{zz}/\mu H_0 < 1$, (d) asymmetry parameter $\eta \equiv (\phi_{xx} - \phi_{yy})/\phi_{zz}$, and ($e$) orientation with respect to H_0 and the rotation axis of the principal axes of the electric field gradient tensor ϕ_{ij}.

In section 2 below we specialize the results of Part I for $I = 5/2$, and for the crystal rotation axis being chosen either parallel or perpendicular to one of the principal axes of ϕ_{ij}. These results are used in subsequent sections to analyze our experimental data for the Al^{27} resonance in a single crystal of $LiAl(SiO_3)_2$ (spodumene) in which it is known from crystal symmetry that one of the principal axes of ϕ_{ij} at both the Li and the Al sites must coincide with the b axis of the monoclinic crystal. Some results on the central component of the Al^{27} line have been reported in a preliminary communication (4), and are now extended and supplemented by additional measurements on the satellites.

[1] *Manuscript received April 28, 1953.*
Contribution from the Department of Physics, University of British Columbia, Vancouver, B.C. Work supported by grants from the National Research Council of Canada.

[2] *Past holder of a Research Council of Ontario Scholarship. Now with the Physics Department, McMaster University, Hamilton, Ontario.*

[3] *Past holder of a Research Council of Ontario Scholarship; present holder of a National Research Council of Canada Fellowship.*

Section 3 describes the spodumene samples used, and outlines the experimental procedure.

Section 4 presents the experimental results on the Al^{27} line in spodumene. The dependence of the line frequencies on H_0 is verified. The new method of spin determination proposed in Part I is illustrated by using it to confirm the known spin $I = 5/2$ for Al^{27}. The orientation of the principal axes of ϕ_{ij}, and the value of η at the Al sites, and the absolute value of the quadrupole coupling constant for Al^{27} in spodumene are obtained by analyzing the experimental results in terms of the second order perturbation theory of Part I which is summarized in section 2.

Section 5 brings together the results on Li^7 in spodumene reported in an earlier paper (8) and the new results on Al^{27}, and contains a brief discussion of these results.

2. SUMMARY OF RELEVANT THEORY FROM PART I, SPECIALIZED FOR $I = 5/2$

A nucleus of half integral spin I gives rise to a resonance line consisting of a central component $(\frac{1}{2} \leftrightarrow -\frac{1}{2})$, and $I - \frac{1}{2}$ pairs of satellites $m \leftrightarrow m - 1$, $-(m-1) \leftrightarrow -m$ with $3/2 \leqslant m \leqslant I$. For $I = 5/2$ there will be an "inner" pair of satellites $(m = 3/2)$, and an "outer" pair $(m = 5/2)$.

The frequency difference between two members of a pair of satellites depends only on odd powers of the quadrupole coupling constant $C_z \equiv eQ\phi_{zz}/h$ and, if third order effects are negligible, is given in terms of the angle of rotation θ of the crystal about any axis perpendicular to H_0 by:

$$\begin{aligned}(\nu' - \nu'')_m &= \tfrac{1}{2}(2m-1)\,(a + b\cos 2\theta + c \sin 2\theta) \\ &= \tfrac{1}{2}(2m-1)\,[a + R\cos 2(\theta - \delta)] \\ &= \tfrac{1}{2}(2m-1)\,(L_0 + L_1 s)\end{aligned} \tag{1}$$

where

$$s \equiv \cos^2(\theta - \delta)\,. \tag{2}$$

The quantities a, b, c, R, δ, L_0, L_1, are expected to be independent of m and H_0, and can be obtained from a Fourier analysis of the experimental curve of $\nu' - \nu''$ against θ.

The shift from the unperturbed Larmor frequency ν_0 of the frequency $\bar{\nu}$ of the central component, or of the center of gravity of a pair of satellites $\bar{\nu}_m = (\nu' + \nu'')_m/2$, depends only on even powers of C_z and, if fourth order effects are negligible, is given by:

$$\begin{aligned}\bar{\nu}_m - \nu_0 &= n + p\cos 2\theta + r \sin 2\theta + u\cos 4\theta + v \sin 4\theta \\ &= n + P\cos 2(\theta - \gamma) + U\cos 4(\theta - \delta)\,.\end{aligned} \tag{3}$$

The coefficients n, p, r, u, v, P, U are expected to be inversely proportional to H_0, and to depend on m, and can be obtained from a Fourier analysis of the experimental curve of $\bar{\nu}_m - \nu_0$ against θ. For a rotation axis parallel to a principal axis $\gamma = \delta$ holds, and specifies the orientation of a second principal axis relative to $\theta = 0$. For a rotation axis perpendicular to a principal axis $\gamma = \delta = 0$ if θ is measured from the position in which the known principal axis is either parallel or perpendicular to H_0. In both these cases of $\gamma = \delta$ equation [3] may be rewritten in the form

[4] $$\bar{\nu} - \nu_0 = K_0 + K_1 s + K_2 s^2$$

with s defined by equation [2], and K_i related to n, P, U of equation [3] by:

[5] $$\begin{aligned} n &= K_0 + \tfrac{1}{2}K_1 + \tfrac{3}{8}K_2, \\ P &= \tfrac{1}{2}(K_1 + K_2), \\ U &= \tfrac{1}{8}K_2. \end{aligned}$$

In a good crystal, in which all the $2I$ components of a resonance line are clearly visible, the nuclear spin I can be obtained simply by counting the line components. However, as will be explained in section 5, crystal imperfections and impurities may so broaden and weaken the satellites that either none at all are visible, as was the case with some of the spodumene samples in the present experiments, or the outer ones are so blurred and weak, that in counting the number of line components one can not be certain that none have been missed. Nevertheless, as long as the second order frequency shift of the central component and the frequency difference of only one pair of satellites (the strongest innermost pair) can be measured, the nuclear spin can be determined from a rotation about any arbitrary axis by combining the experimental values of U from equation [3] for the central component ($m = 1/2$), and of R from equation [1] for the innermost pair of satellites ($m = 3/2$) in the expression

[6] $$(I + \tfrac{3}{2})(I - \tfrac{1}{2}) = 32\nu_0 U/R^2.$$

Here ν_0 is the unperturbed Larmor frequency corresponding to the value of H_0 at which U has been measured.

If the orientation of some one of the principal axes of ϕ_{ij} is known from crystal symmetry we can use it as the X rotation axis, and choose Y and Z rotation axes in the plane perpendicular to it. We choose the X and Y axes to coincide respectively with the b and c axes of spodumene. If we do not restrict the value of the asymmetry parameter $\eta = (\phi_{xx} - \phi_{yy})/\phi_{zz}$ to the range $0 \leqslant \eta \leqslant 1$ we may name the principal axes at will. We shall choose the principal axis coincident with the X rotation axis as the x principal axis corresponding to the eigenvalue $\phi_{xx} = -\frac{1}{2}(1 - \eta)\phi_{zz}$. The y and z principal axes must then lie in the YZ plane. Let δ denote the angle between the Y rotation axis and the y principal axis corresponding to the eigenvalue $\phi_{yy} = -\frac{1}{2}(1 + \eta)\phi_{zz}$. A positive δ will mean that a positive rotation of the crystal about the X axis will bring the yz axes into the position originally occupied by the YZ axes. To analyze the experimental data completely we must determine δ, η, and the absolute value of the quadrupole coupling constant referred to the z axis $|C_z| \equiv |eQ\phi_{zz}/h|$. For $I = 5/2$ the latter two quantities are related to a_X and R_X of equation [1] by:

[7] $$\eta = 1 + \frac{4a_X}{R_X - a_X}, \quad |C_z| = \tfrac{10}{3}\,|R_X - a_X|\,.$$

If at least one pair of satellites is visible a_X, R_X, δ may be obtained directly from an analysis of the experimental curve of the form of $\nu' - \nu''$ in equation [1] for the X rotation. $\theta_X = 0$ is chosen when the Y axis coincides with H_0.

If all the satellites are blurred out by crystal imperfections, and only the central component is visible, then, provided the second order shift of equation [3]

is measurable, δ may be obtained by observing the value of θ_X about which $(\bar{\nu} - \nu_0)_X$ is symmetric, while R_X and a_X may be calculated from the experimental values of U_X, P_X, and n_X of equation [3]. For $I = 5/2$, $m = 1/2$ the relevant formulae are:

$$[8] \qquad \begin{aligned} R_X &= 2[\nu_0 U_X]^{\frac{1}{2}}, \\ a_X &= -3\nu_0 P_X/R_X; \text{ or } a_X{}^2 = 2\nu_0[n_X + \tfrac{7}{9}U_X]. \end{aligned}$$

Thus, when second order effects are measurable, a complete analysis is possible with a single rotation about the X axis whether any satellites are visible or not. Rotations about the Y and Z axes will confirm some of the above results, but do not by themselves lead to a complete analysis when only first order effects are observable. When second order effects are observable the Y and Z rotations will give all the information except the sign of δ.

Since the Y and Z axes are known to be perpendicular to a principal axis, $c_Y = c_Z = 0$ and $\delta_Y = \delta_Z = 0$. If satellites are visible, then a_Y, $b_Y = R_Y$, a_Z, $b_Z = R_Z$ are obtainable directly from an analysis of the experimental curves of the form of equation [1], and a check on a_X and $b_X = R_X \cos 2\delta$ may be obtained with the aid of the identities:

$$[9] \qquad \begin{aligned} a_X &= \tfrac{1}{2}(b_Y - a_Y) = -\tfrac{1}{2}(b_Z + a_Z), \\ b_Y &= -\tfrac{1}{2}(3a_Y + b_Y) = \tfrac{1}{2}(3a_Z - b_Z). \end{aligned}$$

If only first order effects are measurable, c_X, $R_X = (b_X{}^2 + c_X{}^2)^{\frac{1}{2}}$, and $\delta = \frac{1}{2}\tan^{-1}(c_X/b_X)$ will remain undetermined by the Y and Z rotations. If second order effects are measurable, then the Y and Z rotations will give checks on $|c_X|$, R_X, and $|\delta|$, as well as on a_X and b_X, from measurements on the central component alone, irrespectively of whether any satellites are visible. The sign of c_X relative to a_X, b_X, and also the sign of δ will remain undetermined by the Y and Z rotations. The computation for $I = 5/2$, $m = 1/2$ proceeds as follows. We first obtain $b_Y = R_Y$ and $b_Z = R_Z$ from experimental values of U_Y, U_Z with the aid of analogues of the first of equations [8]. We then obtain a_Y and a_Z in terms of R, n, P, U from:

$$[10] \qquad \begin{aligned} a_Y &= -\tfrac{1}{9}R_Y \pm \left[\left(\frac{R_Y}{9}\right)^2 + 2\nu_0\left(n_Y + \tfrac{7}{9}U_Y - \frac{P_Y}{3}\right)\right]^{\frac{1}{2}}, \\ a_Z &= \tfrac{1}{9}R_Z \pm \left[\left(\frac{R_Z}{9}\right)^2 + 2\nu_0\left(n_Z + \tfrac{7}{9}U_Z + \frac{P_Z}{3}\right)\right]^{\frac{1}{2}}. \end{aligned}$$

$c_X{}^2$ is then computed from the alternative expressions:

$$[11] \qquad \begin{aligned} c_X{}^2 &= -(3\nu_0 P_Y + R_Y a_Y) = -9\nu_0(n_Y + \tfrac{7}{9}U_Y) + \tfrac{9}{2}a_Y{}^2, \\ c_X{}^2 &= \quad (3\nu_0 P_Z + R_Z a_Z) = -9\nu_0(n_Z + \tfrac{7}{9}U_Z) + \tfrac{9}{2}a_Z{}^2. \end{aligned}$$

a_X and b_X are computed from the identities [9]. Corresponding to the two values of a_Y in equation [10] two different sets of a_X, b_X, $c_X{}^2$ are obtained consistent with the Y rotation, and similarly two different sets consistent with the Z rotation. That set is selected from each rotation which is consistent with a set from the other rotation. Then $R_X = (b_X{}^2 + c_X{}^2)^{\frac{1}{2}}$ and $|\delta| = \frac{1}{2}\tan^{-1}(|c_X|/b_X)$ are computed. The values of η and $|C_z|$ can then be found from equation [7].

The above describes the evaluation of $|C_z|$, η, and δ from the experimentally obtained coefficients of $\nu' - \nu''$ and $\bar{\nu} - \nu_0$ of equations [1] and [3]. Conversely,

TABLE I

VALUES OF SELECTED COEFFICIENTS K_i IN $\bar{\nu} - \nu_0 = K_0 + K_1 s + K_2 s^2$ FOR $I = 5/2$. THE x PRINCIPAL AXIS OF ϕ_{ij} CORRESPONDING TO THE EIGENVALUE $-\frac{1}{2}(1 - \eta)\phi_{zz}$ COINCIDES WITH THE X ROTATION AXIS. THE y PRINCIPAL AXIS CORRESPONDING TO THE EIGENVALUE $-\frac{1}{2}(1 + \eta)\phi_{zz}$ MAKES AN ANGLE δ WITH THE Y ROTATION AXIS. $C_z \equiv eQ\phi_{zz}/h$

Axis	Line component	$K_0/(C_z^2/800\nu_0)$	$K_1/(C_z^2/800\nu_0)$	$K_2/(C_z^2/800\nu_0)$
Y	Central	$(3 + \eta)^2$	$-6\{2\eta(1 + 3\eta) + 5(3 + \eta)(1 - \eta)\cos^2\delta\}$	$9[2\eta - (3 + \eta)\cos^2\delta]^2$
	"Inner" sat.	$\frac{5}{8}(3 + \eta)^2$	$-\frac{3}{4}\{2\eta(5 + 7\eta) + 13(3 + \eta)(1 - \eta)\cos^2\delta\}$	$(21/8)[2\eta - (3 + \eta)\cos^2\delta]^2$
Z	Central	$4\eta^2 - 12(3 + \eta)(2 + \eta)\cos^2\delta + 9(3 + \eta)^2\cos^4\delta$	$-6\{2(3 - \eta)(2 - \eta) - (3 + \eta)(13 - \eta)\cos^2\delta + (3 + \eta)^2\cos^4\delta\}$	$9[(3 - \eta) - (3 + \eta)\cos^2\delta]^2$

if $|C_z|$, η, and δ are known from one rotation, the values of $\nu' - \nu''$ and $\bar{\nu} - \nu_0$ for other rotations discussed below may be conveniently computed in the case of $I = 5/2$ from the following formulae.

The first order frequency splitting for the X rotation is given by the last of equations [1] with the coefficients L_0, L_1 determined by:

$$[12] \qquad L_0 = \tfrac{3}{10} C_z, \qquad L_1 = -\tfrac{3}{20} C_z(3 + \eta) .$$

The second order frequency shifts for those Y, Z rotations which are discussed below are given by equation [4] with the coefficients K_t listed in Table I.

The third order contribution to the frequency splitting for the X rotation is given for the "inner" satellites ($m = 3/2$) by:

$$[13] \qquad \frac{9}{2000}\frac{C_z^3}{\nu_0^2}\left[-\frac{11}{16}\eta^2 + s_X(3+\eta)\frac{288 + 402\eta + 113\eta^2}{96} - s_X{}^2(3+\eta)^2\frac{251 + 44\eta}{64} + s_X{}^3(3+\eta)^3\frac{385}{384}\right]$$

and for the "outer" satellites ($m = 5/2$) by:

$$[14] \qquad \frac{9}{1000}\frac{C_z^3}{\nu_0^2}\left[-\frac{1}{16}\eta^2 - s_X(3+\eta)\frac{432 + 258\eta + 37\eta^2}{96} + s_X{}^2(3+\eta)^2\frac{279 + 86\eta}{64} - s_X{}^3(3+\eta)^3\frac{365}{384}\right].$$

Equations [12], [13], [14] give the correct relative sign of the first and third order contributions to $\nu' - \nu''$, but the absolute sign will remain undetermined. Setting $\eta = 0$, $C_z = 40\Delta\nu/3$, and $s_X = 1 - z^2$, or $\delta = 0$ and $s_Y = z^2$, or $\delta = \frac{1}{2}\pi$ and $s_Z = 1 - z^2$, will reduce the above to agree with equations (22)–(24) of Pound (5) after the small correction given in footnote 4 of Ref. (7) has been made.

3. APPARATUS AND EXPERIMENTAL PROCEDURE

We have experimentally checked the second order theory outlined above in the case of the Al^{27} resonance in a single crystal of $LiAl(SiO_3)_2$ (spodumene). A projection of the structure of spodumene on the (010) plane is given in Fig. 1. A detailed description of the crystal structure of spodumene was given in Ref. (8), and will not be repeated here.

Several different samples of spodumene were used to study the Al^{27} resonance, and to improve the accuracy of some of the Li^7 results of our earlier paper (8). Although it would have been advantageous to have used the same sample for all the measurements, several different samples were in fact used because the better specimens were not available in the earlier stages of the experiment, and it was not considered worth while to repeat the measurements.

1. Samples of spodumene Nos. 1X, 1Y, 1Z, which were used in the early experiments reported in Ref. (4) to study the central component of the Al^{27} line, were cut from the same milky cleavage mass of spodumene from which we obtained the sample used for our observations on the Li^7 resonance in Ref. (8). To improve the line intensity by providing a favorable filling factor for the oscillator coil separate samples were used for the X, Y, and Z rotations. Each of these samples was cut into roughly cylindrical shape with the X, Y, Z axes

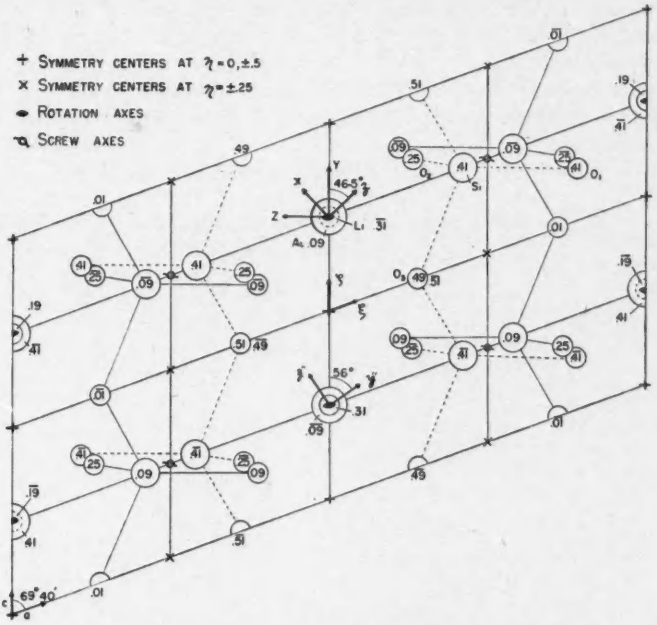

FIG. 1. Projection of a unit cell of monoclinic spodumene on the (010) plane. The b axis, which is perpendicular to the page, was used as the X rotation axis, and coincides with the y and x'' principal axes of the field gradient tensors ϕ_{ij} at the Li and Al sites respectively. The Y and Z rotation axes, and the x, z and y', z'' principal axes of ϕ_{ij} at the Li and Al sites respectively are shown in the diagram.

of rotation chosen in turn along the crystallographic b and c axes and the third direction perpendicular to both. The cylinders are approximately 30 mm. long and 15 mm. in diameter. The axis of rotation is the only crystallographic direction known reasonably accurately in each of these cylinders, so the Li^7 lines were used to determine the position of the other two crystallographic axes. Therefore the discussion on crystal alignment errors given in Ref. (8) in connection with the Li^7 measurements applies equally well here. The central ($m = 1/2$) component of the Al^{27} resonance was quite strong in these samples, but the two pairs of satellites expected for the known spin $I = 5/2$ for Al^{27} were not visible at all. This nonappearance of the expected satellites is believed to be due to crystal imperfections and impurities as described in section 5. All the original measurements on the central component of the Al^{27} line reported in our preliminary communication (4) were made with this set of three crystal samples.

2. A smaller colorless crystal was then obtained in which only the c axis could be unambiguously determined from its external appearance. This crystal, No. 2Y, was also cut in the shape of a cylinder (14 mm. in length along the c axis, 11 mm. in diameter). Although much smaller than the 1X, 1Y, 1Z crystals this sample clearly showed the five components of the Al^{27} line. The measure-

ments on the angular dependence of the frequencies of the "inner" pair of satellites ($m = 3/2$) for the Y rotation were made by rotating this crystal about its c axis.

3. The analysis of measurements on samples 1X, 1Y, 1Z indicated a discrepancy of 2° in the values of the angle δ, made by the Y and Z axes with respect to the two principal axes lying in the YZ plane, as determined from the X rotation and from the Y and Z rotations. Since θ_X, the angle of rotation about

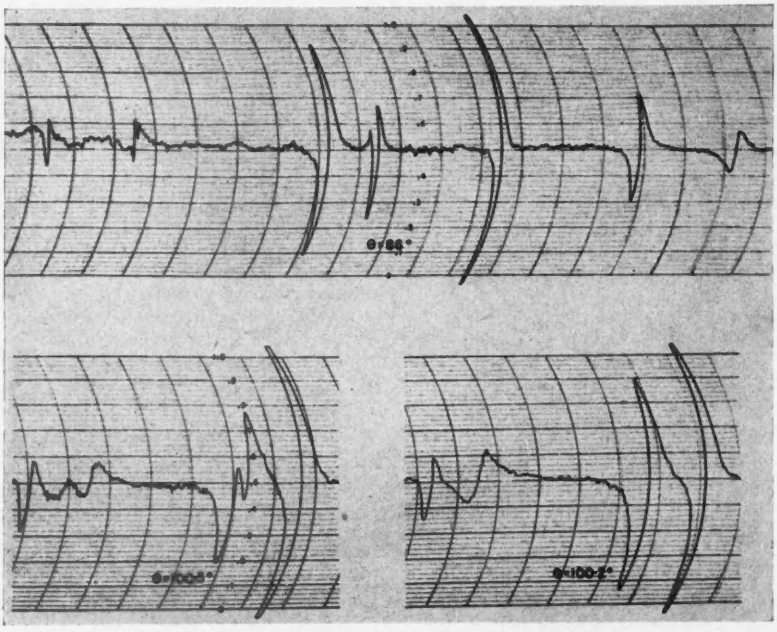

FIG. 2. Selected traces of the recorded derivative of the Al^{27} absorption line in spodumene sample No. 3X at $H_0 = 6130$ gauss corresponding to $\nu_0 = 6.806$ Mc./sec. (*a*) $\theta_X = 86°$. Sweep rate is approximately 54 kc./sec. per division. The lines and their approximate frequencies in Mc./sec. are from right to left: "outer" satellite of Al^{27} line 6.458, "inner" satellite 6.585, central component 6.769, Cu^{63} line 6.930, second "inner" satellite 7.009, second "outer" satellite 7.307, Cu^{65} line 7.420. The Cu lines are not symmetric because some dispersion mode is mixed in with the absorption mode owing to the phase shift of the H_1 r-f. field penetrating the metal of the oscillator coil. The more abundant Cu^{63} isotope gives the stronger line. (*b*) $\theta_X = 100.2°$. Sweep rate is approximately 27 kc./sec. per division. The lines and their approximate frequencies in Mc./sec. are from right to left: central component of Al^{27} line 6.756, the two coalesced "inner" satellites 6.794, the two coalesced "outer" satellites 6.903, Cu^{63} line 6.930. (*c*) $\theta_X = 100.5°$. Same as *b*, except that both pairs of coalesced satellites have begun to split up.

the X axis, was measured with reference to the position of the x and z principal axes of the field gradient tensor at the Li^7 sites, whose orientation with respect to the c axis was itself uncertain by $\pm$ 2°, as explained in Ref. (8), it was decided to improve this last measurement. Crystal No. 3X (11 × 13 × 12 mm.) was obtained which also was colorless and which had two nearly perfect (110) cleavage planes. Their intersection defined the c axis. The angle between the two cleavage planes was almost exactly 94°, in agreement with the value ex-

pected from the known crystal constants. The bisector of this angle was taken as the b axis, and the crystal was rotated about this axis. The position of the c axis of this crystal with respect to the magnetic field H_0 could be determined to within 1°. The positions of zero splitting for the Li^7 lines were observed for this crystal, and they indicated that an error of 1.5° had been made in the value of δ_X for Li^7 reported in Ref. (8). The new improved value of $\delta_X = 46.5° \pm 1°$ for Li^7 (to replace the value of $48° \pm 2°$ reported earlier), and the value of

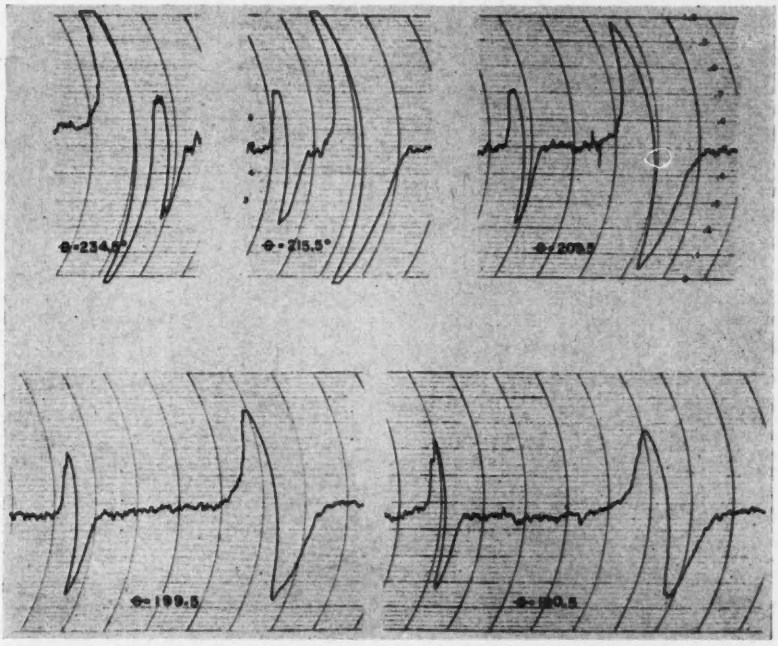

FIG. 3. Selected traces of the recorded derivative of the Al^{27} absorption line in spodumene sample No. 1X immersed in a solution of aluminum chloride. The small narrow signal in each case is the solution signal at the unperturbed Larmor frequency $\nu_0 = 7.453$ Mc./sec., corresponding to $H_0 = 6714$ gauss. The other signal, whose frequency depends on crystal orientation, is the central component of the Al^{27} line in spodumene. The sweep rate is approximately 8 kc./sec. per division.

$\delta = 56° \pm 1°$ for Al^{27} (obtained as the final value of the measurements described below, in agreement with the directly observed $9° \pm \frac{1}{2}°$ difference between those positions of sample 1X which give the maximum splitting between the Li^7 satellites, and the maximum shift of the central component of the Al^{27} line) are shown in Fig. 1. This same sample No. 3X was also used to provide some information on the dependence of the Al^{27} satellite frequencies on the magnetic field H_0, and on crystal position. The five components of the Al^{27} line in this crystal may be clearly seen in Fig. 2a, in which the Cu^{63} and Cu^{65} lines due to the copper in the coil windings are also easily recognizable. As the crystal is rotated, the Al^{27} line components change in frequency, while the copper lines do not.

The recording nuclear magnetic resonance spectrometer and the crystal mount used in this work have been described in Ref. (8).

When the central component of the Al^{27} line was studied in crystals 1X, 1Y, 1Z the crystals were immersed in a solution of aluminum chloride which gave the unperturbed line of frequency ν_0. For each crystal position the spectrometer was set to run through both the signal $\bar{\nu}$ from the crystal, and the signal ν_0 from the solution, giving traces such as those shown in Fig. 3. The frequency differences between the two signals were measured by the method described in Ref. (8).

In the case of the satellites of the Al^{27} line studied in crystals No. 2Y and No. 3X, the frequencies ν' and ν'' of each member of the pair were measured individually by using several closely spaced frequency meter settings in the immediate neighborhood of each signal, and interpolating between these known frequencies. ν_0 was obtained by removing the crystal and replacing it with a test tube of aluminum chloride solution.

4. EXPERIMENTAL RESULTS AND CALCULATIONS

In all the experimental results reported below it is estimated that the individual frequencies could be measured to $\pm$ 1 kc./sec., and the angular position of the crystal sample to $\pm \frac{1}{2}°$ relative to an arbitrary zero on the crystal mount scale whose position with respect to the magnetic field could in turn be determined to $\pm$ 1°.

The following theoretical conclusions were verified.

(*a*) If, and only if, second and higher order effects are negligible a crystal position can be found for which all the line components simultaneously coalesce at the unperturbed Larmor frequency ν_0. As reported in our earlier paper (8), the components did all simultaneously coalesce at ν_0 in the case of the Li^7 line in spodumene for which the quadrupole coupling constant is small. In the Al^{27} line in spodumene investigated in the present paper the components do not all coalesce for any crystal position, indicating an appreciable second order effect.

(*b*) In the absence of measurable third order effects, but irrespectively of the presence or absence of second order effects, the first order splitting $\nu' - \nu''$ between two members of a pair of satellites should vanish in a crystal position which is the same for all satellite pairs for a given line, and which is independent of H_0. Fig. 2 shows representative traces obtained with sample No. 3X, described in section 3, in three positions in a magnetic field of $H_0 = 6130$ gauss, calculated from the known gyromagnetic ratio for Al^{27} and the measured value of $\nu_0 = 6.806$ Mc./sec. for Al^{27} in aluminum chloride in solution. At $\theta_X = 86°$ the five components of the Al^{27} line are widely separated and are clearly visible in addition to the two lines due to Cu^{63} and Cu^{65} in the oscillator coil winding. As the crystal is rotated about its b axis (chosen as the X rotation axis) the copper lines remain at their fixed frequencies, while the components of the Al^{27} line gradually change their position. By the time $\theta_X = 100.2°$ has been reached the lower frequency member of each pair of satellites has crossed over to the high frequency side of the central component, and has coalesced with the other

member of the same pair as shown in Fig. 2*b*. The coalesced pairs lie at frequencies recorded in Table II. A further small rotation of the crystal to $\theta_X = 100.5°$ already produces a noticeable tendency of both coalesced satellite

TABLE II

DEPENDENCE ON THE MAGNETIC FIELD H_0 OF THE FREQUENCY SHIFT $\bar{\nu} - \nu_0$ OF THE CENTRAL COMPONENT AND OF THE CENTERS OF GRAVITY $\bar{\nu} - \nu_0 = \frac{1}{2}(\nu' + \nu'') - \nu_0$ OF THE "INNER" AND "OUTER" SATELLITES OF THE Al^{27} LINE IN SAMPLE NO. 3X IN THE POSITION $\theta_X = 100°$ IN WHICH THE SPLITTING $\nu' - \nu''$ OF THE SATELLITE PAIRS VANISHES

ν_0, Mc./sec.	H_0, gauss	$1/\nu_0$, relative	Central component ($m = \frac{1}{2}$)			"Inner" satellites ($m = 3/2$)			"Outer" satellites ($m = 5/2$)		
			$\bar{\nu}$, Mc./sec.	$\bar{\nu} - \nu_0$, Mc./sec.	$\bar{\nu} - \nu_0$, relative	$\nu' = \nu'' = \bar{\nu}$, Mc./sec.	$\bar{\nu} - \nu_0$, Mc./sec.	$\bar{\nu} - \nu_0$, relative	$\nu' = \nu'' = \bar{\nu}$, Mc./sec.	$\bar{\nu} - \nu_0$, Mc./sec.	$\bar{\nu} - \nu_0$, relative
3.662	3300	1.000	3.570	−.092 ±.001	1.000	3.643	−.019 ±.001	1.000	3.843	.181 ±.001	1.000
6.806	6130	0.539	6.756	−.050 ±.001	0.54 ±.01	6.794	−.012 ±.001	0.63 ±.06	6.903	.097 ±.001	0.535 ±.005
9.884	8903	0.371	9.849	−.035 ±.001	0.38 ±.01	9.876	−.008 ±.001	0.42 ±.05	9.952	.068 ±.001	0.376 ±.005

pairs to split as shown in Fig. 2*c*. Thus the position of zero splitting can be found with considerable accuracy, and as expected turns out to be the same for both the "inner" ($m = 3/2$) and the "outer" ($m = 5/2$) satellite pairs. The magnetic field was then changed to $H_0 = 3300$ gauss and $H_0 = 8903$ gauss, corresponding to $\nu_0 = 3.662$ Mc./sec. and $\nu_0 = 9.884$ Mc./sec. respectively. The position of zero splitting was determined for each of the three values of H_0 used, and was found to differ by not more than $\frac{1}{2}°$ between the two extreme values of H_0 used. This indicates that third order effects must be quite small at this crystal position.

(*c*) In the absence of measurable fourth order effects the magnitude of the second order frequency shift $\bar{\nu} - \nu_0$ of the central component, or of the center of gravity of a pair of satellites, should be inversely proportional to H_0 for a given crystal position, and for a given line component should have the same form of dependence on the angular position of the crystal independently of H_0. Fig. 4 gives the measured values of $\bar{\nu} - \nu_0$ for the central component ($m = \frac{1}{2}$) of the Al^{27} line in sample No. 1X as a function of θ_X for several crystal positions, and for three values of the magnetic field $H_0 = 5657$, 6714, and 8341 gauss corresponding respectively to observed unperturbed Larmor frequencies $\nu_0 = 6.280$, 7.453, and 9.260 Mc./sec. It is seen that the form of angular dependence is unaffected by H_0. The ratios of the reciprocals of the observed Larmor frequencies are 1.000: 0.843: 0.678, while the ratios of the observed frequency shifts, averaged over three points in the neighborhood of the maximum shift at $\theta_X = 192°$, are 1.00: 0.84: 0.66. Since the experimental accuracy in determining the frequency shifts is approximately 2 to 3% the two sets of ratios are in satisfactory agreement. Since no satellites were visible in sample No. 1X, sample No. 3X was later used to obtain the data recorded in Table II

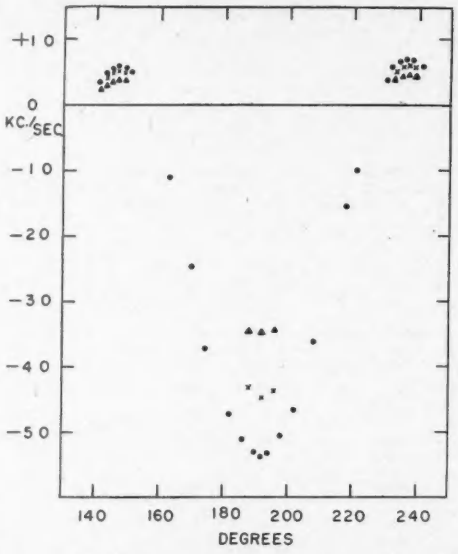

FIG. 4. Dependence on the angular position of spodumene sample 1X of the frequency shift $\bar{\nu} - \nu_0$ of the central component of the Al^{27} line for the X rotation about the crystal b axis at various magnetic field strengths. The dots represent experimental points taken at $H_0 = 5657$ gauss, the crosses at $H_0 = 6714$ gauss, and the triangles at $H_0 = 8341$ gauss. $\theta_X = 0$ when the crystal c axis coincides with the magnetic field H_0.

corresponding to the one position in which the first order splitting vanished for both satellite pairs, so that $\nu' = \nu'' = \bar{\nu}_m$ in both cases. In all cases $\bar{\nu} - \nu_0$ is inversely proportional to ν_0 within experimental error.

Figs. 5, 6, 7 represent experimental values of the shift $\bar{\nu} - \nu_0$ of the central component ($m = 1/2$) of the Al^{27} line as a function of θ for the X, Y, Z rotations

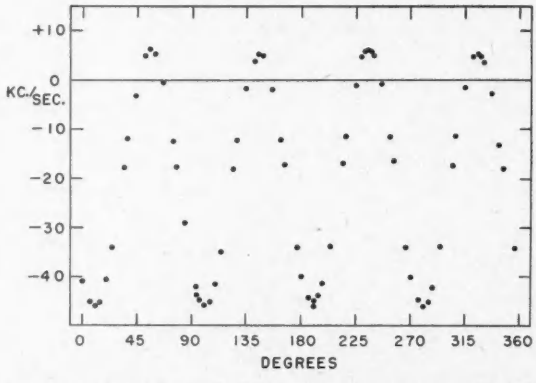

FIG. 5. Dependence on the angular position of spodumene sample 1X of the frequency shift $\bar{\nu} - \nu_0$ of the central component of the Al^{27} line for the X rotation about the crystal b axis. $\theta_X = 0$ when the crystal c axis coincides with the magnetic field H_0. $H_0 = 6714$ gauss, corresponding to $\nu_0 = 7.453$ Mc./sec.

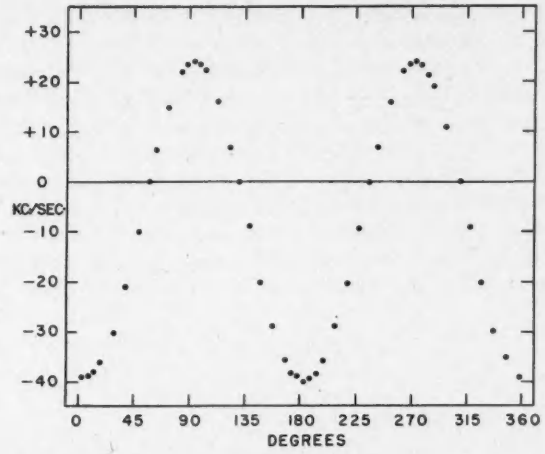

FIG. 6. Dependence on the angular position of spodumene sample 1Y of the frequency shift $\bar{\nu} - \nu_0$ of the central component of the Al^{27} line for the Y rotation about the crystal c axis. $\theta_Y = 0$ was meant to mark the position of the crystal in which the b axis is at 90° to the magnetic field H_0. The curve should be symmetric about this crystal position. The small phase shift indicates a crystal alignment error. $H_0 = 6714$ gauss, corresponding to $\nu_0 = 7.453$ Mc./sec.

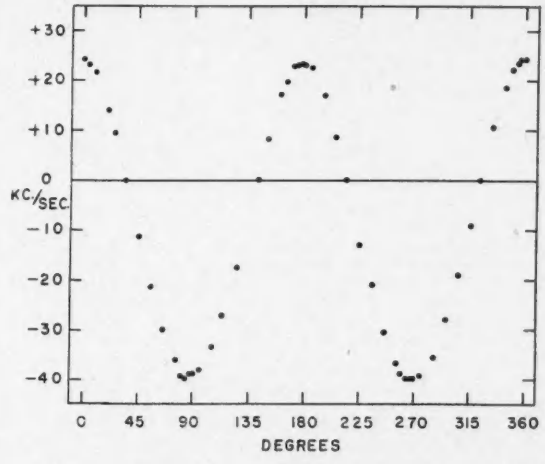

FIG. 7. Dependence on the angular position of spodumene sample 1Z of the frequency shift $\bar{\nu} - \nu_0$ of the central component of the Al^{27} line for the Z rotation about the direction orthogonal to both the b and c crystal axes. $\theta_Z = 0$ was meant to mark the position of the crystal in which the b axis coincides with the magnetic field H_0. The curve should be symmetric about this crystal position. The small phase shift indicates a crystal alignment error. $H_0 = 6714$ gauss, corresponding to $\nu_0 = 7.453$ Mc./sec.

of samples 1X, 1Y, 1Z respectively. The magnetic field H_0 was kept constant at approximately 6714 gauss corresponding to $\nu_0 = 7.453$ Mc./sec. From the symmetry of the spodumene crystal discussed in Ref. (8) it may be deduced

that one of the principal axes of ∇E at the Al sites must coincide with the b crystal axis which was chosen as the X axis. The $\bar{\nu} - \nu_0$ curves for the Y and Z rotations should then be symmetrical about $\theta = 0$ in the case of perfect identification and alignment of the crystal axes with respect to H_0. Since the angular positions of the crystal samples 1X, 1Y, 1Z used in investigating the Al^{27} central component were always obtained with reference to the Li^7 lines it is to be expected that the zeros of the θ_Y and θ_Z scales in Figs. 6 and 7 as obtained from the Al^{27} results should be shifted in the same direction, and by approximately the same amounts as the $+3°$ and $-1°$ shifts which were observed in the case of Li^7 in Ref. (8), and which were ascribed to a slight misalignment of the crystal. In replotting the observations of Figs. 6, 7 in Fig. 8 we therefore have shifted

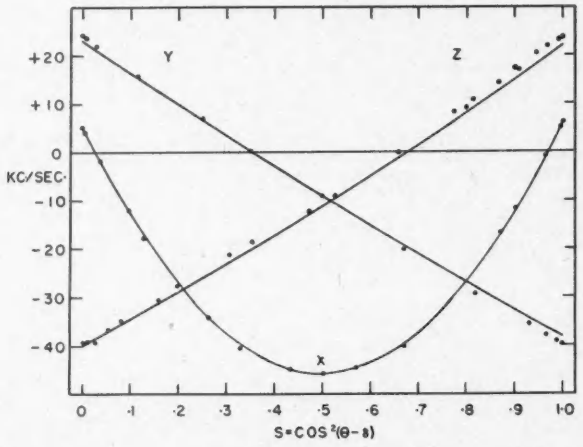

FIG. 8. The points of Figs. 5, 6, 7 replotted as a function of $s \equiv \cos^2(\theta - \delta)$, where δ is the position of the peak of each curve. Each point of Fig. 8 is the average of four symmetrically situated points of the preceding figures. The solid curve X is $(\bar{\nu} - \nu_0)_X = 5.3 - 204s + 205s^2$ which was fitted visually to give the best empirical fit to the points. Curves Y and Z are theoretical curves given by $(\bar{\nu} - \nu_0)_Y = 22.8 - 66.6s + 5.6s^2$ and $(\bar{\nu} - \nu_0)_Z = -39.8 + 52.5s + 9.1s^2$. They were calculated using data obtained from curve X, from curve A of Fig. 11, and from the "inner" satellites of the Al^{27} line in spodumene sample 3X.

the zeros of the θ_Y and θ_Z scales to make the curves symmetrical about $\theta = 0$. In Fig. 5 the peak of the $(\bar{\nu} - \nu_0)_X$ curve for Al^{27} was observed to lie $9° \pm \frac{1}{2}°$ further away from the c axis than the peak of the $(\nu' - \nu'')_X$ curve for Li^7. Using the corrected value of $\delta_{Li} = 46.5° \pm 1°$ for Li^7 obtained from observations on crystal No. 3X as described in section 3, we find the position of the peak of the Al^{27} $(\bar{\nu} - \nu_0)_X$ curve at $\theta_X = \delta = 55.5° \pm 1°$. In replotting the results of Fig. 5 in Fig. 8 the value of $s_X = \cos^2(\theta_X - \delta) = 1$ is chosen to correspond to the peak of this curve.

Since the experimental points of Figs. 5, 6, 7 are reasonably symmetric about the peaks of these curves, indicating that $\gamma = \delta$ in equation [3], which is the condition that equation [3] may be put in the form of equation [4], we have

replotted the data of Figs. 5, 6, 7 in a different way in Fig. 8 with $\bar{\nu} - \nu_0$ plotted against $s \equiv \cos^2(\theta - \delta)$. Each point of Fig. 8 corresponds to the average of the four points of Figs. 5, 6, 7 symmetrically situated with respect to the peaks of the respective curves, viz. $\delta \pm (\theta - \delta)$, $\pi + \delta \pm (\theta - \delta)$. The solid curve X of the expected quadratic form of equation [4] was fitted visually to those experimental points of Fig. 8 which refer to the X rotation. Similar empirical curves of the expected quadratic form of equation [4] (which differ somewhat from the calculated solid curves Y and Z shown in Fig. 8 and described below) were also visually fitted to the experimental points for the Y and Z rotations. This gives us the equivalent of the Fourier analysis referred to in section 2. Table III summarizes the results of this empirical fitting of curves to the experimental points.

TABLE III

VALUES OF COEFFICIENTS (IN KC./SEC.) REQUIRED TO FIT EMPIRICAL CURVES OF THE FORM OF EQUATIONS [4] OR [3] TO THE EXPERIMENTAL POINTS OF FIGS. 5–8 FOR THE CENTRAL COMPONENT ($m = 1/2$) OF THE Al^{27} LINE. $\nu_0 = 7.453$ MC./SEC. $\gamma = \delta$ AND K_0, K_1, K_2 ARE OBTAINED BY VISUAL FITTING. η, P, U ARE CALCULATED FROM EQUATION [5]. UNCERTAINTIES SHOWN ARE ESTIMATES FROM VISUAL FITTING

	X	Y	Z
$\delta = \gamma$	$55.5° \pm 1°$	$0° \pm 1°$	$0° \pm 1°$
K_0	5.3 ± 0.5	24.0 ± 0.5	-39.6 ± 0.5
K_1	-204 ± 1	-70.5 ± 1	$+55.2 \pm 1$
K_2	$+205 \pm 1$	$+6.9 \pm 1$	$+8.4 \pm 1$
$n = K_0 + \frac{1}{2}K_1 + \frac{3}{8}K_2$	-19.9 ± 1	-8.7 ± 1	-8.9 ± 1
$P = \frac{1}{2}(K_1 + K_2)$	$+0.5 \pm 0.2$*	-31.8 ± 1	$+31.8 \pm 1$
$U = \frac{1}{8}K_2$	25.6 ± 0.1	0.86 ± 0.1	1.05 ± 0.1

* *Note. The uncertainty in* $P_X = \frac{1}{2}(K_1 + K_2)_X$ *is estimated to be smaller than that of* K_1 *or* K_2 *individually because greater weight has been given to the points near the two positive peaks of the X curve in Figs. 5 and 8. It is considered that there is a small, but real, difference in the height of the two peaks, which is equal to* $K_1 + K_2$.

Figs. 9 and 10 represent respectively the experimental values of $\nu' - \nu''$ and $\bar{\nu} - \nu_0 = \frac{1}{2}(\nu' + \nu'') - \nu_0$ for the "inner" ($m = 3/2$) satellites of the Al^{27} line as a function of θ_Y for the Y rotation of sample No. 2Y. The magnetic field H_0 was held constant at approximately 5862 gauss corresponding to the observed Larmor frequency for Al^{27} in aluminum chloride of $\nu_0 = 6.508$ Mc./sec. The zero of the θ_Y scale should be chosen at that position of the crystal in which the X(or b) axis is perpendicular to H_0. This position was accurately located by making the observed $\nu' - \nu''$ curve of Fig. 9 symmetrical about this point. This same crystal position was also chosen for $\theta_Y = 0$ for the $\bar{\nu} - \nu_0$ curve of Fig. 10. Since the accuracy of each experimental point is $\pm$ 1 kc./sec., and the total variation of the curve is less than 30 kc./sec., any seeming lack of symmetry of this curve about $\theta = 0°$, 90°, 180°, etc., is not significant. The align-

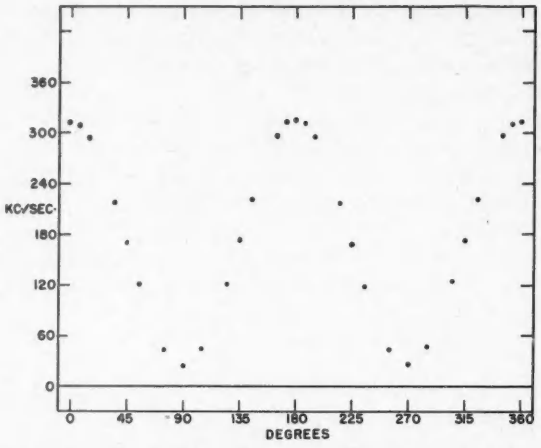

FIG. 9. Dependence on the angular position of spodumene sample 2Y of the frequency difference $\nu' - \nu''$ of the "inner" satellites of the Al^{27} line for the Y rotation about the crystal c axis. $\theta_Y = 0$ corresponds to the position of the crystal in which the b axis is at 90° to the magnetic field H_0. $H_0 = 5862$ gauss, corresponding to $\nu_0 = 6.508$ Mc./sec.

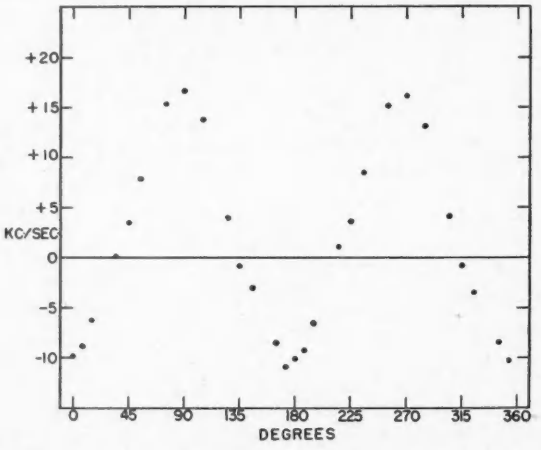

FIG. 10. Dependence on the angular position of spodumene sample 2Y of the frequency shift $\bar{\nu} - \nu_0 = \frac{1}{2}(\nu' + \nu'') - \nu_0$ of the center of gravity of the "inner" satellites of the Al^{27} line for the Y rotation about the crystal c axis. $\theta_Y = 0$ corresponds to the position of the crystal in which the b axis is at 90° to the magnetic field H_0. $H_0 = 5862$ gauss, corresponding to $\nu_0 = 6.508$ Mc./sec.

ment of the rotation axis at right angles to the magnetic field was achieved by adjusting the crystal holder until the two peaks of the $\nu' - \nu''$ curve of Fig. 9 separated by 180° became of the same height. A very slight tilt of the rotation axis with respect to the magnetic field produced a difference of as much as 15 kc./sec. in the height of the two peaks.

A Fourier analysis of the curve of Fig. 9 was made up to the sixth harmonic. The amplitudes of the terms of periods predicted by the first of equations [1] for the Y rotations were: $c_Y = 0$ by the choice of the origin, and $a_Y = 170.8 \pm 0.5$ kc./sec., $b_Y = R_Y = 145.1 \pm 0.5$ kc./sec. The r.m.s. value of the amplitudes of all the other harmonics was found to be 0.43 kc./sec., which differs from zero by less than the experimental error. Expressing this in the linear form of the last of equations [1] we obtain $L_0 = 25.7 \pm 1$ kc./sec., and $L_1 = 290.2 \pm 1$ kc./sec. The solid line A of Fig. 11 shows this straight line which has been

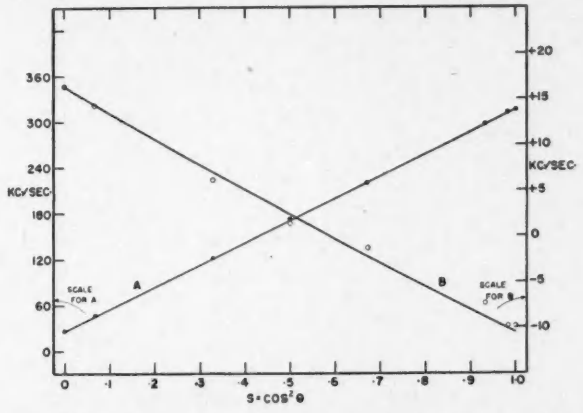

FIG. 11. The points of Figs. 9, 10 replotted as a function of $s_Y \equiv \cos^2\theta_Y$. Each point of Fig. 11 is the average of four symmetrically situated points of Figs. 9, 10. The solid straight line A is $(\nu' - \nu'')_Y = 25.7 + 290.2 s_Y$ which represents an empirical fit to the points of Fig. 11 resulting from a Fourier analysis of the curve of Fig. 9. The solid curve B is the theoretical curve $(\bar{\nu} - \nu_0)_Y = 16.3 - 28.7 s_Y + 1.9 s_Y^2$ calculated from the data obtained from curve A, from curve X of Fig. 8, and from spodumene sample 3X. The experimental points lying on curve B are uncertain by ± 2 kc./sec.

empirically fitted to the experimental points of Fig. 9 replotted against $s = \cos^2\theta_Y$. Each point of Fig. 11 is the average of the four points at $\pm\theta$, $\pm(\pi + \theta)$ of Fig. 9. The points of Fig. 10 are similarly replotted in Fig. 11. The experimental accuracy in this case does not justify an attempt to obtain an independent empirical set of constants in equation [4] to fit these points. Instead of this, the theoretically expected values of these constants were calculated from the data obtained from the preceding curves, as described below. The solid curve B of Fig. 11 is this calculated curve which shows that the observed points are consistent with it.

Some information on the "inner" ($m = 3/2$) satellites was also obtained from the X rotation of sample No. 3X in a field of $H_0 = 6129$ gauss corresponding to $\nu_0 = 6.804$ Mc./sec. Zero splitting was observed at $\theta_X = 100° \pm 1°$ and $\theta_X = 192° \pm 1°$. The expected positions for maximum splitting are then midway at $\theta_X = 146°$, and 90° from the latter position at $\theta_X = 236°$. The observed splittings in these two positions were $\nu' - \nu'' = \pm (885 \pm 2)$ and $\mp (856 \pm 3)$ kc./sec. respectively. Neglecting at this stage any third order effects, whose

possible influence will be discussed at the conclusion of this section, substitution of these data in equation [1] gives: $\delta = 56° \pm 1°$, $a_X = -14.5 \pm 4$ kc./sec., $R_X = 870 \pm 4$ kc./sec., $b_X = R_X \cos 2\delta = -326 \pm 30$ kc./sec.

Table IV lists the values of a, b, R obtained directly from the Y and X rotations of crystals 2Y and 3X respectively, and also computed from the above observations with the aid of identities [9]. It is seen that the a and b values obtained

TABLE IV

VALUES OF a, b, R (IN KC./SEC.) IN EQUATION [1] REQUIRED TO FIT THE OBSERVATIONS ON SAMPLES 2Y, 3X. FOR SAMPLE 2Y, a_Y, b_Y WERE OBTAINED FROM A FOURIER ANALYSIS OF $(\nu' - \nu'')_Y$ GIVEN BY THE POINTS OF FIG. 9 FOR THE "INNER" SATELLITES. THE REMAINING COEFFICIENTS WERE CALCULATED FROM THE IDENTITIES [9]. FOR SAMPLE 3X, a_X, R_X, AND $\delta = 56° \pm 1°$ WERE OBTAINED BY OBSERVING THE POSITIONS AND AMOUNTS OF MAXIMUM POSITIVE AND NEGATIVE SPLITTINGS $(\nu' - \nu'')_X$. b_X WAS COMPUTED FROM $b_X = R_X \cos 2\delta$, AND THE OTHER QUANTITIES FROM THE IDENTITIES [9]

Axis	Sample 2Y			Sample 3X		
	X Calc.	Y Obs.	Z Calc.	X Obs.	Y Calc.	Z Calc.
a	-13 ± 1.0	171 ± 0.5	-158 ± 1.0	-14.5 ± 4	170 ± 15	-156 ± 15
b	-329 ± 1.0	145 ± 0.5	184 ± 1.0	-326 ± 30	142 ± 15	184 ± 15
R	—	145 ± 0.5	184 ± 1.0	870 ± 4	142 ± 15	184 ± 15

from the two rotations agree within experimental error. Sample 3X provides a value of R_X, while sample 2Y provides better values of R_Y and R_Z than sample 3X.

The spin of the Al^{27} nucleus is known from Ref. (2) to be $I = 5/2$. The five components of the resonance line visible in Fig. 2*a* would confirm this if we were sure that no weaker satellites had been missed. To convince ourselves that no weak outer components of the line have been missed, and to illustrate the new method of spin determination proposed in part I, we apply equation [6] to the values of U from Table III, and the values of R from Table IV. We set $\nu_0 = 7.453$ Mc./sec. in equation [6] and compare the possible values of $(I + \frac{3}{2})(I - \frac{1}{2}) = 3, 8, 15$ corresponding to $I = 3/2, 5/2, 7/2$ respectively, with the experimental values of $32\nu_0 U/R^2$, which for the X, Y, Z rotations are respectively $8.05 \pm .10$, 9.7 ± 1, 7.4 ± 1. Thus the values of spin higher than 5/2 can be definitely excluded, and the visible five components confirm $I = 5/2$ for Al^{27}. The large uncertainties in the experimental values of $32\,\nu_0 U/R^2$ for the Y and Z rotations are caused by the large uncertainties in U_Y, U_Z. These are poorly known because in this particular crystal the tensor ϕ_{ij} is such as to give only a very small $\cos 4\theta$ contribution to the frequency shift for the Y and Z rotations.

We now apply the theory of section 2 to determine the absolute value of the quadrupole coupling constant $|C_z|$, the asymmetry parameter η, and the principal axes orientation of the ϕ_{ij} tensor at the Al^{27} sites in spodumene. We obtain five independent determinations of varying accuracy by considering separately the data obtained from: (*a*) sample 1X, central component, X rotation, (*b*) and (*c*) samples 1Y, 1Z, central component, Y and Z rotations treated

simultaneously, (*d*) sample 3X, "inner" satellites, *X* rotation, (*e*) sample 2Y, "inner" satellites, *Y* rotation, combined with the value of R_X from (*d*).

In case (*a*) δ, taken from Table III, and a_X, R_X computed from U_X, P_X of Table III with the aid of equation [8] are listed in Table V.

In cases (*b*), (*c*) equations [8]–[11] applied to the data of Table III give values of a_X, R_X, $|\delta|$, listed in Table V.

TABLE V

SUMMARY OF a_X, R_X, δ, $|C_z|$, η FROM OBSERVATIONS ON FIVE SPODUMENE SAMPLES

Sample	Line component	a_X, kc./sec.	R_X, kc./sec.	δ, degrees	$\lvert C_z \rvert$, kc./sec.	η
1X	Central	-13 ± 5	874 ± 2	55.5 ± 1	2956 ± 20	$0.94 \pm .02$
1Y	Central	-9 ± 17	894 ± 22	$\pm(56.5 \pm 1)$	3010 ± 90	$0.96 \pm .08$
1Z	Central	-1 ± 17	894 ± 22	$\pm(56.5 \pm 1)$	2980 ± 90	$1.00 \pm .08$
3X	"Inner" sat.	-14.5 ± 4	870 ± 4	56 ± 1	2947 ± 20	$0.93 \pm .02$
2Y	"Inner" sat.	-13 ± 1.0	(870 ± 4)	$56.1 \pm .2$	2943 ± 15	$0.941 \pm .005$

In case (*d*) values of δ, a_X, R_X are already given in Table IV. The results for case (*e*) listed in Table IV combined with R_X from case (*d*) give better values of a_X, and of $\delta_X = \frac{1}{2}\cos^{-1}(b_X/R_X) = 56.1° \pm 0.2°$.

All the above values of δ, a_X, R_X and the corresponding values of $|C_z|$ and η calculated from equations [7] are collected in Table V. The best values seem to be those in the last row of Table V.

These values were substituted into the coefficients of equation [4] listed in Table II to give curves Y, Z of Fig. 8, and curve B of Fig. 11. The following expressions were obtained in which the frequency is in kc./sec. For the central component of Fig. 8:

$$[15] \qquad \begin{aligned}(\bar{\nu} - \nu_0)_Y &= (22.8 \pm .2) - (66.6 \pm 1.0)s + (5.6 \pm .3)s^2,\\ (\bar{\nu} - \nu_0)_Z &= (-39.8 \pm .6) + (52.5 \pm 1.9)s + (9.1 \pm .9)s^2.\end{aligned}$$

For the "inner" satellites of Fig. 11:

$$[16] \qquad (\bar{\nu} - \nu_0)_Y = (16.3 \pm .2) - (28.7 \pm .4)s + (1.9 \pm .1)s^2.$$

The slight discrepancy between the calculated values of the coefficients in equations [15], which give the solid curves Y, Z of Fig. 8, and the values of K_i in Table III, which give the best visual fit to the points of Fig. 8, indicates the possibility of a systematic error in the form of a misalignment of the rotation axes in the crystal samples. In the analysis it was assumed that the three rotation axes were mutually orthogonal, whereas actually they could be slightly tilted with respect to their intended positions. In view of this, the estimated limits of error must be increased, and the values finally adopted from Table V are:

$$[17] \qquad |C_z| = 2950 \pm 20 \text{ kc./sec.}, \quad \eta = 0.94 \pm 0.01, \quad \delta = 56° \pm \tfrac{1}{2}°.$$

We conclude with some remarks on the size of the third order effects relative to the first order effects in the *X* rotation of crystal 3X. Substituting into

equations [1], [12], [13], [14] the constants of equation [17], and $\nu_0 = 6.804$ Mc./sec., corresponding to $H_0 = 6129$ gauss used to obtain the data of Table II at zero splitting of both pairs of satellites, and the data leading to part of Table IV at maximum splitting of the "inner" satellites, we obtain the following expressions for $\nu' - \nu''$ (in kc./sec.) in which the first and third order contributions are bracketed separately. For the inner satellites we have:

$$[18] \quad (\nu' - \nu'')_X = (885 - 1753s_X) + (-1.53 + 79.1s_X - 236s_X^2 + 155s_X^3)$$

and for the outer satellites:

$$[19] \quad (\nu' - \nu'')_X = 2(885 - 1753s_X) + (-0.3 - 146s_X + 440s_X^2 - 293s_X^3).$$

The third order contributions in equations [18] and [19] have greatest deviations from zero near $s_X \approx 0.2$ and $s_X \approx 0.8$ amounting respectively to about $+6$ kc./sec. and -10 kc./sec. in the former case, and -14 kc./sec. and $+14$ kc./sec. in the latter case. However, at the position of zero splitting from the first order term ($s_X \approx 0.5$), the third order contributions are only -1.5 and $+0.1$ kc./sec. respectively, and thus within experimental error do not influence the data of Table II. At the positions of maximum splitting of the satellites the third order contribution to the "inner" satellites is -1.5 kc./sec. at $s_X = 0$, and -3.4 kc./sec. at $s_X = 1$. These values were used to arrive at the quoted estimated errors of the measured maximum splittings.

5. DISCUSSION

The experimental results on the Li^7 and Al^{27} nuclei in spodumene obtained in the present paper, and in the earlier work of Ref. (8) are brought together in Table VI. In addition, the fact that for all orientations of the crystal no more than three lines were observed for Li^7 ($I = 3/2$), and no more than five lines for Al^{27} ($I = 5/2$), confirms the deduction from the known crystal symmetry

TABLE VI

SUMMARY OF EXPERIMENTAL RESULTS FOR THE SPODUMENE [$LiAl(SiO_3)_2$] CRYSTAL

	Li^7 sites	Al^{27} sites
$\lvert C_z \rvert \equiv \lvert eQ\phi_{zz}/h \rvert$ in Mc./sec.	$0.0757 \pm .0005$	$2.950 \pm .020$
Q in 10^{-24} cm.^{2}	Unknown, Ref. (1)	$+0.156 \pm .003$ Ref. (2)
$\lvert \phi_{zz} \rvert$ in stat-volts/cm.^{2}	—	2.6×10^{14}
$\eta \equiv (\phi_{xx} - \phi_{yy})/\phi_{zz}$	0.79 ± 0.01	0.94 ± 0.01
ϕ_{xx}/ϕ_{zz}	-0.10	-0.03
ϕ_{yy}/ϕ_{zz}	-0.90	-0.97
Direction of z principal axis of ϕ_{ij}	$46.5° \pm 1°$ from c crystal axis towards a axis	$34° \pm 1°$ from c crystal axis away from a axis
Direction of y principal axis of ϕ_{ij}	Along b crystal axis	$56° \pm 1°$ from c crystal axis towards a axis
Direction of x principal axis of ϕ_{ij}	$43.5° \pm 1°$ from c crystal axis away from a axis	Along b crystal axis

of spodumene that the field gradient tensor ϕ_{ij} must be the same at the four Li sites in the unit cell, and also must be the same at the four Al sites in the unit cell, although, as shown by the results listed in Table VI, the field gradient tensor at the Li sites is quite different in its asymmetry and in the orientation of its principal axes from that at the Al sites. Also, in agreement with crystal symmetry, one of the principal axes of the field gradient tensor at both the Li and the Al sites coincides with the b crystal axis. However, at the Al sites this principal axis corresponds to the eigenvalue of ϕ_{ij} of smallest magnitude, whereas at the Li sites it corresponds to the eigenvalue of ϕ_{ij} of intermediate magnitude.

The orientation of the other two principal axes in the ac plane at both the Li and the Al sites is shown in Fig. 1. It is interesting to note that at the Li sites the z principal axis corresponding to the eigenvalue of greatest magnitude and at the Al sites the y'' principal axis corresponding to the eigenvalue of intermediate magnitude appear to point directly at the projections on the ac plane of the positions of the oxygen ions nearest to the nuclei in question. From the known crystal structure parameters in Fig. 1 it may be calculated that the line joining the projections of the two oxygen ions marked $.\bar{0}\bar{9}$, which are closest to the Li nucleus at $.\bar{3}\bar{1}$, makes an angle of 46° 12′ with the crystal c axis. A similar line joining the projection of the two oxygen ions marked $.\bar{2}\bar{5}$, nearest to the Al nucleus at $.\bar{0}\bar{9}$, makes an angle of 55° 2′ with the c axis, giving a difference of 8° 50′ between the two lines. The observed difference in the angular positions of the z principal axis at the Li sites and the y principal axis at the Al sites is 9° ± 1/2°. The observed angles which these two principal axes make with the c axis are listed in Table VI as 46.5° ± 1° and 56° ± 1° respectively. No attempt has been made as yet to explain this empirical correlation in terms of a theoretical model of the binding of the Li and Al ions in the spodumene crystal, but the observed correlation seems significant.

The numerical value and even the sign of Q for Li^7 are as yet unknown according to Harris and Melkanoff (1), so that no estimates of $|\phi_{zz}|$ at the Li^7 sites can be made at present. The Q for Al^{27} according to Lew (2) is equal to $0.156 \pm .003 \times 10^{-24}$ cm.^{2} This value of Q combined with $|C_z|_{Al}$ in Table VI gives $|\phi_{z''z''}|_{Al} = 2.6 \times 10^{14}$ stat-volts/cm.^{2} at the Al sites in spodumene. This is of the order of magnitude that one would expect for ionic bonds if one allows a factor of 10 decrease due to shielding as suggested by Townes and Dailey (6).

It is of interest to compare the quadrupole coupling constants for Li^7 and Al^{27} in spodumene, as reported in Table VI, with the quadrupole coupling constants for the same two nuclei in other compounds. Logan *et al.* (3) report $C_{Li} = +0.060$ Mc./sec. in the Li_2 molecule and values ranging from +0.408 to +0.172 Mc./sec. in molecules of lithium halides. Pound (5) reports $|C|_{Al} = 2.390$ Mc./sec. in crystalline aluminum oxide. As has been noted before in the case of Cl nuclei the values of $|\phi_{zz}|$ remain of the same general order of magnitude as one examines various compounds of the same general type containing a given nucleus.

We may comment briefly on the nonappearance of the satellites of the Al^{27} line in the milky spodumene samples 1X, 1Y, 1Z, while they are easily observable in the clear samples 2Y and 3X. This is most likely caused by a spread in the local values of ∇E at the various Al sites throughout the crystal due to the presence of impurities and crystal imperfections which are also responsible for the milky appearance of the samples. In accordance with equations [1] and [3] the central component ($m = 1/2$) of the line has no first order dependence of the resonance frequency on ∇E, while the satellites ($m = 3/2$ and $5/2$) do show first order effects. Therefore local variations in ∇E from one nuclear site to another will produce a much greater broadening of the satellites as compared with the central component, and may smear them out so as to make them unobservable. A similar explanation has been offered recently by Watkins and Pound (9) to account for the anomalously weak intensity of resonance lines of some nuclei in cubic crystals.

The new method of measuring nuclear spin proposed in Part I depends on the quadrupole coupling constant for the nucleus in question being large enough to make the second order effect on the angular dependence of the resonance frequency measurable with fair precision. In particular, one must be able to compare the amplitude of the fourth harmonic term in the second order effect with that of the second harmonic term in the first order effect. Thus, that axis of rotation of the crystal should be chosen which emphasizes the fourth harmonic in the second order effect, and then the first order effect should be observed for a rotation about the same axis.

6. ACKNOWLEDGMENTS

The continuing financial support from the National Research Council of Canada in the form of grants to one of us (G.M.V.) is gratefully acknowledged. Two of the authors (H.E.P. and N.G.C.) held scholarships from the Research Council of Ontario, and one (N.G.C.) now holds a Fellowship from the National Research Council. A grant to one of us (H.E.P.) from the B.C. Academy of Sciences made possible a very informative visit to several research centers in California.

REFERENCES

1. Harris, E. G. and Melkanoff, M. A. Phys. Rev. 89: 914. 1953.
2. Lew, H. Phys. Rev. 76: 1086. 1949.
3. Logan, R. A., Coté, R. E., and Kusch, P. Phys. Rev. 86: 280. 1952.
4. Petch, H. E., Volkoff, G. M., and Cranna, N. G. Phys. Rev. 88: 1201. 1952.
5. Pound, R. V. Phys. Rev. 79: 685. 1950.
6. Townes, C. H. and Dailey, B. P. J. Chem. Phys. 20: 35. 1952.
7. Volkoff, G. M. Can. J. Phys. 31: 820. 1953.
8. Volkoff, G. M., Petch, H. E., and Smellie, D. W. L. Can. J. Phys. 30: 270. 1952.
9. Watkins, G. D. and Pound, R. V. Phys. Rev. 89: 658. 1953.

AN EXPERIMENTAL STUDY OF COUNTING LOSSES DUE TO DEAD-TIME EFFECTS[1]

By C. H. Westcott, J. S. Greenberg,[2] and J. S. Kirkaldy

ABSTRACT

When using counting methods for studying instantaneous reactions produced with pulsed accelerators such as synchrotrons or synchrocyclotrons, the systematic errors in counting due to dead-time effects may be considerable. One of us has already published a discussion of the simpler cases of pulsed single-channel counting; the present paper describes experimental investigations designed to extend our knowledge of these corrections, especially to cases of coincidence counting. In Part I of the present paper, the method and apparatus are described, together with calibration procedure; in the course of checking results already known from computation, defects in the functioning of the equipment were uncovered and the correction of these defects is described.

Part II of the paper deals with the problems of coincidence counting at high speed but without the complication of a pulsed source. Difficulties arise in this case unless the rate of occurrence of coincidences is much smaller than the counting rates in the separate counters, a condition which may not be satisfied in many cases in the study of high energy reactions. The corrections for this case have therefore been investigated experimentally and a relatively simple correction formula obtained when chance coincidences are negligible. The dependence of the number of additional chance coincidences on coincidence gate-width is determined both theoretically and experimentally, with satisfactory agreement.

In Part III the investigation is extended to pulsed coincidence counting. A theoretical formula is developed neglecting chance coincidences, for pulse-lengths less than twice the dead-time, and experiments confirm the results and indicate how to extrapolate for longer pulse-durations. A first-order formula for the chance coincidences is also obtained and confirmed.

In all cases near-rectangular pulse-forms are used, but the equipment can readily be modified to study other forms. For the guidance of the user, the principal formulae adopted for determining counting corrections are collected in Appendix III at the end of this paper.

LIST OF SYMBOLS

τ_0 = dead-time (nonextending); τ_c = coincidence resolving time.
$\mathcal{T}$ = pulse-length; p = pulse recurrence rate; $X = \mathcal{T}/\tau_0$.
$f = p\mathcal{T}$ = fraction of total time occupied by pulses.
N = expected total of recorded counts; T = total time.

For single-channel counting:

r = observed counting rate; r_0 = true counting rate; $z = r_0\tau_0$.
If pulsed, the above apply during pulse (r_0 becoming Westcott's (5) ν); r_b = true counting rate between pulses ("background"). $\phi = r/r_0$ = fraction of counts recorded during the pulse; ϕ_b = fraction of background counts recorded.

For coincidence counting:

(N refers to recorded *coincidences* in this case.)
Counting rate in channel I $= N_1 = a + c$
Counting rate in channel II $= N_2 = b + c$
} where the "c" counts are true coincidences.
Mean fraction recorded in channel I $= \rho_1 = 1/(1 + \overline{a + c} \cdot \tau_0)$.
Mean fraction recorded in channel II $= \rho_2 = 1/(1 + \overline{b + c} \cdot \tau_0)$.

[1] *Manuscript received January 26, 1953.*
Contribution from the Radiation Laboratory, McGill University, Montreal, Que.
[2] *Now at Massachusetts Institute of Technology; co-author of Part I only.*

Conditional probability (knowing a count in channel I at $t = 0$ to have been recorded) of a count occurring in dt at t in channel II $= F_2(t)dt$. Conditional probability (same condition) of such a count being recorded $= P_2(t)$.
Correlation correction factor $= \gamma = P_2(-\epsilon)/\rho_2$. ϵ = an infinitesimal quantity (as usual).
Effective transferred counting rate $= \beta/1.08$ (such that the losses of coincidences for $N_1 = c$, $N_2 = \beta/1.08 + c$ are the same as for the original $a + c$ and $b + c$ respectively, the 1.08 being a correction factor).
If pulsed, above apply during pulse; a_0, b_0, and c_0 are similar to a, b, and c, but refer to the interpulse period ("background"). ϕ = fraction of coincidences recorded during the pulse; ϕ_0 = ditto if $\tau_c = 0$; ϕ_2 = ditto if $\tau_c = 0$, $\mathscr{T} = 2\tau_0$; ϕ_b = ditto during background period.

PART I
APPARATUS AND SINGLE-CHANNEL COUNTING RESULTS

1. Introduction

The problem of the corrections required for the loss of counts due to the finite resolution of a counting system has already been treated theoretically by one of us (5), for the cases which arise when working with accelerators which give short "pulses" or "bursts" of particles at regular intervals. These corrections can be quite considerable, even if the dead-time of the counting system is quite small, on account of the bunching of the particles being counted, so that the instantaneous counting rate during the "burst" is quite high. However, the calculations show that, for pulsed counting, the corrections to be applied to the observed counting rates are never greater than they would be if this high instantaneous counting rate were maintained continuously. Since exact computation was possible only for a rectangular accelerator-pulse and the theory for coincidence counting, even with rectangular pulses, was incomplete, it was felt worth while to undertake an experimental study of these corrections, and to design the equipment so that both nonrectangular pulse-forms and coincidence methods could be studied. The present paper describes a systematic investigation of the problems of single-channel and coincidence counting, using nearly-rectangular pulse-forms; the equipment is to be kept available in case further study is later required using the actual pulse-profile of the McGill cyclotron, or for triple or higher-order coincidence systems.

While it is in many cases possible to count comparatively slowly, or to use the very high-speed techniques developed in recent years, and so avoid having to make appreciable corrections for dead-time effects, it remains desirable for accurate measurement of counting rates to be able to count fast in appropriate circumstances, and a knowledge of the errors thus incurred is then essential. Geiger Counters, with their long dead-times, will generally not be used in the type of work under consideration; with proportional counters, having dead-times (including that of the associated circuits) of perhaps one or a few microseconds, the considerations of this paper may be quite important. Scintillation counters using modern techniques and circuits may have a much faster response, so that the considerations of this paper become applicable when the accelerator

pulse is of comparably shorter duration, e.g. with impulsive beam extraction from a synchrocyclotron, when the pulse length is usually comparable with one r-f. cycle, or, say, 30–50 mμsec. For scintillation counters used with longer-pulse accelerators, the results of Part II of this paper are likely to be of prime interest, since, with pulse lengths much greater than the dead-time, quasi-steady conditions prevail. However, our investigation shows that even in this relatively simple case of coincidence counting, the evaluation of the corrections is not straightforward unless the ratio of the "singles" to the coincidence counting rate is large.

An important consideration in our investigation is the choice of a nonextending (2, 4) dead-time. In practice, where dead-time corrections are important, the actual dead-time used must be accurately known; this is often most easily achieved by adding a circuit giving an accurately-known dead-time somewhat longer than the maximum which would otherwise be present. Such a circuit can be made accurately nonextending (i.e., a count following within the dead-time of an earlier count does not extend that dead period). We have therefore chosen to study the errors caused when the dead-time is constant and nonextending, for the sake of definiteness. The only equally definite alternative, a dead-time extending until a full τ_0 after the last count to occur within the dead period, seldom occurs in practice and is not easy to generate artificially.

To simplify our investigation, we have used dead-times (generated artificially) which are much longer than those that will occur in practice. We can then neglect the inherent dead-times of our counters and use amplifiers with a rather poor frequency response; the accurate calibration of the dead-time circuits used is also simplified. The pulses used are also artificial, and are made longer than the pulse-lengths of the accelerator concerned by the same large time-scaling factor (1000 or more). The randomness of the counts within the pulse-period is provided by using α-particles from polonium, the pulses being produced by means of a rotating shutter; the pulse-form then becomes, strictly, a probability function for the occurrence of counts, and may be changed by altering the shape of the polonium source or the shutter aperture. The interval between the pulses is not scaled up by the same time-scale factor, but the pulse spacing is maintained large enough for events in successive pulses to be independent, and reasonably high counting rates are thereby maintained.

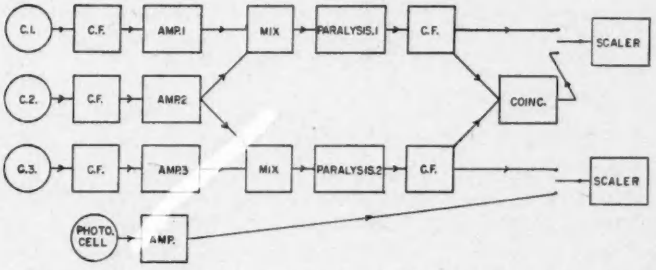

FIG. 1. Block diagram of equipment used (C. 1, 2, 3 = proportional counters; C.F. = cathode follower).

To enable us to study coincidence counting, we employ three counters instead of one, all three being exposed to the source for the same (or very closely the same) pulse-period. The three amplifiers are followed by a mixer (Fig. 1) and two counting channels, each containing a dead-time circuit. In this way a count occurring in the center counter C.2. simulates an event (a "true" coincidence) in which a particle passes through both counters of the coincidence pair; counts in either of the other two counters simulate an event in which one only of the counters is triggered. The system of three counters thus simulates the behavior of a two-counter coincidence system. The photocell channel shown on Fig. 1 is for counting the revolutions of the rotating shutter. Both of the dead-time circuits and the coincidence circuit had, of course, to be accurately calibrated and all three could be adjusted to give dead-times or a coincidence resolution continuously variable within very wide limits.

2. *Apparatus*

2.1. *Vacuum Chambers and Counters*

Fig. 2 is a diagram of the main vacuum chamber used showing the location of the source, shutter wheel, and three proportional counters. When in use

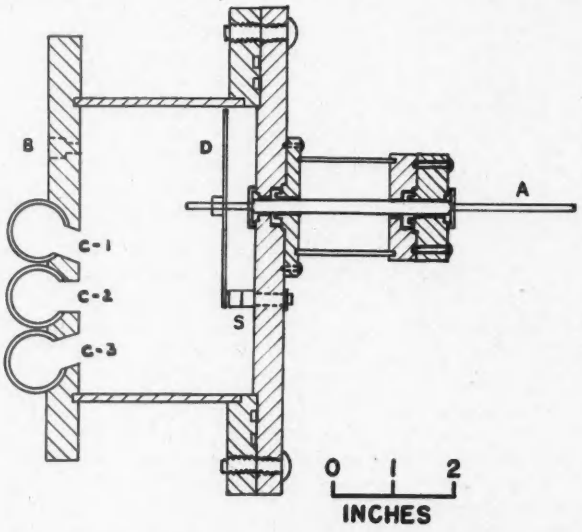

FIG. 2. Vacuum chamber assembly. *A*, spinning shaft; *B*, pumping and filling tube; C-1, C-2, C-3, counters; *D*, slotted disk; *S*, α-particle source.

it is filled with 99% pure commercial methane to a pressure of 24 cm. Hg, and forms a housing for the source and counters so that the α-particles, having passed through this gas only, arrive at the counters with a suitable velocity and give large bursts of ionization. This gas filling also gives good proportional counter operation. On the wall of the chamber opposite the source are three half-inch square openings into the three counters. Baffles are provided for varying the

effective counter openings, so that the relative numbers of α-particles entering the three counters can be varied as required. The polonium source used gives a practically constant source of monokinetic α-particles with the randomness in time postulated in the theory. A 1/20 h.p. d-c. motor fed from a stabilized power supply with separately variable field and armature rheostats is used to spin the rotating shutter at a controlled but variable speed, and a polished flat milled on the hub of the pulley on the disk shaft reflects a beam of light once per revolution onto a photocell so that the rate of rotation of the disk can be accurately measured on one of the scaling units. With a disk having a single 30° opening, pulse lengths of 1 to 10 msec. are available and the intervals between the pulses are ample to ensure that events in one pulse do not affect the next. The exact pulse envelope can be found by counting with the disk stationary at various positions, and, using sources of different widths, more or less steep-sided pulses can be produced, as shown in the experimental results (Fig. 3) for the two arrangements generally used in the work described in this paper.

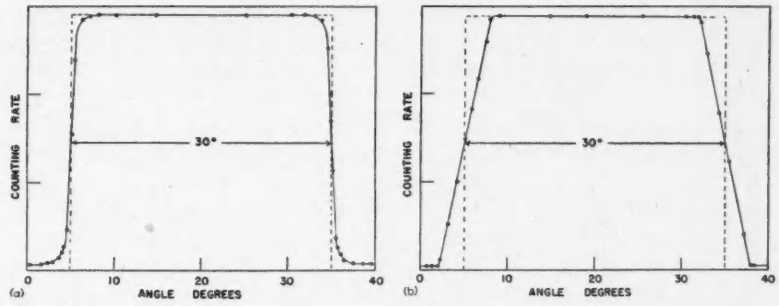

FIG. 3. Measured pulse profiles. (*a*) Narrow source, 0.020 in. wide. (*b*) Wide source, tapered (radially), width at center line 0.158 in.

The usual cylindrical geometry of counter is used, with 7/8 in. internal diam. brass tubing of 3/64 in. wall as cathodes, and 6 mil diameter tungsten wires 2 in. long for the anodes. The cathodes form part of the vacuum chamber and are grounded, a common anode voltage (usually 1600 v.) being used, with a separate 1-megohm anode load for each counter.

2.2. *Electronic Equipment*

As already mentioned, "fast" amplifiers are unnecessary for this work, and an obsolete National Research Council model having a maximum pass frequency of about 30 kc. per sec. was used. One trouble was that these gave overshoots following each signal-pulse (about -15 v. following a $+70$ v. signal), but our α-particle pulses were large and uniform (a typical bias-curve having a plateau of slope 0.09% per volt from 15 to 63 v. bias) so that we were able to choose a discriminator bias such that the superposition of a -15 v. overshoot would not cause a following count to be missed.

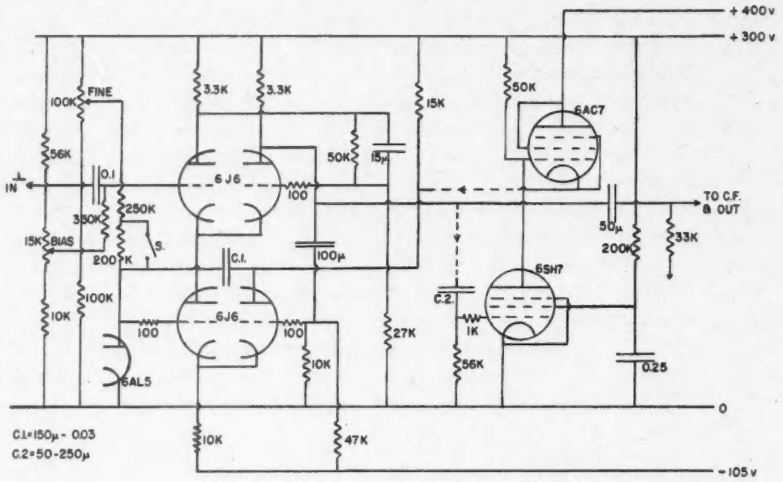

FIG. 4. Discriminator and paralysis circuit. Additional tubes (to right of dotted connections) were added to eliminate defect of original circuit (see text). Capacitances are in microfarads.

The discriminator and paralysis circuit (Fig. 4) is a modified version of the circuit described by Cooke-Yarborough (1), which meets our specification of a nonextending dead-time very well, since during the "dead" period the upper 6J6, into which signals are fed, is completely inoperative, being in series with the nonconducting anode of the lower 6J6. The duration of the dead-time, set by C.1. and the resistors from the 6AL5 plate to a positive supply, is made variable in our case from 11 to nearly 5000 μsec., precision resistors being used so that the calibration would be stable. At the end of the dead-time the circuit recovers immediately, independent of any counts which may have occurred during the paralysis period, unless the signal voltage at the end of this period is still above the discriminator level, in which case the dead-time is extended until the voltage falls below discrimination level, thus avoiding counting a signal initiated before the end of the dead-time. Unfortunately, the circuit has one serious defect; if, immediately after the end of a dead period, it is retriggered by a new count, the second dead-time may be considerably foreshortened. For, at the instant of recovery, C.1. is discharged, and it normally recharges through the 15K resistor and the 6AL5, the rate of recharge being limited by the former; if the circuit is retriggered before this process is completed the 6AL5 plate and 6J6 grid, whose rate of rise determines the dead-time, are not driven as far negative as usual. To correct this fault we add the two additional tubes shown in Fig. 3. The 6SH7, normally in grid current, is fed with "pips" from differentiation of the dead-time square-wave; the positive pip has no effect, but at the end of the dead-time the negative pip cuts the tube off and applies a positive "pip" to the 6AC7 grid. The latter then acts as a cathode follower and feeds current in parallel with the 15K to recharge C.1. The plate and screen loads of the 6SH7 must be so adjusted

that the 6AC7 is cut off during the dead period and does not affect the duration of the dead-time. It is found necessary to vary C.2. from its normal 50 pf. up to 100 or 250 pf. for the two largest settings of C.1., to give adequate recovery, but for the smaller values of C.1. a constant C.2. is acceptable. The effect of this modification on the counting rates observed is discussed in §3.1 below.

The remaining circuits follow normal practice. The mixing is obtained using parallelled cathode-followers, and the coincidence unit is a Rossi circuit preceded by square-wave generating pairs which can be calibrated for coincidence resolving time.

2.3. *Calibration*

The required condition of known, accurately reproducible, paralysis and resolving times made a careful calibration of these circuits essential. In this process, use was made of a double pulse generator constructed in this laboratory by Mr. A. Densmore, which gave recurring pairs of pulses of continuously variable amplitude and time separation, as well as "marker" pips of 5, 20, and 100 kc. per sec. frequency locked to the first pulse of each pair. The marker frequencies were set against a crystal oscillator and later checked by direct counting into scalers. In the first method used for calibrating the dead-time circuits, the pulse-pair spacing was set against these markers, using an oscilloscope, and then the paralysis control set until the second pulse was just on the point of being recorded or suppressed. A completely independent method of calibrating shown in Fig. 5 was also used for confirmation; starting from a set

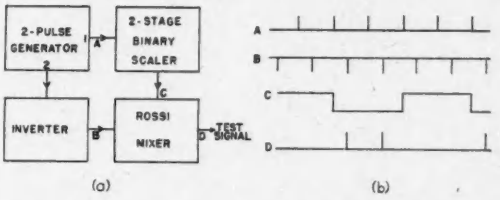

FIG. 5. (*a*) Equipment and (*b*) wave forms for system used for calibrating paralysis circuits.

of uniformly-spaced pulses, alternate pairs were removed, and the resulting signals fed into the paralysis circuits to be calibrated. The spacing of each pair could then be deduced simply by counting the total number of counts per unit time, the reciprocal of which is just twice the pair-spacing. The removal of the alternate pairs avoided the paralysis circuit under test ever being in a condition of almost continuous paralysis, in which some of its working voltages might have taken on abnormal values.

The accuracy of the final calibration is believed to be about $\pm \frac{1}{2}$ μsec. up to $\tau_0 = 50$ μsec. and $\pm 1\%$ or better thereafter. Above about $\tau_0 = 1500$ μsec. the accuracy is thought to tend to $\pm \frac{1}{2}\%$, since the results of the two methods agree within this accuracy. There has been some evidence of drift of the calibrations, but with no systematic long-period tendency, and as far as is known

always within a 1% range. We feel that an error exceeding 1% in calibration is very unlikely, except of course for $\tau_0 < 50$ μsec.

The coincidence unit has been calibrated similarly, mostly by the first method; the required accuracy is not so great in this case, but we believe the calibration is good to ± 1%. The discriminator bias is not strictly required absolutely, and has been calibrated less exactly than the dead- and resolving-times; both the direct observation of pulse-sizes on a calibrated oscilloscope and comparison with the calibrated Harwell (1) scalers have been used, and the accuracy obtained is probably about 2%.

3. *Experimental Methods and Results*

3.1. *Single-channel Continuous Counting*

As a check of the behavior of the system, unpulsed counting was first studied, using a source giving a counting rate of about 200 per sec. and with the shutter open (disk stationary). Paralysis times varying from 10 μsec. to 4500 μsec. were chosen successively, and for each the count registered on the scaler in five minutes was determined, giving for each determination a statistical (r.m.s.) error never greater than 0.5%.

Theory for this case states that $r = r_0/(1 + r_0\tau_0)$, where r is the observed and r_0 the true counting rate, and τ_0 the dead time. This expression may also be written $1/r = 1/r_0 + \tau_0$. We may therefore plot the reciprocal of the counting rate against the dead-time and should thus obtain a line of unit slope. Fig. 6

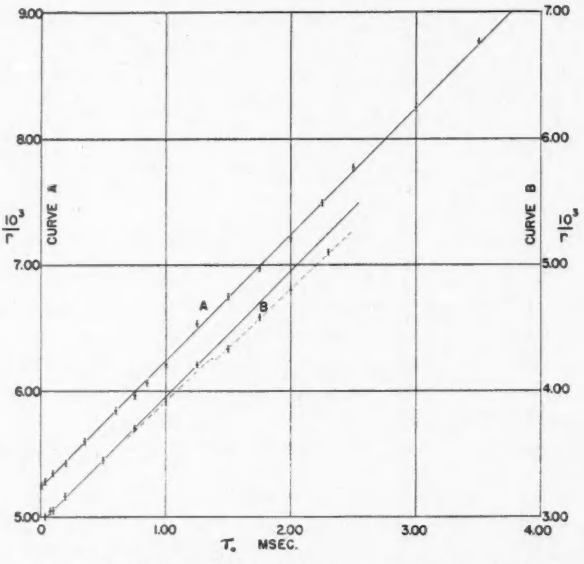

FIG. 6. Experimental verification of law of loss in continuous counting; $1/r = 1/r_0 + \tau_0$. *A*, with recovery circuit; *B*, without recovery circuit. Vertical lines represent ± statistical r.m.s. errors.

shows the results obtained, the curve B being the original results before the two-tube recovery circuit (Fig. 4) was built into the paralysis circuit. It is seen that the mean slope of this line is about 0.93, and that there is evidence of a "break" at $\tau_0 = 1400$ μsec. This is the point on the calibration where a change of range occurs, C.1. being increased from 0.006 to 0.03 μf. The discrepancy was found to be due to the incomplete recharging of C.1., previously described, which naturally became more marked at this point. Curve A of Fig. 6 shows the results obtained after incorporating the correcting circuit. This curve not only serves to demonstrate the agreement of our results with theory, but also serves as a check on the calibration accuracy—the statistical error of most of the points corresponds to a calibration error of only 0.6%. It is seen that the agreement of the experimental points with the theoretical unit slope line is good.

3.2. *Single-channel Pulsed Counting*

In this case the theoretical curves with which comparison is to be made are those of Fig. 4 of Westcott's paper (5). The experiments described below also test the effect of using trapezoidal instead of rectangular pulses. Several sources, giving 200–400 counts per sec., were used; narrow sources gave a very nearly rectangular pulse (Fig. 3*a*), while a wider source gave the trapezoid of Fig. 3*b*; these are typical curves as obtained experimentally (§2.1 above). By varying the dead-times used, various values of the parameter z (counting rate during pulse multiplied by dead-time) from 0.2 to unity could be obtained, to correspond to the calculated curves.

For each "run", the true counting rate during the pulse is first observed by counting with the shutter open and a very small dead-time, for which correction was readily made. A high statistical accuracy is readily obtained with the high counting rates used. The dead-time to be used for a given z is then computed and applied. A number of values of X ($= \mathcal{T}/\tau_0$) are then chosen, and for each the required speed of the shutter-disk computed. During these computations the "background" count may be observed, by counting with the shutter closed (tests were also made to ensure that the "background" was substantially independent of disk angle within the "closed" sector). Then the observations are made for the various shutter-speeds, for each of which a total counting time of 20 to 30 min. was used, divided into several shorter periods interspersed with readings at different speeds to minimize effects of drift of any kind. Periodically during the "run", counts were made with the disk stationary (either closed or open); it was generally found that these counts remained steady within statistical errors, and no appreciable changes in conditions (e.g., due to gas contamination attributable to imperfect vacuum seal at the rotating spindle) were revealed. For each nominal value of X, the speeds of rotation were averaged, taking total revolutions ÷ total time, equivalent to averaging $1/X$'s, or averaging along rectangular hyperbolae on the graphs; the error resulting from this averaging was always quite small, since the speeds seldom varied more than ± 5%, and in any case the theoretical curves are almost hyperbolic themselves over small ranges.

The equation (17) of Westcott (5) was used to correct for the background; in the notation of the present paper it becomes

$$[1] \qquad N/T = \phi f r_0 + (1 - f)\,\phi_b r_b - p r_b \tau_0\,(z/[1 + z]),$$

the left-hand side being the observed counting rate and ϕ the fraction of the counts which record during the pulse. ϕ_b, the corresponding fraction during the "background" period, never differs appreciably from unity in our work, and f, for a single 30° open-sector shutter, is, of course, 1/12 (see List of Symbols above for the other quantities). The last term in this equation is never more than $\frac{1}{3}\%$ of the total counts, and is only computed to a first order—it represents the effect of counts near the end of a pulse suppressing background, and background counts just before a pulse suppressing part of the pulse.

We thus obtain a ratio ϕ, the fraction of counts (corrected to no background) which record, for a given dead-time (given z), and we may plot this against X to obtain curves similar to the theoretical ones cited. A small correction (usually less than 0.1%) is sometimes necessary if the dead-time chosen does not make z exactly the required nominal value when the final average counting rate is put in the computations (we make this correction assuming $\phi \propto 1/(1 + z)$). The points on Fig. 7 are obtained in this way, and are shown superimposed on

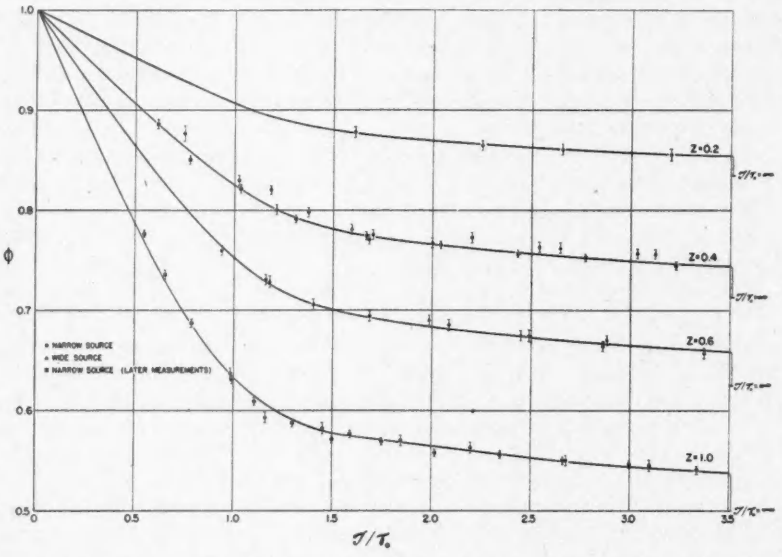

FIG. 7. Experimental verification of law of loss for pulsed counting. Vertical lines represent ± statistical r.m.s. errors.

theoretical curves. The standard errors of the observed points are shown, being usually about $\frac{1}{2}\%$ or slightly smaller. On the same curves are shown points obtained with the wider source (Fig. 3*b*).

It should be noted that the standard errors quoted are not simply the usual $\sqrt{N}$. The existence of correction terms increases the errors somewhat, but there

is also a factor tending to reduce them. For continuous counting with a dead-time (§3.1 above, or $X = \infty$ in §3.2) the formula is known rigorously; the fraction recorded being $1/(1 + z)$, it is known that the fractional statistical variance is reduced and becomes $\frac{1}{\sqrt{N}} \cdot \frac{1}{1+z}$.* In estimating the variances of our measured values for pulsed counting, we have assumed that a similar effect occurs, although to a slightly smaller extent; that, in fact, if the counts accidentally come rather more closely than expected, there is a greater probability that suppression due to dead-time effects will occur. The factor by which this reduces the statistical error is taken as slightly nearer unity than the "fraction recorded" (ordinate of Fig. 7), to be on the safe side.

3.3. *Discussion of Results—Single-channel Pulsed Counting*

It is seen that the fit of the experimental points on the curves of Fig. 7 is quite close throughout. The fact that the points for the wide source (triangular points on the figure) do not differ significantly from the others shows that a trapezoidal pulse like that of Fig. 3*b* gives results very closely equivalent to the rectangular pulse from which it is obtained by a symmetrical distortion. The circular and square points on the figure, obtained with the narrow source, are for pulse-profiles much nearer to the ideal rectangular form (effective source-width nearly eight times smaller), so that their values cannot depart at all significantly from those which the ideal pulse would have given.

A closer examination of the original measurements (circular and triangular points on figure) shows some signs of systematic error; most of the points considered individually have reasonable errors, but on the average the points for the curve for $z = 0.4$, for example, tend to lie above the curve. The $z = 0.2$ curve is free from this effect, and for $z = 0.6$ and 1.0 it is only about $\frac{1}{3}\%$, compared with $1\frac{1}{4}\%$ for $z = 0.4$. We have since discovered (cf. §9 below) that noise pickup from the motor driving the shutter occasionally causes high readings. In later measurements, using a filter to cut out this noise, and shutter-wheels with either two 45° or four 18° open sectors (to increase counting rates and reduce errors due to background fluctuations, see §9), we have obtained the points shown as square points on the figure. These agree extremely well with the theoretical curves.

We therefore conclude that the agreement between our measurements and the theory is entirely satisfactory. It is also clear that the nonrectangularity of the pulses used in this work is of no consequence. In any actual application the pulses are likely to depart further from the ideal rectangular form, but by measurements of the type described above the necessary corrections can be quickly evaluated. Imperfect knowledge of the exact pulse-profile is likely to be one of the major sources of inaccuracy in such work; it is therefore still

**The variance of the time for a fixed number N of counts is unchanged, but the time required is lengthened by $N\tau_0 (= zT)$; the fractional variance is therefore $\frac{1}{\sqrt{N}} \cdot \frac{1}{1+z}$ and is the same for $(\partial T/T)_{N\text{const}}$ as for $(\partial N/N)_{T\text{const}}$, since $N \propto T$. Cf. Elmore (2).*

desirable to reduce the dead-time used as much as is possible without otherwise complicating the arrangements used. An over-all fraction recorded of more than 60% is also desirable; if this condition is satisfied there is in general no reason why the correction for dead-time effects should not be made to give a final result of over-all accuracy of $\frac{1}{2}$ to 1% provided a sufficient number of counts can be taken.

PART II
COINCIDENCE COUNTING, UNPULSED

4. *Outline of the Problem*

When coincidence techniques are used, the problem becomes more complicated; a coincidence may be lost by the suppression of either of its component counts, or it may be "restored" if the suppressing count, or some other in the same channel, is within τ_c of the coincident event, and; as in all cases, "random" coincidences may also arise from two unrelated counts. Further analysis shows that if the rate of occurrence of coincident events is much less than that of other counts in either channel, the problem is readily soluble, but if not, the solution is quite difficult.

Now it happens that the principal fields of use of the coincidence technique in the past have been in cosmic rays and β–γ and γ–γ correlation studies, and in either case at least one of the counters receives many counts which are not coincident with those in the other (or others, where more than two counters are used). In β–γ work, for example, even if every β-ray is accompanied by a coincident γ-quantum, and no other γ's are present, both solid angle considerations and the inefficiency of most counters in detecting γ-rays result in the β-ray counter at least, and usually both, receiving many counts of which the counterpart does not cause a coincident count in the other counter. In such cases the two channels are effectively uncorrelated, and the proportion of true coincidences recorded is simply the product of the two recording probabilities ρ_1 and ρ_2 in the separate channels; only the computation of "restored" or "random" coincidences presents any difficulty, and if τ_c is fairly small, the usual approximate formula for the latter generally suffices.

However, in the detection of heavy particles resulting from reactions induced by a synchrocyclotron or similar machine, coincidence techniques may be used to establish the range (or energy) of a product of the reaction, or simply to eliminate unwanted events such as those due to neutrons, and in such cases the proportion of noncoincident events may not be large. It is just in such arrangements, too, that high counting speeds during the cyclotron "pulse" are used, and result in relatively large dead-time corrections being likely. This case is therefore of particular interest, especially when accurate quantitative results (e.g., proton–proton or other scattering laws) are required.

In the following section, we give some elementary theoretical considerations concerning this case, and follow this with a description of the experiments performed. We defer consideration of "restored" or "random" coincidences until later, taking first the case of τ_c very small. Although we have been able to find plausible arguments for believing that the formulae we put forward have

more than a purely empirical basis, we have not been able to find any precise solution of the theoretical problem. Nevertheless, the results given should be sufficiently accurate for interpreting any experimental results of the type considered.

5. *Elementary Theory*

Following the methods used for the single channel case, we postulate that a nonextending dead-time of value τ_0 occurs in each counting channel. We also take the coincidence resolving time τ_c to be very small, so that essentially no chance coincidences occur. Considering coincidences between only two channels, we therefore see that a coincidence will be recorded under these conditions if and only if neither of the constituent counts is suppressed. For either channel considered separately the probability of recording of any count is given by the well-known (4) formula $\rho_1 = 1/(1 + N_1\tau_0)$ or $\rho_2 = 1/(1 + N_2\tau_0)$, where, as listed above, N_1 and N_2 are the true counting rates and the ρ's the probabilities of nonsuppression in the respective channels. These *a priori* probabilities apply to any count whether or not it is a member of a coincident pair; thus if the N_1 counts per second in channel I comprise c coincident events and a noncoincident events, the average number of coincident events per second *for which the count in channel I is recorded* will be $\rho_1 c$. (We take $N_1 = a + c$, while $N_2 = b + c$, the c's being coincident.)

To compute the number of recorded coincidences per second, therefore, we first enumerate all those coincident events which record in channel I, and for each enquire whether it is also recorded in channel II. Unfortunately the probability ρ_2 is now inapplicable, for the probabilities of recording in the two channels are not independent; we require to know the *a posteriori* or "conditional" probability of a count in channel II being recorded *when a simultaneous count in channel I is known to have recorded*. Were the two channels completely uncorrelated, we would simply have $\rho_1\rho_2 c$ as the required coincidence recording rate; this is in fact true if c/N_1 and c/N_2 are both negligibly small. In any other case we must introduce a factor γ, which we shall see to be greater than unity, giving as the coincidence recording rate $\gamma\rho_1\rho_2 c$. The conditional probability in channel II must then be $\gamma\rho_2$, while clearly we must obtain the same result if we consider channel II first, the conditional probability in channel I then being $\gamma\rho_1$ with the same value of γ. Our problem then reduces to the computation of γ, i.e., of the conditional probability defined above, noting that γ must be in a form symmetrical for interchange of a and b.

The reason for the correlation between the two channels is that, once it is known that a count has been recorded in channel I (at $t = 0$, say, zero time being located successively in the process of enumeration at the instant of every coincident event recorded in channel I), it becomes quite unlikely that another coincident count can have occurred in the interval from $t = -\tau_0$ to 0 since such an event, unless itself suppressed in channel I, would have suppressed the count in question, which is known not to have been suppressed. Therefore the *a posteriori* expected rate of occurrence of counts in channel II ($F_2(t)$, say) must be taken as only b during the interval mentioned, instead of $b + c$ as at all

other times. This expression is, in fact, an approximation, since a coincident count in the interval $-\tau_0 < t < 0$ may be suppressed in channel I by an earlier noncoincident count,* and thus not produce a dead-time to suppress the count at $t = 0$, while the noncoincident count* may be early enough not to suppress this count either; the coincident counterpart of such a count may then occur, unsuppressed, in channel II, and suppress the counterpart $t = 0$ count in this channel; in such a multiple contingency one of the "c" counts may still occur in channel II in the "prohibited" interval. In general these multiple contingencies are unlikely, and no satisfactory theory including all such cases has been developed, so that as a first approximation we neglect all such cases, and adjust our formulae later, empirically, to allow for them. On this basis, then, we proceed, noting in the meantime that most of these multiple contingencies vanish if $a = 0$, i.e., if there are no noncoincident counts in the first channel.

The correlation may be easily seen if we take the special case $a = b = 0$, i.e., all counts coincidences. Then the behavior of the two channels must be identical; any count suppressed in one channel will also be suppressed in the other (100% correlation), and in this case $\rho_1 = \rho_2 = 1/(1 + c\tau_0)$; the loss rate for coincidences must be given by the same factor, i.e., $\gamma\rho_1\rho_2 = \rho_1$ or $\gamma = 1/\rho = 1 + c\tau_0$. Remembering that for c small compared with N_1 and N_2, $\gamma = 1$ (0% correlation), we see that it is reasonable that γ should always lie between unity and $1 + c\tau_0$.

5.1. *Evaluation of* γ

Knowing $F_2(t)$, we can readily proceed to calculate $P_2(t)$, which we define as the probability that a count which occurs in channel II at time t will be recorded, with the usual prior condition. Then the probability of a recorded count occurring in channel II in dt at t is given by $P_2(t)F_2(t)dt$, which is the g function of Feather (3), whose method we use (his f being our F). Feather's equation is then

$$[2] \qquad P_2(t) = 1 - \int_{t-\tau_0}^{t} P_2(t)F_2(t)\,dt$$

and expresses the fact that the probability of suppression of a count is that of a recorded count having occurred in the previous interval of length τ_0.

Differentiating equation [2] with respect to t and substituting for F_2 the value $b + c$ for $t < -\tau_0$ and b for $-\tau_0 < t < 0$, we obtain, for $-\tau_0 < t < 0$,

$$[3] \qquad \frac{dP_2(t)}{dt} = \rho_2(b + c) - b.P_2(t)$$

where we have inserted the value ρ_2 for the undisturbed value of $P_2(t)$ which occurs for $t < -\tau_0$ (cf. Fig. 8).

Integration of (3) yields

$$P_2(t).e^{bt} - \rho_2\, e^{-b\tau_0} = \rho_2(b + c)\int_{-\tau_0}^{t} e^{bt}\,dt,$$

which yields for the value of the required conditional probability at $t = 0$ (strictly, for t infinitesimally before zero)

$$P_2(-\epsilon) = \rho_2[1 + \{1 - e^{-b\tau_0}\}c/b].$$

*—*or a coincident count of which the counterpart is itself suppressed.*

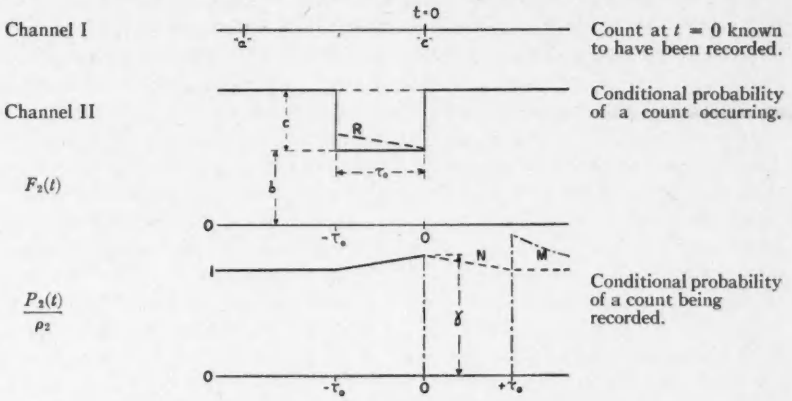

FIG. 8. Illustrating the relations between the probabilities involved.

Remembering that this probability must be $\gamma\rho_2$, we obtain

[4] $$\gamma = 1 + [1 - e^{-b\tau_0}]c/b.$$

Comparing this with Fig. 8,* we see that the reduction in the *a posteriori* expectation of counts in channel II before $t = 0$ gradually raises the probability of a count in that channel being recorded by a factor which rises to the γ given above just before $t = 0$ (if a count actually records at this time there is a discontinuity in P_2 at zero time). The value of γ obtained takes the value of $1 + c\tau_0$ in the limit $b \to 0$, a value which is required when $a = b = 0$ (100% correlation case). We note, however, that our expression does not contain a; this quantity represents noncoincident counts in channel I. These are mainly responsible for the "multiple contingencies" mentioned above, which we have been neglecting and which make it likely that some of the "c" counts in the interval $-\tau_0 < t < 0$ will still coexist with a recorded count at $t = 0$ in channel I. The function F_2 should therefore be modified as shown dotted at R (Fig. 8); immediately before $t = 0$ it retains the value b, but at earlier times its value is increased. This occurs to some extent even if $a = 0$ (cf. footnote, p. 872 above), but mainly to an extent depending on the value of a.

Now expression [4] above depends on the fractional depth $(c/(b + c))$ of the "well" in F_2, i.e. on the ratio c/b, as we see by writing it in the form $\gamma = 1 + (1 - e^{-(b/c)(c\tau_0)})c/b$; we may therefore hope to allow for the multiple contingencies by reducing this fractional depth suitably, i.e., by increasing b to a value β whose value will depend on a as well as b (taking $\beta > b$, of course). In fact, this is saying that the fractional increase of P_2 in the range $-\tau_0 < t < 0$ (Fig. 8) depends on the fractional depth in the "well" in F_2. We retain c unchanged to preserve the limiting form $1 + c\tau_0$; we then obtain

[5] $$\gamma = 1 + [1 - e^{-\beta\tau_0}]c/\beta.$$

*Note that the left-hand scale of ordinates in Fig. 8 is $P_2(t)/\rho_2$, not $P_2(t)$.

The evaluation of β in terms of a and b is left to experiment, remembering that it must be symmetrical with respect to interchange of these quantities. How valid this argument is will be seen by comparison with the experiments described below.

5.2 *Effect of Finite Coincidence Resolution Time*

In addition to the true coincidences recorded at the rate $\gamma\rho_1\rho_2 c$ per second, there is the possibility of recording coincidences between two noncoincident counts or between one count of a coincident pair and a noncoincident count. In either case, the counts in the two channels must occur within a time interval of less than τ_c, for a coincidence to be recorded. If we take $\tau_c < \frac{1}{2}\tau_0$, there can never be more than one recorded count in one channel within τ_c of any count in the other channel, so that the question of whether such a combination records as one or two coincidences cannot arise. We shall go further and take $\tau_c \ll \tau_0$ initially, considering only the coefficient of the linear term in the expansion of the counting rate in a series of powers of τ_c; the experimental results which follow show that this approximation is quite accurate enough for most practical cases.

There are in fact three possible cases which contribute additional recorded coincidences, viz., accidental coincidences between an "a" count in channel I and a "b" count in channel II; "restored" coincidences between a "c" in I and a "b" in II, and the inverse between an "a" in I and a "c" in II; and coincidences between a "c" in I with a different "c" count in *II*, which is highly unlikely and can only arise if the opposite partner of each count is suppressed. The last contingency contributes nothing to the linear term in τ_c, and will not be further considered.

Before proceeding, we must note the form of $P_2(t)$ for positive t, having remarked that for negative t the form is the same as that already considered, regardless of whether the count which is known to be recorded at $t = 0$ is an "a" (noncoincident) or a "c" (coincident) count. However, if it is a coincident count which leads to a recorded coincidence, we know that channel II is dead from $t = 0$ to $+\tau_0$, and thereafter $P_2(t)$ rises suddenly to unity and then follows a curve similar to those of Fig. 3 of Westcott's paper (5). This is shown in Fig. 8 (curve M) above. If, however, a count is *not* recorded in channel II at $t = 0$, we obtain curve N (Fig. 8) by continuing to apply equation [2], $P_2(t)$ gradually reverting from its value of $\gamma\rho_2$ at $t = 0$ to a value of ρ_2.

Enumerating the possibilities in a total time T, we obtain for the observed number of coincidences

$$\rho_1(a + c)T\left[\gamma\rho_2\frac{c}{a + c} + \int_{-\tau_c}^{-\epsilon} P_2(t)F_2(t)\,dt + \int_{+\epsilon}^{+\tau_c} P_2(t)F_2(t)dt\right]$$

where the factor outside the bracket is the number of counts recorded in channel I, for each of which an integral has to be taken over the allowed range ($-\tau_c$ to $+\tau_c$) of the probability of a recorded count occurring in channel II. The contribution to the integral in the excluded range $-\epsilon$ to $+\epsilon$ is due solely to true coincidences, and is given by the first term within the bracket. For either of the other integrals we may substitute $P_2(\pm\epsilon)F_2(\pm\epsilon)$ for $P_2(t)F_2(t)$, with the sign

appropriate to the range of integration used, since the remaining terms in the Taylor expansion $P(t)F(t) = P(0)F(0) + tP(0)F'(0) + tP'(0)F(0) + \ldots$, when integrated over a range of width τ_c, only give terms in τ_c^2 and higher powers. We must, of course, take the appropriate case for all $P_2(+\epsilon)$ as explained above, i.e. for the case when a count is recorded in channel II we have no contribution to the latter integral since $P_2(t)$ is zero throughout the range $0 < t < \tau_0$. If there is a coincident count but it has been suppressed in channel II, the probability that this suppression has ceased in a time $t < \tau_0$ is approximately equal to t/τ_0, and when this is put in the integral the t factor again places the result in the τ_c^2 category, which we are neglecting. Up to the first power of τ_c, therefore, we can neglect the positive integral for all cases where the count in channel I was a "c" count. We then have for the expected rate of recording coincidences:

$$\gamma\rho_1\rho_2 c + \rho_1(a + c)\int_{-\tau_c}^{-\epsilon} P_2(t)F_2(t)\,dt + \rho_1 a\int_{+\epsilon}^{+\tau_c} P_2(t)F_2(t)\,dt.$$

Substituting $P_2(\pm\epsilon) = \gamma\rho_2$, $F_2(-\epsilon) = b$, $F_2(+\epsilon) = b + c$, we obtain as our final expression a coincidence recording rate of

[6] $$N/T = \gamma\rho_1\rho_2[c + (2ab + bc + ca)\,\tau_c + \text{higher order terms}^*].$$

It is of interest to compare this formula with the one normally used for computing random coincidences in the absence of dead-time effects (i.e., $\gamma\rho_1\rho_2 = 1$). Our correction reads $(2ab + bc + ca)\tau_c$, or $\tau_c[N_1(N_2 - c) + (N_1 - c)N_2]$, compared with the $2N_1N_2\,\tau_c$ normally used. The latter expression is clearly incorrect when $N_1 = N_2 = c$ (i.e., $a = b = 0$), for which there can be no random coincidences, and for this case at least our expression is correct; it must, however, be remembered that our expression was proved for $\tau_c < \tau_0/2$, so that it may not apply to the case commonly considered, when $\tau_0 = 0$.

6. *Experiments on Unpulsed Coincidence Counting*

The apparatus used has already been described, consisting of a polonium source facing three proportional counters, whose relative apertures can be varied by using sliding baffles, but since only continuous counting was being studied, the rotating shutter was not used. The counters, fed from a common H.T. supply, are each followed by a cathode follower and amplifier (Fig. 1), and each amplifier has a built-in attenuator which can be used to correct gross differences in the size of the output pulses of the separate counting chains, as well as by switching in maximum (about 50 db.) attenuation, to cut out effectively all signals from any one channel at will. The use of a mixer unit to make the system simulate the behavior of *two* counters used in coincidence has already been described. The sliding baffles enable the relative proportion of coincident and noncoincident events in either channel to be varied at will. The same dead-time was invariably inserted into the two counting channels; the scalers could be connected to measure either the total count in either channel or the number of coincidences.

The setting of the discriminator bias called for some care. The signals from the different counter-amplifier chains were not all of the same size, and while the

*Shown in §6.3 below to be negligible in most cases of practical importance.

bias curves for any one chain were good (cf. §2.2), the latitude available if the "a" and "c" counts in channel I, and the "b" and "c" in channel II, were all to be on the "plateau" region was somewhat restricted. Also, as before, the discriminator bias settings had to be at least 15 v. below the general signal size used, in case a signal should happen to be superimposed on the rather long negative overshoot "tail" of a previous signal—these overshoots seldom exceeded 15 v. in size. A further condition required was that the number of counts from chain "c" recorded in the two channels must be identical; this check was readily made by turning off chains "a" and "b" (using the built-in attenuators) and setting the bias controls carefully within the 25 v. range still allowable. Within this range the plateau slope was found to be about 0.15% per volt, and by careful settings the two counts could be made equal to about 1 count in 4000, and this adjustment would remain good to about 1 in 2000 over the period of a normal "run" (4 to 10 hr.), providing, as was our invariable practice, that the equipment had been left running at least $1\frac{1}{2}$ hours so that it would become steady before the settings were made.

The counting rates of the separate chains were then measured carefully, using a low dead-time setting (11 μsec.). As a check, "a", "b", and "c" were measured separately, using the attenuators to cut out the unwanted signals, as explained above ("c" was measured in both channels as a further check), and then all attenuators were turned up and the combined rates "$a + b$" and "$b + c$" were measured. Each of these measurements involved of the order of 200,000 to 400,000 counts, to give high statistical accuracy; each figure was then corrected for the loss due to the 11 μsec. dead-time, which never exceeded 0.75%, and the "sum" figure compared with the separate figures. This same procedure was repeated at the end of a "run" and in the middle of "runs" exceeding four hours, and if a significant change or failure of the "summation" check was found, the "run" was rejected. We thus know our "expectation" values, as a, b, and c were called, to a statistical accuracy of better than $\pm 0.2\%$.

For the actual measurements, the coincidence unit was attached, and the first check made was that of measuring the coincidence rate without increasing the dead-time, which is very closely equal to the "c" already measured. Then the dead-time was increased in suitable steps and the coincidence rate observed. It was often found profitable to measure in the same run either or both of the alternatives available by cutting off the "a" or the "b" signals using the attenuators. In this way, information was obtained about what happened when only one channel had noncoincident signals, with a minimum of extra time used and without having to measure the "expectations" separately for these alternatives. These measurements were made with a coincidence resolution setting of the minimum available, viz., 3 μsec. The correction for random coincidences with this setting is very small, as will be seen from the measurements described in §6.3 below, and agrees very closely with that predicted by the theory already given. For each value of the dead-time, an average of about 50,000 coincidences were counted, so that the statistical accuracy of the result was high (less than 0.5% error).

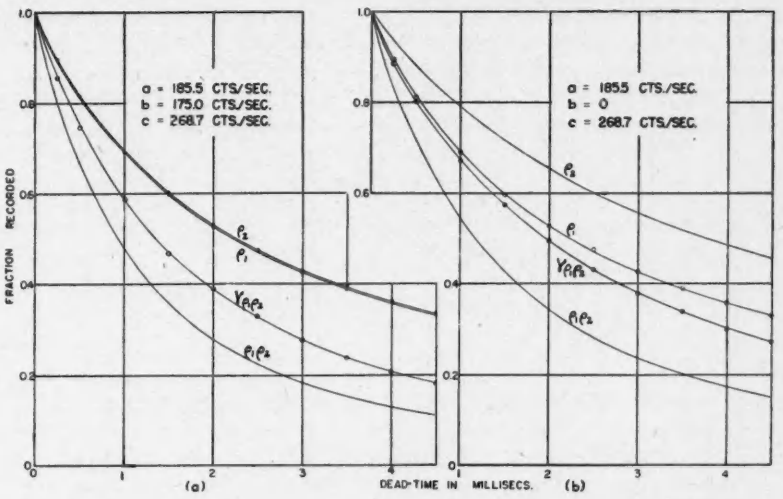

FIG. 9. Two cases showing reduction in observed counts as dead-time is increased. The upper two curves show fractions recorded in separate channels (in (*b*) ρ_2 is computed, not measured). The lowest curve would give the fraction of coincidences recorded if correlation could be neglected. The intermediate curve includes the correction factor γ; good agreement with the observed points is shown.

A typical set of results thus obtained is shown in Fig. 9. This illustrates what happens when a, b, and c are nearly equal. In Fig. 9*a*, the decrease in counting rate in the separate channels as a function of τ_0 was measured during the same run; this was done sufficiently often to satisfy ourselves, using plots similar to those of Fig. 6, that the system was working as intended, and in later runs this check was generally omitted. The upper two curves of Fig. 9*a*, then, represent the variation of ρ_1 and ρ_2, while the lowest curve is the computed product $\rho_1\rho_2$, which would represent the variation of the coincidence rate if interchannel correlation could be neglected. The experimental curve (marked "$\gamma\rho_1\rho_2$") clearly differs considerably from the one computed in this manner, and it is seen that even for small loss-rates (10 to 15%) the difference is quite appreciable. Fig. 9*b* shows for comparison a set of results obtained with chain "*b*" attenuated out—in this case ρ_2 was computed and not directly observed.

For each set of results as described, the ratios a/c and b/c are fixed by the baffles and cannot be changed (except to substitute zeros). About twenty runs have been made with different combinations of these ratios, for each of which we have results comparable to Fig. 9. Each run was reduced to a plot of γ against $c\tau_0$, and typical plots of this type are shown in Fig. 10. This method of plotting the results is quite sensitive to experimental errors, in that the main reduction factors $\rho_1\rho_2$ have been divided out, and only the smaller correlation factor plotted—in particular, any error in the calibration of τ_0 used would displace the curve appreciably, since the ρ's used in the reduction to γ would then be in

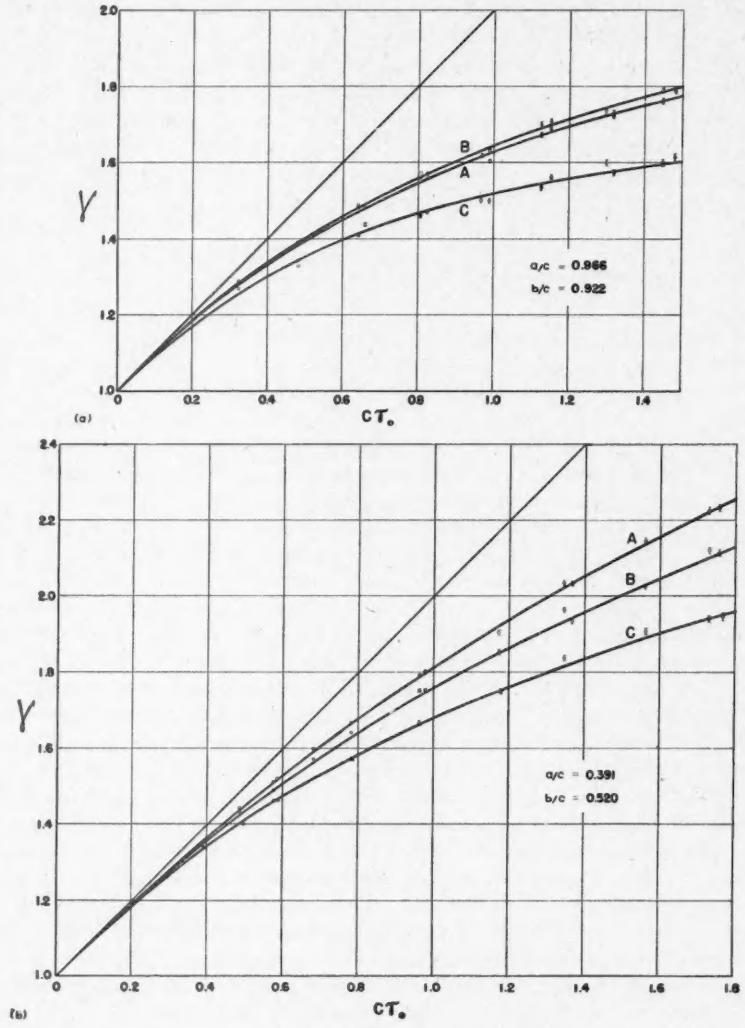

FIG. 10. (*a*), (*b*) Determination of correlation correction factor γ.

error, and the curves would be displaced even more in ordinate than in abscissa. Note also that by plotting $\gamma - 1$ instead of γ, we further emphasize the percentage error of any point (see §6.2 below).

6.1. *Results and Discussion*

All the γ vs. $c\tau_0$ curves which we obtain are of the same form and can be transformed into one another by suitable expansion or contraction of both

ordinate and abscissa scales (the two by the same factor). This was first noticed by accident when two early curves were being compared, but turns out to be general. All the curves have, as we might expect, a tangent of unit slope at the origin ($\gamma = 1, \tau_0 = 0$), through which, of course, they all pass by definition. A single parameter fit was therefore attempted, and it was found that the simplest exponential form having unit slope at the origin, viz.,

$$\gamma - 1 = K\,(1 - e^{-c\tau_0/K}),$$

fitted all the curves within experimental error. Here $1 + K$ is the asymptote of γ, but theory (§5.1 above) indicates that an interpretation in terms of β, using $K = c/\beta$, so that

$$\gamma - 1 = (1 - e^{-\beta\tau_0})c/\beta,$$

is more likely to be fruitful.

Accordingly, relations between the β determined experimentally from the γ vs. $c\tau_0$ plots and the parameters a/c and b/c were sought. In the cases where one of these parameters was zero, the relation was easy to find; the best fit was obtained by using $\beta = 1.08$ times whichever parameter was not zero. The possible significance of the 1.08 factor will be discussed below. It should be remarked here that β is a very sensitive parameter, small changes in the values found for γ producing much greater changes in the computed value of β (see §6.2 below). This does not make an exact empirical determination of the law connecting β with a, b, and c easy. Conversely, an inexact law for β will have very little effect in calculating an error in a practical case unless results of an unusually high accuracy are required. We should also note that the absolute counting-rates are only significant in relation to a given dead-time, and if we double all counting-rates and simultaneously halve the dead-time, the counting losses will be unchanged. It follows that we must be able to express β/c as a function of a/c and b/c only, without using a, b, or c separately.

In analyzing the results obtained, the cases where a/c and b/c were approximately equal were next considered, and it was found that the ratio of β/c to the mean parameter $(a + b)/2c$ varied from about 1.6 for β/c large up to about 2 for β/c fairly small. The figure of 2 suggests that $\beta/c \approx a/c + b/c$ when all three quantities concerned are small, while for a and b large compared with c we have approximately

$$\beta/c = 1.08\sqrt{(a/c)^2 + (b/c)^2}.$$

The theoretical discussion given above does not help us very much at this stage, but for the case where a/c and b/c are both fairly small, we can pursue matters a little further theoretically. When a and b are zero, the counts form a succession of coincidences, both channels performing identically so that either both counts are recorded or both are suppressed. An occasional noncoincident count will disturb this sequence, but unless the rate of counting (measured by $c\tau_0$) is quite high, the disturbance will soon cease by the occurrence in both channels of an unsuppressed condition, following which the next coincidence will record and things proceed as before (cf. Fig. 11). If therefore a second noncoincident count occurs (and is not suppressed), it will again upset the system

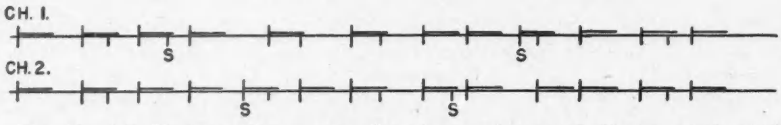

FIG. 11. This illustrates the sequence when there are few noncoincident counts (marked *S*). Vertical lines through axis, recorded counts; below axis only, suppressed counts; horizontal lines above axis, dead-times.

for a short time, during which some coincidences may be lost, but it will be immaterial whether this next noncoincident count is in channel I or channel II. The loss of coincidences will therefore depend only on the total number of noncoincident counts, and not on how they are distributed between the channels. Since $\beta \approx b^*$ if $a = 0$, we see that $\beta \approx a + b^*$ should express conditions correctly if a/c and b/c are both small. However, when the noncoincident counts cease to be occasional, we shall obtain a law of diminishing returns, for the disturbance due to a noncoincident count in one channel may overlap that due to a count in the other channel; in the limiting case for which a/c and b/c exceed unity, it is not an unreasonable guess to try writing $\beta \approx \sqrt{a^2 + b^{2*}}$ by analogy simply with the way two random errors add when they occur together.

With these ideas in mind, Fig. 12 was constructed. Here the observed β/c is plotted against a number of functions of a/c and b/c, such that when either

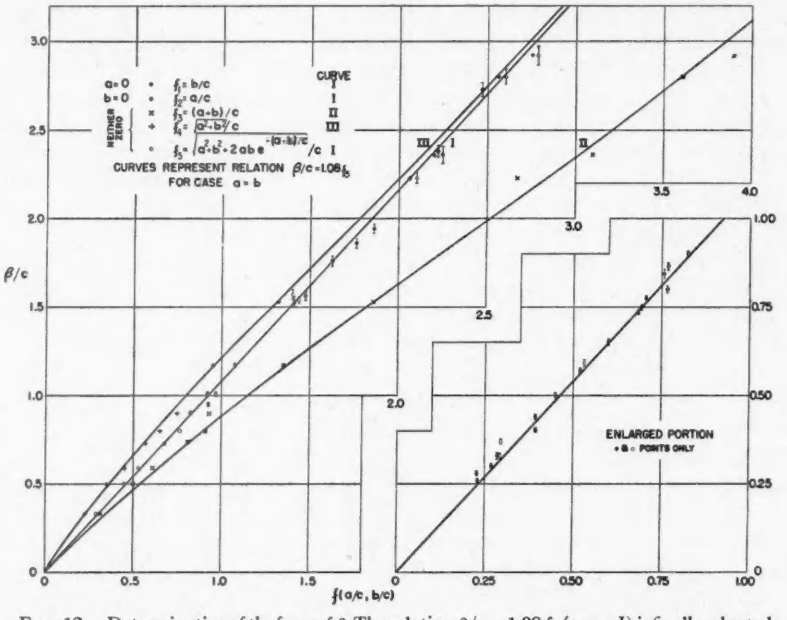

FIG. 12. Determination of the form of β. The relation $\beta/c = 1.08 f_5$ (curve I) is finally adopted. Curves II and III then apply only if $a = b$; for $a \neq b$, points nearer curve I will be expected (e.g. points shown for $\beta/c = 0.90$, 2.225). Curves II and III are not shown in the enlarged portion.

**The 1.08 factor (see below) is neglected in the present discussion.*

parameter is zero (so-called single parameter points) the function equals the other parameter. Hence for the single parameter case, we obtain the black circles for all functional forms; these lie quite well on the line of slope 1.08, as already explained. For the double-parameter points, two functions were first used, the left-hand point in each case being obtained with $f(a/c, b/c) = \sqrt{a^2 + b^2}/c$, and the right-hand point with $f = (a + b)/c$. The one set of points are asymptotic to the 1.08-slope line at high values, and the other at low values. Several other functions were tried to give a fit, and the best (as well as one whose form seems reasonable for this type of problem) is:

$$f\left(\frac{a}{c}, \frac{b}{c}\right) = \frac{\sqrt{a^2 + b^2 + 2ab.e^{-(a+b)/c}}}{c}.$$

Using this functional form, the open-circle points are obtained, which we see lie well on the 1.08-slope line along with the single-parameter points. Several points are included for which a/b is appreciably different from unity (say about 3 or $\frac{1}{3}$) and these are seen to fit as well as the points with a and b about equal, which were the ones considered above in discussing the form of the expression for β. The $e^{-(a+b)/c}$ term was chosen from among several alternatives as best representing the required transition from the sum law to the root-sum-of-squares law considering all the double-parameter points. Considering that β is such a sensitive parameter and that the errors shown are statistical estimates and that some additional systematic error is known to be present, the fit obtained must be regarded as very good.

It only remains to consider the 1.08 coefficient, which Fig. 12 shows to be required for both single-parameter and double-parameter points. This we believe to be a representation of the multiple contingencies which we neglected in §§5 and 5.1 in considering Fig. 8, and which were responsible for the shape shown as dotted line R in that figure, effectively reducing the depth of the "well" or increasing b/c. A closer study indicates that a slight variation of the 1.08 figure, to 1.10 for $0 < \beta/c < 1$ and to 1.06 for $2 < \beta/c < 3$, gives a slightly better fit, but we do not consider the change either established or significant. In any application of these formulae to actual cases, the extreme sensitivity of β, i.e., the insensitivity of the results to small changes of β, will render the variation involved negligible.

We thus obtain our final result:

[7] $$\gamma = 1 + [1 - e^{-\beta\tau_0}]c/\beta, \text{ where } \beta = 1.08\sqrt{a^2 + b^2 + 2ab.e^{-(a+b)/c}}.$$

6.2. *Statistical Errors*

We have already pointed out that the average single measurement is made with about 50,000 counts, which, using the usual $1/\sqrt{N}$ law, would indicate a statistical accuracy of $\pm 0.45\%$ in determining each value of γ. In drawing a γ vs. $c\tau_0$ curve to obtain a value of β, several points, usually four or five, are taken into account, so that the curve may be considered located to an accuracy of about $\pm 0.25\%$ in the significant region (other points, for lower values of $c\tau_0$, do not contribute significantly to the determination of β). As already mentioned, a systematic error may arise from the calibration of τ_0, since the value

used affects the ρ's used in computing γ. In §2.3 reasons were given for believing these calibrations good to about 0.5% originally; from the internal consistency of runs taken with the same parameters (a/c and b/c) on different days, and from the occasional single-channel checks (of the type shown in Fig. 6), we believe that the calibration remains constant to better than 0.5% on most occasions, although one or two small discrepancies have been found which could be due to a calibration change of about 0.5% over a long period. There is no sign of a continuing undirectional change, and if the discrepancies are in fact due to calibration errors they may be the result of temperature changes or other unknown erratic causes.

The percentage change in γ resulting from a calibration error of 0.5% in τ_0 depends on what part of the curves we are using, but is usually 0.5 to 0.7% in the regions actually employed for finding β. The value of $c\tau_0$ used as abscissa is also affected, tending to diminish the effect of the error in γ. Since we believe 0.5% to be the extreme calibration error, we feel justified in attributing a 0.25% r.m.s. error from calibration sources, to be added to the statistical 0.25% giving an effective total of 0.35% error in the γ used to obtain β. The error due to the statistical uncertainty of a, b, and c (about 0.12%) is nearly negligible by comparison. This means that in a typical case $\gamma - 1$ is known to about $\pm$ 1%. The vertical lines shown on the graphs (Figs. 10 and 12) are the r.m.s. errors from statistical sources only; where none are shown, as on Fig. 9, the errors are smaller than the points drawn. The error in β resulting from a given percentage error in γ varies with the parameters used, being largest when β/c is small or a small value of $c\tau_0$ is used for the determination; for a typical case of $\beta/c = 0.5$ and $c\tau_0 = 1$, we find the percentage error in β to be about ten times the percentage error in γ(we have already remarked that β is a sensitive parameter). We see, thus, that in spite of the relatively high accuracy of our original measurements, an error of about 3.5% may be expected in β for this case. Considering this, the fit obtained in Fig. 12 must be regarded as quite satisfactory.

We have assumed in the above that the $1/\sqrt{N}$ law holds for the fractional statistical error of a measurement involving N counts. While the consistency of our results appears to agree fairly well with this assumption, it should be noted that this result has only been proved for randomly-distributed counts. As mentioned in §3.2, in single-channel counting, the dead-time effect actually reduces the fractional statistical variance of the counting rates observed; in the limit, when the number of counts per dead-time is large, the counts become regular, spaced at intervals slightly greater than τ_0, giving a fractional variance much less than $1/\sqrt{N}$. We believe this result does not hold for coincidence counting, owing to the chance factor as to whether the same count is recorded in the second channel as in the first. Indeed, at high counting rates the conditions may tend to resemble those of Fig. 11; starting from any recorded coincidence, we see that both channels "reopen" together, and the next coincidence recorded in channel I has a high chance of recording in channel II also. This condition continues until a noncoincident count suppresses one member of a coincident pair. Thereafter the dead-time in the channels may remain "out of

phase" for a period, especially if the counting rate is high. A coincident event recorded in, say, channel I only, may suppress in that channel the next coincident event recorded in channel II, while this event in turn may suppress the channel II member of the next coincidence which is recorded in channel I. Thus first a bunch of coincidences may record, and then a bunch be missed. The bunches are particularly long if c is large while a/c and b/c are fairly small (but not zero, when the single channel result would be obtained, and the variance would diminish). However, in most conditions of practical importance the departures from the $1/\sqrt{N}$ law do not appear large. We have investigated the point experimentally for a few cases, and find that on some occasions the variance may be slightly less than the $1/\sqrt{N}$ law would predict, and in others somewhat greater but that in most practical cases the use of the $1/\sqrt{N}$ law would be a fair approximation.

6.3. *Effect of Coincidence Resolution Time*

All the above results were taken with a very short coincidence resolution time, and corrections made to $\tau_c = 0$. This presented no difficulty, since equation [6], without the higher order terms, was found to be followed very closely in all cases. Several runs were made to demonstrate this, with different a/c and b/c parameters and various values of τ_c (always keeping $\tau_c < \frac{1}{2}\tau_0$ as required by the theory) and the resulting counting-rates, plotted against τ_c, are found to lie quite close to straight lines of the expected slope. Examples, given in Fig. 13, as well as our other curves, show that the curvature of the lines obtained is quite small. However, we notice a systematic tendency for the points to lie above the theoretical straight lines, especially when the first-order coefficient $(ac + bc + 2ab)/c$ is rather small, and although this effect does not appear definitely as a curvature, it may be due to the neglected terms. The discrepancy is not large, seldom exceeding 1% of the total count if $\tau_c < 0.2\,\tau_0$, a condition which is usually fairly easily obtained in practical cases. It is in any case desirable in accurate work to make τ_c as small as possible, since this minimizes all the corrections for additional coincidences, and the slight uncertainty in the correction term merely adds strength to the argument. We have therefore felt it unnecessary to analyze the discrepancy further; the results we have obtained agree with our theory within the degree of accuracy we may expect from the latter, and are likely to be quite accurate enough in almost every practical case.

6.4. *Conclusion*

Although we have been unable to obtain a complete theory to support our investigation, our experimental results have indicated quite clearly what corrections are necessary for the dead-time losses and random coincidences for a two-channel coincidence system with appreciable correlation between the channels, and the accuracy of our work is believed to be more than sufficient for obtaining reliable correction factors for any ordinary experimental investigation using the techniques envisaged in this work. The formulae finally adopted are given in Appendix III below.

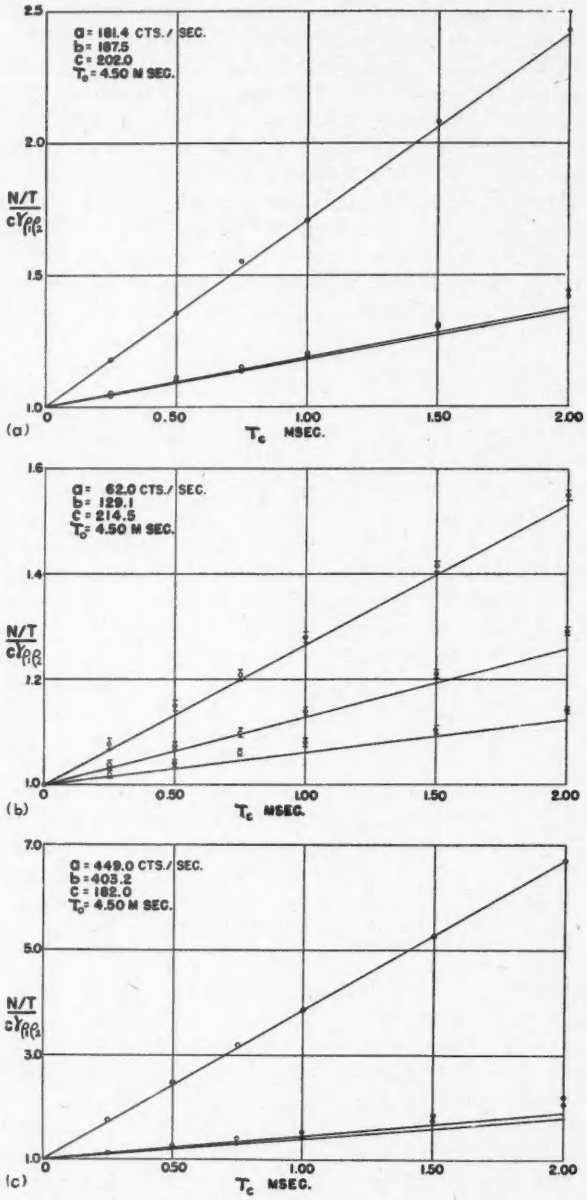

FIG. 13. Three examples showing increase in total counting rate due to chance coincidences. The lines are calculated from equation [6] without higher order terms; points are experimental.

PART III
PULSED COINCIDENCE COUNTING

7. *Outline of Method*

We now consider the problem of coincidence counting (two counters being used) under "pulsed" conditions, such as apply when a synchrocyclotron or other intermittent accelerator is used, to produce reactions of which the instantaneous products are to be counted. The equipment used has already been fully described. The experimental procedure was a combination of the procedures used previously, the "expectations" or total counting rate for each type of count (a, b, and c) were determined as described in §6, with the shutter open (and stationary), and similar measurements were made with the shutter in a closed position (a_0, b_0, and c_0, in this case, c_0 being the most important). These "expectation" measurements were made with a small dead-time; for the observations, a suitably large dead-time τ_0, the same in each channel, was chosen and the number of coincidences was observed for a series of different speeds of rotation of the shutter-wheel; a second scaling unit was used simultaneously to determine the number of revolutions of the wheel. The measurements thus obtained were corrected for "background" count and then expressed in terms of the fraction of coincidences recorded during the pulse-period (ϕ), which is the quantity whose determination is the object of the present investigation. In addition, the number of additional ("random") coincidences, which depends on τ_c, the coincidence resolving time, is studied in the present work.

8. *Theoretical Considerations*

It is profitable to consider at the outset what theoretical predictions can be made for this case. Firstly, if the pulses are very long, so that $\mathcal{T}$ (the pulse duration) is large compared with τ_0, the transition effects at the beginning of the pulse are negligible, and the results for continuous counting apply; this gives $\phi = \gamma\rho_1\rho_2$. On the other hand we may readily compute exact expressions for ϕ if $\mathcal{T}/\tau_0 < 1$, and this procedure has been extended to cover the range $1 < \mathcal{T}/\tau_0 < 2$. It does not appear practicable to extend the calculations further, the gap being filled by experimental investigation.

8.1. *Calculations for* $\tau_c \simeq 0$

Initially we neglect all "random" coincidences, i.e., we take τ_c to be infinitesimal; this point will be dealt with later. When $\mathcal{T}/\tau_0 < 1$, the pulse lasts less than one dead-time, and only one count can be recorded in either channel; only if the first count within the pulse is a coincident count *in each channel* can a coincidence be recorded. Considering channel I first, and using the notation explained above, we note that both the $a + c$ counts together, and the a and c counts separately, form random sets. The probability of the first count occurring within dt at time t from the beginning of the pulse (assumed rectangular) is then given by $(a + c)$. $e^{-(a+c)t}\,dt$, and the probability that it is a coincidence is $c/(a + c)$. If then the first count is a coincidence and occurs in dt at t (probability $c.e^{-(a+c)t}\,dt$), it will record, and we may ask whether the same count records in channel II, to give a recorded coincidence. We now know, however, that no coincident count has occurred between $t = 0$ and time t; accordingly, in channel II, the

only count that can occur in this interval is a noncoincident (called a "*b*") count. The probability that no such count has occurred is e^{-bt}, and if this is the case the coincidence will record in both channels. The probability of a recorded coincidence in dt at t is therefore obtained by multiplying these probabilities, which are independent (the b counts in channel II being quite independent of anything in channel I), giving $c.e^{-(a+b+c)t}\,dt$. The expected number of recorded coincidences during the whole pulse is therefore, for $\mathscr{T} \leqslant \tau_0$

$$c\int_0^{\mathscr{T}} e^{-(a+b+c)t}dt = \frac{c}{a+b+c}(1 - e^{-(a+b+c)\mathscr{T}}).$$

Dividing by $c\mathscr{T}$, the expected average number of coincidences occurring during the pulse, we obtain as the fraction recording, the function

[8] $$\phi = f(y) = (1 - e^{-y})/y, \text{ where } y = (a + b + c)\mathscr{T}.$$

Note that $f(y)$ is the same function as was obtained (5) for single-channel counting for $\mathscr{T} \leqslant \tau_0$, y being then $\mathscr{T}$ multiplied by the single-channel counting rate ν($= r_0$ of the present paper), but that the $a + b + c$ appearing in [8] above is not a counting rate which actually occurs anywhere in our system. Thus the coincidence problem can be fitted exactly to a single-channel curve (Westcott's (5) Fig. 4) over the range $\mathscr{T}/\tau_0 \leqslant 1$, but unfortunately the fit does not extend beyond this range; the following table shows the variation of asymptotic values of ϕ (as $\mathscr{T} \to \infty$) for curves which all have the same form over the initial range $\mathscr{T} \leqslant \tau_0$.

$a\tau_0$	$b\tau_0$	$c\tau_0$	ϕ for $\mathscr{T} = \tau_0$	ϕ for $\mathscr{T} \to \infty$
0.3	0.3	0.3	65.8%	48.4%
0.4	0.1	0.4	65.8%	49.2%
0*	0*	0.9	65.8%	52.6%

**This is effectively the single-channel case.*

We see, then, that the fraction of coincidences recorded decreases from 100% (for very short pulses) to a final steady value of $\gamma\rho_1\rho_2$ as the pulse length ($\mathscr{T}$) increases, following a curve similar to that obtaining for single-channel counting, but significantly different therefrom. We have therefore extended the theory to the case $1 < \mathscr{T}/\tau_0 < 2$, (see Appendix I); the results for some typical cases are given in Fig. 14, together with experimental results to be considered later. We note that the theoretical curve for coincidence measurements still differs appreciably at $\mathscr{T} = 2\tau_0$ from the corresponding theoretical curve for single-channel counting with the same asymptotic value, but the difference is smaller than that existing for $\mathscr{T} = \tau_0$.

While this theory extends only as far as $\mathscr{T} = 2\tau_0$, and the labor involved in extending it to $3\tau_0$ appears to be prohibitive, a very close approximation for longer pulses can be obtained following the methods used in considering the single-channel problem (5). Remembering that the function ϕ, the fraction recorded, is in fact an average over a varying instantaneous probability function (cf. Westcott's (5) Fig. 3), we may take the exact probability function for the

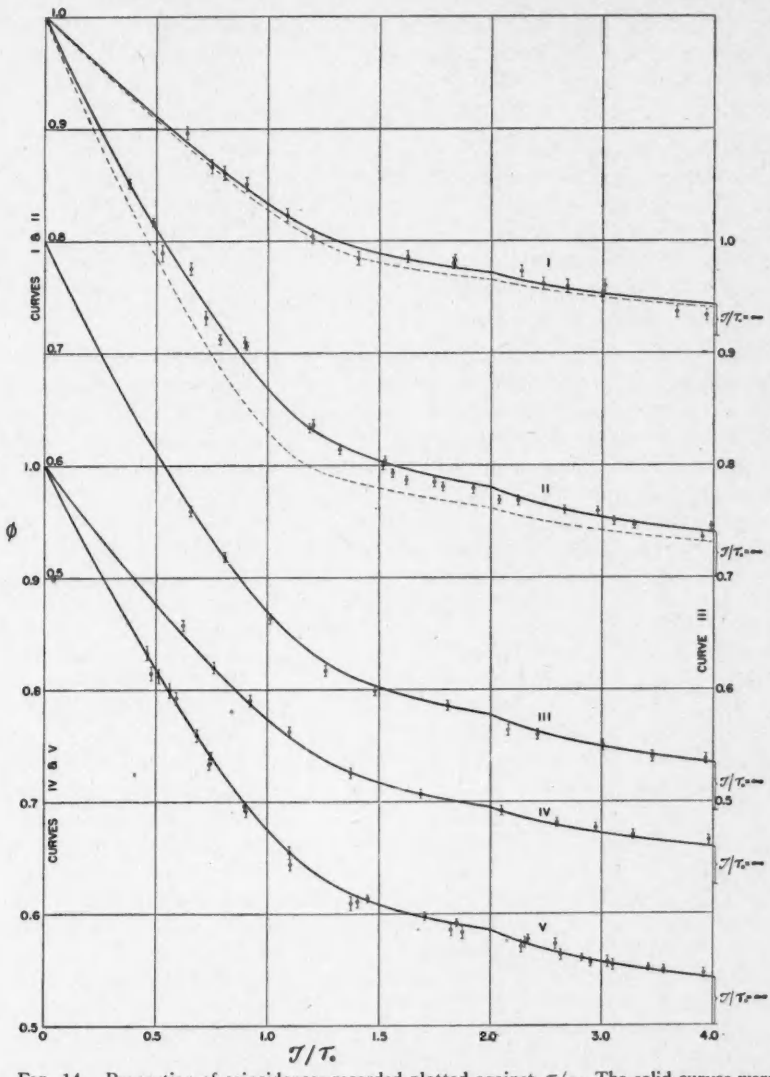

FIG. 14. Proportion of coincidences recorded plotted against $\mathcal{J}/\tau_0$. The solid curves were calculated using equation [8] for $\mathcal{J} \leqslant \tau_0$, equation [14] for $1 < \mathcal{J}/\tau_0 \leqslant 2$, and equation [9] for $\mathcal{J}/\tau_0 > 2$. The lower ends of the brackets on the right of the curves show the asymptotic values of ϕ for $\mathcal{J} \to \infty$. The dotted (comparison) curves are for single-channel counting with the same asymptotic value. Errors shown on experimental points are statistical only. Note the change in abscissa scale at $\mathcal{J}/\tau_0 = 2$.

Curves	I	II	III	IV	V
$a\tau_0$	0.056_9	0.133_1	0.334_5	0.172_3	0.261_7
$b\tau_0$	0.119_3	0.279_5	0.290_5	0.178_6	0.281_3
$c\tau_0$	0.197_0	0.458_3	0.237_4	0.190_5	0.301_3

first $2\tau_0$ of the pulse, and substitute the steady state counting probability $\gamma\rho_1\rho_2$ for the remaining period. The average over the whole pulse then gives a value of ϕ of

$$[9] \qquad \gamma\rho_1\rho_2 + 2\,[\phi_2 - \gamma\rho_1\rho_2]\tau_0/\mathscr{T}\ (\mathscr{T} > 2\tau_0)$$

where ϕ_2 is the value of ϕ for $\mathscr{T} = 2\tau_0$. This corresponds on Fig. 14 to drawing a rectangular hyperbola having the known asymptotic value and starting from the point $(\phi_2, 2\tau_0)$, as has in fact been done in drawing this figure. The justifications for this procedure are that the same method gave a satisfactory approximation for the single-channel case and that the measurements described below give results agreeing with those calculated in this way.

8.2. *Calculations for Finite* τ_c

For brevity, we discuss this problem also in terms of two limiting cases, viz., the infinite pulse-length (for which the corrections are given by equation [6]) and a pulse-length less than one dead-time. The latter case, while perhaps of limited practical use, serves to indicate the bounds of applicability of the continuous counting approximation and to guide the experimental investigation, which includes cases of $\mathscr{T} > \tau_0$.

For the case $\mathscr{T} \leqslant \tau_0$, we invoke the condition $2\tau_c < \tau_0$ (cf. §5.2), and initially assume $\tau_c < \mathscr{T}$. Then in addition to the true coincidences already enumerated, recorded coincidences will arise from either "restored" (cf. §4) or "random" coincidences. We note that coincidences between different "c" counts cannot occur since only the first count in the pulse in each channel can record; similarly, coincidences cannot be "restored" by a recorded count following the end of the dead-time due to the suppressing count.

"Restored" counts can therefore only arise from a noncoincident count in one channel which precedes the coincident count recorded in the other channel by less than τ_c, and "random" coincidences can only occur when neither count is a coincident one. To evaluate the former we write down the probability $c\,e^{-(a+c)t_1}\,dt_1$ of a "c" count recording in channel I in dt_1 at time t_1 and multiply by the (quite independent) probability $b\,e^{-bt_2}\,dt_2$ of a "b" count recording in channel II in dt_2 at t_2 (we know, of course, that no "c" occurs here, since $t_2 < t_1$). To integrate correctly we must note that for $t_1 < \tau_c$, the coincidence gate is t_1 rather than τ_c; the contribution to the recorded coincidences is therefore:

$$\int_{\tau_c}^{\mathscr{T}} bce^{-(a+c)t_1} \int_{t_1-\tau_c}^{t_1} e^{-bt_2} dt_2\, dt_1 + \int_0^{\tau_c} bce^{-(a+c)t_1} \int_0^{t_1} e^{-bt_2} dt_2\, dt_1$$

$$[10] = \frac{c}{a+c}\,[1 - e^{-(a+c)\tau_c}] - \frac{c}{a+b+c}\,[e^{-(a+b+c)\mathscr{T}}(e^{b\tau_c} - 1) + 1 - e^{-(a+c)\tau_c}].$$

To this we must add the coincidences restored in channel I, obtained by interchanging a and b in the above expression; the random coincidences are obtained similarly but starting with the probability $a.e^{-(a+c)t_1}\,dt_1$ of an "a" count occurring at t_1—the result is therefore the same expression [10] but with a and c interchanged. We further add the latter expression with a and b subsequently interchanged, to allow for the case when the "a" count precedes the "b" instead of vice versa. The final result is

$$[11] \qquad 2 - e^{-(a+c)\tau_c} - e^{-(b+c)\tau_c} - \frac{a+b+2c}{a+b+c}(1 - e^{-(a+b+c)\mathcal{T}}) + \frac{(a+c)\,e^{b\tau_c} + (b+c)\,e^{a\tau_c}}{a+b+c}(e^{-(a+b+c)\tau_c} - e^{-(a+b+c)\mathcal{T}}).$$

It is convenient to expand this expression as a power series in τ_c; doing this and dividing by the expected number of coincidences per pulse ($c\mathcal{T}$) to give a fraction recorded and adding $\phi_0 = (1 - e^{-(a+b+c)\mathcal{T}})/(a+b+c)\mathcal{T}$, the fraction recorded when $\tau_c = 0$, we obtain

$$[12] \qquad \phi = \phi_0\left\{1 + \frac{(ac + bc + 2ab)\tau_c}{c} + O(\tau_c^2)\right\}.$$

We see that the fractional increase of the number of recorded coincidences due to the first order term in τ_c is the same as for continuous counting (equation [6]). However, the higher order terms are not always negligible, a point which will be further discussed below.

We have so far excluded the case of $\tau_c \geqslant \mathcal{T}$; in this case a coincidence is recorded whenever a recorded count occurs within the same pulse in both channels. For this case we may write $\mathcal{T}$ for τ_c throughout equation [11] above, irrespective of the actual value of τ_c, the last term then dropping out. This case is rather unlikely in practice, and no further work has been done on it.

9. *Experimental Results—Pulsed Coincidence Counting*

Since the theory for this case only needs supplementing by experiment for the transitional regions between known limiting values, only a few representative cases have been investigated experimentally. The cases used are $a/c \approx b/c \approx 1$, $a/c \approx 0.3$, $b/c \approx 0.6$, and $a/c \approx 1.4$, $b/c \approx 1.2$, with several different values of the dead-time. For ease of comparison with the single-channel curves, the dead-time was always chosen so that the fraction counted for the asymptotic case of continuous counting was the same as that for one of the existing single-channel curves, viz., 1/1.4, 1/1.6, or 1/2, corresponding to the original curves for $z = 0.4$, 0.6, or 1.0 respectively; this fraction is, of course, the quantity $\gamma\rho_1\rho_2$. This asymptotic value was confirmed by continuous counting, for each case, and was always found to agree with the computed value within statistical error (about $\pm$ 0.4%). The "expectation" and "background" counting rates were carefully measured at the beginning and end of each running period, using the "summation" check described in §6; any run for which the expectation values on repetition showed deviations considerably greater than statistically expected were discarded. The background coincidence rate c_0 was measured about every 15 min. during runs (with the shutter-wheel stopped in the "closed" position) and the total count available for determining this quantity was usually about 5000, giving a statistical variance of $\pm$ 1.4%. Since the "background" only contributes about 5% of the total counts this accuracy is quite adequate for our purpose. The frequent repetition of the "background" measurement served to show up any drift in its value. It was found that the bias curve was much steeper for the background counts than for the counts obtained with

the shutter open, so that any small change in over-all gain, H.T. voltage, or discriminator level could change the background rate appreciably. On a few occasions this was found to occur; the expectation values a, b, and c usually changed also, by smaller but still detectable amounts, since they were measured much more accurately (statistical error $\pm 0.3\%$). The runs in which this happened were completely discarded. Some spurious counts had been found to originate from sparking at the brushes of the motor and from electrostatic fields building up on the rotating sector. Each run was therefore monitored by observation of the "c" amplifier output on the oscilloscope, and occasionally the counter H.T. was switched off and the motor left running to check that no spurious counts were arising from this source.

For most of the measurements a shutter was used having four open sectors, each 18° wide with 72° closed sectors between them. This gave faster counting than the original single 30° open sector, and the relative importance of the "background" count occurring during the closed periods was reduced, since the closed/open ratio was 4: 1 instead of 11: 1 as in the earlier measurements. An alternative shutter-wheel was also available, having two 45° open sectors; this was used when longer pulse-lengths were required.

The pulse envelopes defined by the various rotating sectors were carefully measured (cf. Fig. 3) so that the pulse widths are known to an accuracy of $\pm 0.3\%$. In the case of the 45°-sector wheel, the two apertures differed from one another by 3.4%, while with the 18°-sector wheel, one aperture was nearly 4% larger than the other three; in each case the mean aperture of the sectors was used in computation, the error caused by this averaging process being negligible.

A "run" consisted in taking measurements of the counting rate with the wheel spinning at a number of known rates, corresponding to different values of $\mathscr{T}/\tau_0$. Usually about 20,000 counts were taken for each point, giving a statistical accuracy $(1/\sqrt{N})$ of $\pm 0.7\%$. In every case τ_c was made very small ($\simeq 3\mu$sec.) so that the correction for random coincidences was quite negligible in comparison with statistical error. The correction for "background" was made using the relation (cf. equation [1] for the single channel case)

$$N/T = \phi fc + (1 - f)\, c_0 - \delta. \qquad [13]$$

The main correction is the subtraction of the counts expected during the periods when the shutter is closed; the small additional correction δ represents the suppression of counts in the early part of the pulse due to "background" counts occurring just before the pulse starts, and a similar effect at the end of the pulse. The evaluation of δ is given in Appendix II. In most practical cases this term is quite negligible, but in our work, with the pulses fairly close to one another, it is just large enough to be significant.

The values of ϕ obtained after applying these corrections have been plotted as functions of the pulse-length in units of the dead-time $(\mathscr{T}/\tau_0)$. Theoretical curves are shown on Fig. 14, together with the relevant experimental results. For curves I and II of that figure, comparison curves are also given (dotted in the figure) which show the results for single-channel counting with the same

asymptotic value. The latter are seen to be significantly lower than the coincidence curves in the regions investigated, and similar differences would have appeared if dotted curves had been plotted for comparison with the other curves (III to V). Most of the curves were repeated on several occasions and were found in every case to be reproducible within the experimental error. The agreement between experiment and theory is quite good considering the rather large experimental errors discussed below. Curve IV represents the average of two runs on the same day. This is considered to be an exceptionally reliable result as the constancy of the expectation values and the background was excellent over the running period of 10 hr.; the agreement with the theoretical curves is particularly good in this case. We may conclude also that the agreement between the solid curves and the experimental points remains good when $\mathcal{T} > 2\tau_0$, so that the approximations used in obtaining equation [9] appear to be fully justified and to give predictions quite accurate enough for making corrections in actual counting experiments of the type envisaged in this work.

Measurements of the effect of increasing τ_c were carried out under the same conditions and with the same precautions; all readings were taken for $\gamma\rho_1\rho_2 \simeq 0.5$ and the counting rates were recorded for discrete values of $\mathcal{T}/\tau_0$, viz., 0.48, 0.77, 1.00, 1.56, and 3.05. For the cases in which $\mathcal{T} < \tau_0$, we have drawn solid curves in Fig. 15 using equation [11], §8.2, and the experimental points fully confirm the results. For the longer pulse-lengths the only theoretical comparison available is the first-order correction (equation [6]) corresponding to the straight

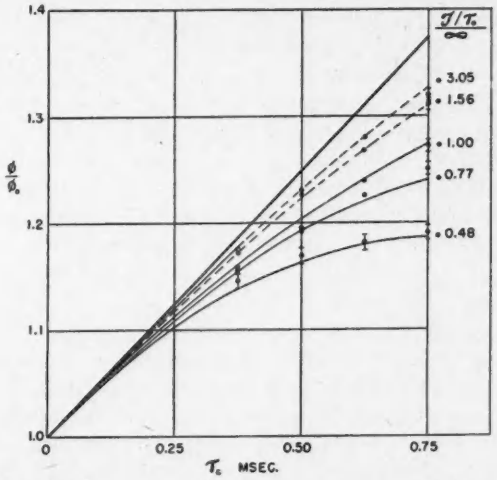

FIG. 15. Fractional increase in recorded coincidences plotted against τ_c. The solid curves were calculated using equation [11]. Broken curves ($\mathcal{T}/\tau_0 > 1$) are fitted to the experimental points. The asymptote was calculated using equation [12] (last term omitted). For the sake of clarity, the experimental points for $\tau_c \leqslant 0.25$ msec. (which confirm the curves) and most of the statistical errors have been omitted.

a = 165.8 counts per sec. c = 206.3 counts per sec.
b = 127.6 counts per sec. τ_0 = 1.60 msec.

line shown (tangent to all curves at the origin). The dotted curves for these cases are purely empirical; we note that as $\mathscr{T}/\tau_0$ increases the importance of the higher-order terms diminishes, as we would expect, since for continuous counting (§5.2) they were generally found to be negligible.

However, as mentioned in §8.2, the higher order terms are by no means negligible for $\mathscr{T}/\tau_0 = 1$; for example, for $\mathscr{T} = \tau_0 = 1.6$ msec., $\tau_c = 0.75$ msec., and the counting rates shown for Fig. 15, the higher order terms represent a decrease of counting rate of about 7–8% of the total counting rate, or 10% of the rate for $\tau_c \approx 0$ (a figure obtained both from computations and from measurement). But for $\mathscr{T} \geqslant \tau_0$, with $\tau_c < 0.1\ \tau_0$ and $(a + b + c)\tau_0 < 0.8$, for example, the higher order terms are quite small; these two numerical limits are interdependent, so that if $(a + b + c)\tau_0$ is reduced, τ_c may be somewhat increased before the higher order terms become appreciable, and as $\mathscr{T}$ increases above τ_0, the limits become progressively wider. There is therefore a wide range of conditions, including most cases of practical importance, where only the first order correction term need be employed.

9.1. *Discussion of Errors*

The statistical deviations as shown on the figures have been calculated assuming the $1/\sqrt{N}$ law which was shown in §6.2 to apply fairly closely for coincidence measurements of this type. In addition, we have frequently obtained fluctuations appreciably larger than those predicted statistically, probably due to causes already mentioned. These must contribute to the uncertainty of the experimental points. In a typical case a variation of $\pm$ 10% in the background rate would lead to a corresponding uncertainty of $\pm$ 0.3% in ϕ. Although these variations may not be random it seems justifiable to assign an r.m.s. error of 0.3% due to fluctuations in the background giving a total r.m.s. error of about $\pm$ 0.8%. The theoretical curves corresponding to the various runs will be subject to further error since their calculation depends on the measured "expectation" values and especially on an accurate knowledge of the dead-time. The latter should seldom be in error by more than $\pm$ 0.5% (cf. §§2.3, 6.2). It is possible on this basis to assign an r.m.s. error of the order of $\pm$ 0.2% from this cause. The observed scatter of the points agrees reasonably with these estimated errors.

9.2. *Conclusions—Pulsed Coincidence Counting*

Exact expressions for the expected coincidence counting rate under pulsed conditions have been derived for rectangular pulses of length less than twice the dead-time and an approximate expression has been proposed for the cases $\mathscr{T} > 2\tau_0$. All these theoretical formulae have been confirmed by experiment to an accuracy of better than 1%. Further, we have investigated theoretically and experimentally the corrections to be made for the finite resolution time of the coincidence system. An exact method of calculation has been presented for the case of $\mathscr{T} \leqslant \tau_0$ while the corrections obtained in §5.2 for continuous counting have been shown to be correct for the case of $\mathscr{T} > \tau_0$ within limits which can nearly always be met in practice. It must be remembered, however, that the theoretical results are strictly true only for rectangular pulses which will seldom,

if ever, be what is used. We, therefore, intend to maintain the equipment operative in case measurements on pulses of other specified shapes should be required. In many cases, however, the results obtained by using an equivalent pulse-length (cf. Westcott (5), §5) will be sufficiently accurate. It is also necessary to realize that our expressions are only accurate if the dead-time used is of the nonextending type. Finally, all our formulae express the expected counting rate in terms of the true counting rate while it is the converse we need in practice. For the transcendental correction equations involved, solution by methods of successive approximation is necessary but generally the convergence is fast enough for the work involved in the evaluation not to be prohibitive.

10. ACKNOWLEDGMENTS

The authors would like to express their thanks to Messrs. G. Tweeddale and A. Densmore for their assistance in constructing the equipment and Dr. J. S. Foster for making available to us the facilities of the Radiation Laboratory. This investigation was supported by a grant from the National Research Council of Canada, and one of us (J.S.G.) is indebted to the Province of Quebec for a scholarship covering a part of the period in which the work was carried out.

APPENDIX I

Computations for $\tau_0 < \mathscr{T} < 2\tau_0$

When $\mathscr{T}/\tau_0$ exceeds unity, it is possible to have a second recorded count in one or both channels; formula [8] still expresses the probability that the first count in both channels is a recorded coincidence. To obtain the total rate of recording coincidences, we have to add expressions covering the following contingencies:

(*i*) a second coincidence recorded in both channels, following a first recorded coincidence (the latter being included in the enumeration by means of equation [8] extended to the range $1 \leqslant \mathscr{T}/\tau_0 \leqslant 2$),

(*ii*) following a noncoincident count in channel I, a coincidence is recorded (with either no preceding count in channel II or a coincident count of which the opposite number in channel I was suppressed),

(*iii*) as (*ii*), but with channel I read for channel II, and vice versa,

(*iv*) a coincidence is recorded following noncoincident counts in both channels. An analysis of all possible combinations has shown this to be a complete enumeration; the proviso in brackets in (*ii*) being necessary to prevent multiple enumeration of the case covered by (*iv*). In the cases (*ii*) to (*iv*) one must also be careful to exclude cases where the second count in each channel is a coincident one, but not the same one, each corresponding to a count suppressed in the opposite channel. To simplify the computation of (*iv*) we split it into two parts, considering first the case when the noncoincident count in channel I precedes that in channel II, and then adding in the term for channels interchanged.

Case (*i*).—The probability for this is written as the probability of the first coincidence coming at t_1 multiplied by the probability of the second coming at time $t_2 + \tau_0$ (i.e., after an interval $t_2 - t_1$ following the end of the first dead-

time), all computed in channel I, and multiplied by the probability that no noncoincident ("*b*") count arises in the "open" intervals (which total t_2) in channel II to suppress either count in that channel; this contributes to the expectation of coincidences recorded the integral:

$$\int_0^{t_2} c\, e^{-(a+c)\,t_1} dt_1 \int_0^{\mathscr{T}-\tau_0} c\, e^{-(a+c)(t_2-t_1)} e^{-b\,t_2} dt_2$$

$$= \int_0^{\mathscr{T}-\tau_0} \int_0^{t_2} c^2 dt_1 e^{-(a+b+c)\,t_2} dt_2,$$

which can be evaluated and divided by the expected number of coincidences $c\mathscr{T}$, to give the contribution to the fraction recorded.

Case (*ii*).—Here we postulate an "*a*" count at time t_1 and a coincidence at $t_c + \tau_0$, with $t_c > t_1$, so the expected number of *c* counts recorded in channel I is:

$$\int_0^{t_c} a e^{-(a+c)\,t_1} dt_1 \int_0^{\mathscr{T}-\tau_0} c\, e^{-(a+c)(t_c-t_1)} dt_c = \int_0^{\mathscr{T}-\tau_0} ac\, dt_1\, e^{-(a+c)\,t_c} dt_c$$

which must be multiplied by the contingent probability in channel II. This is *either* that no counts occur in this channel before $t_c + \tau_0$, *or* that a coincident count occurs in the τ_0 following t_1, but no "*b*" count occurs in the remaining "open" interval. In the former case the whole period up to $t_c + \tau_0$ is "open" to "*b*" counts, while a "*c*" count could only occur in the period (duration τ_0) in which it would have been suppressed in channel I, so that the partial probability may be written $e^{-b(t_c+\tau_0)}\, e^{-c\tau_0}$. The latter case requires a coincident count to occur during the period τ_0, but since the coincident count at time $t_c + \tau_0$ is to record, we cannot allow a coincident count to record in channel II later than time t_c. We can, therefore, only have a coincident count occurring in the interval from t_1 to t_c (noting that the former is less than the latter). We must therefore have a coincident count (more than one would do, since only one would record) in the interval of length $t_c - t_1$ (otherwise the case is enumerated elsewhere); the probability for this is $1 - e^{-c(t_c-t_1)}$. We must further have no "*b*" count in the remaining "open" period, which now totals t_c. The total contingent probability for channel II is therefore

$$e^{-b(t_c+\tau_0)}.e^{-c\tau_0} + (1 - e^{-c(t_c-t_1)})\,.\,e^{-b\,t_c}$$

which must be multiplied by the integral given above. Note that the new expression contains t_1, so that the relevant term must be included in the inner integral before it is evaluated. The integral is

$$\int_0^{\mathscr{T}-\tau_0} \int_0^{t_c} ac\, e^{-(a+b+c)\,t_c} [e^{-(b+c)\tau_0} + 1 - e^{-c(t_c-t_1)}]\, dt_1\, dt_c.$$

Case (*iii*).—This is obtained by interchanging *a* and *b* in the above expression.

Case (*iv*).—Here we have exactly the same integral for channel I as in (*ii*) above, but the conditional probability in channel II is different. We now have to write the probability that one "*b*" count occurs in the period up to time t_c, but no other "*b*" in the "open" period before $t_c + \tau_0$, nor any "*c*" count where it would record. We can, in fact, write $b.dt_2$ for the probability of the

"b" count occurring in dt_2 at t_2; we then require that there shall be no other "b" count either in the period from 0 to t_2 or from $t_2 + \tau_0$ to $t_c + \tau_0$, i.e., in a total period of duration t_c—the probability of this is e^{-bt_c}, independent of t_2, with only the obvious proviso $t_2 < t_c$. We must in addition provide that no "c" count occurs where it would be recorded, but in formulating the integral for channel I we have automatically excluded this possiblity for all periods except the dead-time following t_1; this period must necessarily overlap that following t_2, since both terminate before $t_c + \tau_0$; the latter must be less than $\mathscr{T}$, which cannot exceed $2\tau_0$ for the case we are considering, so that we have two dead-times of duration τ_0 both wholly within a period $< 2\tau_0$ long. The amount of the dead-time following t_2 which does not overlap that following t_1 is therefore $|t_1 - t_2|$, and it is for this period that we must specify that no "c" count occurs which could record in channel II. If t_1 occurs before t_2, this period occurs at the end of the dead-time following t_2, otherwise it occurs at the beginning of this dead-time. In either case, the required probability is given by $e^{-c|t_1-t_2|}$, giving for the total contingent probability in channel II

$$\int_0^{t_c} b.e^{-bt_c}\, e^{-c|t_1-t_2|}\, .\, dt_2.$$

Having thus sufficiently specified that no unwanted counts occur, we have ensured that the "b" count at t_2 will be recorded, so that no further term is needed to express this condition.

To evaluate the integral, it is convenient to exclude cases for which $t_1 > t_2$, and to add these in later by taking the result obtained with "a" and "b" interchanged. We then have the integral:

$$\int_{t_c=0}^{\mathscr{T}-\tau_0} abc.e^{-(a+b+c)t_c} \int_{t_2=0}^{t_c} \int_{t_1=0}^{t_2} e^{-ct_2} e^{+ct_1}\, dt_1\, dt_2\, dt_c,$$

where we must first integrate with respect to t_1, then t_2, and finally t_c. We must then add the interchanged expression, noting that the case $t_1 = t_2$ is unlikely (it is, in fact, a random coincidence and is computed as such).

The final result for the expected fraction of coincidences which are recorded is then obtained by summing all four cases, including the two expressions for the last case, adding the original expression (equation [8]), and dividing the result by the expected number of coincidences $c\mathscr{T}$, as explained under (*i*) above. The result valid for $1 \leqslant \mathscr{T}/\tau_0 \leqslant 2$ is

$$[14]\quad \frac{1}{(a+b+c)\mathscr{T}}\Bigg[1 - e^{-(a+b+c)\mathscr{T}} + \left\{\frac{1 - e^{-(a+b+c)(\mathscr{T}-\tau_0)}}{a+b+c} - (\mathscr{T}-\tau_0)e^{-(a+b+c)(\mathscr{T}-\tau_0)}\right\} \times \left\{a+b+c+\frac{2ab}{c} + e^{-c\tau_0}[ae^{-b\tau_0} + be^{-a\tau_0}]\right\} + \frac{ac+bc+2ab}{c^2}\left\{e^{-(a+b+c)(\mathscr{T}-\tau_0)} - \frac{c+(a+b+c)\,e^{-(a+b+2c)(\mathscr{T}-\tau_0)}}{a+b+2c}\right\}\Bigg]$$

and this is the expression used for computing the theoretical curves of Fig. 14 for this range of $\mathscr{T}/\tau_0$.

APPENDIX II

In equation [13] f is the fraction of the total time occupied by pulses; in obtaining the second term, we assume that the "background" counting rates are so low that suppression of counts in the "background" period by other "background" counts can be neglected (i.e., we take $\phi_b = 1$). The term δ expresses the effect of counts late in the pulse in suppressing background counts, and of background counts just before the pulse in suppressing counts within the pulse. These two effects are approximately equal, as was shown by one of us (5); the argument used is not quite rigorous for the coincidence case, but since the whole correction is small, we feel it is sufficiently accurate to compute one of these effects (the former of the two stated above) and double the result to allow for the other. For computing this small correction we also make the approximation that the suppression probabilities near the end of the pulse have reached those prevailing in unpulsed counting conditions (this is obviously a poor approximation for $\mathscr{T}/\tau_0 < 1$). Then the probability that channel I is "dead" at the moment the pulse ends is taken as $\rho_1(a + c)\tau_0 = D_1$, say, with a similar expression (D_2) for the second channel. On the average these "dead" periods persist for a time $\tau_0/2$ after the pulse has ended, during which period an average of $c_0\tau_0/2$ "background" coincidences occur. If there are p pulses per second, we have then an average of $pc_0\tau_0/2$ coincidences per second subject to this effect, and, since random coincidences during the "background" period are negligible, we may say that these coincidences will be lost (and therefore be included in the correction term δ) if either or both of the channels are dead. The difficulty is to compute the probability of this, knowing the probabilities of the separate channels being "dead", but realizing that these probabilities are correlated. If they were uncorrelated, the required probability would be $D_1 + D_2 - D_1D_2$, but remembering that of the $\rho_1(a + c)$ per second suppressing events in channel I (or $\rho_2(b + c)$ in channel II), $\gamma\rho_1\rho_2 c$ are coincident and only contribute once to the probability required, we obtain then for the probability of either, or both, of the channels being dead, the following expression

$$\tau_0[\gamma\rho_1\rho_2 c + \rho_1(a + c.\overline{1 - \gamma\rho_2}) + \rho_2(b + c.\overline{1 - \gamma\rho_1}) - \rho_1\rho_2(a + c\,.\,\overline{1 - \gamma\rho_2})(b + c\,.\,\overline{1 - \gamma\rho_1})\tau_0]$$

giving for the average number of counts per second suppressed in this way:

$$[15] \quad \frac{pc_0\tau_0}{2}\left[\rho_1(a+c)+\rho_2(b+c) - \rho_1\rho_2\{\gamma c+\tau_0(a+c.\overline{1 - \gamma\rho_2})(b+c.\overline{1 - \gamma\rho_1})\}\right].$$

In this expression we have neglected the correlation between the occurrences in the two channels of counts which do not record as coincidences, but we feel that this approximation is allowable in a small correction term. This result must be doubled, as explained above, to allow for effects at the beginning of the pulse, although in fact the argument is somewhat different for this case, and doubling is only justifiable if $a_0/c_0 = a/c$ and $b_0/c_0 = b/c$. In some of our cases the left-hand sides of these equations are distinctly larger than the right-hand sides; for this and some other reasons we may have underestimated the

quantity δ. The approximation of removing the terms in $c.\overline{1 - \gamma\rho}$ from the negative product term at least makes a correction of the required sign, giving

[16] $$\delta = pc_0\tau_0^2[\rho_1(a + c) + \rho_2(b + c) - \rho_1\rho_2(\gamma c + ab\tau_0)].$$

This approximation is quite adequate for our purposes, since δ is commonly less than 0.5% and seldom exceeds 1% of the total counts, even at the highest wheel speeds used (p large), while the statistical error of our results is usually about $\pm$ 0.6% and there may be a systematic error as large as 0.4% from an imperfect knowledge of the magnitude of the background itself.

APPENDIX III

Summary of Procedure for Correcting Observed Coincidence Counting Rates

I. *Unpulsed Counting*

(i) Correction for finite coincidence resolution time:

[6] $$N/T = \gamma\rho_1\rho_2[c + (2ab + bc + ca)\tau_c + \text{higher terms}].$$

Higher terms almost always negligible (cf. §6.3).

(ii) Determination of γ

[5] $$\gamma = 1 + [1 - e^{-\beta\tau_c}]c/\beta$$

[7] $$\beta = 1.08\sqrt{a^2 + b^2 + 2ab\,.\,e^{-(a+b)/c}}$$

II. *Pulsed Counting*

(i) Correction for background:

[13] $$N/T = \phi fc + (1 - f)\,c_0 - \delta.$$

For δ, see Appendix II (equation [15] or [16]).

(ii) Correction for finite coincidence resolution time:

[12] $$\phi = \phi_0\left[1 + \frac{(2ab + bc + ca)}{c}\tau_c + O(\tau_c^{\,2})\right].$$

For conditions when last term is negligible, see last paragraph, §9.

(iii) Calculation of ϕ_0:

[8] $$\text{If } \mathcal{T} \leqslant \tau_0,\ \phi_0 = \frac{1 - e^{-(a+b+c)\mathcal{T}}}{(a + b + c)\mathcal{T}}.$$

If $\tau_0 < \mathcal{T} \leqslant 2\tau_0$, ϕ_0 given by equation [14] (Appendix I).

[9] If $\mathcal{T} > 2\tau_0$, $\phi_0 = \gamma\rho_1\rho_2 + 2[\phi_2 - \gamma\rho_1\rho_2]\tau_0/\mathcal{T}$

where ϕ_2 = the value of ϕ_0 for $\mathcal{T} = 2\tau_0$ from equation [14].

REFERENCES

1. COOKE-YARBOROUGH, E. H. J. Sci. Instruments, 26: 96. 1949.
2. ELMORE, W. C. Nucleonics, 6 (1): 26. 1950.
3. FEATHER, N. Proc. Cambridge Phil. Soc. 45: 648. 1949.
4. RUARK, A. E. and BRAMMER, F. E. Phys. Rev. 52: 322. 1937.
5. WESTCOTT, C. H. Proc. Roy. Soc. (London), A, 194: 508. 1948.

NOTE

GRAIN SIZE IN ILFORD G5 EMULSIONS*

By E. Pickup

During the course of work on the processing of emulsions, electron microscope photographs were taken of unprocessed and processed emulsions. Similar photographs have been published,** but we have not previously seen any results for G5 emulsions. The grain size and its distribution is of some importance in any detailed consideration of ionization energy losses along the tracks of particles in emulsions. To make full use of any future increase in grain sensitivity a smaller grain size will be necessary for electron sensitive emulsions.

The unprocessed emulsion used was from Ilford batch No. Z6658 (December, 1952), 400 microns thick, and a sample of the emulsion was dissolved with warm water, the solution being well stirred, and specimens collected on standard holders (on formvar on copper grids) for use in a 50,000 kv. electron microscope. Fig. 1*a* shows a reproduction of the silver bromide grains. These are almost spherical and fairly uniform in size. Measurements on 330 grains gave an optimum grain diameter of 0.31 μ, 78% of the grains having diameters between 0.25 and 0.38 μ, with the grain size ranging from 0.1 to 0.45 μ. Fig. 2 shows the grain size distribution measured for the unprocessed emulsion. The groups of grains in Fig. 1a_2 probably represent grains as they are originally packed in the emulsion. When the electron beam intensity is increased the halide grains are unstable, and in a few seconds silver forms locally in small threads and beads about the original grain, which becomes hollow with a faint black outline, a similar phenomenon being observed by Winand** with C2 emulsions. Fig. 1*b* shows the appearance of the grains after a more intense electron bombardment than for Fig. 1*a*. It should be noted that Fig. 1*a* shows some evidence of "print-out" effect, but not enough to affect the size distribution results.

Photographs of G5 emulsions, processed in the usual way by the temperature development method (about 40 min. on the hot plate with amidol developer) after exposure to cosmic rays in a balloon flight, showed grain sizes ranging from 0.05 or less to 0.6 μ. The emulsion was dissolved in warm water and, owing to the relatively sparse concentration of grains this time, it was necessary to enrich the solution by centrifuging to obtain thin enough specimen films showing several grains. There were many small grains such as always appear in emulsions processed this way. It appears unlikely that most of these are

* *Issued as N.R.C. No. 3020.*

** *See Von Ardenne, M. Z. angew. Phot. Wiss. u. Tech. 2: 14. 1940; Hall, C. E. and Schoen, A. L. J. Optical Soc. Am. 31: 281. 1941, for ordinary emulsion grains; Winand, L. Fundamental mechanisms of photographic sensitivity. Butterworth's Scientific Publications, London. 1951. p. 286 for C2 emulsions; Knowles, W. and Demers, P. Phys. Rev. 72: 535. 1947, for some grain sizes.*

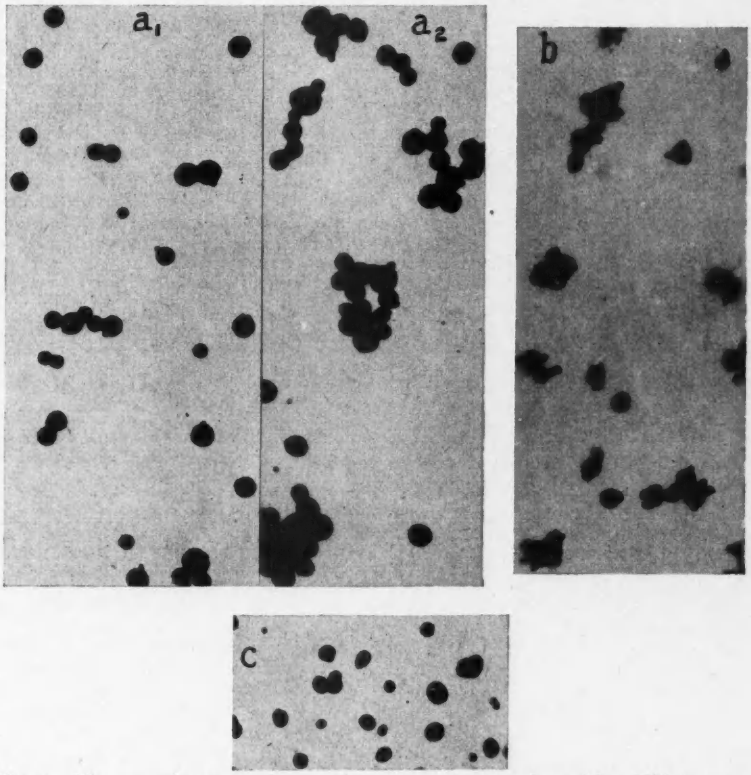

FIG. 1. Electron microscope photographs: a_1, a_2, unprocessed emulsion 9500× magn.; b, unprocessed emulsion after intense electron bombardment, 9500× magn.; c, processed emulsion, 5300× magn. (electron microscope magn. 4000× with 5–10% accuracy).

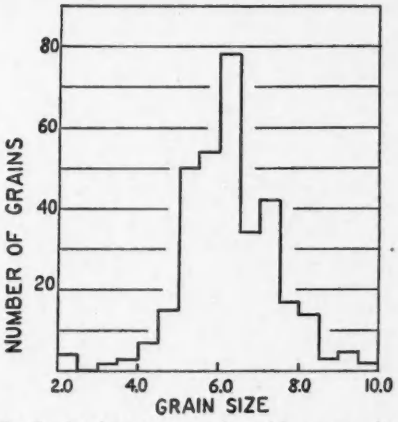

FIG. 2. Grain size distribution for unprocessed emulsion; one unit of size = 0.05 microns.

due to any partial or forced development of silver bromide grains.* Most of the grains along the tracks of minimum ionization particles in this emulsion, viewed under an optical microscope, are of the larger sizes. Fig. 1*c* shows some grains in the processed emulsion. The grains (silver) are approximately spherical, and are unaffected by increasing the intensity of the electron beam.

We are indebted to Mr. W. J. Forsyth of Dr. W. H. Barnes's group here, who made the specimens and electron microscope exposures.

* *According to a private communication from Mr. C. Waller, Ilford Limited, they are probably due to colloidal silver particles, which are responsible for yellow stain, and they are also found in the gelatin layer in sandwich emulsion.*

RECEIVED APRIL 16, 1953.
DIVISION OF PHYSICS,
NATIONAL RESEARCH COUNCIL,
OTTAWA, CANADA.

Under this heading brief reports of important discoveries in physics may be published. These reports should not exceed 600 words and, for any issue, should be submitted not later than six weeks previous to the first day of the month of issue. No proof will be sent to the authors.

Note on Some Neutron Capture γ-Rays from Magnesium*

We have reported elsewhere (4) preliminary measurements made with a pair spectrometer on the energies and intensities of the γ-rays produced by thermal neutron capture in magnesium. We wish to report here some results obtained from a more detailed study of one of these γ-rays. This is the γ-ray denoted by the letter F, for which the energy quoted was 6.39 ± 0.05 Mev. and the intensity 5 photons per 100 captures. It was not clear whether this γ-ray was the ground state γ-ray in Mg^{27} or the γ-ray representing the transition to the second excited state of Mg^{25}. The neutron binding energy of Mg^{27} may be obtained by adding the binding energy of the deuteron (5), 2.226 ± 0.003 Mev., to the Q value 4.207 ± 0.006 Mev. (2) for the reaction $Mg^{26}(d, p)Mg^{27}$. The result obtained is 6.433 ± 0.007 Mev. The energy of the transition between the compound state formed at the neutron binding energy of Mg^{25} and its second excited state (1) is 6.347 ± 0.007 Mev. The two γ-rays, both of which should be weak but detectable, have energies which were too close together for the resolution of the apparatus originally used in the study of neutron capture γ-rays. No other transitions in Mg^{25} or Mg^{26} are expected to produce γ-rays with energies near these values. Owing to interest in the intensity of the ground state transition in Mg^{27}, we decided to investigate the coincidence peak produced by the γ-ray F in more detail.

The results obtained with a new and more accurate apparatus (with a line width of 100 kev.) are shown in Fig. 1. Two γ-rays appear in place of the single peak F; we denote these by F_1 and F_2. Their energies are respectively 6.440 ± 0.008 Mev. and 6.358 ± 0.007 Mev. The γ-ray F_1 has an energy in good agreement with that expected of the ground state γ-ray in Mg^{27}. The energy of F_2 is somewhat greater than that expected for the transition to the second excited state in Mg^{25} but the discrepancy is less than the sum of the probable errors of the two energy determinations. No other γ-ray is expected to have a similar energy in the magnesium spectrum and there can be little doubt that this γ-ray is to be identified with this transition.

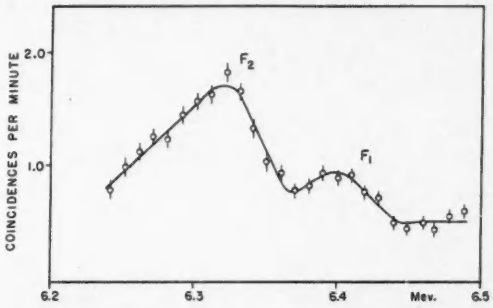

FIG. 1. Coincidence spectrum of magnesium capture radiation near 6.3 Mev. Line width 100 kev.

The intensities were determined by comparing the peak counting rates with that produced by the peak J of the magnesium spectrum. It was assumed that the background under peaks F_1 and F_2 was constant at the value shown beyond peak F_1 in Fig. 1. The measured intensity of the γ-ray J (which is caused by capture in Mg^{24}), obtained on the basis of the original nickel comparison measurement (4) and with a new calibration of the counting efficiency of the pair spectrometer (3), is about 0.7 photon per capture in natural magnesium.** With this value for J, we find that the intensity of F_1 is 1.3, and that of F_2, 3.5 photons per 100 captures

*Issued as A.E.C.L. No. 49.

***The intensity would appear to be too high for it corresponds to an intensity of 1.40 photons per capture in Mg^{24}. This figure is based on the isotopic capture cross sections for the magnesium isotopes given by Pomerance (Phys. Rev. 88: 412. 1952). However, the estimated error of Pomerance's figures is sufficient to account for the discrepancy.*

in natural magnesium. Since Mg^{26} is known to contribute (6) about 10% of the total thermal capture cross section of natural magnesium, the γ-ray F_1, therefore, is equivalent to about 13 photons per 100 captures in pure Mg^{26}. This value is higher than that of the corresponding ground state γ-ray in Si^{29} (2% per capture), which is also a pure magnetic dipole radiation and is emitted between states with the same orbital configuration, but the difference is probably not significant.

We have used this occasion to determine more carefully the energy of the γ-ray J. The mean of several measurements made with different resolutions is 3.918 ± 0.004 Mev. This result is in good agreement with the difference (3.918 Mev.) between the neutron binding energy of Mg^{25} (7.323 ± 0.008 Mev.) and the energy of the level at 3.405 ± 0.007 Mev. Another possibility, but one in less satisfactory agreement with the energy measurements, is that the γ-ray J represents the energy of the transition between the state at 3.898 ± 0.008 Mev. and the ground state.

1. ENDT, P. M., ENGE, H. A., HAFFNER, J. W., and BUECHNER, W. W. Phys. Rev. 87: 27. 1952.
2. ENDT, P. M., HAFFNER, J. W., and VAN PATTER, D. M. Phys. Rev. 86: 518. 1952.
3. KINSEY, B. B. and BARTHOLOMEW, G. A. Can. J. Phys. 31: 537. 1953.
4. KINSEY, B. B., BARTHOLOMEW, G. A., and WALKER, W. H. Phys. Rev. 83: 519. 1951.
5. MOBLEY R. C. and LAUBENSTEIN, R. A. Phys. Rev. 80: 309. 1950.
6. SEREN, L., FRIEDLANDER, H. N., and TURKEL, S. H. Phys. Rev. 72: 888. 1947.

RECEIVED MAY 15, 1953.
ATOMIC ENERGY OF CANADA LIMITED,
CHALK RIVER, ONTARIO.

B. B. KINSEY
G. A. BARTHOLOMEW

CANADIAN JOURNAL OF PHYSICS

Notice to Contributors

GENERAL: Manuscripts should be typewritten, double spaced, and the **original and one extra copy** submitted. Style, arrangement, spelling, and abbreviations should conform to the usage of this Journal. Names of all simple compounds, rather than their formulas, should be used in the text. Greek letters or unusual signs should be written plainly or explained by marginal notes. Superscripts and subscripts must be legible and carefully placed. Manuscripts should be carefully checked before being submitted, to reduce the need for changes after the type has been set. If authors require changes to be made after the type is set, they will be charged for changes that are considered to be excessive. **All pages, whether text, figures, or tables, should be numbered.**

ABSTRACT: **An abstract of not more than about 200 words, indicating the scope of the work and the principal findings, is required.**

ILLUSTRATIONS:

(i) *Line Drawings:* All lines should be of sufficient thickness to reproduce well. Drawings should be carefully made with India ink on white drawing paper, blue tracing linen, or co-ordinate paper **ruled in blue only**; any co-ordinate lines that are to appear in the reproduction should be ruled in black ink. Paper ruled in **green, yellow, or red should not be used** unless it is desired to have all the co-ordinate lines show. Lettering and numerals should be neatly done in India ink preferably with a stencil (**do not use typewriting**) and be of such size that they will be legible and not less than one millimeter in height when reproduced in a cut three inches wide. All experimental points should be carefully drawn with instruments. Illustrations need not be more than two or three times the size of the desired reproduction, but the ratio of height to width should conform with that of the type page. **The original drawings and one set of small but clear photographic copies are to be submitted.**

(ii) *Photographs:* Prints should be made on glossy paper, with strong contrasts; they should be trimmed to remove all extraneous material so that essential features only are shown. Photographs should be submitted **in duplicate**; if they are to be reproduced in groups, one set should be so arranged and mounted on cardboard with rubber cement; the duplicate set should be unmounted.

(iii) *General:* **The author's name, title of paper, and figure number should be written in the lower left hand corner (outside the illustration proper) of the sheets on which the illustrations appear.** Captions should not be written on the illustrations, but typed together at the end of the manuscript. All figures (including each figure of the plates) should be numbered consecutively from 1 up (arabic numerals). **Each figure should be referred to in the text.** If authors desire to alter a cut, they will be charged for the new cut.

TABLES: Each table should be typed on a separate sheet. Titles should be given for all tables, which should be numbered in roman numerals. Column heads should be brief and textual matter in tables confined to a minimum. **Each table should be referred to in the text.**

REFERENCES: **These should be listed alphabetically by authors' names, numbered in that order, and placed at the end of the paper.** The form of literature citation should be that used in this Journal. **Titles of papers should not be given.** The first page only of the references cited should be given. **All citations should be checked with the original articles.** Each citation should be referred to in the text by means of the key number.

REPRINTS: A total of 50 reprints of each paper, without covers, are supplied free to the authors. Additional reprints will be supplied according to a prescribed schedule of charges. On request, covers can be supplied at cost.

Approximate charges for reprints may be calculated from the number of printed pages, obtained by multiplying by 0.6 the number of manuscript pages (double-spaced typewritten sheets, 8½ in. by 11 in.) and making allowance for space occupied by line drawings and half-tones (not inserts). The cost per page is tabulated at the back of the reprint request form sent with the galley.

Contents

Page

A Rapid-scanning Auroral Spectrometer—*D. M. Hunten* - - - - 681

The Photoelectric Constants of Iodine— *D. C. West* - - - - - - 691

Meteorological Variations in the Quantity of Atmospheric Ozone over Edmonton (Lat. 53° 34′ N. Long. 113° 31′ W.)—*E. H. Gowan and R. E. Leppard* - - - - - - - - - - - - - - - 702

The Design of an Automatic Recording Electroscope and Its Use to Determine Half-lives in Radioactive Decay—*Rosalie M. Bartholomew, F. Brown, W. D. Howell, W. R. J. Shorey, and L. Yaffe* - 714

Photo-alpha Reactions in Nuclear Emulsions—*C. H. Millar and A. G. W. Cameron* - - - - - - - - - - - - - - - - - 723

Effect of Radar Sensitivity on Meteor Echo Durations—*D. W. R. McKinley* - 758

Grid Ionization Chamber Measurements of Electron Drift Velocities in Gas Mixtures—*W. N. English and G. C. Hanna* - - - - 768

The $O^{16}(\gamma, n)O^{15}$ and $O^{18}(\gamma, p)N^{17}$ Reactions—*R. Montalbetti and L. Katz* - 798

The Decay of the Populations of Neon Atoms in the $2p^5 3s$ Levels—*Donald J. Eckl* - - - - - - - - - - - - - - - - - - 804

Second Order Nuclear Quadrupole Effects in Single Crystals. Part I. Theoretical—*G. M. Volkoff* - - - - - - - - - - - - - - 820

Second Order Nuclear Quadrupole Effects in Single Crystals. Part II. Experimental Results for Spodumene—*H. E. Petch, N. G. Cranna, and G. M. Volkoff* - - - - - - - - - - - - - - - 837

An Experimental Study of Counting Losses Due to Dead-time Effects—*C. H. Westcott, J. S. Greenberg, and J. S. Kirkaldy* 859

Grain Size in Ilford G5 Emulsions—*E. Pickup* - - - - - - - - 898

Letter to the Editor:

Note on Some Neutron Capture γ-Rays from Magnesium—*B. B. Kinsey and G. A. Bartholomew* - - - - - - - - - 901

Printed in Canada *by* University of Toronto Press